

LANCASTER UNIVERSITY

DOCTORAL THESIS

**Mid-Infrared Resonant Cavity-Enhanced
Photodetectors**

Author:

Andrew BAINBRIDGE

Supervisor:

Dr. Andrew R. J. MARSHALL

*A thesis submitted in fulfillment of the requirements
for the degree of Doctor of Philosophy*

in the

**Quantum Nanotechnology Group
Physics Department**

September 22, 2022

Declaration of Authorship

This thesis has not been submitted in support of an application for another degree at this or any other university. It is the result of my own work. Where there is exception to this specific reference has been made to the work of others. Many of the ideas in this thesis were the product of discussions with my supervisor Dr Andrew Marshall.

LANCASTER UNIVERSITY

Abstract

Faculty of Science and Technology

Physics Department

Doctor of Philosophy

Mid-Infrared Resonant Cavity-Enhanced Photodetectors

by Andrew BAINBRIDGE

Resonant cavity-enhanced photodetectors can be utilised for spectroscopic sensing, due to their narrow, adjustable spectral responses. The narrow response can be designed to align with an absorption peak of a target molecule, whilst also not covering neighbouring absorption peaks. Therefore, these detectors can offer an intrinsically high spectral selectivity. This thesis reports on the design, fabrication and analysis of resonant cavity-enhanced photodetectors for sensing in the mid-infrared. The structures all use III-V semiconductor alloys and employ distributed Bragg reflectors as high-reflectivity, highly selective and highly tunable mirrors. Fabricated detectors demonstrate the expected narrow, enhanced responses with full-widths at half-maximum of < 30 nm and enhancement factors of > 10 . The tunability of the spectral responses is also demonstrated through the fabrication of structures with the same layer materials, but differing resonance wavelengths. The dependence of the resonance wavelength on the layer thicknesses is utilised with a novel concept of wavelength chirped resonant cavity-enhanced photodetectors. In these structures, the layer thicknesses are graded across a single wafer to create an array of detectors with spectral responses that shift across the wafer. Fabricated arrays demonstrate the benefit of the spectral response variation for spectroscopic sensing. The hyperspectral measurements can determine significantly more detailed spectral information than is possible by a single resonant cavity-enhanced photodetector. This wavelength chirp concept opens up the possibility of a solid-state spectrometer based on resonant cavity-enhanced photodetectors.

Papers and Presentations

Papers Published

- Craig, AP, Al-Saymari, F, Jain, M, **Bainbridge, A**, Savich, GR, Golding, T, Krier, A, Wicks, GW and Marshall, ARJ 2019, 'Resonant cavity enhanced photodiodes on GaSb for the mid-wave infrared', Applied Physics Letters, vol. 114, no. 15, 151107. <https://doi.org/10.1063/1.5082895>
- Letka, V, **Bainbridge, A**, Craig, AP, Al-Saymari, F and Marshall, ARJ 2019, 'Resonant cavity-enhanced photodetector incorporating a type-II superlattice to extend MWIR sensitivity', Optics Express, vol. 27, no. 17, pp. 23970-23980. <https://doi.org/10.1364/OE.27.023970>
- Letka, V, Craig, AP, **Bainbridge, A** and Marshall, ARJ 2020, 'A superlattice-based resonant cavity-enhanced photodetector operating in the long-wavelength infrared', Applied Physics Letters, vol. 117, no. 7, 073503. <https://doi.org/10.1063/5.0013553>
- **Bainbridge, A**, Mamic, K, Hanks, LA, Al-Saymari, F, Craig, AP and Marshall, ARJ 2020, 'Resonant Cavity Enhanced Photodiodes in the Short-Wave Infrared for Spectroscopic Detection', IEEE Photonics Technology Letters, vol. 32, no. 21, pp. 1369-1372. <https://doi.org/10.1109/LPT.2020.3025977>
- **Bainbridge, A**, Craig, AP, Al-Saymari, F, Krier, A and Marshall, ARJ 2021, 'Resonant Cavity-Enhanced Photodiodes for Spectroscopy of C-H Bonds', physica status solidi (a). <https://doi.org/10.1002/pssa.202100056>
- **Bainbridge, A**, Hanks, LA, Craig, AP and Marshall, ARJ 2022, 'Resonant Cavity-Enhanced Photodiode Array for Miniaturised Spectroscopic Sensing', Optics Express, vol. 30, no. 3, pp. 3230-3237. <https://doi.org/10.1364/OE.444547>

Oral Presentations at Conferences

- **Bainbridge, A**, Craig, AP and Marshall, ARJ 2019, 'SWIR Spectroscopic Sensing Using RCE Detectors', presented at UK Semiconductors, Sheffield.

- Letka, V, **Bainbridge, A**, Craig, AP, Al-Saymari, F, Marshall, ARJ, B.F., A (ed.), G.F., F (ed.), J.L., M (ed.), L., Z (ed.) and (SPIE), TSOP-OIE 2020, 'Extension of resonant cavity-enhanced photodetection into the MWIR and LWIR ranges using a Ga-free type-II strained-layer superlattice', Paper presented at Infrared Technology and Applications XLVI, United States, 27/04/20 - 8/05/20. <https://doi.org/10.1117/12.2557508>
- **Bainbridge, A**, Craig, AP and Marshall, ARJ 2021, 'Design and Analysis of InAs-based Resonant Cavity Enhanced Photodiodes', presented at MIOMD, Surrey, 01/09/2021 - 03/09/2021.
- **Bainbridge, A** and Marshall, ARJ 2022, 'Resonant cavity-enhanced photodetectors arrays for multispectral sensing', Paper presented at SPIE Photonics West, 22/01/2022 - 27/01/2022
- Mamic, K, **Bainbridge, A**, Hanks, L and Marshall ARJ 2022, 'InGaAsSb for cut-off tuned SWIR detectors', presented at UK Semiconductors, Sheffield.
- Hanks, L, Mamic, K, **Bainbridge, A**, Craig, AP, Klos, K, Castano, FJ and Marshall, ARJ 2022, 'Development of Quasi-Planar $\text{In}_{0.14}\text{Ga}_{0.86}\text{As}_{0.10}\text{Sb}_{0.90}$ pBn Devices for Spectroscopic Sensing', presented at UK Semiconductors, Sheffield.
- **Bainbridge, A**, Craig, AP, Hanks, L and Marshall, ARJ 2022, 'Resonant Cavity Enhanced Photodetectors on GaSb with a chirped response', presented at UK Semiconductors, Sheffield.

Contents

Declaration of Authorship	iii
Abstract	vi
Papers and Presentations	vii
1 Introduction	1
2 Background	5
2.1 Device Architectures	5
2.1.1 Photoconductor	5
2.1.2 p-n Junction Photodiode	6
2.1.3 <i>nBn</i>	6
2.2 Dark Current Mechanisms	7
2.2.1 Majority Carrier Drift Current	8
2.2.2 Tunnelling Current	8
2.2.3 Generation-Recombination Current	8
2.2.4 Diffusion Current	10
Auger Generation	10
Shockley-Read-Hall Generation	12
2.2.5 Surface Current	13
2.2.6 <i>nBn</i> Current Mechanisms	13
2.3 Resonant Cavity Structures	14
2.3.1 Distributed Bragg Reflectors	15
2.3.2 Cavities	17
2.3.3 Advantages	19

2.3.4	Disadvantages	21
2.4	Modelling	22
2.4.1	Transfer Matrix Method	22
2.4.2	Transmission Line Model Method	28
2.4.3	Electric Field	33
2.4.4	Model Program Implementation	34
3	Literature Review	39
3.1	SWIR Photodetectors	39
3.2	Resonant Cavity Enhancement	42
3.3	Refractive Indices of III-V Semiconductors	53
3.4	Absorption Coefficients of III-V Semiconductors	55
3.5	Spectral Gas Sensing	57
3.5.1	Miniaturisation	61
4	Experimental Methods	65
4.1	Molecular Beam Epitaxy	65
4.2	X-Ray Diffraction	70
4.3	Device Processing	73
4.3.1	Photolithography	74
4.3.2	Chemical Etching	76
4.3.3	Thermal Evaporation of Contacts	77
4.3.4	Plasma Enhanced Chemical Vapour Deposition	79
4.3.5	Reactive Ion Etching	79
4.3.6	SU-8 Passivation/Dielectric	80
4.3.7	Design of Mask for RCE-PDs	82
4.4	Characterisation	85
4.4.1	Transmittance	85
4.4.2	Reflectance	88
4.4.3	Spectral Response	89
4.4.4	Dark Currents	91
4.4.5	Optical Wafer Mapping	93

5	Results I: Short-Wave Infrared RCE-PDs	97
5.1	Cavity	97
5.2	GaSb/AlAsSb DBRs	101
5.3	Complete SWIR RCE-PD	103
5.3.1	MBE Growth	107
5.4	X-Ray Diffraction Analysis	108
5.5	Optical Properties	110
5.6	Spectral Response	113
5.6.1	Responsivity/QE	113
5.6.2	Resonance Wavelength Temperature Dependence	113
5.6.3	Quantum Efficiency Temperature Dependence	115
5.6.4	Bandwidth Temperature Dependence	119
5.7	Electrical Properties	121
5.7.1	Dark Current	121
5.7.2	Activation Energies	124
5.7.3	Dependence on Absorber Thickness	126
5.7.4	Specific Detectivity	127
5.8	Spectral Tuning	128
5.9	Conclusions and Future Work	131
5.9.1	Future Work	133
6	Results II: Mid-Wave Infrared RCE-PDs	135
6.1	InAs/AlAsSb nBn	136
6.2	GaAsSb/AlAsSb DBRs	139
6.3	Complete RCE-PD on InAs Substrate	141
6.4	Optical Properties	146
6.4.1	Transmittance and Reflectance	146
6.4.2	Responsivity/QE	148
6.4.3	Resonant Peak	150
6.5	Electrical Properties	154
6.5.1	Dark Currents	154
6.5.2	Specific Detectivity	156

6.6	Conclusions and Future Work	158
6.6.1	Future Work	159
7	Results III: Chirped RCE-PDs	161
7.1	Theory and Purpose	161
7.2	Design Parameters, Considerations and Modelling	165
7.2.1	Epitaxial Chirp Method	165
7.2.2	Cavity Only Thickness Gradient	168
7.2.3	DBR only Chirp	173
7.2.4	Cavity and DBR Chirp	176
7.3	Experimental Results for InGaAsSb RCE-PDs	179
7.3.1	Chirped Cavity Only Samples	180
	5/2 λ Cavity - Attempt 1	180
	5/2 λ Cavity - Attempt 2	181
	5/2 λ Cavity - Attempt 3	183
7.3.2	Chirped Cavity and DBRs Sample	185
7.4	Spectrum Recreation Tests	188
7.5	Analysis	191
7.5.1	Thickness Gradient Coefficient	191
7.5.2	Angular Dependence	192
7.5.3	Temperature Dependence	193
7.5.4	FWHM	193
7.5.5	Linear Array Design	195
	Cavity Shielding	197
7.6	Conclusions	198
7.6.1	Future Work	199
8	Review of Research and Future Work	201
8.1	Review of Research	201
8.2	Future Work	203
	Bibliography	205

List of Figures

- 1.1 Transmittance spectra of a selection of gas species with absorption peaks in the mid-infrared. Spectra for methane (CH_4), carbon dioxide (CO_2), carbon monoxide (CO) and nitrous oxide (N_2O). Data from NIST.¹ 2
- 1.2 Zoomed transmittance spectra from figure 1.1 with the region covered by InAs detectors (purple) and a narrow region preferable for methane only sensing (red). The purple region covers significant absorption by other substances, but the red region does not. 3
- 2.1 Sketch of a photoconductor band diagram. Incoming photons generate electron-hole pairs that can freely travel in either direction, towards the contacts. The direction of travel is usually controlled by an applied bias voltage. E_v is the valence band energy, E_F is the Fermi level and E_c is the conduction band energy. 6
- 2.2 Sketch of a p-n junction photodiode band diagram. Incoming photons generate electron-hole pairs that can diffuse in the direction of the arrows. In the depletion region the in-built voltage causes carrier drift. Movement of electrons in the opposite direction to that shown is blocked by the depletion region. E_v is the valence band energy, E_F is the Fermi level and E_c is the conduction band energy. 7
- 2.3 Sketch of the band diagram of an nBn . Incoming photons generate electron-hole pairs that can diffuse in the direction of the arrows. Diffusion of electrons in the opposite direction is blocked by the barrier. E_v is the valence band energy, E_F is the Fermi level and E_c is the conduction band energy. 7

2.4	Sketch of the both tunnelling current mechanisms. Band-band tunnelling from the valence band to the conduction band directly and TAT via defects in the bandgap. E_v is the valence band energy and E_c is the conduction band energy.	9
2.5	Sketch of the depletion region SRH mechanism. Electrons are promoted from the valence band to the conduction band in the depletion region via traps in the bandgap. Electrons and holes are subject to drift in the direction of the solid arrows. E_v is the valence band energy and E_c is the conduction band energy.	9
2.6	Sketch of the Auger 1 process. An energetic conduction band electron, E_c , transfers its energy to another electron in the valence band, E_{v-HH} . The valence band electron is promoted to the conduction band and a heavy hole is left behind in the valence band.	11
2.7	Combined figure showing the mechanisms for diffusion current generation in an nBn structure. Including the band-to-band Auger 1 process, defect assisted neutral region SRH and band-to-band photogeneration.	13
2.8	Simplified paths of light through an RCE-PD (left) and a conventional detector (right). In the conventional structure light is mostly absorbed on a single pass through the structure. In contrast, in the RCE-PD structure the light passes through the cavity multiple times, in a cycle between the mirrors.	14
2.9	A simple illustration of the light paths in a distributed Bragg reflector. At each interface the incident light is partially transmitted and partially reflected. If the wavelength of the incident light matches the design of the DBR then the reflected waves will interfere constructively.	16
2.10	Modelled reflection spectrum of DBRs with 5, 10 and 15 pairs of layers. n_H and n_L of 3.82 and 3.15 respectively were used. The plot highlights the increasing maximum reflection as the number of repeats in the DBR is increased. The plot is modelled following the transfer matrix method, detailed in section 2.4.1.	17

- 2.11 An example of the light transmitted through a molecule, the transmission spectrum is for methane. With nothing in the path of the light, it is transmitted equally at all wavelengths. With a specific substance in the path, the light is highly transmitted at some wavelengths and partially absorbed at other wavelengths. The absorption spectrum is determined by the substance in the light path. 20
- 2.12 An example of the transfer of the electric field through a smooth interface between layers. There is a forward travelling component on both sides of the interface, E_0^+ on the left and $E_1'^+$ on the right. There is also a backward travelling component on both sides, E_0^- on the left and $E_1'^-$ on the right. 24
- 2.13 An example of the propagation of the electric field through a homogeneous layer. There is a forward travelling component at all points in the layer, E_0^+ at the left hand interface and $E(x)^+$ at distance x from the interface. There is also a backward travelling component on both sides, E_0^- at the left hand interface and $E(x)^-$ at distance x from the interface. 25
- 2.14 An example of the propagation of the electric field through a structure with N layers. Layers are labelled 1 to N from the left. Forward travelling waves with a $+$ and backward travelling waves with a $-$. The field to the right of each interface is labelled with a $'$ and with no apostrophe for the fields on the left. 26
- 2.15 An example of a transmittance and reflectance spectrum for a structure with no absorption in the cavity. Note: the lines coincide, so are difficult to distinguish. Both the transfer matrix model (dotted line) and transmission line model (solid line) are plotted. The input structure is designed to have a resonant wavelength at $\sim 3.3 \mu\text{m}$ 35
- 2.16 An example of the electric field in the structure for the resonance wavelength. The wave starts off in air on the left and travels through the DBRs (blue areas). A standing wave is formed, with a peak in the centre of the cavity (red area). The transmitted wave continues through the substrate (green area). 36

2.17	An example of the electric field in the structure for an off-resonance wavelength. The wave starts off in air on the left and travels through the DBRs (blue areas). The low amplitude wave does not have an anti-node at the centre of the cavity (red area). The transmitted wave is much lower amplitude in comparison to the incident wave and continues through the substrate (green area).	36
2.18	A colourmap of the electric field in the structure as a function of wavelength. The electric field through the structure is calculated for each wavelength, as shown in figures 2.16 and 2.17, with the electric field denoted by the colour. For resonant wavelengths, <i>e.g.</i> 3.3 μm , the amplitude of the field in the structure is enhanced. For non-resonant wavelengths, <i>e.g.</i> 3.1 μm , the amplitude of the field in the structure is reduced.	37
3.1	First vertical cavity laser structure, from H. Soda <i>et al.</i> ¹⁰³ , with an emission wavelength of 1.2 μm . It was named a 'surface-emitting injection laser' by the authors and it demonstrated the possibility of a resonant cavity perpendicular to the wafer surface.	43
3.2	Example of a VCSEL with two DBRs, from Geels <i>et al.</i> ¹⁰⁵ , with an emission wavelength of 970 nm. This is one of the first reported structures to use two DBRs as the reflectors, with no metallic reflector used.	45
3.3	A) Structure of an RCE-pin with InAs absorber, the bottom reflector is a DBR and the top reflector is the interface with air. B) Responsivity of the same RCE-pin. A clear resonance can be seen at 3.15 μm . This is one of the first reports of RCE-PDs in this spectral region. Both from Green <i>et al.</i> ¹¹⁴	48
3.4	Spectral response of a PbTe RCE-PD from Wang <i>et al.</i> ¹¹⁵ This structure utilise two DBRs as the reflectors, reducing the broadband response in comparison to previous structures without a top DBR.	48

3.5	A) Structure of an InAs RCE-PD. B) Spectral response of the same InAs RCE-PD. Both from O’Loughlin <i>et al.</i> ⁷ This structure is the most similar reported RCE-PD from the literature to the structures presented in this thesis. The use of two DBRs creates a high finesse cavity, with a narrow spectral response.	49
3.6	A) Sketch of a gas measurement setup utilising a broadband detector. The light from a broadband source passes through the gas chamber first, then through two filters onto separate detectors. B) Example spectral responses of the two channels in the setup. Each of the two filters allows different parts of the spectrum to be transmitted, resulting in differing spectral responses at the detectors. Both from J. Hodgkinson and R.P. Tatam ⁶	59
3.7	Example of a gas sensing setup using a QCL source, from Weidmann <i>et al.</i> ¹⁴⁵ The light from the laser passes through the flowing gas chamber and then directly into the detector. There is no filter or reference detector as in the previous, broadband light source setup.	60
3.8	An example of a gas sensing setup with a diffractive grating. Light source and detectors are both broadband. Multiple gas species can be measured simultaneously. The broadband light is split into multiple narrow bands that are directed onto separate detectors. The colour of the light is a visual aid and does not imply the wavelength.	61
3.9	Spectral filter design for miniaturised gas sensors, from Ayerden and Wolffenbuttel. ¹⁵¹ The tilted mirror acts to vary the path length of the resonator, thereby varying the spectral response across the detector array. The spectrum of incident light can be recreated from the current measurements of the entire array along with prior knowledge of the spectral responses.	62
3.10	Folded metasurface spectrometer design, from Faraji-Dana <i>et al.</i> ¹⁵² The design of the folded metasurfaces aims to split the light apart based on wavelength. Shorter wavelength light takes a path that focuses it on the right hand side of the detector array, while longer wavelength light is focused on the left hand side of the detector array.	62

- 3.11 Compositionally graded nanowire spectrometer, from Yang *et al.*¹⁵³
 The composition of the $\text{CdS}_x\text{Se}_{1-x}$ nanowire varies from one end to the other, resulting in a corresponding variation in the spectral response. 63
- 3.12 SEM image of a fabricated random scattering spectrometer chip, from Redding *et al.*¹⁵⁴ The incident light is randomly scattered, in a repeatable way, onto the detector channels on the outside of the semicircle. The spectrum falling on each detector is unique and allows for the spectrum of the incident light to be reconstructed. 64
- 4.1 Atomic visualisation of epitaxial layers in comparison to the substrate. (not to scale). In lattice-matched layers the atomic spacing of the epitaxial layers matches the spacing of the substrate. If the layers are strained then the atomic spacing of the two layers matches parallel to the interface, but is mismatched parallel to the growth direction. If the layers are relaxed then the atomic spacing is mismatched in all dimensions between the substrate and the epilayer. 68
- 4.2 Example of a HR-XRD measurement of a single layer grown on a substrate (red) and calculated diffraction curve (blue). The epilayer is lattice-mismatched with respect to the substrate, seen here by the differing diffraction angles of the two peaks. The size of the mismatch is determined by the angle between the two peaks. 73
- 4.3 Single resist photolithography steps - for subsequent etching or deposition. Starting with a clean wafer, (A), a layer of resist is spun onto it, (B), before the wafer is heated to harden the resist, (C). A mask is placed on top of the resist, (D), to protect specific areas from exposure to light. The subsequent exposure to ultraviolet light causes a chemical reaction in the exposed parts of the resist, (E). When submerged in a developing solution, MF-CD-26, only the exposed parts of the resist react with the solution and are removed, (F). 75

- 4.4 Exposure patterns of the resist after development. A) Underexposure B) Correct exposure C) Overexposure. In the underexposed resist the gap between the fingers is very narrow. In the correctly exposed resist the gap is approximately the same width as the fingers. In the overexposed resist the gap is wider than fingers. The colours are due to microscope lighting and do not signify exposure differences. 76
- 4.5 Two resist photolithography and thermal evaporation steps for metal contact deposition. Starting with a clean wafer, (A), a first layer of resist, a lift-off-resist, is spun onto it, (B), before the wafer is heated to harden the resist, (C). This resist is used to aid removal of the second resist later. The second resist is spun on, (D), and baked (E). A mask is placed on top of the resist, (F), to protect specific areas from exposure to light. The subsequent exposure to ultraviolet light causes a chemical reaction in the exposed parts of the resist, (G). When submerged in a developing solution, MF-CD-26, only the exposed parts of the resist react with the solution and are removed, (H). The metal is evaporated onto the exposed surfaces of the wafer, partially on the wafer surface and partially on the resist surface, (I). To leave only the metal on the wafer surface the resist, and metal above it, is stripped off. Removal of the second resist is aided by the more soluble lift-off-resist below, (J). 78
- 4.6 Post-growth device fabrication steps. (A) Epitaxial growth of layer III-V semiconductor structure. (B) Top DBR etch. (C) Contact layer etch. (D) SiN deposition. (E) Contact deposition. (F) Etch to define mesas. (G) SU-8 deposition. (H) Bond pad deposition. 83
- 4.7 An example of a transmittance spectrum for an RCE-PD. The significant elements have been labelled. The stopband is the spectral region with very low transmission through the structure. The resonant mode is the wavelength that is highly absorbed in the cavity of an RCE-PD. . 86

- 4.8 3D render of the internal beam path of the FTIR. (not to scale) The light source emits the infrared light, that is then reflected off a focusing mirror, through an aperture of chosen diameter and then into the interferometer. The interferometer splits the light into two paths, of varying distance, which then are both directed off of another focusing mirror and through the sample. The light transmitted through the sample is then focused onto a detector. 87
- 4.9 Beam path of the reflectance accessory for the FTIR. Image altered from datasheet.¹⁶⁹ The light from the internal interferometer of the FTIR is directed via a series of mirrors onto the surface of the sample at a set angle. The reflected light is then directed out of the accessory and onto the internal FTIR detector. 88
- 4.10 Measurement circuit for spectral response measurements using an FTIR. The sample is held inside a temperature-controlled cryostat, which is evacuated by a turbo pump. Light from the FTIR interferometer is directed onto the sample. The current generated in the device is measured through connection to a preamp, that provides a bias voltage and converts the current into a voltage signal. The analogue voltage signal is read by the FTIR electronics and converted to a digital reading. 90
- 4.11 An example of a responsivity spectrum of an RCE-PD. The resonant response is the sharp peak at $\sim 2.6 \mu\text{m}$ and there is an underlying broadband response that cuts off at $\sim 2.8 \mu\text{m}$ 92
- 4.12 Equipment setup for measurement of dark currents. The sample sits inside a probestation with cooling provided by liquid nitrogen. The temperature is regulated on the plate the sample sits by resistive heating. The temperature of the inner chamber wall is also controlled by the same combination. The chamber is evacuated by turbo pump. Current measurements are taken by probing the device, connected to a sourcemeter that provides a bias voltage and reads the current. . . . 93

- 4.13 An example of a resonance wavelength colourmap for a chirped RCE-PD. The x and y axis are the position on the wafer and the colour indicates the resonance wavelength at that location. 95
- 5.1 The theoretical cutoff wavelength as a function of the indium fraction for InGaAsSb lattice-matched to GaSb. The points are calculated based on equation 5.1, proposed by Adachi¹⁷². 99
- 5.2 Calculated valence and conduction band energies of an $\text{In}_{0.25}\text{Ga}_{0.75}\text{As}_{0.22}\text{Sb}_{0.78}$ and $\text{Al}_{0.36}\text{Ga}_{0.64}\text{Sb}$ *nBn* structure,¹⁷⁶ to demonstrate the band offsets between the layers. The conduction band (blue) has a large energy offset between the absorber and the barrier, whilst the valence band (orange) has a very small energy offset between the two layers. 100
- 5.3 Example of the cavity structure for a detector with a target wavelength of 2.2 μm . From the bottom the purposes of the layers are: cavity spacer, absorber, barrier and contact layer. The layer thicknesses are calculated to put the centre of the absorber at the centre of the optical path length of the cavity. 101
- 5.4 Modelled reflectance spectrum for an AlAsSb/GaSb DBR with varying numbers of layers. The transfer matrix model was used to create this figure, see section 2.4.1. The peak reflectance increases with number of pairs in the DBR, but tends to a maximum 100% limit. 103
- 5.5 Structure of the fabricated RCE-PD targeted at sensing in the SWIR. The two contacts are placed on top of the InGaAsSb contact layer. The mesa is defined by etching through the contact layer. The area covered by the negative contact is much larger than the device mesa. 105
- 5.6 Modelled colourmap of the resonance quantum efficiency as a function of both absorber thickness and number of top DBR repeats. The bottom DBR is set to 13 repeats and the structure follows figure 5.5. The green dot indicates the position of the fabricated structure. With the set parameters, the highest QE is modelled to be at around 40 nm absorber thickness with 5 repeats in the top DBR. 106

- 5.7 $\omega - 2\theta$ HR-XRD scan of the SWIR targeted epitaxial RCE-PD structure. The GaSb and AlAsSb epilayer peaks align closely with the substrate peak. The InGaAsSb and AlGaSb peaks are ~ -300 arcsecs lower (Sb rich) and the InAsSb is significantly mismatched at -1800 arcsecs. 109
- 5.8 Measured transmittance spectrum of the fabricated SWIR RCE-PD (purple) and modelled (red). The resonance peak of the measured spectrum is at a longer wavelength than modelled, indicating higher layer thicknesses in the cavity. 111
- 5.9 Colourmap of transmittance at the resonance wavelength, as a function of both absorption coefficient and GaSb refractive index. Both of these parameters are not easily controllable, but they are also not precisely known at the wavelengths of interest. This plot shows the significant effect of changes in these parameters on the resonance transmission, indicated by the colour. 112
- 5.10 Normalised spectral response of the SWIR RCE-PD at room temperature. An applied bias voltage of -100 mV is used. The resonant response is at $2.25 \mu\text{m}$ and an underlying broadband response is seen at lower wavelengths, with a cutoff at $2.4 \mu\text{m}$ 114
- 5.11 Left: Measured (squares) and modelled (circles) temperature dependence of the resonant peak wavelength of an RCE-PD with InGaAsSb absorber. The modelled used takes into account only changes in refractive indices of the layers. Right: Measured, normalised spectral response at temperatures between 225 K and 350 K, with 25 K steps. The data is plotted normalised for ease of peak comparison, so the amplitude at the resonance wavelengths is not meaningful. 116
- 5.12 (A) Measured quantum efficiency spectra for the RCE-PD. Increasing temperature going down, from 225 K to 350 K, with 25 K steps. (B) Temperature dependence of the quantum efficiency at resonance, the values are taken from the peaks of (A) and the uncertainties are determined through comparison with measurements at five other bias voltages. 116

- 5.13 Modelled dependence of the QE at the resonance wavelength on the absorption coefficient of the absorber. As expected, the QE increase rapidly with absorption coefficient at lower absorption. However, there is also a slight decrease as the absorption coefficient gets much higher. This is due to the high single-pass absorption in the cavity reducing the reflectance from the bottom DBR and damping the standing wave affect. 118
- 5.14 Measured FWHM of the resonance of the SWIR RCE-PD. At the lower temperatures there is linear increase in FWHM with temperature of 0.05 nm/K. There is a significant decrease above 300 K, possibly caused by enhanced noise in the measurements. 120
- 5.15 Modelled FWHM of the resonance for variations in absorption coefficient (bottom axis) and GaSb refractive index (top axis). Both of these parameters cannot be controlled and are subject to not well known temperature dependencies. The data can be used to infer the necessary variation in these parameters to cause the FWHM shift seen in the measured RCE-PD. 122
- 5.16 Temperature dependent dark current density for the SWIR RCE-PD from 77 K to 350 K, with 25 K steps. On the line of the orange arrow the current density increases monotonically with increasing temperature. . 123
- 5.17 Arrhenius plot derived from the dark current density measurements in figure 5.16, at a bias voltage of -100 mV, and in temperature steps of 25 K. Blue squares are the measured data points, and the blue line represents an activation energy of 319 meV. The orange line is a comparison to the heuristic Rule 07, which represents the minimum Auger limited dark currents for MCT detectors. 125
- 5.18 Arrhenius plot of the RCE-PD (blue squares) and the reference detector (green squares),⁶⁷ both with bias voltages of -100 mV. The blue line represents an activation energy of 319 meV and the green line represents an activation energy of 419 meV. 127

- 5.19 Specific detectivity at the resonance wavelength as a function of temperature and bias voltage for the RCE-PD (connected squares). Value for a conventional InGaAsSb nBn at 300 K (purple circle).⁶⁷ Comparison value to a commercially available extended-InGaAs photodiode with a peak at 2.2 μm and at a temperature of 250 K (orange triangle).¹⁹⁴ 128
- 5.20 A) Structures of XAB1219 (2.2 μm resonance) and XAB1388 (2.6 μm resonance). The longer resonance wavelength of XAB1388 is achieved with thicker DBRs and a thicker cavity (optical path length scaled linearly with resonance wavelength). B) Room temperature QE spectra of both structures. blueThe thicker layers of XAB1388 result in a longer resonance wavelength. The differences in peak QE and shape of the spectrum are not due to the thicker layers specifically, and are caused by variations in absorber alloy composition, different etchstop material, crystal growth quality and other variations. The structures are only intended as a comparison of resonance wavelength. 130
- 5.21 Normalised transmittance measurements of two samples, one with cavity absorption (red) and one without (black). The structure with cavity absorption has a lower resonant mode in the stopband, due to higher absorption at the resonant mode wavelength. 131
- 6.1 300 K normalised response of a bulk InAs nBn . This wafer was grown on the same MBE, with comparable growth parameters to the RCE-PD structures in this chapter. Therefore, it represents a very high similarity to material used for the RCE-PD structures. 136
- 6.2 Calculated valence and conduction band energies of a InAs/AlAsSb/InAs nBn .¹⁷⁶ The figure demonstrates the band offsets between the layers. The conduction band (blue) has a large energy offset between the absorber and the barrier, whilst the valence band (orange) has a very small energy offset between the two layers. 138

- 6.3 Modelled comparison of the reflectivity of DBRs constructed from GaSb/AlAsSb (blue) and GaAsSb/AlAsSb (pink). Solid lines represent 7 pair DBRs and the dashed line represents a 9 pair DBR. The lower refractive index delta of the GaAsSb/AlAsSb DBR results in lower peak reflectivity and a narrower stopband. The reflectivity can be increased with more repeats in the DBR. The transmission matrix model was used for all calculations. 140
- 6.4 Left: modelled reflectivity curves for GaAsSb/AlAsSb DBRs with numbers of pairs between 3 and 17. The peak reflectivity increases monotonically with increasing pairs, and the stopband edge gets sharper. Right: peak reflectivity taken from the plot on the left. 141
- 6.5 Model of peak QE as a function of both number of layer pairs in the top DBR and absorber thickness. The number of repeats in the bottom DBR was set at 12. The green dot indicates the position of the fabricated structure. The colour represents the peak QE in the modelled spectrum, with the transfer matrix model used. 142
- 6.6 Structure of the fabricated RCE-PD designed to target the MWIR spectral region. The structure uses an InAs and AlAsSb nBn in the cavity, surrounded by two DBRs with GaAsSb/AlAsSb layers and an InAs substrate. The device mesas are defined by etching the contact layer at the top of the cavity. 143
- 6.7 HR-XRD measurement of the fabricated MWIR RCE-PD (black). Modelled diffraction curve (purple). The highest peak is assumed to be the substrate material, InAs. The second peak on the right is caused by slightly As-rich AlAsSb at ~ 200 arcsecs from the substrate peak. The GaAsSb layers are the cause of the shoulder to the left of the substrate peak. 145
- 6.8 Normalised transmittance at normal incidence (red) and reflectance at 30° (blue) measurements on the epitaxial MWIR RCE-PD. The difference between the peaks at the resonant mode can be used to estimate the fraction of light that is absorbed in the structure. 146

- 6.9 Temperature dependent quantum efficiency spectra for the RCE-PD. 25 K steps between 200 K and 375 K. A bias voltage of -0.3 V is applied across the device for all measurements. The resonance peak shifts slightly longer with increasing temperature. 149
- 6.10 Temperature dependence of both the resonance wavelength (black) and cutoff wavelength of the InAs absorber (pink), for the MWIR RCE-PD. The resonance wavelength has a much lower temperature dependence than the cutoff wavelength, 0.27 nm/K and 2.3 nm/K, respectively. 150
- 6.11 A) Measured FWHM (black) and modelled FWHM based on temperature dependent refractive indices (purple). The measured FWHM has a high temperature dependence below 300 K and a moderate dependence above. The dependence of FWHM on refractive indices is less than the measured dependence at all temperatures. B) Measured FWHM (black) and modelled FWHM dependency on absorption coefficient (red). The dependence of the absorption coefficient at the resonance wavelength with temperature is not well known, but the range of 3000 cm^{-1} to 7000 cm^{-1} is realistic. The dashed red line follows the high temperature dependence of the measured FWHM and represents a $\frac{d\alpha}{dT}$ of 18 cm^{-1} K^{-1} 153
- 6.12 Left: Temperature dependent dark currents for the MWIR RCE-PD, between 100 K and 375 K, with 25 K steps. Right: Arrhenius plot derived from the dark current density with a bias voltage of -0.3 V (black). The black lines represents an activation energy of 302 meV. There are comparisons to Rule 07 (purple) and a conventional InAs nBn (orange).²⁵ 155
- 6.13 Peak specific detectivity measurements for the MWIR RCE-PD, using responsivity and dark current measurements. The specific detectivity decreases with temperature with an applied bias voltage of -0.3 V, but the different temperature dependencies of responsivity and dark current density result in a low temperature dependence of the specific detectivity. 157

- 7.1 Modelled spectral responses of an example RCE-PD structure to demonstrate the dependence on layer thicknesses. All layer thicknesses are scaled equally in comparison to a nominal 100 % structure (green line). Layer thicknesses between 85 % (black line) and 115 % of the nominal structure are modelled (teal line). 162
- 7.2 Top: theoretical spectral responses of 11 pixels. For simplicity the peak QE and FWHM are identical for all, but the resonance wavelength is shifted for each device. Bottom: calculated response of the same pixels due to monochromatic light with a wavelength of 3.4 μm . The response between each pixel varies, due to the shift in resonance wavelength. 164
- 7.3 Visualisation of the inside of the MBE. Demonstrating the beam from a single cell onto the wafer. Without rotation, one side of the wafer is closer to the source cell (l_1) and one side is further from it (l_2). The flux onto the wafer is dependent on distance from the source cell, so if there is a distance variation, one side of the wafer receives a higher flux. 166
- 7.4 Left: conventional SWIR RCE-PD, the structure presented in chapter 5. Right: thickness graded cavity SWIR RCE-PD. The graded structure is almost identical to the conventional RCE-PD, but contains an additional layer in the cavity that is thickness graded. This also results in a thicker cavity, $m\lambda/2$, where $m \geq 2$ 169

- 7.5 Modelled dependence of the resonance wavelength on both design cavity optical path length, between $m = 1$ and $m = 6$ in $m\lambda/2$, and the thickness variation of the cavity GaSb layer between 85 % and 115 % of the design thickness. For $m = 1, 2, 3$ the variation in the GaSb thickness results in a corresponding linear change in the resonance wavelength. For $m = 4, 5, 6$ small variations in the GaSb thickness results in a linear change in resonance wavelength. However, larger variations in the GaSb thickness also contain a step change in the primary resonance wavelength at the point when the neighbouring resonance peak is closer to the ideal for the cavity thickness, *i.e.* the cavity thickness is closer to $(m \pm 1)\lambda/2$ than $m\lambda/2$ 170
- 7.6 A) Modelled QE spectra for SWIR RCE-PD structures with cavity optical path lengths between λ ($m = 1$) and $7/2\lambda$ ($m = 6$). The secondary peaks become slightly more prominent with increasing cavity thickness. B) Modelled QE spectra for SWIR RCE-PD structures with a design cavity optical path length of $5/2\lambda$ and variations of the thickness of cavity GaSb layer between 85 % and 115 % of the design thickness. The secondary peaks become much more prominent with variations in cavity thickness away from the ideal design thickness. 172
- 7.7 Left: conventional SWIR RCE-PD, the structure presented in chapter 5. Right: thickness graded DBR SWIR RCE-PD. The graded structure is almost identical to the conventional RCE-PD, but the GaSb layers in the DBR are graded in thickness. The cavity thickness is $\lambda/2$ for this structure. 174
- 7.8 A) Modelled dependence of the resonance wavelength on thickness of the GaSb layers in the DBRs. The variation in GaSb thickness results in a linear variation in resonance wavelength across the entire range. B) Modelled QE spectra for structures with DBR GaSb layer thicknesses between 85 % and 115 % of the design thickness. The shape and amplitude of the QE spectrum does not change significantly and the amplitude of the secondary peaks does not increase significantly either. The shift in resonance wavelength is the only notable effect. . . 175

- 7.9 Modelled transmittance spectrum of a SWIR RCE-PD with thicker optical path lengths of GaSb layers in the DBR. The optical path lengths of the GaSb layers are $1.15\lambda/4$, away from the ideal $\lambda/4$. Even 15% higher than ideal thickness only results in a shift of the resonant mode (teal line) of 24 nm away from the centre of the stopband (purple line). 176
- 7.10 A) Modelled dependence of the resonance wavelength on thickness of the GaSb layers. A nominal 1λ thick cavity is used for both cavity only and cavity + DBR chirped calculations. A $1/2\lambda$ thick cavity is used for DBR only chirped calculations. Grading the DBRs causes a much larger variation in the resonance wavelength in comparison to grading the cavity. B) Modelled transmittance spectrum for the SWIR RCE-PD structure with the half of the cavity thickness graded and the DBRs scaled by 115% of the design thickness. The combination of DBR and cavity grading results in a only a very small shift of the resonant mode (teal line) away from the centre of the stopband (purple line) of 7 nm. 178
- 7.11 A) Structure of the first chirped RCE-PD attempt (XAC1076). The structure is comparable to the one presented in chapter 5, with an increased cavity thickness of $5\lambda/2$. B) Colourmap of the resonance wavelength across XAC1076. There is a clear one-dimensional variation in the resonance wavelength across the wafer. 180
- 7.12 Left: Measured QE spectra for three pixels on XAB1229. The pixels are separated by 6 mm and 8 mm approximately along the dimension of the resonance chirp. The resonance wavelength shifts with position on the wafer, but the prominence of the secondary resonance does as well. Right: colourmap of resonance wavelength across the wafer. There are two regions of approximately one-dimensional variations in the resonance wavelength, separated by a step change in the middle. The step change is where the cavity thickness becomes closer to the next $m\lambda/2$ ideal thickness. 182

- 7.13 Structures of three fabricated samples, XAB1229/XAB1379 and XAB1380. Both structures are based on the one presented in chapter 5, with changes including a GaAs substrate (for higher transparency), an interfacial misfit array (IMF - to reduce dislocations caused by lattice mismatch) and thickness graded layers. Only the cavity GaSb is graded in XAB1229/XAB1379. Both the cavity GaSb and the GaSb in the DBRs is graded in XAB1380. 184
- 7.14 Colourmap of the resonance wavelength determined from transmittance spectra on sample XAB1379. There are two zones of one-dimensional variation in the resonance wavelength and a step change in between caused by the large thickness variation in the cavity only. The step change is the point where the relative amplitudes of the major and minor resonances swap over. 184
- 7.15 A) Measured normalised response of pixels along a linear array on sample XAB1380. There are significant secondary resonances, caused by the use of a thick cavity, but shift in primary resonance wavelength is linear. Inset: non-normalised spectral response of the primary resonances. B) Colourmap of the resonance wavelength determined from transmittance spectra on sample XAB1380. Despite the presence of secondary resonances, the primary resonance wavelength shift is linear and in approximately one dimension. There is no step change due to the use of thickness graded DBRs as well as the thickness graded cavity. 187
- 7.16 Measured photocurrents of pixels along a linear array (sample XAB1380) under illumination from four single-wavelengths of light. The current is normalised by the peak response for each pixel and the four curves are also normalised with respect to the peak of the curve. The coloured lines are fitted Gaussians, as a guide to the eye. 190
- 7.17 The angular dependence of the resonance wavelength, determined from reflectance measurements on the unprocessed XAB1380 sample. Inset: The normalised reflectance curves from which the resonance wavelengths were extracted, from the resonant modes. 193

- 7.18 The temperature dependence of the primary resonance wavelength for a single pixel on XAB1380. There is a clear linear dependence across the entire temperature range. 194
- 7.19 Modelled normalised responses due to single wavelength of incident light (2104 nm - vertical line) of a linear array with a resonance shift of 4 nm/pixel. Each plotted line represents the response of a comparable linear array, only with different FWHM for the resonant responses - from 40 nm to 10 nm. Lower FWHM results in fewer pixels responding to the monochromatic light. 195
- 7.20 Modelled normalised responses due to incident light with two wavelengths, 20 nm apart - vertical lines, of a linear array with a resonance shift of 4 nm/pixel. Each plotted line represents the response of a comparable linear array, only with different FWHM for the resonant responses - from 40 nm to 10 nm. Lower FWHM results in less overlap of the responses to the two separate monochromatic light wavelengths. 196
- 7.21 Comparison of the spectral response for pixels with surface passivation and metallic shielding (green) and without (orange). The surface passivation and metallic shielding reduces the prominence of the broadband response, without affecting the resonant response. 197

List of Tables

3.1	Compilation of reports of fabricated semiconductor RCE-PDs and selected properties.	52
5.1	The approximate refractive indices at 2.0 μm and bandgaps for III-V materials lattice-matched to GaSb. ⁶¹ The range of values for the quaternary materials indicates the values for the ternary alloys at either end of their composition scale.	102
5.2	Fitting parameters for the Varshni equation. * denotes parameters that have been calculated by interpolation, for $E_0(0)$ bowing parameters from Adachi ¹⁷² are used.	115
6.1	Bandgaps for selected III-V alloys, lattice-matched to InAs. Values calculated from parameters suggested by S. Adachi. ¹⁷²	137
6.2	Approximate refractive indices at 3.3 μm for materials lattice-matched to InAs. Refractive index ranges for quaternaries are determined from the refractive indices of the binary/ternary alloy at either end of the composition scale.	139

List of Abbreviations

RCE-PD	Resonant Cavity Enhanced Photodiode
DBR	Distributed Bragg Reflector
MIR	Mid-Infrared
NIR	Near-Infrared
SWIR	Shortwave-Infrared
MWIR	Midwave-Infrared
LWIR	Longwave-Infrared
QE	Quantum Efficiency
PECVD	Plasma Enhanced Chemical Vapour Deposition
RIE	Reactive Ion Etching
XRD	X-Ray Diffraction
MBE	Molecular Beam Epitaxy
SEM	Scanning Electron Microscopy
FTIR	Fourier Transform Infrared Spectroscopy

Physical Constants

Speed of light	$c = 2.997\,924\,58 \times 10^8 \text{ m s}^{-1}$
Pi	$\pi = 3.14159$
Planck's constant	$h = 6.626\,070\,04 \times 10^{-34} \text{ m}^2 \text{ kg s}^{-1}$
Boltzmann constant	$k_B = 8.6173 \times 10^{-5} \text{ eV K}^{-1}$
Vacuum permeability	$\mu_0 = 1.256\,637\,062\,12 \times 10^{-6} \text{ H m}^{-1}$

List of Symbols

λ	Wavelength	μm
R_i	Responsivity	A W^{-1}
η	Quantum efficiency	%
D^*	Specific detectivity	$\text{cm Hz}^{1/2} \text{W}^{-1}$
I	Current	A
J	Current density	A cm^{-2}
R	Reflectance	Dimensionless
r	Reflection coefficient	Dimensionless
t	Transmission coefficient	Dimensionless
T	Transmittance	Dimensionless
n_0	Refractive index of originating medium	Dimensionless
n_s	Refractive index of substrate	Dimensionless
n_H	Refractive index of high-index layer	Dimensionless
n_L	Refractive index of low-index layer	Dimensionless
N	Number of pairs of layers	Dimensionless
E	Electric field	V m^{-1}
x	Distance from interface	cm
Z_{air}	Characteristic impedance of air	Ω
$Z_{substrate}$	Characteristic impedance of the substrate	Ω
Z_{0i}	Characteristic impedance of layer i	Ω
Z_i	Total impedance through layer i	Ω
Z_{struc}	Total impedance of the structure	Ω
γ	Propagation constant	cm^{-1}
α	Absorption coefficient	cm^{-1}
β	Phase constant	cm^{-1}

l	Layer thickness	cm
λ_0	Design wavelength	μm
$\Delta\lambda$	Stopband width	μm
ω	angular frequency	rad

Chapter 1

Introduction

The interactions between photons and molecules are characterised by the wavelengths that are absorbed and emitted. The molecular structure determines these wavelengths and, as a result, each substance has its own set of characteristic wavelengths. Optical sensing of electromagnetic radiation at these wavelengths can be used to identify a substance and determine the concentration. The characteristic absorption wavelengths for a selection of substances can be seen in figure 1.1.

A range of photon-sensing detectors are commonly available, and each detector covers a specific spectral band. For example, InAs detectors cover a spectral range in the near to mid-wave infrared ($\sim 1 \mu\text{m}$ to $\sim 3.5 \mu\text{m}$)² and HgCdTe detectors can cover a large spectral range ($\sim 2 \mu\text{m}$ to $\sim 25 \mu\text{m}$).³ These detectors convert photons, with energies higher than the absorber bandgap, into electron-hole pairs. The current or voltage induced by the photon absorption can then be measured to determine the power of the incident photon flux.

Sensing of a specific substance, *e.g.* methane (CH_4), requires a detector that is sensitive at the characteristic absorption wavelength(s). Photons absorbed by the substance will not fall onto the detector and, therefore, not contribute to the current or voltage measurement. In this example, the presence of methane could be determined by a reduction in the output current of an InAs detector. However, since each detector is sensitive over a portion of the spectrum the output of the detector is also dependent on absorption at other wavelengths within its spectral band. With reference to figure 1.1 it can be seen that an InAs detector also covers absorption peaks

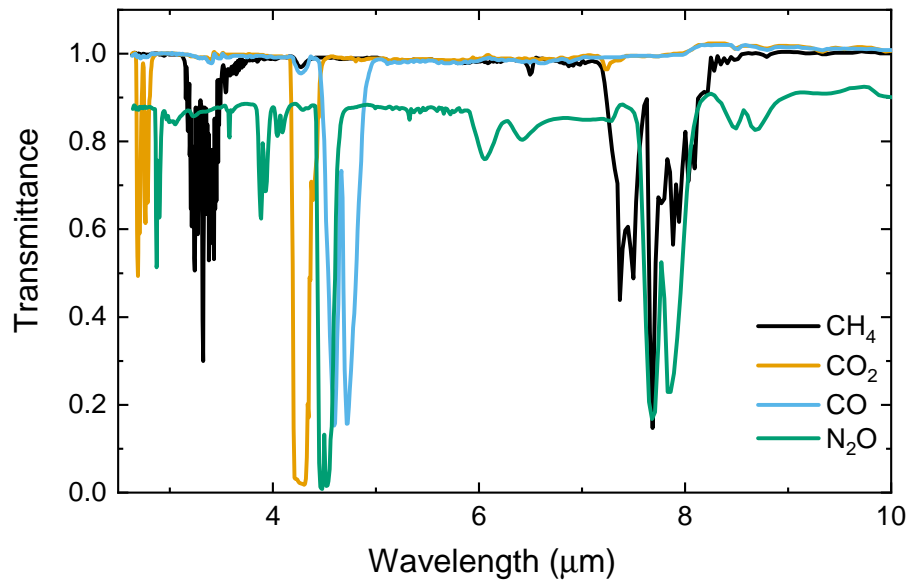


FIGURE 1.1: Transmittance spectra of a selection of gas species with absorption peaks in the mid-infrared. Spectra for methane (CH_4), carbon dioxide (CO_2), carbon monoxide (CO) and nitrous oxide (N_2O). Data from NIST.¹

of both carbon dioxide (CO_2) and nitrous oxide (N_2O). As a result, measurements of the methane concentration are skewed if these other gases are present.

To measure specific substances, without interference, it is necessary to decrease the width of the spectral band that is sensed by the detector. An illustration of this is shown in figure 1.2. The wavelengths covered by an InAs detector are highlighted by the purple region, whilst the narrower spectral band that only covers the methane absorption peak is highlighted by the red region. To remove the influence of the other gases on a measurement of methane the spectral band needs to be reduced to ~ 300 nm, or less. This can be achieved through the use of external components, such as filters or prisms.

Resonant cavity enhanced photodetectors (RCE-PDs) are an alternative to external filters. The structure integrates a filter, of sorts, to reduce the width of the spectral band that is seen by the absorbing layer. Two integrated mirrors form a spectrally selective cavity which controls the spectral band and deselects all wavelengths outside of the narrow band. The full spectrum of incident light falls onto the surface of the structure, but only a narrow spectral band is transmitted all the way to the absorbing layer. Therefore, only this narrow band of light contributes to the measured

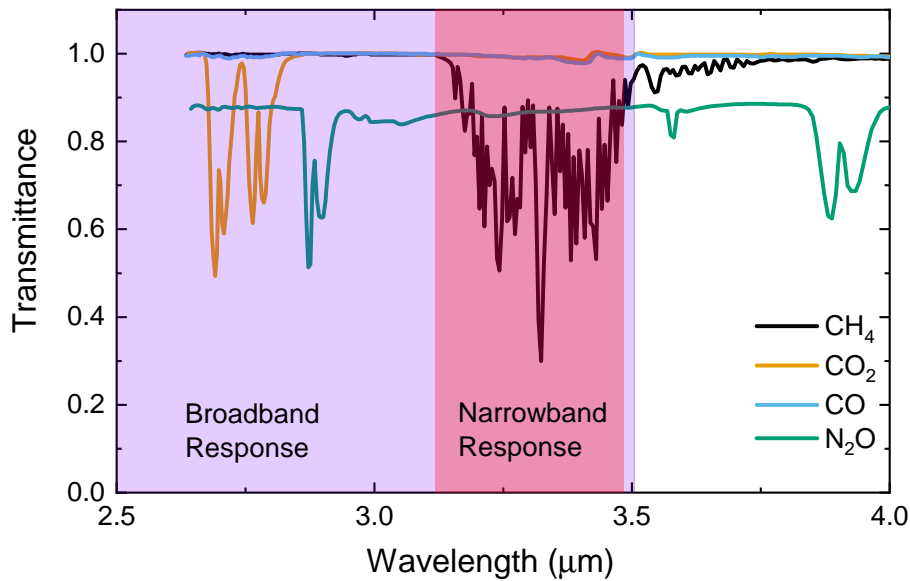


FIGURE 1.2: Zoomed transmittance spectra from figure 1.1 with the region covered by InAs detectors (purple) and a narrow region preferable for methane only sensing (red). The purple region covers significant absorption by other substances, but the red region does not.

output current or voltage from the detector.

The narrow spectral response of RCE-PDs has previously led to their use in other applications where this is a desirable characteristic. One significant example is for optical communications, where multiple channels can be separated based on closely spaced wavelengths.[4] The wavelengths used for this application are usually up to $1.55\ \mu\text{m}$, the C-communications band.⁵ Spectral sensing is possible with RCE-PDs at these wavelengths and lower, however, the absorption peaks of many substances are much stronger in the mid infrared (MIR).⁶ Therefore, RCE-PDs designed to sense at wavelengths in the MIR can take advantage of the increased absorption.

RCE-PDs utilise two mirrors to form a Fabry-Perot cavity, which resonates and enhances light within narrow spectral bands based on the distance between the two mirrors. The mirrors can be any reflective surface, such as metal or a distributed Bragg reflector (DBR). RCE-PDs have been demonstrated with metallic mirrors, DBRs and a combination of the two. There are different advantages to each of these combinations that are discussed in chapter 2. However, it is the DBR based structures that can get closest to the ideal of specific narrow band detection. There is always at least a small component of the light seen by the absorber that is outside of the desired

narrow band, but the use of DBRs promises to reduce the broadband response to negligible levels.

The aim of this project is to investigate RCE-PDs for spectral sensing in the MIR. Demonstration of detectors using two DBR mirrors have proven the possibilities for creating high-finesse, low spectral-bandwidth resonant cavities.[7] Further study is required to fully understand MIR RCE-PDs and to demonstrate the RCE-PD concept in new spectral regions. Multiple, different material systems are required to create high-performance detectors for each spectral band in the infrared. This work investigates RCE-PDs using III-V semiconductor material systems, in particular InAs and InGaAsSb absorber materials are used. Each absorber material only absorbs photons efficiently and with low noise within a spectral band close to the cutoff wavelength of the material. As such the use of narrower bandgap absorbers is required as the target wavelength increases. The choice of absorber material has a knock-on effect on the rest of the structure, including DBR materials and substrate choice. This work aims to understand these design choices and implement the ideal combinations into structures targeting specific regions in the infrared spectrum.

Chapter 2 explains the necessary background physics and theories to understand and design resonant cavity devices. The mathematical modelling of the optical properties of these structures is also discussed. In chapter 3 a review of the history of resonant cavity structures is presented, with emphasis on comparisons of the previously reported structures. A brief review of optical gas sensing technologies is also included, with a focus on recent reports of miniaturised integrated detectors with wavelength filtering designs. Chapter 4 describes all of the experimental techniques used for fabrication and testing of the RCE-PDs. The first two results chapters, 5 and 6, comprise of the results for RCE-PD structures targeting wavelengths in the short-wave infrared region and RCE-PD structures targeting wavelengths in the absorption region of C-H bonds ($\sim 3.0 \mu\text{m}$ - $\sim 3.5 \mu\text{m}$). The final results chapter, 7, presents the concept of chirped wavelength RCE-PD arrays, a novel design intended for hyperspectral sensing on a single wafer. The theory, design, fabrication and results are described.

Chapter 2

Background

This chapter presents the key concepts necessary to understand photodetectors, and in particular resonant cavity-enhanced photodiodes (RCE-PDs). The first section, [2.1](#), introduces the necessary background physics of photodetectors, with a focus on the nBn structures. Section [2.3](#) introduces the basics of the resonant cavity structures used in the designs, with discussion of the advantages and disadvantages in sub-sections [2.3.3](#) and [2.3.4](#) in comparison to more conventional photodiodes. Finally, section [2.4](#) describes the theoretical models that are used throughout this work to model the optical properties of the RCE-PD structures.

2.1 Device Architectures

There are a number of basic device structures which modern semiconductor-based photodetectors are based upon. This section briefly describes the key architectures and the differences between them. There is a focus on the noise mechanisms in each structure and how that has driven device design.

2.1.1 Photoconductor

Photoconductive detectors are the most basic form of semiconductor photodetector. They can be comprised of only a single layer, with a bandgap smaller than the energy of the absorbed photons. An incoming photon can promote an electron in the valence band into the conduction band, leaving a hole in the valence band, [figure 2.1](#). An applied bias voltage is required for the electrons and holes to drift to

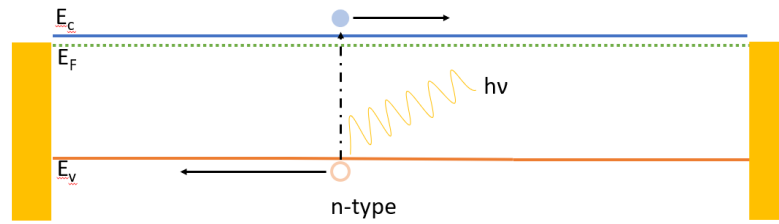


FIGURE 2.1: Sketch of a photoconductor band diagram. Incoming photons generate electron-hole pairs that can freely travel in either direction, towards the contacts. The direction of travel is usually controlled by an applied bias voltage. E_v is the valence band energy, E_F is the Fermi level and E_c is the conduction band energy.

the contacts. The current flow between the contacts can be measured to infer the detection of light through the photo-excitation process. The conductivity increases when absorbed photons generate free-carriers, resulting in an increased current for the same applied bias voltage.⁸

2.1.2 p-n Junction Photodiode

A photodetector can be based on a p-n junction, figure 2.2. A simple p-n photodiode contains two layers, one p-doped and one n-doped. The different doping creates an offset of the valence band and conduction band at the interface. This offset acts as a barrier to the flow of majority carriers.⁹ At the junction there is initially diffusion of the majority carriers that creates a depletion region, which is depleted of free charge carriers. This diffusion creates an in-built electric field across the junction.

In the same process as the photoconductor, an incoming photon with enough energy can promote an electron into the conduction band and leave behind a hole in the valence band. If the photon is absorbed in the depletion region an applied bias voltage is not required because the in-built electric field in the depletion region can sweep minority carriers towards the metal contacts.¹⁰

2.1.3 nBn

The final device architecture to be discussed is the nBn photodetector, that is a relatively recent addition.¹¹ The nBn structure can be described as a photoconductor with a barrier, 'B', in the middle. An nBn is created with an n-type absorbing region, a barrier layer with a large conduction band offset and negligible valence band offset

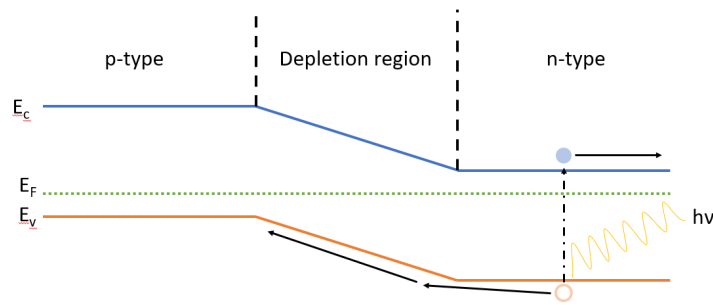


FIGURE 2.2: Sketch of a p-n junction photodiode band diagram. Incoming photons generate electron-hole pairs that can diffuse in the direction of the arrows. In the depletion region the in-built voltage causes carrier drift. Movement of electrons in the opposite direction to that shown is blocked by the depletion region. E_v is the valence band energy, E_F is the Fermi level and E_c is the conduction band energy.

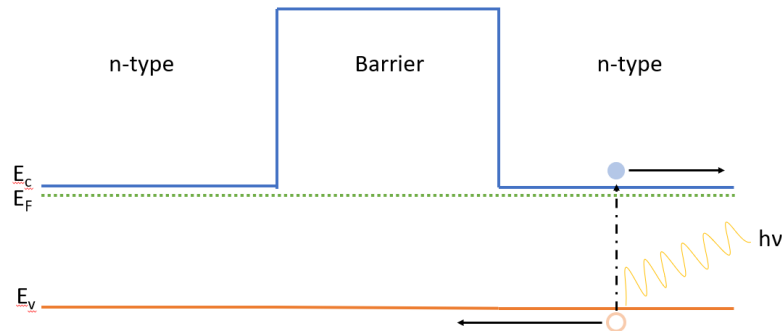


FIGURE 2.3: Sketch of the band diagram of an nBn . Incoming photons generate electron-hole pairs that can diffuse in the direction of the arrows. Diffusion of electrons in the opposite direction is blocked by the barrier. E_v is the valence band energy, E_F is the Fermi level and E_c is the conduction band energy.

and a second n-type region, figure 2.3. In this configuration the barrier blocks the flow of majority electrons, in the conduction band, but does not impede the flow of holes in the valence band.

2.2 Dark Current Mechanisms

Dark current is any current that is generated inside a photodetector not due to the absorption of photons. This section describes some of the dark current mechanisms present in semiconductor photodetectors, with a focus on those that are most relevant to the nBn architecture used in the RCE-PD test samples.

2.2.1 Majority Carrier Drift Current

Majority carrier drift current only occurs when there is no barrier to the flow of the majority carriers. It occurs when an electric field is applied between two metal contacts, to cause the drift of majority carriers to the contacts.¹² Of the presented device architectures, this current only occurs in the photoconductor, which has a flat conduction band. The pn junction has the depletion region, which acts as a barrier and the nBn contains a barrier layer with a large conduction band offset.¹¹

The temperature dependence of the majority carrier drift current is directly proportional to the temperature dependence of the majority carrier concentration.¹³ The majority carrier concentration generally increases with increasing temperature, resulting in a corresponding increase in the drift current. The activation energy of this current mechanism also varies with the majority carrier concentration.¹²

2.2.2 Tunnelling Current

Tunnelling currents occur when carriers find a way through the barriers that are designed to block their flow.¹⁴ The carriers can tunnel through the depletion region, directly between the valence band and conduction band. They can also tunnel through a current barrier via mid bandgap defects, called trap-assisted-tunnelling (TAT).¹⁵ Tunnelling currents are usually suppressed in the nBn architecture, because there is not commonly any significant overlap between the valence band and conduction band energies.¹⁶ Figure 2.4 visualises the two types of tunnelling mechanisms.

Both tunnelling current mechanisms have very little temperature dependence,¹² because the carriers are not promoted to higher energy levels. As a result the activation energy is approximately zero.

2.2.3 Generation-Recombination Current

Generation-recombination currents are caused by carrier drift due the in-built electric field in the depletion region of pn junctions. Carriers are thermally generated through defects states located in the bandgap of the depletion region. This process

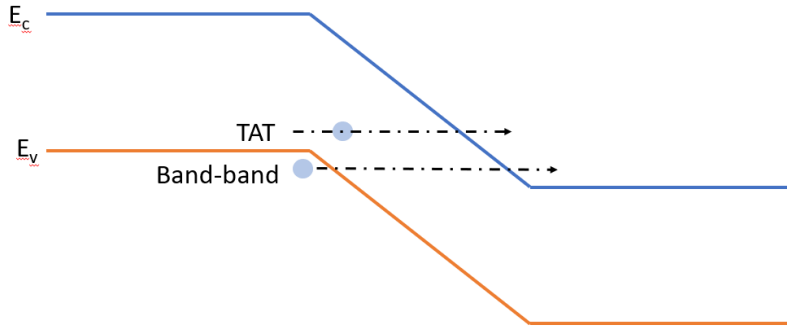


FIGURE 2.4: Sketch of the both tunnelling current mechanisms. Band-band tunnelling from the valence band to the conduction band directly and TAT via defects in the bandgap. E_v is the valence band energy and E_c is the conduction band energy.

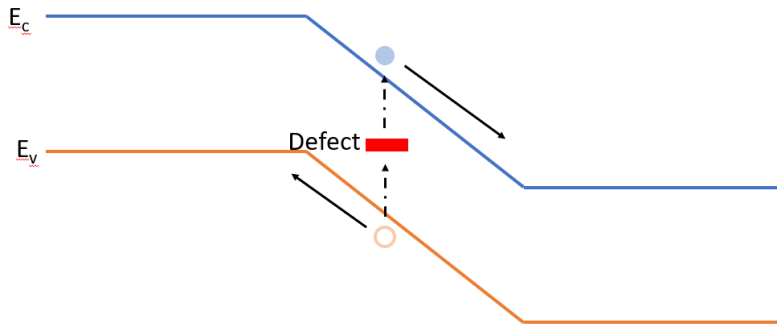


FIGURE 2.5: Sketch of the depletion region SRH mechanism. Electrons are promoted from the valence band to the conduction band in the depletion region via traps in the bandgap. Electrons and holes are subject to drift in the direction of the solid arrows. E_v is the valence band energy and E_c is the conduction band energy.

is also called depletion region Shockley-Read-Hall (SRH) generation.¹⁷ Figure 2.5 visualises the depletion region SRH process.

The generation-recombination currents are dependent on the defect density, due to the process utilising energy levels within the bandgap. There is also a dependence on the intrinsic carrier concentration, which has temperature dependence given by⁹

$$n_i \propto \exp\left(-\frac{E_g}{2kT}\right), \quad (2.1)$$

where E_g is the bandgap of the depletion region, k is the Boltzmann constant and T is temperature. The current density in the depletion region due to SRH is then given

by⁹

$$J_{d-SRH} = \frac{qw}{\tau_{eff} \sqrt{N_c N_v} \exp(-\frac{E_g}{2kT})}. \quad (2.2)$$

Where w is the width of the depletion region, τ_{eff} is the effective carrier lifetime, n_i is the intrinsic carrier concentration, q is the electron charge, N_c is the density of states for the conduction band and N_v is the density of states for the valence band. The activation energy of the depletion region SRH generation is given by¹⁷

$$E_a^{d-SRH} \approx \frac{E_g}{2}. \quad (2.3)$$

In the depletion region the Fermi level is in the middle of the bandgap, making it energetically favourable for electrons to be promoted via trap states in the centre of the bandgap.¹⁸ Hence, the activation energy is half of the bandgap. Ideal nBn structures do not contain depletion regions, which leads to no generation-recombination currents in an ideal device.¹¹ Although, it should be noted that depletion of the absorber can occur in nBn structures.¹⁹

2.2.4 Diffusion Current

In quasi-neutral regions, *i.e.* not the depletion region, free-carriers can be generated by multiple processes - in either n-type regions, intrinsic regions or p-type regions. In the nBn designs there are only n-type regions, so processes that occur in those regions are the focus here. Carriers that are generated in quasi-neutral regions must diffuse to the contacts (or the depletion region) and result in the diffusion current.²⁰ Diffusion currents are also formed by photo-generated carriers in the absorber layer, but in this section only dark current mechanisms are covered.

Auger Generation

Auger generation is a band-to-band process with a few variations.²¹ In an ideal n-type semiconductor layer, the generation is most significantly due to the Auger 1

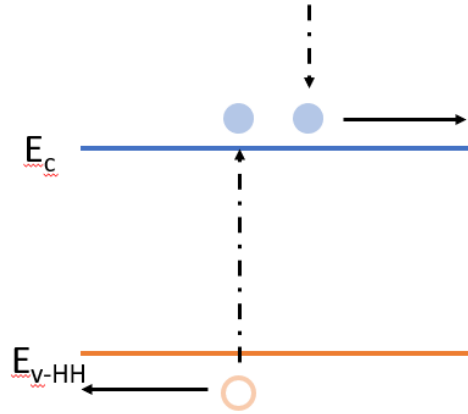


FIGURE 2.6: Sketch of the Auger 1 process. An energetic conduction band electron, E_c , transfers its energy to another electron in the valence band, E_{v-HH} . The valence band electron is promoted to the conduction band and a heavy hole is left behind in the valence band.

process.²² In the Auger 1 process there is an energy transfer from an energetic conduction band electron to a valence band electron. The valence band electron is promoted to the conduction band and a heavy hole is left behind in the valence band, visualised in figure 2.6.²³ This process is non-radiative, and occurs across the bandgap - hence, band-to-band.

In the long diffusion length limit, *i.e.* the thickness of the absorber \ll the diffusion length, the current density due to Auger 1 generation is given by²⁴

$$J_{A1} = q \sqrt{\frac{D_p}{\tau_p} \frac{n_i^2}{N_d}} = q \sqrt{\frac{D_p}{\tau_p} \frac{1}{N_d}} N_c N_v \exp\left(-\frac{E_g}{kT}\right). \quad (2.4)$$

Where D_p is the hole diffusion coefficient, n_i is the intrinsic carrier concentration, τ_p is the minority carrier diffusion lifetime and N_d is the donor concentration. The long diffusion length limit is expected to apply in the absence of high defect levels. The activation energy of the Auger 1 process, is then given by²²

$$E_a^{A1} \approx E_g. \quad (2.5)$$

Shockley-Read-Hall Generation

Shockley-Read-Hall generation in the neutral region is usually much smaller than the SRH generation in the depletion region of a pn photodiode. However, since ideal nBn structures do not contain a depletion region, it is possible that the neutral region SRH generated diffusion current might contribute significantly to the overall dark current. The neutral region SRH process is similar to the depletion region SRH, electrons are promoted from the valence band to the conduction band via trap states in the bandgap. However, in the n-type neutral regions the Fermi level is shifted closer to the conduction band.²⁵ The current density of the neutral region SRH mechanism in the long diffusion length limit is given by²²

$$J_{n-SRH} = \frac{qn_i^2 v \sigma L_{abs} N_{defect}}{N_d} = \frac{qv \sigma L_{abs} N_{defect}}{N_d} N_c N_v \exp\left(-\frac{E_g}{kT}\right). \quad (2.6)$$

Here, v is the electron velocity, σ is the defect capture cross section, L_{abs} is the layer thickness and N_{defect} is the defect density. The activation energy of neutral region SRH in an ideal nBn is expected to be the same as for the Auger 1 process, *i.e.* approximately match the bandgap of the absorber material, following²²

$$E_a^{n-SRH} \approx E_g. \quad (2.7)$$

Although this is dependent on the Fermi level sitting close to or in the conduction band. The activation energy is reduced if the Fermi level moves below the band edge.¹² A significant difference between the Auger 1 process and the SRH process in the neutral region is the dependencies on material defects. Auger 1 is only dependent on the intrinsic carrier concentration, and is not affected by material defects. Neutral region SRH is dependent on both intrinsic carrier concentration and the defect density. The result of this is that a low-defect device, that is diffusion current limited, is likely to have an Auger 1 dominated dark current. A similar, high-defect device is likely to have a higher dark current, possibly caused by higher neutral region SRH.

2.2.5 Surface Current

The surface of a semiconductor structure can behave differently to the bulk semiconductor. All the previous current generating mechanisms relate to the bulk semiconductor, but the mechanisms that generate current at the surface of the structure are the same as in the bulk material.¹² The dark current that flows on the surface can be significantly increased, due to higher defect densities and differences in the Fermi level. If not properly controlled, surface currents can dominate the dark current of pn photodiodes.²⁶ In *nBn* structures the presence of a conduction band barrier blocks the flow of surface currents.²⁷

2.2.6 *nBn* Current Mechanisms

To aid comparison, the diffusion current generating mechanisms are visualised on a single band diagram in figure 2.7. Minority carrier currents generated via the Auger 1 process, neutral-region Shockley-Read-Hall process and photogeneration are free to flow unimpeded by the barrier. Surface currents, SRH generated currents and majority carrier currents are all blocked by the conduction band barrier.

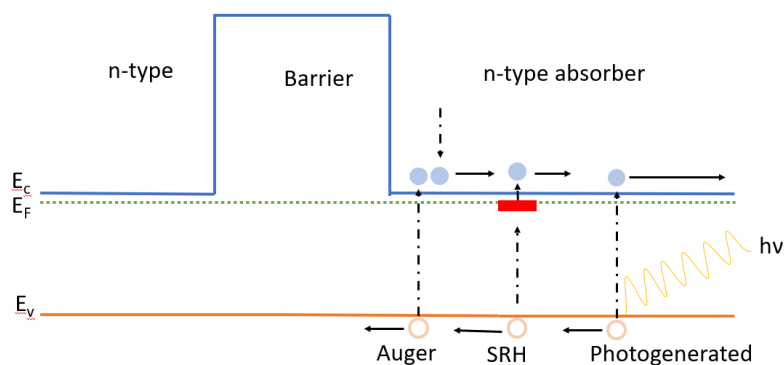


FIGURE 2.7: Combined figure showing the mechanisms for diffusion current generation in an *nBn* structure. Including the band-to-band Auger 1 process, defect assisted neutral region SRH and band-to-band photogeneration.

2.3 Resonant Cavity Structures

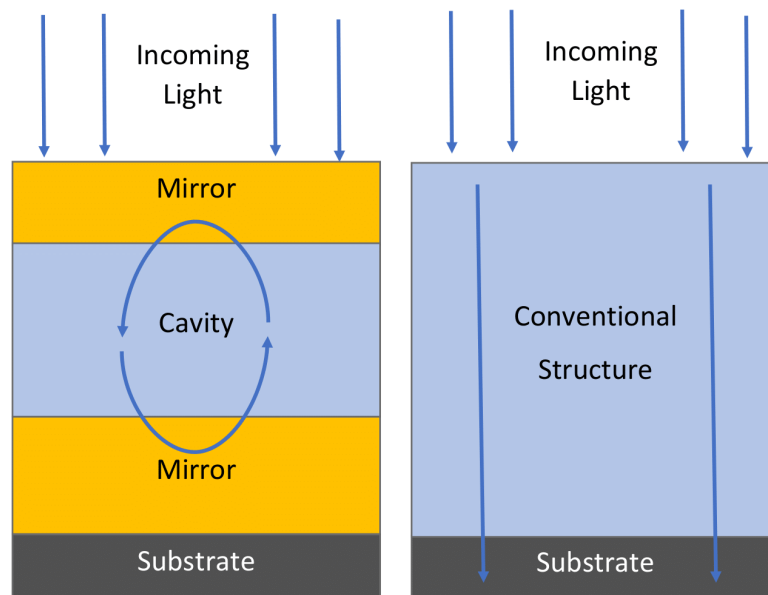


FIGURE 2.8: Simplified paths of light through an RCE-PD (left) and a conventional detector (right). In the conventional structure light is mostly absorbed on a single pass through the structure. In contrast, in the RCE-PD structure the light passes through the cavity multiple times, in a cycle between the mirrors.

Resonant cavity structures can be separated into two main elements: mirrors and the cavity. The purpose of the mirrors is to reflect the incoming light through the cavity multiple times, while the cavity separates the mirrors and is where the light is absorbed. A mirror behind the absorbing layer will reflect photons that have not been absorbed on the first pass back through the absorbing layer - increasing the total absorption of the device. A second mirror in front of the absorbing layer will similarly reflect photons that have not been absorbed on the first two passes and create a cycle of reflections between the two mirrors. This can also be understood by considering the electric field in the cavity. At the resonance wavelengths there is constructive interference between the forwards and backwards travelling waves, which leads to an enhanced electric field in the cavity. Away from the resonance wavelengths the two waves interfere destructively, leading to a reduced electric field in the cavity. Figure 2.8 highlights these differences between conventional detectors and RCE-PDs.

The mirrors could be any material that reflects light, for example gold or silver, however to create a device that is highly spectrally selective the mirrors need to only reflect certain wavelengths of light. This can be achieved by using distributed Bragg reflectors (DBR).

2.3.1 Distributed Bragg Reflectors

A distributed Bragg reflector, DBR, is a multi-layer stack of two alternating layers. The two layers consist of one low refractive index material (n_L) and one refractive high index material (n_H) with optical path lengths equal to a quarter of the design wavelength (λ_0). The thicknesses of the layers, t , are then given by

$$t = \frac{\lambda_0}{4n} \quad (2.8)$$

Incident light is reflected at every interface between the each layer - as shown in figure 2.9. At the interfaces going from a low refractive index to a high refractive index a phase change of 180° is introduced. For wavelengths close to λ_0 the total phase change relative to the incident light of all the reflected light is either 0 or a multiple of 360° . Therefore, the light reflected from each interface interferes constructively. This allows for the total reflectivity of the DBR to be increased by each interface.

If the wavelength of incident light is not close to λ_0 the optical path lengths of the DBR layers will not be a quarter of the incident wavelength. In this case, the light reflected from each interface will not be in phase with the incident light, and the different parts of reflected light will partially interfere destructively. Therefore, there will be a mixture of reflection and transmission for these wavelengths of light. So, the structure can give a very high reflectance for some wavelengths, at the same time 50 % or lower reflectance at other wavelengths. This is the basis for the spectral selectivity of resonant cavity-enhanced devices.

To determine the maximum reflectance of a DBR,

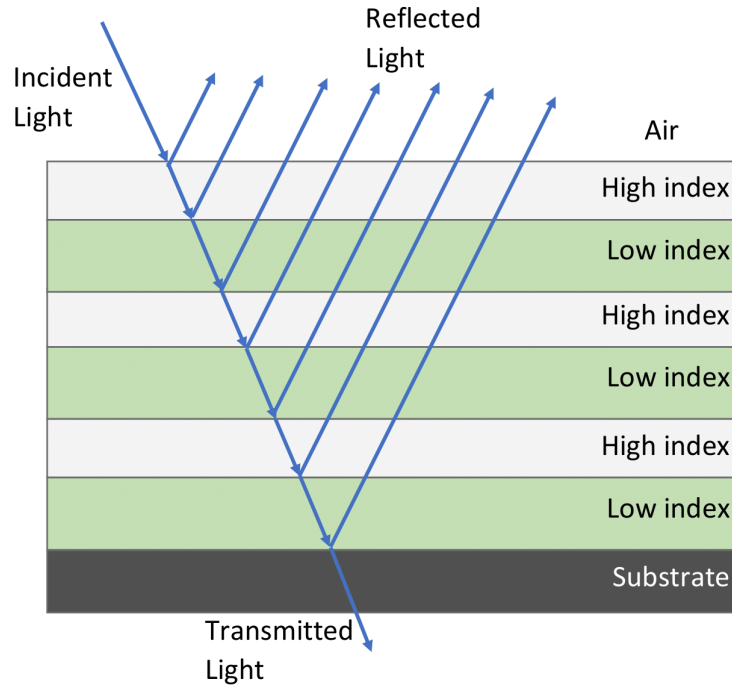


FIGURE 2.9: A simple illustration of the light paths in a distributed Bragg reflector. At each interface the incident light is partially transmitted and partially reflected. If the wavelength of the incident light matches the design of the DBR then the reflected waves will interfere constructively.

$$R = \left[\frac{n_0 n_H^{2N} - n_s n_L^{2N}}{n_0 n_H^{2N} + n_s n_L^{2N}} \right]^2 \quad (2.9)$$

can be used²⁸ - n_0 and n_s are the refractive indices of the originating medium and the substrate, respectively. n_H is the refractive index of the high index material and n_L is the refractive index of the low index material. N is the number pairs of layers in the structure. This equation assumes that there is no absorption in the structure and that the incoming light is at normal incidence.

The reflectance spectrum for a DBR shows two distinct zones, a high reflectance zone called the stopband, which is centred on the wavelength λ_0 and low reflectance zones either side of the stopband. The stopband width is dependent on the design wavelength (λ_0) and the refractive indices of the two layers, given by²⁹

$$\Delta\lambda \sim \frac{4}{\pi} \lambda_0 \arcsin \left(\frac{n_H - n_L}{n_H + n_L} \right). \quad (2.10)$$

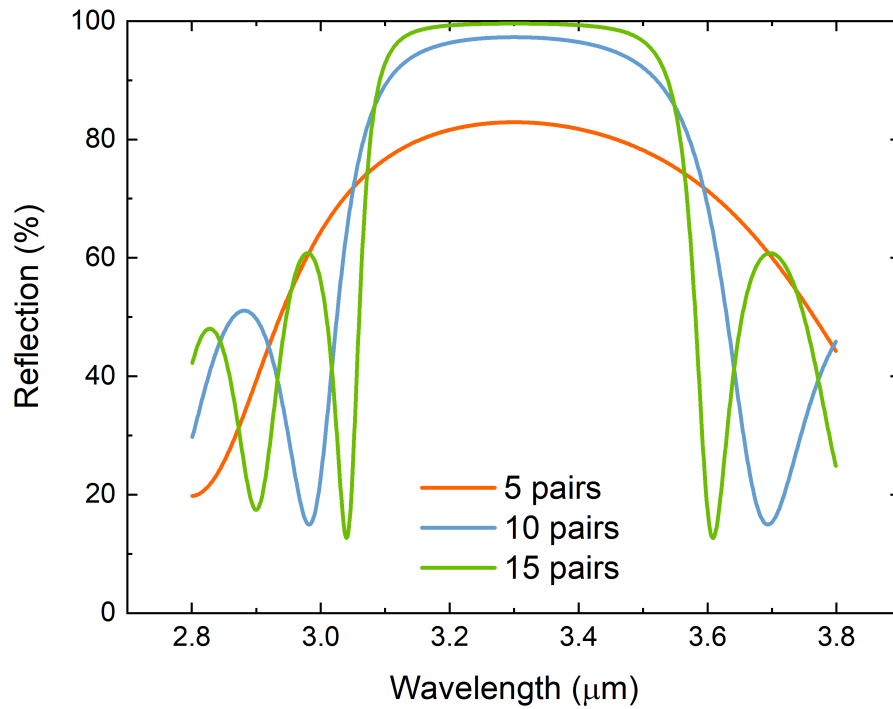


FIGURE 2.10: Modelled reflection spectrum of DBRs with 5, 10 and 15 pairs of layers. n_H and n_L of 3.82 and 3.15 respectively were used. The plot highlights the increasing maximum reflection as the number of repeats in the DBR is increased. The plot is modelled following the transfer matrix method, detailed in section 2.4.1.

In figure 2.10, example reflection spectra are modelled using the transfer matrix method, detailed in section 2.4.1. The maximum reflectance follows equation 2.9, and a monotonic increase of the maximum reflectance with number of layers can be seen. The model uses refractive indices of 3.82 and 3.15 for the high and low refractive indices respectively. Spectra for DBRs with 5, 10 and 15 pairs of layers are included for comparison. The maximum reflection increases with the number of pairs, whilst the stopband edge gets sharper and more defined as the number of pairs increases.

2.3.2 Cavities

To create a functional resonant cavity-enhanced device there needs to be an absorbing cavity between two DBRs. The cavity could contain almost any conventional photodetector structure, such as a pn junction, pin or nBn as well as emitter structures to create resonant cavity-enhanced emitters. Resonant cavity structures are already commonly used in commercial applications, with widespread utilisation of

vertical-cavity surface-emitting lasers (VCSELs).³⁰ VCSELs are a resonant cavity-enhanced device and share many similarities with RCE-PD structures.³¹ It is also possible to integrate photodetectors inside a VCSEL.^{32,33} The focus of this work is on detectors, so only these structures will be discussed in more detail.

Light at the design wavelength of the DBRs is enhanced most strongly in the cavity if the optical path length of the cavity is a multiple of half the design wavelength. This requires the total thickness of the cavity (t_C) to follow

$$t_C = m \frac{\lambda_0}{2n_C}, \quad (2.11)$$

where n_C is the average cavity refractive index and m is any positive integer. This thickness relation keeps light at the design wavelength in phase through the cavity and means that all the reflected light will interfere constructively in the cavity.

Light at wavelengths outside of the design wavelength will not be in phase with all reflected waves throughout the structure and, therefore, will interfere destructively in the cavity. Light at wavelengths within the stopband of the DBRs will be mostly reflected by the whole structure, whilst all other wavelengths will be partially reflected and partially transmitted through the whole structure. Only light at wavelengths that satisfy the resonance condition - equation 2.11 - will be strongly absorbed in the cavity.

The constructive interference of light reflected by both of the DBRs creates a standing wave in the cavity. For a $\lambda_0/2$ cavity optical path length the peak of the standing wave will be at the centre of the cavity. For the highest possible absorption, the absorption layer(s) of the detector structure should be placed at the peak of the standing wave - at the centre of the cavity. The other layers in the cavity are designed around this consideration. For a pn junction within a cavity the depletion region should be at the centre of the cavity. For an nBn placed within a cavity the absorber should be at the centre of the cavity. To satisfy equation 2.11 with the absorber positioned in the centre of the cavity it is necessary to include a filler layer beneath the absorber.

Other than the total thickness and positional considerations already mentioned, the design considerations of the cavity are similar to the conventional structure that the cavity layers are based upon. The most significant difference between a pn junction or nBn in a cavity compared to a conventional structure is the thickness of the absorption layers. Due to the resonant enhancement effect of the cavity, the layers can be much thinner than a conventional detector. This can be thought of as the light making multiple passes through the absorbing layer, increasing the effective optical path length of the region where the light could be absorbed, thereby allowing for a thinner absorbing layer without decreasing the total absorption of the device.

2.3.3 Advantages

Section 2.3 describes the general structure of a resonant cavity-enhanced photodetector, without detailing the benefits of such a structure. In this section the advantages compared to conventional detectors are laid out.

For RCE-PD structures that use DBR mirrors either side of the cavity the spectral band of light that causes an electrical response in the detector is much narrower than for conventional detectors. The wavelengths that cause a significant spectral response in the detector are only those that stay in phase throughout the round trip through the DBRs and the cavity. The spectral width of this band is determined by a combination of factors including the number of repeats of the layers in the DBRs and the refractive index difference between the two DBR materials. By changing these factors the width of the spectral response of the detector can be tuned. The high spectral selectivity possible with RCE-PDs is a substantial benefit in many applications where specific detection of certain wavelengths of light is necessary. One such application is spectroscopy - specifically the detection of substances by measurement of their absorption spectrum. Each substance only absorbs light at specific wavelengths - their absorption peaks, shown in figure 2.11 - that distinguish substances. By measuring the light at a wavelength that coincides with an absorption peak the presence of a particular substance can be determined as well as the concentration of the substance. RCE-PDs can be used for this application because of the narrow spectral response that can be designed to align with a specific absorption peak, and

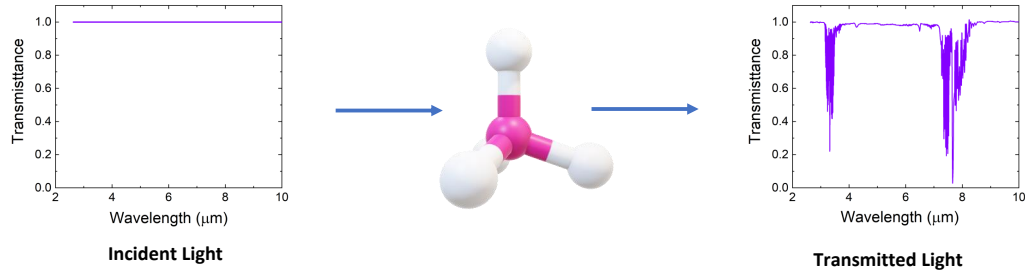


FIGURE 2.11: An example of the light transmitted through a molecule, the transmission spectrum is for methane. With nothing in the path of the light, it is transmitted equally at all wavelengths. With a specific substance in the path, the light is highly transmitted at some wavelengths and partially absorbed at other wavelengths. The absorption spectrum is determined by the substance in the light path.

deselecting all light from nearby spectral regions; conventional broadband detectors could not do this without additional components, such as external filters or large spectrometers.

A significant change that can be made to absorption region of an RCE-PD compared to a conventional detector is the use of a much thinner absorption layer. The resonant enhancement in the cavity increases the absorption per unit length of the absorption layer, allowing for a thinner layer to be used without compromising on the overall absorption of light. A thinner absorber is actually necessary to avoid dampening the resonance. The most significant benefit of reducing the thickness of the absorption layer is the reduction of the undesirable dark currents. The dark currents that are most significant in nBn detectors are dependent on the thickness of the absorption layer. The neutral region Shockley-Read-Hall mechanism scales approximately linearly with absorber thickness, following equation 2.6²², partially repeated here

$$J_{SRH} = \frac{qn_i^2 v \sigma L_{abs} N_{defect}}{N_d}. \quad (2.12)$$

Where q is the electron charge, n_i is the intrinsic carrier concentration, v is the electron velocity, σ is the defect capture cross section, L_{abs} is the layer thickness, N_{defect} is the defect density and N_d is the donor concentration. Currents generated by Auger

1 mechanisms also scale linearly with absorber thickness,³⁴ following²²

$$J_{A1} = \frac{qL_{abs}N_d}{2\tau_{A1}}, \quad (2.13)$$

where τ_{A1} is the Auger 1 lifetime. Reducing these currents improves the signal-to-noise ratio of the detector and allows smaller signals to be detected.

The absorber thickness can be reduced due to the resonant enhancement, but also, the responsivity and quantum efficiency, QE, of an RCE-PD can be increased in comparison to a conventional detector - even with a thinner absorber layer. Conventional detectors are usually limited by the reflection of incident light off of the top layer in the structure, whilst RCE-PDs do not have this limitation for wavelengths close to the resonant wavelength. Light at these wavelengths is coupled-in to the cavity, with only a small fraction reflected off of the top DBR. Whilst the reflection from a semiconductor to air interface is approximately 30 %, which reduces the maximum possible quantum efficiency in a conventional detector by the same amount, the reflection off of the top DBR in an RCE-PD can be less than a few percent. It should be noted that the reflection at the top interface of conventional structures can also be reduced by an anti-reflection layer. The exact quantum efficiency of each structure is determined by combination of factors, but the combination of decreased dark currents and increased QE increases the highest possible specific detectivity above the conventional detector limit.

2.3.4 Disadvantages

Whilst there are many applications where the characteristics of RCE-PDs offer significant advantages, there are drawbacks that mean they would not be the right choice for all applications. For example, if an application does not require the narrow spectral response then it is unlikely to be the best choice.

In comparison to conventional bulk semiconductor photodiodes, the RCE structures are significantly more complex, both from a design perspective and a fabrication perspective. The design considerations imposed by the cavity, *e.g.* thickness and

layer positioning, reduce the options available. At the same time the DBRs most commonly used in RCE devices significantly increase the overall thickness of the structure. For epitaxially grown layers, this results in an increase in growth time, an increase in calibration requirements and an increase in the required precision. The end result is a higher fabrication cost for RCE-PDs.

2.4 Modelling

To be able to understand, design and fabricate resonant cavity structures it is beneficial to model the optical properties. This has been done by two separate methods, the transfer matrix method 2.4.1 and the transmission line model method 2.4.2. Both models take input parameters of thicknesses, absorption coefficients and refractive indices of the layers, as well as the wavelength of the incident light. The output of reflectance, transmittance and responsivity spectra can be used to compare the optical properties of different structures to improve and understand the designs.

2.4.1 Transfer Matrix Method

The transfer matrix method calculates the optical transfer through interfaces and the propagation through layers by using matrices to describe the changes to the electric field.³⁵ To determine the total transmittance and reflectance for the entire structure the transfer properties for each interface and the propagation through each layer needs to be calculated separately, which can then be combined to create the so called system-matrix for the entire structure. The presented calculations follow the derivations of R.B. Balili,³⁶ although this method is well used by other researchers for modelling multi-layer structures,^{37,38} including VCSELs and RCE-PDs.^{39,40}

First, the transfer properties of each interface can be described by the interface matrix T , which is determined by the Fresnel coefficients of the interface⁴¹. This method assumes that the interfaces are smooth, which is considered reasonable based on SEM images and correlation between measured and modelled reflectivities. Therefore, the Fresnel coefficients can be determined simply by the refractive indices either side of the interface:

$$r_{0,1} = \frac{n_0 - n_1}{n_0 + n_1} \quad (2.14)$$

$$t_{0,1} = \frac{2n_0}{n_0 + n_1}, \quad (2.15)$$

where $r_{0,1}$ is the reflection coefficient and $t_{0,1}$ is the transmission coefficient. n_0 is the refractive index of the layer on the side of the incident light and n_1 is the refractive index of the layer on the side of the transmitted light, as shown in figure 2.12. In these equations the subscript number denotes the layer number, the '+' denotes a wave travelling to the right on the diagram, the '-' denotes a wave travelling to the left on the diagram in figure 2.12 and the '' denotes the field to the right of the interface.

The Fresnel coefficients can be combined into vector form to relate the electric fields before and after the interface

$$\begin{pmatrix} E_0^+ \\ E_0^- \end{pmatrix} = \frac{1}{t_{0,1}} \begin{pmatrix} 1 & r_{0,1} \\ r_{0,1} & 1 \end{pmatrix} \begin{pmatrix} E_1'^+ \\ E_1'^- \end{pmatrix}. \quad (2.16)$$

This then leads to the interface matrix:

$$\mathbf{T}_{0,1} = \frac{1}{t_{0,1}} \begin{pmatrix} 1 & r_{0,1} \\ r_{0,1} & 1 \end{pmatrix} \quad (2.17)$$

A matrix for each interface can be constructed in the same way, using the refractive indices either side of the interface.

To calculate the propagation through a layer the dispersion relation for a homogeneous layer can be used, where the wavevector \vec{k}_i is dependent on the vacuum wavelength of the incident light λ and the complex refractive index of the layer \mathbf{n}_i . The complex refractive index combines the real part of the refractive index, n_i , and

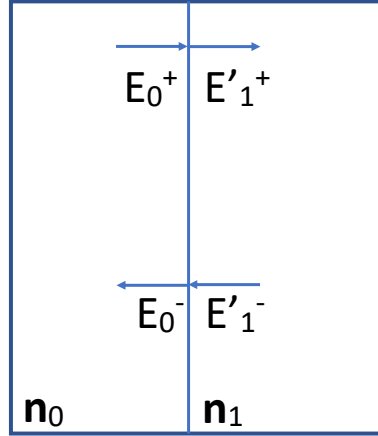


FIGURE 2.12: An example of the transfer of the electric field through a smooth interface between layers. There is a forward travelling component on both sides of the interface, E_0^+ on the left and E_1^+ on the right. There is also a backward travelling component on both sides, E_0^- on the hand and E_1^- on the right.

the absorption coefficient, α_i , by following⁴²

$$\mathbf{n}_i = n_i + j \frac{\alpha_i \lambda}{4\pi}. \quad (2.18)$$

Here j is used to denote an imaginary number.

The dispersion relation is then obtained through⁴³

$$\vec{k}_i = \frac{2\pi n_i}{\lambda}. \quad (2.19)$$

The propagation through each layer can be calculated by using the standard equation for one dimensional propagation through a homogeneous layer⁴⁴,

$$\vec{E}(x) = E_0^+ \exp(j\vec{k}x) + E_0^- \exp(-j\vec{k}x). \quad (2.20)$$

Here, x is the one-dimensional change in position, \vec{E}_0 is the electric field at the start of the layer and $\vec{E}(x)$ is the electric field at a distance from the start of the layer, x , as

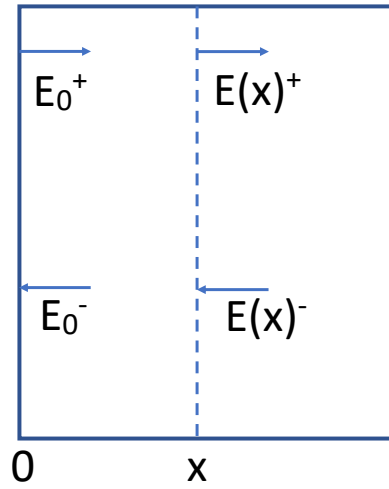


FIGURE 2.13: An example of the propagation of the electric field through a homogeneous layer. There is a forward travelling component at all points in the layer, E_0^+ at the left hand interface and $E(x)^+$ at distance x from the interface. There is also a backward travelling component on both sides, E_0^- at the left hand interface and $E(x)^-$ at distance x from the interface.

shown in figure 2.13.

This can be written in vector form:

$$\begin{pmatrix} E(x)^+ \\ E(x)^- \end{pmatrix} = \begin{pmatrix} \exp(j\vec{k}x) & 0 \\ 0 & \exp(-j\vec{k}x) \end{pmatrix} \begin{pmatrix} E^+ \\ E^- \end{pmatrix}. \quad (2.21)$$

The propagation matrix, or **P**-matrix, for the layer can then be extracted, *i.e.*

$$\mathbf{P}_i = \begin{pmatrix} \exp(j\vec{k}x_i) & 0 \\ 0 & \exp(-j\vec{k}x_i) \end{pmatrix}. \quad (2.22)$$

This is for layer i , which utilises the thickness of the layer x_i .

Combining the transfer and propagation matrices for each layer in the structure can be used to determine the relationship between the electric fields before the top interface, E_0 , and after the bottom interface, E'_{N+1} :

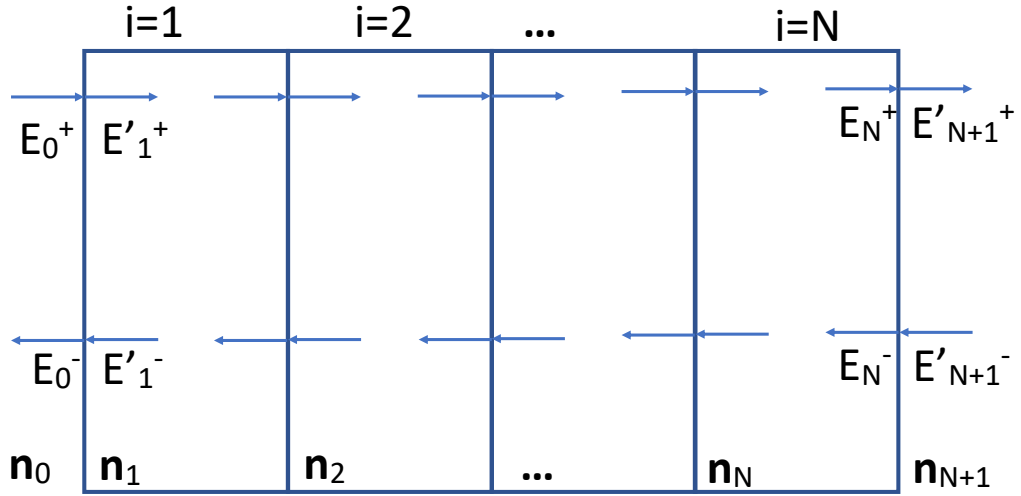


FIGURE 2.14: An example of the propagation of the electric field through a structure with N layers. Layers are labelled 1 to N from the left. Forward travelling waves with a $+$ and backward travelling waves with a $-$. The field to the right of each interface is labelled with a $'$ and with no apostrophe for the fields on the left.

$$\begin{pmatrix} E_0^+ \\ E_0^- \end{pmatrix} = \mathbf{T}_{0,1} \left[\prod_{i=1}^N \mathbf{P}_i \mathbf{T}_{i,i+1} \right] \begin{pmatrix} E'_{N+1}^+ \\ E'_{N+1}^- \end{pmatrix}, \quad (2.23)$$

of the structure shown in figure 2.14.

The matrix that connects the two electric fields is called the system matrix

$$\mathbf{S} = \mathbf{T}_{0,1} \left[\prod_{i=1}^N \mathbf{P}_i \mathbf{T}_{i,i+1} \right] = \begin{pmatrix} S_{00} & S_{01} \\ S_{10} & S_{11} \end{pmatrix}, \quad (2.24)$$

which is a 2×2 matrix given by the product of all the interface and propagation matrices for the entire structure.

Substituting equation 2.24 into equation 2.23 relates the electric fields by the system matrix:

$$\begin{pmatrix} E_0^+ \\ E_0^- \end{pmatrix} = \begin{pmatrix} S_{00} & S_{01} \\ S_{10} & S_{11} \end{pmatrix} \begin{pmatrix} E'_{N+1}{}^+ \\ E'_{N+1}{}^- \end{pmatrix}. \quad (2.25)$$

Once the system matrix has been calculated it can be used to determine the transmittance and reflectance of the entire structure, by comparing the electric fields either side of the structure. Assuming that there is no backward travelling wave after the last interface, equation 2.25 becomes:

$$\begin{pmatrix} E_0^+ \\ E_0^- \end{pmatrix} = \begin{pmatrix} S_{00} & S_{01} \\ S_{10} & S_{11} \end{pmatrix} \begin{pmatrix} E'_{N+1}{}^+ \\ 0 \end{pmatrix} \quad (2.26)$$

The reflection coefficient of the entire structure, r , is the ratio of the backward travelling wave E_0^- to the forward travelling wave E_0^+ before the first interface. By separating the vector equation 2.26 into equations for E_0^+ and E_0^- the ratio can be determined by the ratio of the equations, *i.e.*

$$\frac{E_0^-}{E_0^+} = \frac{S_{10} E'_{N+1}{}^+}{S_{00} E'_{N+1}{}^+} = \frac{S_{10}}{S_{00}} = r. \quad (2.27)$$

The transmission coefficient of the entire structure, t , can be determined in a similar way - as the ratio of the forward travelling wave after the final layer, $E'_{N+1}{}^+$, to the forward travelling wave before the first layer, E_0^+ . From the vector equation 2.26, the two quantities can be related:

$$E_0^+ = S_{00} E'_{N+1}{}^+. \quad (2.28)$$

Rearranging equation 2.28 reveals the transmission coefficient.

$$t = \frac{E'_{N+1}{}^+}{E_0^+} = \frac{1}{S_{00}} \quad (2.29)$$

Both t and r are Fresnel coefficients, that relate ratios of the electric fields, but for performance comparisons of the real devices the most relevant metric is the ratios relating the incident electromagnetic power to the reflected power and transmitted power. The reflectance, R , can be obtained from the reflection coefficient by taking the square of the magnitude:

$$R = r^2 \quad (2.30)$$

The transmittance, T , can be obtained in a similar way, by taking the square of the magnitude of the transmission coefficient. However, the value must be normalised by taking the ratio of the phase velocities of the input and exit waves. For a top-illuminated device, that operates with the incoming light incident on the top layer of the device first, the normalisation simplifies to the ratio of the refractive indices of the substrate, $n_{\text{substrate}}$, and air, n_{air} . The transmittance is then given by

$$T = \frac{n_{\text{substrate}}}{n_{\text{air}}} t^2. \quad (2.31)$$

2.4.2 Transmission Line Model Method

As an alternative method to the transfer matrix method, a second model is also used. This method treats the entire structure as a transmission line, following the derivations of M. Ünlü and S. Strite⁴⁵. Previous examples of optical transmission line model implementations include, simulation of solar cells,⁴⁶ photonic crystal waveguides⁴⁷ and thin film optical filters⁴⁸.

Transmission line models are more commonly used in electrical engineering and acoustic engineering to model the travel of waves through bounded channels, such as wires for communication signals⁴⁹ or narrow tubes for sound⁵⁰.

In electrical transmission lines a transmission line model can be used to calculate the way that the electromagnetic wave of an alternating current behaves through the line.⁵¹ In a homogeneous infinite wire the wave will transmit in one direction only,

with the amplitude only dependent on any attenuation by the material. In a finite length wire there will be reflection off the end of the wire, which will interfere with the incident wave and form a standing wave in the line.

The main parameter involved is the impedance of the transmission line; in electrical engineering this is defined as the ratio of the voltage to the current in the line,⁵² in acoustic engineering it is defined as the product of the density of the medium and the velocity of the sound.⁵³ In applications involving electromagnetic radiation the impedance of the wave, Z , is defined as the ratio of the electric field, E , to the magnetic field,⁵¹ H , *i.e.*

$$Z = \frac{E}{H}. \quad (2.32)$$

In the example of the electrical transmission line, it is undesirable to have any reflections from the end of the line. Reflections result in transmission loss. The reflections can be eliminated by matching the impedance of the line to the impedance of the terminating medium.⁵⁴ So, the purpose of a modelling the transmission line is to allow accurate matching of the impedances.

For the purpose of modelling a transmission of the wave through a semiconductor structure, the process of light travelling through a multi-layer structure can be considered in the same way as the AC current travelling through a wire. Each layer in the structure is treated as a homogeneous two-dimensional channel, similar to the wire in the electrical example. However, the purpose is to determine the transmission and reflection at each interface. In contrast to electrical transmission, in resonant cavity structures the formation of a standing wave in the cavity is desirable for high absorption.

For a single element transmission line, *e.g.* a single homogeneous semiconductor layer, the impedance of the line can be used to determine the reflection coefficient, r , for the wave by using⁵⁵

$$r = \frac{Z - Z_0}{Z + Z_0}, \quad (2.33)$$

where Z is the impedance of the line and Z_0 is the impedance of the terminating medium. If the two impedances match then there will be zero reflection.

The reflectance of the structure can be determined from the total impedance of the structure and the impedance of the terminating medium. For all the presented structures, the impedance of the terminating medium is the characteristic impedance of air. The characteristic impedance of a medium is the impedance for a wave that is propagating in a single direction, with no reflected component, and is given by⁵⁶

$$Z_0 = \sqrt{\frac{\mu}{\epsilon}}. \quad (2.34)$$

μ is the magnetic permeability and ϵ is the electric permittivity.

For air the magnetic permeability and electric permittivity can be approximated by the vacuum permeability, μ_0 , and the vacuum permittivity, ϵ_0 , respectively. ϵ_0 are related to μ_0 by

$$\epsilon_0 = \frac{1}{\mu_0 c^2}. \quad (2.35)$$

By referring to equations 2.34 and 2.35 it can be seen that the characteristic impedance of air can be approximated by

$$Z_{\text{air}} \approx \mu_0 c = 1.256\,637\,062\,12 \times 10^{-6} \text{ H m}^{-1} \times 299\,792\,458 \text{ m s}^{-1} \approx 376.7 \, \Omega, \quad (2.36)$$

using the speed of light in a vacuum, c .

The second quantity needed for equation 2.33, the total impedance of the structure, Z_{struc} . To determine the total impedance of the structure, each layer needs to be treated as an individual transmission line segment. The impedance of the structure is built up by starting with the characteristic impedance of the substrate, which acts as the start of the transmission line. The total complex impedance from the start of the line to the end of each segment is then determined using the characteristic impedances of each layer

$$Z_{0i} = \sqrt{\frac{\mu}{\epsilon}} \approx \frac{Z_{\text{air}}}{\mathbf{n}_i}, \quad (2.37)$$

and the propagation constant for the same layer

$$\gamma_i = \frac{\alpha_i}{2} + j\beta_i. \quad (2.38)$$

The characteristic impedance of layer i is approximated by the impedance of air, Z_{air} , and by the refractive index of the layer, \mathbf{n}_i . The propagation constant is determined by the absorption coefficient of the layer, α_i , and the phase constant, which is given by

$$\beta_i = \frac{2\mathbf{n}_i\pi}{\lambda}. \quad (2.39)$$

Using the values obtained for each layer from equations 2.37 and 2.38 the total impedance, from the substrate to the end of the i^{th} layer, is built up iteratively:⁵⁸

$$Z_i = Z_{0i} \frac{Z_{i-1} + Z_{0i} \tanh(\gamma_i l_i)}{Z_{0i} + Z_{i-1} \tanh(\gamma_i l_i)}, \quad (2.40)$$

where l_i is the thickness of the i^{th} layer. Z_i is the total impedance through all layers from the first to the i^{th} layer and acts as the input impedance to layer $i + 1$. Therefore, the total impedance of the structure, Z_{struc} , is given by the equation 2.40 after Z_i has

been transformed through every layer in the structure, *i.e.* for a structure with N layers

$$Z_{struc} = Z_{0N} \frac{Z_{N-1} + Z_{0N} \tanh(\gamma_N l_N)}{Z_{0N} + Z_{N-1} \tanh(\gamma_N l_N)}. \quad (2.41)$$

Here, Z_{0N} is the characteristic impedance of the final layer, Z_{N-1} is the total impedance of all layers from 1 to $N - 1$, γ_N is the propagation constant of the final layer and l_N is the thickness of the final layer. Then Z_{struc} and Z_{air} can be input into equation 2.33 to obtain the reflection coefficient of the entire structure:

$$r = \frac{Z_{struc} - Z_{air}}{Z_{struc} + Z_{air}}. \quad (2.42)$$

In the same way as the transfer matrix method, the fraction of reflected power of the incident light - the reflectance, R - is given by

$$R = |r|^2. \quad (2.43)$$

The calculation of the transmission coefficient of the entire structure, t , is analogous to calculation of the transmission coefficients between the layers in the transfer matrix method, given in equation 2.15. In the transmission line model the refractive indices in equation 2.15 are replaced by the total structure impedance and the characteristic impedance in the terminating medium of the wave, $Z_{substrate}$, *i.e.*⁵⁹

$$t = \frac{2Z_{substrate}}{Z_{substrate} + Z_{struc}}. \quad (2.44)$$

The fraction of the power of the incident light that is transmitted is given by

$$T = \frac{Z_{substrate}}{Z_{struc}} |t|^2. \quad (2.45)$$

The calculation is again similar to the one described for the transfer matrix method, equation 2.31. The square of the transmission coefficient is normalised by the ratio of the phase velocities of input and exit mediums, which in a transmission line can be given by the impedances of the line and the terminating medium, respectively.

2.4.3 Electric Field

The calculations in the previous sections, 2.4.1 and 2.4.2, can be used to calculate the overall parameters of the structure, such as reflectance and transmittance, but do not detail what is happening inside the structure. Since the effect of the resonant cavity structures is to enhance the electric field inside the cavity, it is useful to calculate the electric field through the structure. This can be achieved by using the equations of the transfer matrix method in section 2.4.1, specifically equations 2.16 and 2.21.

Starting with the electric field in the substrate, \vec{E}_{sub} , which is assumed to be the fraction of transmitted light obtained from equation 2.29 travelling forward and a backward travelling component that is zero - this comes from treating the substrate as infinitely thick, and therefore there will be no reflections off of the substrate to air interface. This is a good approximation for substrates with some attenuation, *e.g.* GaSb for wavelengths below 1.7 μm , but is imperfect for transparent substrates.⁶⁰

The field is then transformed through the interface with the first layer to determine the field inside the first layer of the structure, *i.e.*

$$\begin{pmatrix} E_1^+ \\ E_1^- \end{pmatrix} = \frac{1}{t_{1,sub}} \begin{pmatrix} 1 & r_{1,sub} \\ r_{1,sub} & 1 \end{pmatrix} \begin{pmatrix} E'_{sub} \\ 0 \end{pmatrix}. \quad (2.46)$$

From this point the propagation matrix is used to determine the phase change through the layer

$$\begin{pmatrix} E(x)^+ \\ E(x)^- \end{pmatrix} = \begin{pmatrix} \exp(-j\vec{k}x) & 0 \\ 0 & \exp(j\vec{k}x) \end{pmatrix} \begin{pmatrix} E_1^+ \\ E_1^- \end{pmatrix}, \quad (2.47)$$

where x is the distance from the substrate. The sign inside the exponential, $\exp(-j\vec{k}x)$ is flipped because the position is chosen to be zero at the interface between the top layer of the structure and air.

This process is repeated for the interface between the first and second layer and propagation through the second layer, and then the rest of the structure in the same way. The magnitude of the electric field at each point is the sum of the absolute value of the two components. Through this calculation the electric field throughout the entire structure can be determined.

2.4.4 Model Program Implementation

None of the calculations detailed in sections 2.4.1 - 2.4.3 are difficult to do manually, but for multiple implementations they would be very time consuming. To compare structures it is necessary to construct spectrally dependent plots of reflectance and transmittance, so the calculations need to be repeated for every wavelength of interest. To be able to quickly and reliably calculate the optical parameters of any structure the calculations were implemented as a Python script that was written and during this work.

The input into the script consists of a structure file that contains the parameters for each layer: thickness, absorption coefficient and refractive index. The thicknesses are determined by following the rules laid out in section 2.3. The absorption coefficients are measured experimentally where possible, or taken from the literature *e.g.*⁶¹ - the coefficient is assumed to be zero in all layers other than the absorber material, at the design wavelength. This is approximately achieved in practice by choosing materials with wider bandgaps than the absorber. For the refractive indices, values from the literature are used.⁶¹⁻⁶⁴ It should be noted that the values for the refractive indices of III-V semiconductor alloys are less well studied at the mid-infrared wavelengths in comparison to visible and near-infrared. Therefore, some variation between the model and measured results is likely to come from the uncertainty in the refractive indices.

The calculations for both methods are implemented in the form of loops that iterate

through each layer to determine the final optical reflectance and transmittance of the entire structure. An example of the reflectance and transmittance spectra output from the Python script are shown in figure 2.15.

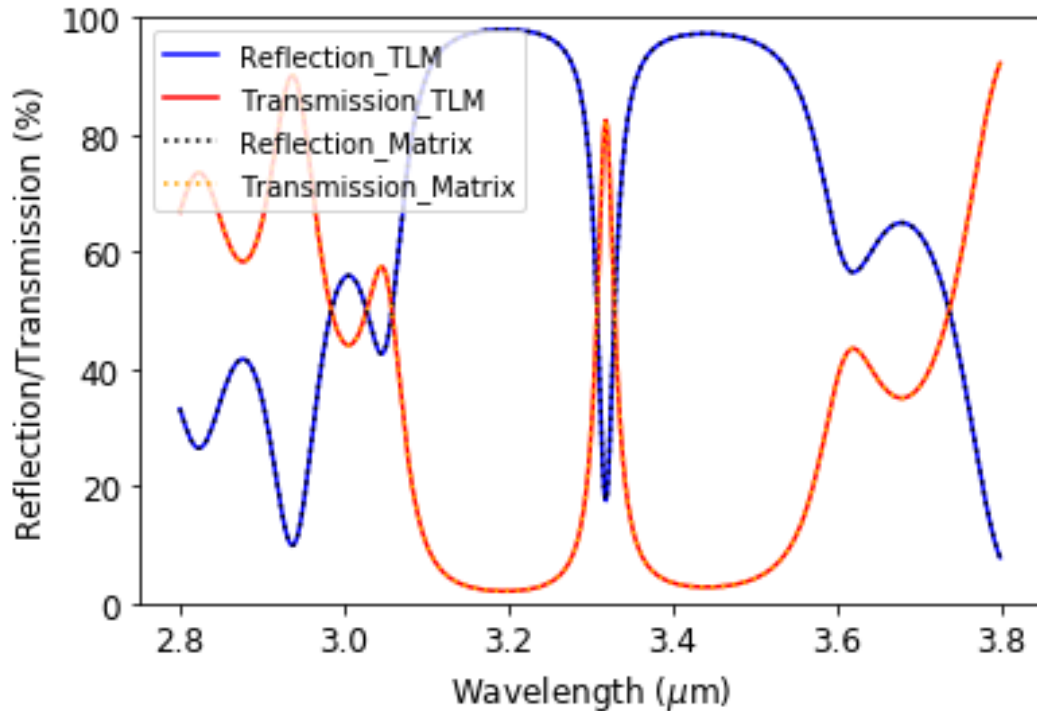


FIGURE 2.15: An example of a transmittance and reflectance spectrum for a structure with no absorption in the cavity. Note: the lines coincide, so are difficult to distinguish. Both the transfer matrix model (dotted line) and transmission line model (solid line) are plotted. The input structure is designed to have a resonant wavelength at $\sim 3.3 \mu\text{m}$.

Examples of the electric field through the structure are shown in figure 2.16, for a wavelength of light close to the resonance wavelength, and figure 2.17, for a wavelength not close to the resonance wavelength. The difference between an enhanced electric field and a damped electric field can be seen clearly. Calculations of the electric field in the structure as a function of the wavelength can be plotted to visualise the effects of the resonant enhancement, an example is shown in figure 2.18.

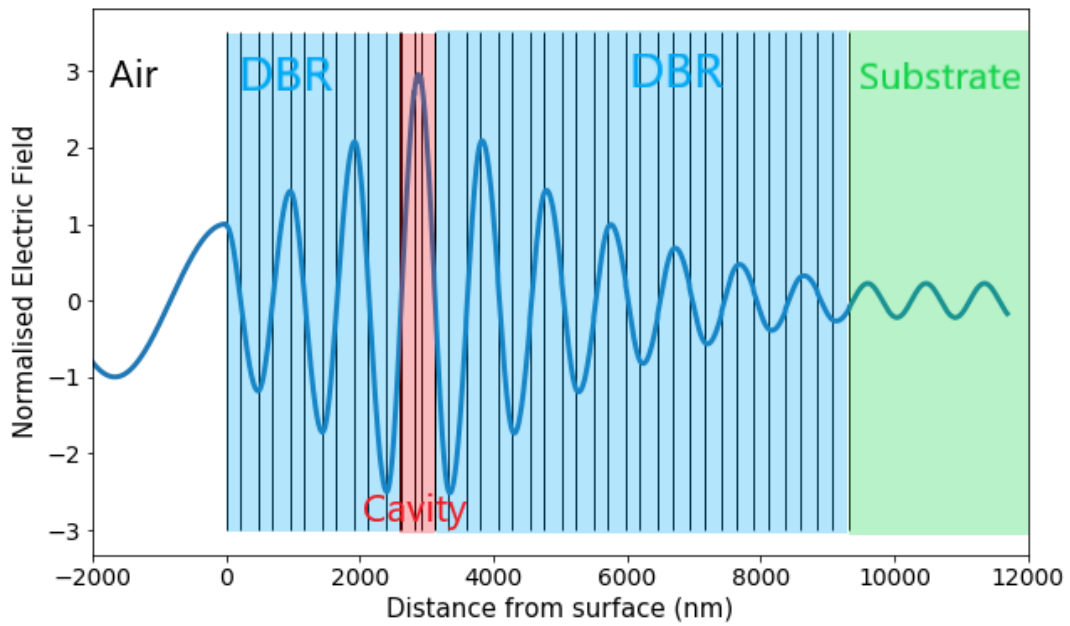


FIGURE 2.16: An example of the electric field in the structure for the resonance wavelength. The wave starts off in air on the left and travels through the DBRs (blue areas). A standing wave is formed, with a peak in the centre of the cavity (red area). The transmitted wave continues through the substrate (green area).

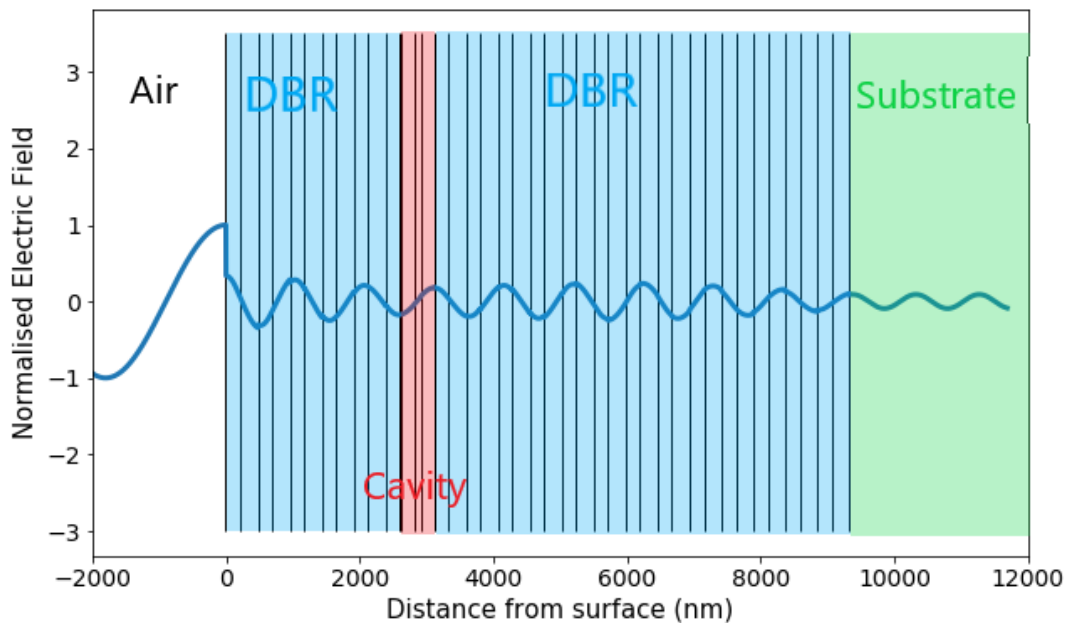


FIGURE 2.17: An example of the electric field in the structure for an off-resonance wavelength. The wave starts off in air on the left and travels through the DBRs (blue areas). The low amplitude wave does not have an anti-node at the centre of the cavity (red area). The transmitted wave is much lower amplitude in comparison to the incident wave and continues through the substrate (green area).

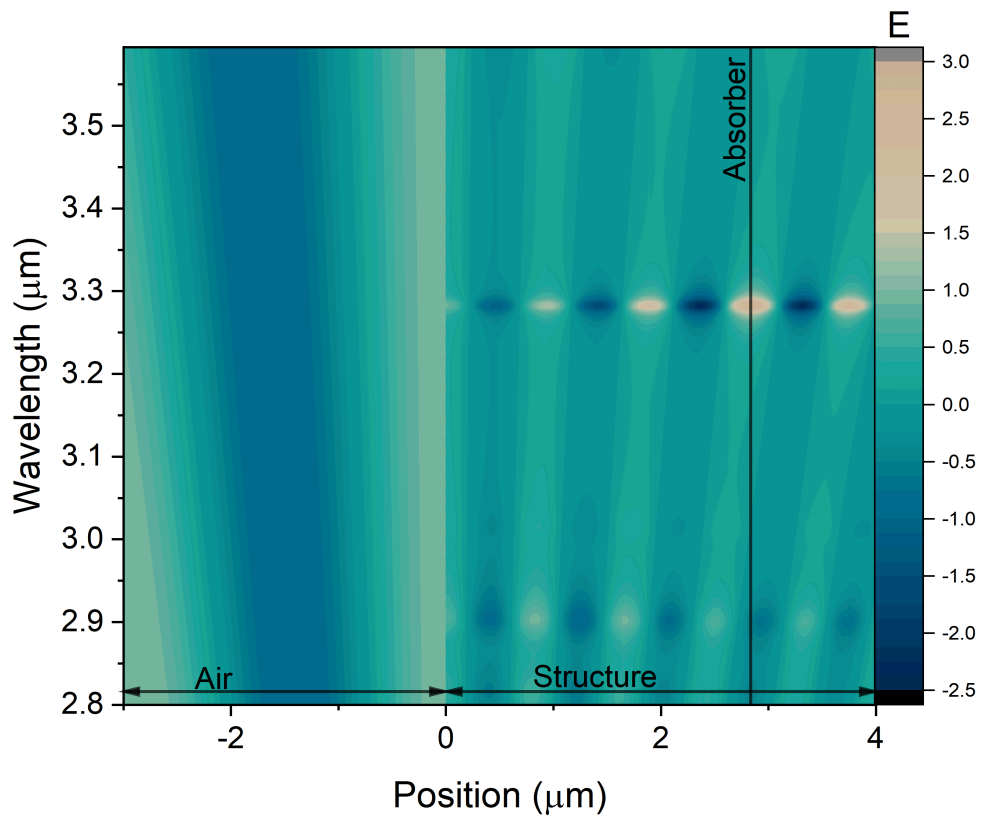


FIGURE 2.18: A colourmap of the electric field in the structure as a function of wavelength. The electric field through the structure is calculated for each wavelength, as shown in figures 2.16 and 2.17, with the electric field denoted by the colour. For resonant wavelengths, *e.g.* $3.3 \mu\text{m}$, the amplitude of the field in the structure is enhanced. For non-resonant wavelengths, *e.g.* $3.1 \mu\text{m}$, the amplitude of the field in the structure is reduced.

Chapter 3

Literature Review

This chapter provides a summary of previous reports of resonant cavity enhancement for optical detectors and related topics. In the section 3.1 the materials and structures used in SWIR photodetectors are discussed. In section 3.2 reports of cavities are investigated, followed by the first use in optical devices. Special consideration is given to the first structures that utilise two DBRs to form the cavity.

Sections 3.3 and 3.4 review reports of measured refractive indices and absorption coefficients, respectively, for selected III-V alloys. The values from the literature are used in the optical simulation of the resonant cavities - see chapter 2.4. Attention is also given to an exploration of one of the most significant applications of RCE-PDs, spectral gas sensing. Previous methods and the detectors used are discussed. This chapter intends to provide an overview of all the significant reports that have made the current work possible.

3.1 SWIR Photodetectors

In the part of short-wave infrared region targeted in this work, from 2.0 μm to 2.8 μm , there are multiple material systems that can be used for light detection. This spectral region is also sometimes called the extended short-wave infrared (eSWIR) and is covered by certain alloys of InGaAs,⁶⁵ HgCdTe,⁶⁶ InGaAsSb,^{67,68} certain type-II superlattice structures,⁶⁹ and certain quantum well structures.⁷⁰

The most well established material system is mercury-cadmium-telluride ($\text{Hg}_{1-x}\text{Cd}_x\text{Te}$ or MCT), which can be tuned to absorb light over a large portion of the infrared spectrum by varying the alloy composition.⁷¹ For sensing in the SWIR, a cutoff wavelength between 2 μm and 3 μm is achieved with a cadmium fraction of between 0.4 and 0.5.⁷² As a mature technology, high-performance HgCdTe detectors are commercially available. Available from Vigo are uncooled photovoltaic detectors with a room temperature specific detectivity of $3 \times 10^{10} \text{ cm}\sqrt{\text{Hz}}/\text{W}$ in the SWIR.⁷³ Also from Vigo, a cooled detector operating at 230 K shows improved performance, with a specific detectivity of $3 \times 10^{11} \text{ cm}\sqrt{\text{Hz}}/\text{W}$.⁷⁴ A similar uncooled HgCdTe detector from Thorlabs has a specific detectivity in the SWIR of $1 \times 10^{10} \text{ cm}\sqrt{\text{Hz}}/\text{W}$.⁷⁵

As well as the commercially available HgCdTe detectors, more recent research has led to reports of higher performance detectors. Şaşmaz has reported a detector with a cutoff wavelength just over 2 μm and a room-temperature specific detectivity of $1 \times 10^{11} \text{ cm}\sqrt{\text{Hz}}/\text{W}$.⁷⁶ The performance of commercial detectors is also continuing to improve. A recent HgCdTe photovoltaic detector by Teledyne Judson is advertised to have a specific detectivity of $1.1 \times 10^{11} \text{ cm}\sqrt{\text{Hz}}/\text{W}$ at room temperature and up to 2.5 μm .⁷⁷

Other than HgCdTe, the SWIR spectral region can also be sensed by other bulk semiconductor materials, specifically some III-V alloys. InGaAs is commonly grown lattice-matched on an InP substrate, to give a cutoff wavelength of 1.7 μm . However, it can be grown mismatched, with a higher indium fraction to extend the wavelength up to about 2.5 μm .⁷⁸ Commercially available extended-InGaAs detectors from Teledyne Judson have specific detectivities up to $8 \times 10^{10} \text{ cm}\sqrt{\text{Hz}}/\text{W}$ at room temperature, and $5 \times 10^{12} \text{ cm}\sqrt{\text{Hz}}/\text{W}$ at 198 K.⁷⁹ Similar commercial detectors are also available from Hamamatsu,⁸⁰ with a room temperature specific detectivity of $9 \times 10^{10} \text{ cm}\sqrt{\text{Hz}}/\text{W}$, and EOC,⁸¹ with a room temperature specific detectivity of $5 \times 10^{10} \text{ cm}\sqrt{\text{Hz}}/\text{W}$.

Extended-InGaAs detectors are relatively well-developed. So, the commercially available single-element detectors offer similar performance to the best reported devices

in the literature. Recently reported extended-InGaAs focal-plane-arrays demonstrated specific detectivities at 205 K of $7.5 \times 10^{11} \text{ cm}\sqrt{\text{Hz}}/\text{W}$.⁸²

Extended-InGaAs is commonly grown lattice-mismatched on InP, Si, or GaAs substrates, which can cause dislocations that deteriorate device performance.⁸³ One option to avoid the mismatched growth is to utilise an absorber of InGaAsSb with an alloy composition lattice-matched to a GaSb substrate. This bulk material can be tuned to have a cutoff wavelength between $1.8 \mu\text{m}$ and $3 \mu\text{m}$ by varying the alloy composition.⁸⁴ Detectors utilising an InGaAsSb absorber have been demonstrated, with specific detectivities at room temperature of $1 \times 10^{10} \text{ cm}\sqrt{\text{Hz}}/\text{W}$, by A.P. Craig *et al.*,⁶⁷ $2.3 \times 10^{10} \text{ cm}\sqrt{\text{Hz}}/\text{W}$, by N. Li *et al.*,⁸⁵ $4.8 \times 10^{10} \text{ cm}\sqrt{\text{Hz}}/\text{W}$, also by N. Li *et al.*⁶⁸ and $2.2 \times 10^{10} \text{ cm}\sqrt{\text{Hz}}/\text{W}$, by I. Shafir *et al.*⁸⁶

InAs and InAsSb can also be grown lattice-matched to GaSb, and can sense in the SWIR region. However, they have higher cutoff wavelengths - $3.5 \mu\text{m}$ for InAs and higher again for InAsSb, depending on the antimony fraction. The theoretical limit of specific detectivity is dependent on the cutoff wavelength, and decreases with cutoff wavelength.⁸⁷ So, higher performance can be achieved with a material with a cutoff wavelength close to the target wavelength. In the SWIR region InAs photodiodes can act as the absorber material, but with lower potential performance than the bulk InGaAsSb, for example. Commercial InAs photodiodes are available, with specific detectivities of $4.5 \times 10^9 \text{ cm}\sqrt{\text{Hz}}/\text{W}$ at room temperature,⁸⁸ and $1 \times 10^9 \text{ cm}\sqrt{\text{Hz}}/\text{W}$.² Similarly, InAsSb detectors can sense in the SWIR, but with lower possible performance. Commercial InAsSb detectors are available, with specific detectivities of $6 \times 10^8 \text{ cm}\sqrt{\text{Hz}}/\text{W}$ at room temperature,⁸⁹ and recent research on InAsSb detectors has also demonstrated room-temperature specific detectivity of $5 \times 10^9 \text{ cm}\sqrt{\text{Hz}}/\text{W}$.⁹⁰

Bulk semiconductor absorbers have historically been the most studied, due to simpler design and growth constraints, but sensing in the SWIR spectral region can also be achieved by a variety of superlattice and quantum well structures.⁹¹ InGaAs/GaAsSb quantum well structures promise to reduce the lattice-mismatch, and therefore dark currents, seen in bulk extended-InGaAs detectors. This has been

tested by B. Chen *et al.*, with a room temperature specific detectivity of $3 \times 10^9 \text{ cm}\sqrt{\text{Hz}}/\text{W}$, although improved performance is expected to be possible.⁹² A similar superlattice structure, with layers of InGaAs and GaAsSb has been demonstrated for sensing up to $2.4 \mu\text{m}$ by Y. Uliel *et al.*⁹³ The characterised device showed a room temperature specific detectivity of $1.7 \times 10^{10} \text{ cm}\sqrt{\text{Hz}}/\text{W}$.

For sensing up to $2.5 \mu\text{m}$ type-II superlattices with layers of InAs, GaSb and AlSb have been demonstrated by A.M. Hoang *et al.*⁹⁴ These structures showed specific detectivities at room temperature of $1.7 \times 10^{10} \text{ cm}\sqrt{\text{Hz}}/\text{W}$ and at 150 K of $1 \times 10^{13} \text{ cm}\sqrt{\text{Hz}}/\text{W}$. A more recent report, also by A.M. Hoang *et al.*, shows a similar structure to have a specific detectivity at 77 K and $2 \mu\text{m}$ of $2 \times 10^{13} \text{ cm}\sqrt{\text{Hz}}/\text{W}$.⁹⁵

3.2 Resonant Cavity Enhancement

The theoretical understanding of the physics of resonant cavity enhancement were first discussed in 1833 by George Airy.⁹⁶ In his book he lays out the mathematical derivations of the transmission and reflection of light through a multi-layer structure, and the resulting interference spectra are discussed. This work led to the creation of multiple types of interference based devices by the end of the 19th century,^{97,98} including resonant cavities, or Fabry-Perot cavities, which were first reported by Charles Fabry and Alfred Perot in 1899.⁹⁹ Their setup used two glass plates with silver coatings as the mirrors. Interference of the forward and backward travelling waves, between the two mirrors, produced sharp interference fringes at the wavelengths of constructive interference.

Initially, the Fabry-Perot cavity concept was applied most significantly to spectroscopy applications. For example, the measurement of atomic emission lines was made by passing the light through a cavity, with light only transmitted when the emission wavelength aligned with the resonance wavelength.^{100,101} There are many other uses of this kind of Fabry-Perot cavity, but the scope of the rest of this chapter is limited to their use in optical detectors and semiconductor devices.

The first report of resonant cavity enhancement in semiconductor devices was made in 1976 by J.J. Goedbloed and J. Jooston.¹⁰² Their combined theoretical and experi-

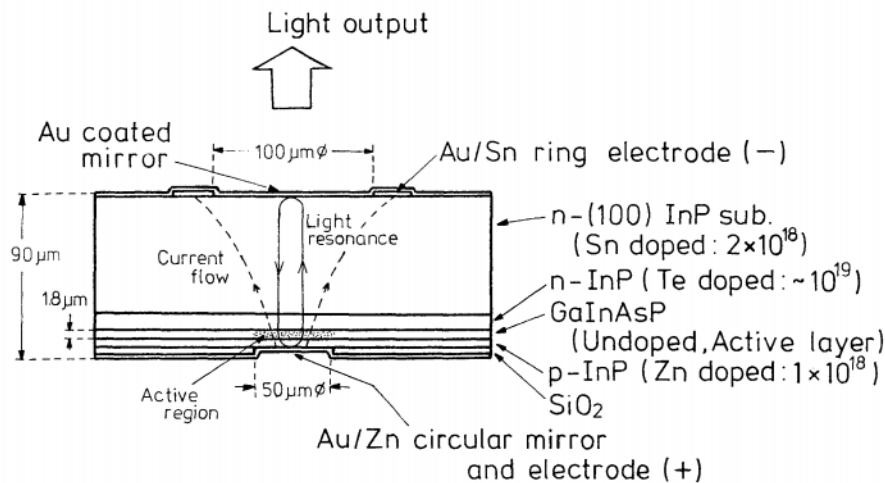


FIGURE 3.1: First vertical cavity laser structure, from H. Soda *et al.*¹⁰³, with an emission wavelength of $1.2\ \mu\text{m}$. It was named a 'surface-emitting injection laser' by the authors and it demonstrated the possibility of a resonant cavity perpendicular to the wafer surface.

mental work demonstrates the interference caused by multiple reflections between two mirrors on the responsivity of an avalanche photodiode, APD. In their devices the two mirrors were the top and bottom metallic contacts, utilised as mirrors and contacts simultaneously. The main result from their measurements is the impact of the resonant enhancement on the measured responsivity - peaks and troughs are seen as a result of the interference.

Not long after the first semiconductor resonant enhancement was demonstrated, the first vertical emitting laser utilising two metallic mirrors was proposed and fabricated. Called a 'surface-emitting injection laser' by the authors, Haruhisa Soda *et al.*¹⁰³ the structure (figure 3.1) demonstrated the possibilities of a resonant cavity perpendicular to the wafer surface. The resonant enhancement was determined mainly by the reflectivities of the two mirrors and the thickness of the active layer. Vertical cavity lasers have many of the same properties and requirements as resonantly enhanced photodetectors, so the initial development is considered here in parallel with the development of early semiconductor resonant cavity detection structures.

These first structures for both detectors and emitters utilised metal mirrors deposited on top of the semiconductor material. These mirrors provide relatively high reflectivity, however the reflectivity is approximately broadband - there is no wavelength

selection associated with the mirrors. This means that light of all wavelengths can enter the cavity initially, and the wavelengths that are enhanced are controlled only by the optical path length between the two mirrors. However, the simplicity and higher tolerance fabrication process offer insight into the decisions to use metallic mirrors. These first structures were grown by liquid-phase epitaxy (LPE), which does not offer the precision of thickness required for repeatable DBR layers. In contrast, the thickness of the evaporated metallic mirrors does not have to be precise to achieve good control of the reflectance.

The advent of resonant cavity-enhanced structures with DBR mirrors coincided with the widespread adoption of higher precision epitaxial growth techniques. Both metal-organic chemical vapour deposition (MOCVD) and molecular beam epitaxy (MBE) can produce layers with much higher precision than LPE. The first structure to create a resonant cavity with a DBR was reported by A. Chailertvanitkul *et al.* in 1985.¹⁰⁴ They reported a InGaAsP/InP laser with a resonant mode at $\lambda = 1.4 \mu\text{m}$. The significant advance here was the demonstration of matching the optical path lengths of the DBR layers to the total optical path length of the cavity. This is necessary, so that the reflectivity at the emission wavelength is high. A mismatch would dampen the resonance and possibly stop the device from working if the mismatch is large enough.

Extensive research into VCSELs in the late 1980's and 1990's led to many improvements on the designs, including the use of two DBRs. An example of these structures, reported by R.S.Geels and L.A. Coldren in 1990,¹⁰⁵ is shown in figure 3.2. Metallic contacts are still used, to provide the current to the active region, but they are not used for reflection purposes.

Coinciding with advances in DBR based VCSEL structures, resonant cavity-enhanced detectors are reported more widely from the start of the 1990's. The most significant contributor is M. Selim Ünlü. Starting in 1990 he published a number of significant papers that have become the blueprint for resonant cavity-enhanced detectors and resonant cavity-enhanced light emitting diodes (RC-LEDs). The first reported structure utilises a single DBR at the bottom of the structure, followed by the cavity, which

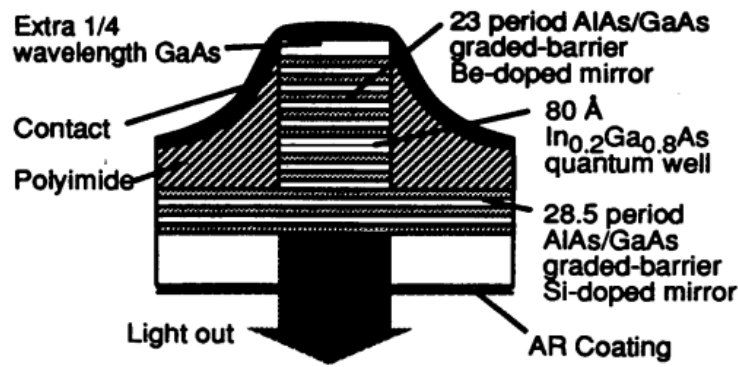


FIGURE 3.2: Example of a VCSEL with two DBRs, from Geels *et al.*¹⁰⁵, with an emission wavelength of 970 nm. This is one of the first reported structures to use two DBRs as the reflectors, with no metallic reflector used.

contains a heterojunction phototransistor, HPT, active region.¹⁰⁶ The top reflector is simply the semiconductor-air interface, which has a reflectivity of $\sim 30\%$. The use of only a singular DBR does reduce the spectral selectivity of the structure, there are two significant resonances and a high broadband response at lower wavelengths. The multiple resonances are due to the choice of a thick cavity, which reduces the free spectral range between neighbouring resonances.

The next significant report from Ünlü *et al.* is a theoretical study of RCE-PDs with DBRs above and below the cavity.¹⁰⁷ The structures are all realistic for epitaxial growth, and demonstrate the possibility of a single, narrow resonant response. The report is a detailed analysis of the simulation of RCE-PD structures, along with a significant comparisons between different structures. The most significant result is the quantum efficiency spectra of two RCE Ge p-i-n structures. The first structure has no layers above the cavity and relies on the semiconductor-air interface for the reflection at the top of the cavity. The second structure has a five pair DBR on top of the cavity. Both structures use a twenty pair bottom DBR. The clear benefit of the top DBR is the much reduced FWHM of the resonance in comparison to the structure without a top DBR. A significant result is the demonstration of cavity thickness variation - thinning the cavity results in a corresponding decrease in resonance wavelength. This report highlights the significance of this property - it is relatively straightforward to change the cavity thickness, and the ability to tune the detector to respond at a specific wavelength is invaluable for certain applications, *e.g.* spectroscopy.

The structures presented up to this point have covered the visible to near-infrared portion of the electromagnetic spectrum. These regions aren't necessarily of most interest, but the structures were possible with well-developed material systems at the time. The spectral region covered by a conventional detector is limited by the cutoff wavelength of the absorber, for example ~ 950 nm for the InGaAs HPT presented by Ünlü *et al.* The exact wavelength of the resonance of resonant cavity-enhanced devices is limited by not only the absorber cut-off wavelength, but also the reflection spectrum of the DBR(s). Theoretically, it is not a limit, because the thickness of the DBR layers can simply be increased to achieve high reflectivity at longer wavelengths. However, thicker DBRs results in longer growth times and more stringent growth-rate consistency requirements. The basic structure of RCE-PDs is explained and analysed in abundant detail in Ünlü and Strite's review paper published in 1995.⁴⁵ However, by this point there is still a lack of experimental results for devices at longer wavelengths. Up to $1.55 \mu\text{m}$ is demonstrated by Corbett *et al.*¹⁰⁸, although this structure utilises metallic mirrors and not the more spectrally specific DBRs.

Similar structures demonstrated in the early 1990's include an MBE grown Schottky photodiode, with an InGaAs absorber.¹⁰⁹ This structure only includes a single DBR, below the cavity. An RCE p-i-n structure utilising an InGaAs absorber was also reported at a similar time by Dentai *et al.*¹¹⁰ A dielectric stack was deposited on top of the cavity, to increase the reflectivity of the native semiconductor-air interface to 73%. At the time, 1991, the resonance wavelength of $1.55 \mu\text{m}$ was described in the title as 'long wavelength' - as this was about the limit of contemporary RCE-PDs.

A lot of the reports on RCE-PDs in the 1990's view the main application of them in high-speed optical communications and interconnects.^{4,45,111-113} High detection speeds in photodetectors are dependent on the thickness of the absorber, and one of the main differences between RCE and conventional detectors is the thickness of the absorber. RCE-PDs can utilise much thinner absorber layers without sacrificing QE. Therefore, they offer the combination of high-speed and high-QE that is desirable for detection of optical communication signals. Structures designed for this purpose

typically utilise a single DBR, below the cavity, and an anti-reflection coating on top of the epitaxial structure to increase the maximum attainable QE. No top DBR allows for a simpler fabrication process to be used.

Later advances in RCE-PDs most significantly focus on demonstrating the RCE-PD concept with novel material systems or extending into new spectral regions. Beyond the 1.55 μm telecommunications band the main application mentioned in most reports is spectral sensing. A structure based on an InAs absorber was presented by A. Green *et al.* in the early 2000's for the purpose of methane sensing.¹¹⁴ Similar to many previous structures, the top mirror was simply the native semiconductor-air interface - figure 3.3a. As stated by the authors, this limits the finesse of the cavity, in return for a simpler fabrication scheme. The measurement spectral response does also include a significant broadband component, as a result - shown in figure 3.3b. Without a top DBR the FWHM is relatively broad, 150 nm, but for the specific purpose of methane sensing the authors do not see this as an issue because the methane absorption peak is a similar spectral width. This report also highlights the characteristic tunability of RCE-PD spectral response. The target resonance wavelength was only ~ 200 nm away from the resonance of the fabricated device. One area of improvement for this structure is the high temperature response. There is no measurable response above 250 K, possibly due to the use of lattice-mismatched materials. InAs is $\sim 7\%$ mismatched to GaAs.

Between the early 2000's and 2010 there are few reports on new RCE-PD structures. In 2010 Wang *et al.*¹¹⁵ reported on the design of and RCE-PD targeted at ~ 3.5 μm , a longer wavelength that had previously been attempted. The design uses two DBRs to also produce a relatively high finesse cavity, and a FWHM of < 100 nm. The responsivity is shown in figure 3.4. As well as increasing the resonant enhancement, the use of a second DBR reduces the broadband response of the detector. Comparison of the responses shown in figures 3.3b and 3.4 demonstrate the increased spectral selectivity that the top DBR introduces.

Another report in 2010, by Asano *et al.*¹¹⁶, extends the RCE-PD concept further into the infrared, with a resonance wavelength of a fabricated device of ~ 4.5 μm . The

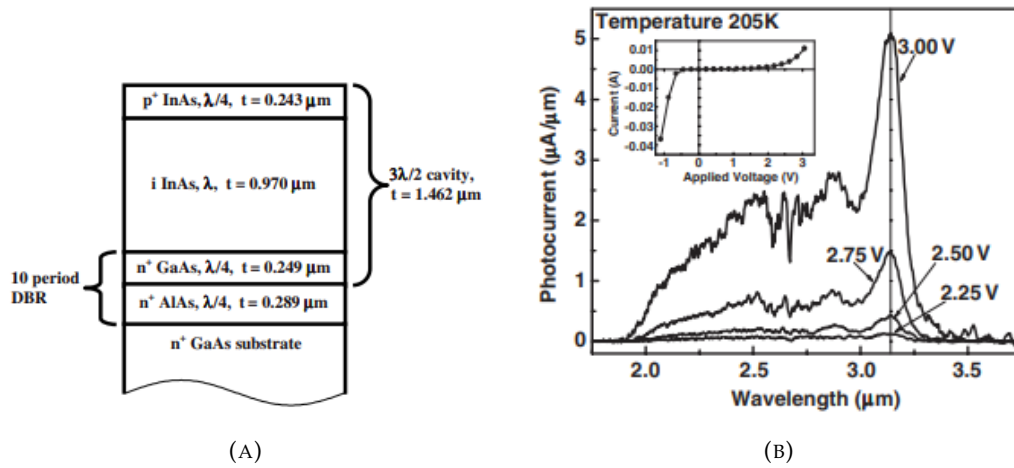


FIGURE 3.3: A) Structure of an RCE-pin with InAs absorber, the bottom reflector is a DBR and the top reflector is the interface with air. B) Responsivity of the same RCE-pin. A clear resonance can be seen at 3.15 μm . This is one of the first reports of RCE-PDs in this spectral region. Both from Green *et al.*¹¹⁴

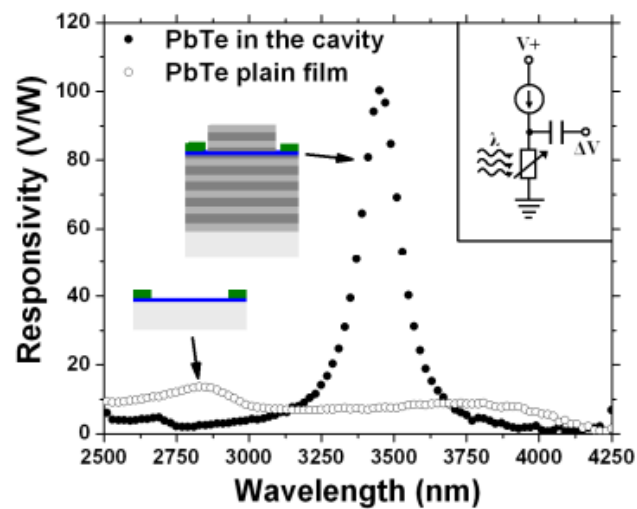


FIGURE 3.4: Spectral response of a PbTe RCE-PD from Wang *et al.*¹¹⁵ This structure utilise two DBRs as the reflectors, reducing the broadband response in comparison to previous structures without a top DBR.

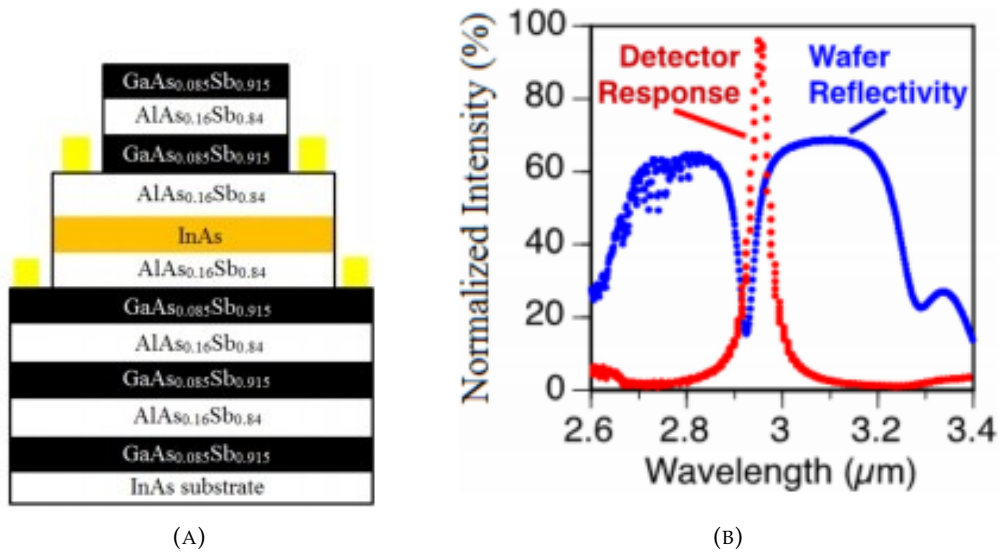


FIGURE 3.5: A) Structure of an InAs RCE-PD. B) Spectral response of the same InAs RCE-PD. Both from O’Loughlin *et al.*⁷ This structure is the most similar reported RCE-PD from the literature to the structures presented in this thesis. The use of two DBRs creates a high finesse cavity, with a narrow spectral response.

structure utilises a novel GaAs/air gap DBR that is created by selectively etching the material between the GaAs layers. The result is a high refractive index contrast between the DBR layers and a high reflectance for just a two pair DBR. However, the combination of few bottom DBR pairs and an air interface top mirror results in a low finesse cavity and very broad resonance of 400 nm.

The next significant report, in 2017, utilises structures that are the most similar to the ones presented in this thesis. The structures, demonstrated by T. O’Loughlin *et al.*⁷, consist of DBRs above and below the cavity and unipolar barrier (nBn) architecture within the cavity. Structures are presented for two different material systems, an InAsSb absorber on a GaSb substrate and an InAs absorber on an InAs substrate. A narrow spectral response, shown in figure 3.5b, is the result of including two DBRs.

Table 3.1 compiles all the reports of RCE-PDs discussed in this section. The chronological order shows the advancements made in RCE-PD structure design from the very first semiconductor-based resonant cavity in 1976, to the most recent reports. In general, structure designs have become more complex. Higher precision epitaxial growth techniques, such as MBE, have made high-quality complex structures possi-

ble. The relatively thin layers involved in RCE-PD structures require the enhanced precision that current reactors provide, in particular due to the dependence of the resonance wavelength on the layer thicknesses.

Metallic mirrors are most common in early RCE-PD structures, because they offer relatively high reflectivity and are simple to deposit. However, they do not offer the high spectral selectivity of a DBR, which have become a more popular option for the bottom DBR. There is no consensus on the best choice of top mirror, even in the most recent reports. A second DBR enhances the spectral selectivity, at the expense of increased complexity. Whereas a simple semiconductor-air interface is a popular choice due to its simplicity and easy fabrication schemes. It is clear from viewing the previous fabricated structures as a whole that the choice of application is a significant factor in the choice of mirrors. There is always a trade-off between simplicity and high-finesse. Resonant cavity enhancement can simply be used to increase the responsivity of a detector by reflecting the photons for a second pass through the absorber, or it can be used to create a very narrow spectral response for sensing at a specific target wavelength.

Author/Paper	Year	Bottom Mirror	Top Mirror	Cavity Structure
Goedbloed <i>et al.</i> ¹⁰²	1976	Metal	Metal	APD
Unlu <i>et al.</i> ¹⁰⁶	1990	AlAs/GaAs DBR	Air	HPT
Chin <i>et al.</i> ¹⁰⁹	1990	AlGaInAs/AlInAs DBR	Air interface	Schottky PD
Kuchibhotla <i>et al.</i> ¹¹⁷	1991	AlAs/GaAs DBR	Air interface	APD
Dental <i>et al.</i> ¹¹⁰	1991	InP/InGaAsP DBR	CaF ₂ layer	pin
Corbett <i>et al.</i> ¹⁰⁸	1993	Metal	Metal	pin
Ornat <i>et al.</i> ¹¹¹	1998	AlAs/GaAs DBR	Air interface	Schottky PD
Gokkavas <i>et al.</i> ¹¹²	1999	AlAs/GaAs DBR	Metal	Schottky PD
Ozbay <i>et al.</i> ¹¹³	1999	AlGaAs/AlAs DBR	Air interface	pin
Shen <i>et al.</i> ¹¹⁸	2000	Metal	Air interface	Quantum Well Infrared Photodetector
Bourdoucen <i>et al.</i> ⁴	2001	AlGaAsSb/AlAsSb DBR	SiN and metal	Schottky PD
Green <i>et al.</i> ¹¹⁴	2003	AlAs/GaAs DBR	Air interface	pin
Jun <i>et al.</i> ¹¹⁹	2004	SiO ₂ /Si DBR	InAs/GaSb DBR	pin
Wehner <i>et al.</i> ¹²⁰	2005	HgCdTe/CdTe DBR	Oxide interface	Photoconductor
Arnold <i>et al.</i> ¹²¹	2005	BaF/PbSe DBR	Metal	Photovoltaic
Wang <i>et al.</i> ¹¹⁵	2010	AsS/Ge DBR	AsS/Ge DBR	Photoconductor
Asano <i>et al.</i> ¹¹⁶	2010	GaAs/air gap DBR	Air interface	Quantum Dot Infrared Photodetector
O'Loughlin <i>et al.</i> ⁷	2017	AlAsSb/GaSb DBR	AlAsSb/GaSb DBR	nBn

TABLE 3.1: Compilation of reports of fabricated semiconductor RCE-PDs and selected properties.

3.3 Refractive Indices of III-V Semiconductors

The optical models of resonant cavity devices all rely on material parameters to be input into the calculations. The refractive indices and absorption coefficient are both required for the modelling. For both of these parameters it is important for an accurate value to be used, because the output spectra from the model can be highly dependent on these values. Measurement of the refractive indices of the III-V semiconductor alloys is out of the scope of this thesis. So, the values used in the modelling all come from the literature.

There are a few ways to measure the refractive index of a thin layer. Ellipsometry is a common technique used to measure very thin layers, down to a few nanometers.¹²² This technique uses elliptically polarised light, reflected off the sample. In simple terms, the refractive index is determined from the complex reflection coefficient of the polarised light.¹²³ For the semiconductor alloys used in this work, it is necessary for them to be grown on a substrate, which has to be taken into account for ellipsometer measurements. So, accurate knowledge of the refractive index of the substrate is necessary for the refractive index of the epilayer to be calculated accurately. Other techniques include, M-lines measurements,¹²⁴ and Michelson interferometer measurements.¹²⁵

There is an inherent limitation in using refractive index values from the literature, that the values are dependent on material preparation, temperature,⁶² and doping level.¹²⁴ So, even perfectly accurate measurements will not match exactly the refractive indices in the fabricated structures used in this work. For some of the alloys used in this work there is also a significant dependence on the exact alloy composition, *e.g.* the fraction of indium in InGaAsSb is unlikely to be exactly the same on two different samples, without significant, time-consuming calibration procedures. So, to get accurate refractive index values to model the fabricated RCE structures it would be necessary to measure the refractive index on an epilayer grown at a similar time and with the exact same growth conditions.

The refractive indices of the III-V semiconductor alloys are all significantly dependent on the wavelength of light. So, the refractive index needs to be measured at the

wavelength of interest for it to be accurate. This is a limitation of a lot of measurements in the literature, they don't all cover the mid-infrared spectral region studied in this work. For each of the alloys there are at least some previous measurements that can be used as an approximate value for modelling.

For undoped GaSb, S. Roux *et al.* present measured values of 3.86 and 3.82 at 2.2 μm and 3 μm , respectively.¹²⁴ These values decrease slightly with increased n-type doping. R. Ferrini *et al.* present a very similar measured value of 3.87 at 2.2 μm .

For InAs, from the data from O. G. Lorimer and W. G. Spitzer a measured value can be calculated of 3.52, at 3.7 μm .¹²⁶ More recently, G. D. Gillen *et al.* have measured InAs over a temperature range, although only at a longer wavelength of 10.6 μm . A 300 K value of 3.49 is given, indicating very little variation with wavelength.⁶²

Both GaSb and InAs are binary alloys, which should have the same composition however they are prepared. However, for the more complex alloys this is not the case. For example, the refractive index of AlAsSb depends on the arsenic fraction of the alloy. One approach to estimate the values of a specific alloy composition is to interpolate between the refractive indices of the constituent binary alloys, *i.e.* AlAs and AlSb. The alloys of $\text{AlAs}_x\text{Sb}_{1-x}$ used in this work have compositions of $x = 0.08$ and $x = 0.16$, so the refractive indices will be close to that of AlSb. At a wavelength of 2.25 μm , C. Alibert *et al.* have measured a refractive index of 3.15 for AlSb.¹²⁷ The measurements do not go as high in wavelength as 3.3 μm , but following the trend line suggests a refractive index of about 3.11 at this wavelength for AlSb. For AlAs, R. E. Fern and A. Onton have measured a value at 2.25 μm of 2.88.¹²⁸ Again, by following the trend to lower photon energy a refractive index at 3.3 μm can be inferred to be about 2.86. The refractive index of AlAs at the lower wavelength is in close agreement with that measured by M. Garriga *et al.* of 2.89 at 2.25 μm .¹²⁹

To get the refractive indices of AlAsSb, linear interpolation can be used with the values from the literature. For $\text{AlAs}_{0.08}\text{Sb}_{0.92}$ at 2.25 μm this calculation gives a refractive index of 3.13. For $\text{AlAs}_{0.16}\text{Sb}_{0.84}$ at 3.3 μm this calculation gives a refractive index of 3.07.

Estimated values for the refractive indices of InGaAsSb and InAsSb can also be obtained through linear interpolation of the refractive indices of the constituent binaries. For InGaAsSb, the values of GaSb and InAs can be used. For InAsSb, the composition used in this work is 91 % InAs, but the 9 % Sb can be accounted for by interpolating with the refractive index of InSb. At a long wavelength of 10.6 μm , and a temperature of 220 K, G. D. Gillen *et al.* have measured the refractive index of InSb to be 3.89.⁶² According to the modelling of S. Adachi, the room temperature refractive index at 2.25 μm is very similar to the measured value at the longer wavelength.⁶¹

The values from the literature are all good estimates for the refractive indices of the layers in the fabricated samples, but are not perfect. The doping level impacts the refractive index. In general, increased doping reduces the refractive index.^{124,130,131} There can also be significant variations due to temperature. In general, the refractive index of III-V semiconductors usually increases with temperature. A temperature dependence of $9 \times 10^{-5} \text{K}^{-1}$ and $36 \times 10^{-5} \text{K}^{-1}$ has been measured for InAs and InSb, respectively.⁶² For AlAs and GaAs temperature dependencies of $14 \times 10^{-5} \text{K}^{-1}$ and $27 \times 10^{-5} \text{K}^{-1}$, respectively, have been measured.⁶³ GaSb has been found to have a temperature dependence of $8 \times 10^{-5} \text{K}^{-1}$.¹³² For the resonant cavity structures, it is important to note that the temperature dependencies of the materials are not all the same.

3.4 Absorption Coefficients of III-V Semiconductors

The absorption coefficient of each layer is another important parameter that needs to be known for the accurate optical modelling of resonant cavity structures. The absorption coefficient determines how much light is absorbed for a certain thickness layer, and accurate values are needed to determine the ideal absorber thickness. It is easier to measure experimentally than the refractive index. A simple absorption coefficient calculation can be done with a transmission measurement through a layer. If the layer thickness is known, and no other sources of attenuation contribute to the transmission measurement, then the absorption coefficient can be calculated by following Beer's law.¹³³

In the optical models for resonant cavity structures, chapter 2, the absorption coefficient is assumed to be zero for all layers other than the absorber. This is not a perfect assumption, but is close enough for accurate modelling to still be achieved. So, the absorption coefficient of the absorber material is most important to know accurately. For this work, the absorber materials are InAs and InGaAsSb. InAsSb is also present in one of the structures and is known to absorb significantly in the mid-infrared.

It is worth noting that the absorption coefficient varies significantly with wavelength, temperature and also the doping level of the material.¹³⁴ So, a quoted absorption coefficient is only accurate for materials with matching parameters. For the RCE-PDs the significant wavelength for the absorption coefficient is the resonance wavelength. For the more complex alloys, *i.e.* InGaAsSb, the absorption coefficient is also significantly dependent on the alloy composition.

InAs is the simplest of the absorber alloys, because the alloy composition is fixed. However, close to the cutoff wavelength the absorption coefficient is strongly dependent on dopant density. At 3.3 μm , the desired resonance wavelength for this absorber, the absorption coefficient has been measured by Dixon and Ellis to vary between $< 10 \text{ cm}^{-1}$ and 4000 cm^{-1} for n-type doping concentration between 10^{16} cm^{-3} and 10^{18} cm^{-3} .¹³⁵ Also for InAs, S. Adachi suggests an absorption coefficient at 3.3 μm of between 1000 and 5000 cm^{-1} .⁶¹ The doping level is not stated.

An accurate value for the absorption coefficient of $\text{InAs}_x\text{Sb}_{1-x}$ is harder to determine from the literature, because the arsenic fraction can vary. In this work the alloy is lattice-matched to GaSb, with a composition of $x = 0.91$. It is also only used in an RCE-PD structure designed to sense at around 2.2 μm , which is far from the cutoff wavelength of all compositions of InAsSb. So, at this wavelength the absorption coefficient is less sensitive to variations in the alloy composition. A.I. D'Souza *et al.* have measured $\text{InAs}_{0.81}\text{Sb}_{0.19}$ to have an absorption coefficient of 8000 cm^{-1} at 2.2 μm .¹³⁶ M. A. Marciniak *et al.* have studied the absorption coefficient of InAsSb at a range of compositions close to lattice-matched to GaSb. There is some variation between in the absorption of the strained epilayers, but of most interest to this work is

the layer of $\text{InAs}_{0.911}\text{Sb}_{0.089}$. This alloy composition was found to have an absorption coefficient of 7800 cm^{-1} at a wavelength of $2.2 \mu\text{m}$.¹³⁷

For the InGaAsSb alloy, any values found in the literature are unlikely to be accurate enough to use with high confidence in simulations. Especially for this work, the exact alloy composition fabricated is difficult to control without significant calibration and the wavelength of interest is close to the cutoff wavelength - and the corresponding high variation in absorption coefficient. An approach used by J. Borrego *et al.* is a weighted mean of the absorption coefficients of the constituent binary alloys.¹³⁸ These are more likely to be accurate and well known. For InGaAsSb an approximate value can be estimated from the absorption coefficients of InAs and GaSb ,¹³⁹ *e.g.* for an alloy of $\text{In}_{0.25}\text{Ga}_{0.75}\text{As}_{0.25}\text{Sb}_{0.75}$ an estimate would be a quarter InAs and three quarters GaSb . At $2.2 \mu\text{m}$ InAs has an absorption coefficient of 4400 cm^{-1} ,¹⁴⁰ and GaSb is close to zero.⁶¹ So, this approach gives an absorption coefficient of 1100 cm^{-1} for $\text{In}_{0.25}\text{Ga}_{0.75}\text{As}_{0.25}\text{Sb}_{0.75}$. Measured absorption coefficients on InGaAsSb alloys are less well studied than the constituent binary alloys. Throughout the literature it is common for optical simulations to assume an absorption coefficient of InGaAsSb , based on wavelength and bandgap.^{86,141,142} However, none of these values of absorption coefficient are likely to be accurate for a layer with different composition, different doping and temperature variations. So, for this alloy accurate simulation is likely to require measurement of a very similar layer to the one used in the full structure.

3.5 Spectral Gas Sensing

One significant application of RCE-PDs is optical (or spectral) gas sensing, which is utilised by many different industries. For example, it is used for process control in factories, locating gas leaks, measurement of gas compositions and environmental air monitoring.

Each type of gas absorbs photons with specific wavelengths, due to the interactions of the photons with the molecules. The absorption wavelengths are specific to each gas as a result of the molecular structures. For example, the energy required for an

electron to change to a higher level orbital is dependent on the type of atom. In this case, for a photon to interact with the electron (transfer its energy) it has to have the specific energy required by the electron to move to a higher energy level. The photon energy, E , is related to the photon wavelength, λ , by

$$\lambda = \frac{hc}{E}, \quad (3.1)$$

where h is Planck's constant and c is the speed of light in a vacuum.

Optical detectors can use the relationship between absorption wavelength and type of molecule to detect specific gases. Some applications, where the gas concentration is high, can simply utilise a measurement of the total attenuation of the incident light. Low concentrations of the target gas species requires a measurement with higher spectral specificity. Other components of the gas sample also absorb light, so the total attenuation cannot be used to measure a specific gas species and measurement of the attenuation at a specific wavelength is necessary to discriminate the target gas species.

In general, gas monitoring requires a light source, an optical detector and a space in between them filled with the gas. This section focuses on the optical detector technology. The most simple setups use a broadband detector with a high spectral response in the absorption region of the target gas. Filters can be used, as shown in figure 3.6, to ensure that the light entering the broadband detector only covers the spectral region of the target gas absorption peak. A second filter that covers a neighbouring spectral region can be used as a reference channel, combined with a second broadband detector.⁶ This setup also uses a broadband light source, so relies on the filters to select the target spectral band.

Another method of targeting only a specific narrow spectral band involves the use of a narrow band light-source *e.g.* a laser. The narrow band of the light source removes the need for filters as only absorption at the specific wavelength of the laser will attenuate the power incident on the detector. Examples include DFB lasers emitting at 1.57 μm ,¹⁴³ VCSELs emitting at $\sim 2.3 \mu\text{m}$ and VCSELs emitting at $\sim 2.0 \mu\text{m}$.¹⁴⁴

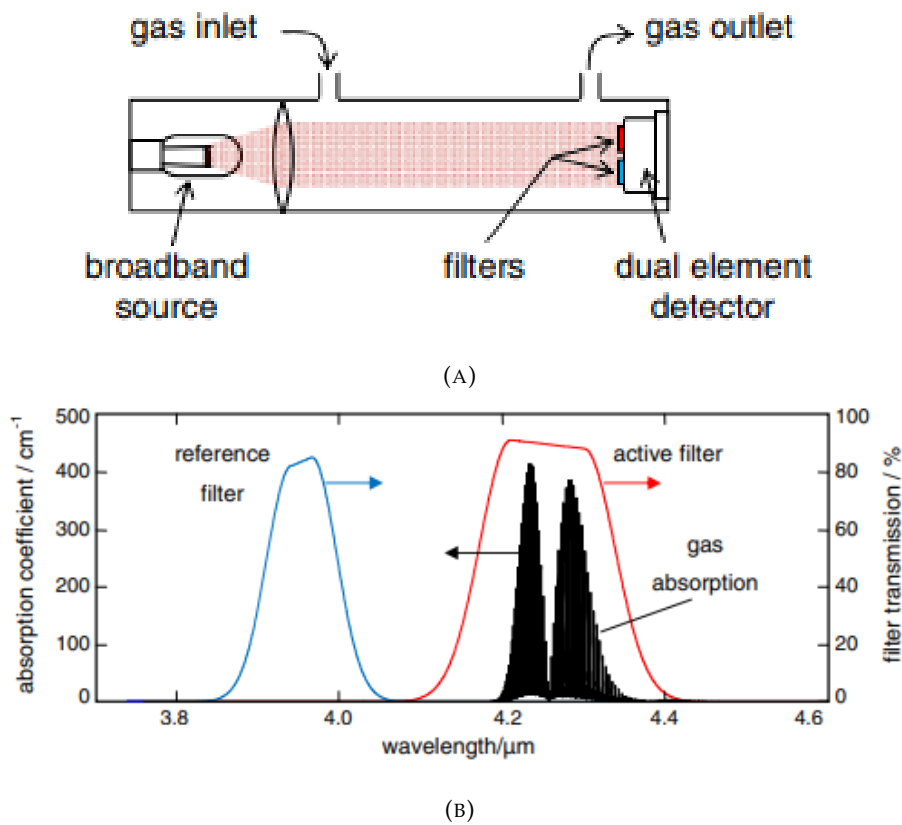


FIGURE 3.6: A) Sketch of a gas measurement setup utilising a broadband detector. The light from a broadband source passes through the gas chamber first, then through two filters onto separate detectors. B) Example spectral responses of the two channels in the setup. Each of the two filters allows different parts of the spectrum to be transmitted, resulting in differing spectral responses at the detectors. Both from J. Hodgkinson and R.P. Tatam⁶

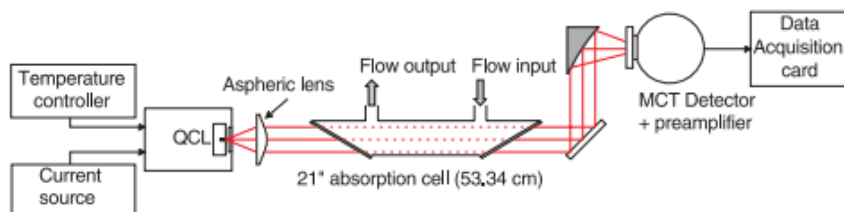


FIGURE 3.7: Example of a gas sensing setup using a QCL source, from Weidmann *et al.*¹⁴⁵ The light from the laser passes through the flowing gas chamber and then directly into the detector. There is no filter or reference detector as in the previous, broadband light source setup.

There are many other examples reported. More recently, quantum cascade lasers (QCL) with highly tunable wavelengths have been demonstrated. The ability to tune the wavelength significantly increases the versatility, as many different gas species can be targeted - although not simultaneously. An example of a setup used for gas sensing with a QCL is shown in figure 3.7, from Weidmann *et al.*¹⁴⁵. The significant difference between setups using broadband sources and laser sources is the filter, the laser setups do not require filters.

Comparison of the two optical gas sensing setups presented so far, figures 3.6a and 3.7, reveals the two options for achieving the required spectral selectivity. Either a narrow band source can be used, or the detected light can be narrow band. For laboratory or factory applications, where size is not an issue, both of these options have been used to measure low concentrations.^{146,147}

Another way to reduce the wavelength range that is detected in gas sensing measurements is to use a dispersive grating. With a grating in the setup, the source and detector can both be broadband and the spectral selectivity comes from the grating dispersing the light by wavelength. Most commonly, the dispersed light is directed onto a detector array, where one edge of the array only sees the lowest wavelength of the light and the opposite side only see the highest wavelength.^{6,148} The gas cell can be the same as for the previous methods discussed, but because a number of wavelengths can be measured simultaneously, it is possible for multiple gases to be measured simultaneously as well. An example of a diffractive grating gas setup is shown in figure 3.8.

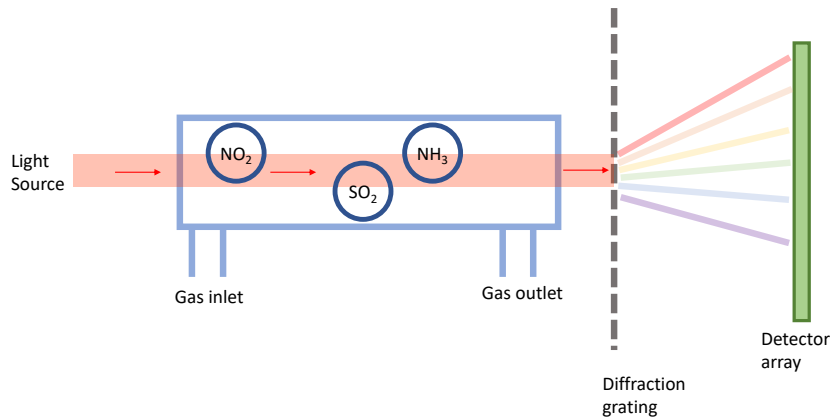


FIGURE 3.8: An example of a gas sensing setup with a diffractive grating. Light source and detectors are both broadband. Multiple gas species can be measured simultaneously. The broadband light is split into multiple narrow bands that are directed onto separate detectors. The colour of the light is a visual aid and does not imply the wavelength.

3.5.1 Miniaturisation

Reduction in size of the equipment is one desirable refinement of optical gas sensors.¹⁴⁹

A number of applications require small size, easily transported equipment. For example, gas leak detection necessarily requires equipment to be moved. The transportability is determined by a number of factors including: size of the source, size of the detector, required extra components and the total power consumption. Miniaturisation can be achieved by reducing multiple factors simultaneously.

Transportable optical gas sensors have a requirement for low power consumption due to battery constraints. A high power QCL would not be able to operate for long on battery power. LEDs have been demonstrated to be able to operate with high power conversion efficiency and the corresponding low power consumption that follows.¹⁵⁰ These can be utilised as sources to reduce the power consumption in comparison to lasers, as well as satisfying the size requirements for the source. However, LEDs do not offer the low spectral bandwidth of lasers, which necessitates a low spectral bandwidth of the detector. Adding traditional filters increases the overall size of the setup and, therefore, is not the ideal solution.

Some proposed solutions for reducing the spectral bandwidth of detectors include novel filtering techniques. N. Pelin Ayerden and Reinoud F. Wolffenbuttel have re-

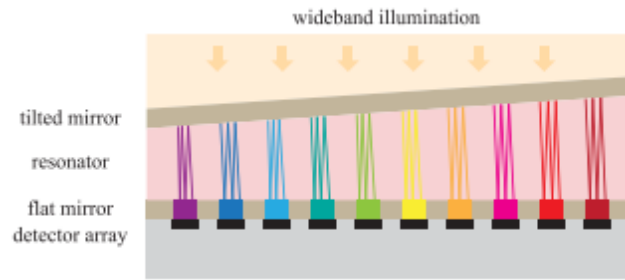


FIGURE 3.9: Spectral filter design for miniaturised gas sensors, from Ayerden and Wolffenbuttel.¹⁵¹ The tilted mirror acts to vary the path length of the resonator, thereby varying the spectral response across the detector array. The spectrum of incident light can be recreated from the current measurements of the entire array along with prior knowledge of the spectral responses.

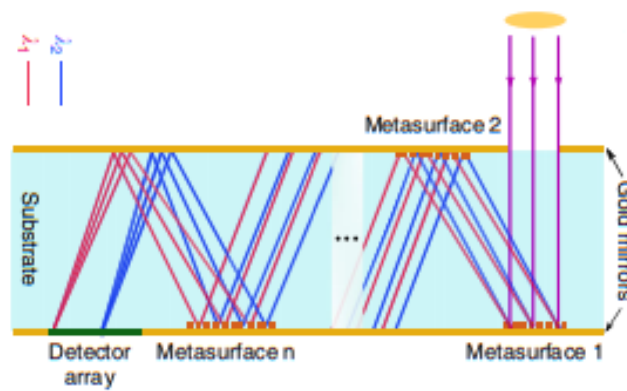


FIGURE 3.10: Folded metasurface spectrometer design, from Faraji-Dana *et al.*¹⁵² The design of the folded metasurfaces aims to split the light apart based on wavelength. Shorter wavelength light takes a path that focuses it on the right hand side of the detector array, while longer wavelength light is focused on the left hand side of the detector array.

ported a structure that utilises two planar mirrors, acting as a Fabry-Perot cavity, to select the band of light that can enter the broadband detector embedded in the bottom mirror. The top mirror is angled, so that the cavity path length varies along the detector array and the transmitted spectral band is shifted along the array. Figure 3.9 shows the proposed design.¹⁵¹

M. Faraji-Dana *et al.* have proposed a concept using folded optical metasurfaces.¹⁵² The incident light is dispersed and focused onto a broadband detector array by a series of metasurfaces on both sides of a transparent substrate. Mirrors either side of the substrate confine the light within the substrate, until the dispersed light reaches the detector array - shown in figure 3.10. Each pixel on the detector array only sees a narrow band of light, which varies between each pixel on the array.

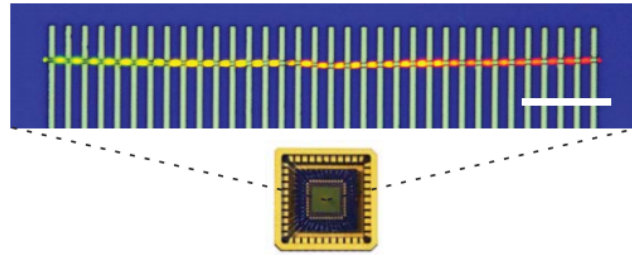


FIGURE 3.11: Compositionally graded nanowire spectrometer, from Yang *et al.*¹⁵³ The composition of the $\text{CdS}_x\text{Se}_{1-x}$ nanowire varies from one end to the other, resulting in a corresponding variation in the spectral response.

A concept described by Z. Yang *et al.* does not create a narrow spectral bandwidth of light at the detector, but rather tunes the spectral responses along an array.¹⁵³ The combined measurements of each device along the array are used to recreate the spectrum of incident light. Absorption by specific gas species would show up as a dip in the spectrum at the absorption wavelengths corresponding to the gas species. The variation in spectral responses of each device is created by a compositional variation of a nanowire, pictured in figure 3.11.

Another approach that aims to recreate the spectrum of incident light is random scattering technique proposed by B. Redding *et al.*¹⁵⁴. The randomly distributed air holes scatter the incident light in all directions in a random (but repeatable) way. A number of broadband detection channels are placed in a semicircle around the scattering medium to measure the scattered light. The spectral response of each channel different from the other channels and so, after an initial determination of the random responses, the incident spectrum can be recreated from the simultaneous measurements of all the channels. Gas species with an absorption peak in the spectral band covered by the spectrometer would cause a dip in the measured spectrum, at the known absorption wavelength. An SEM image of a fabricated chip is shown in figure 3.12.

Overall, all these designs aim to reduce the size of the detector part of the gas sensor and integrated spectral filtering allows for the use of a broadband light source. These reports demonstrate that miniaturisation of optical gas detectors is certainly possible. Narrow band light sources generally suffer from high required input power, whereas broadband sources can be operated at low input powers. Small size broad-

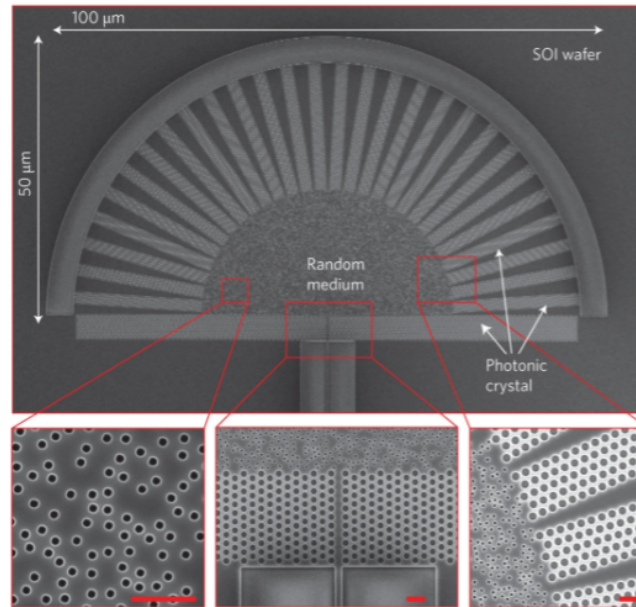


FIGURE 3.12: SEM image of a fabricated random scattering spectrometer chip, from Redding *et al.*¹⁵⁴ The incident light is randomly scattered, in a repeatable way, onto the detector channels on the outside of the semicircle. The spectrum falling on each detector is unique and allows for the spectrum of the incident light to be reconstructed.

band light sources are not novel *e.g.* LEDs, and offer a viable light source for miniaturised optical gas detectors. To accompany the broadband sources, a desirable option for further miniaturisation is (as demonstrated by the detectors discussed in this section) integration of the detector and spectral selection component. Combining both functions into one component removes the need for a separate light filtering component, that would hinder miniaturisation.

Chapter 4

Experimental Methods

All samples described in this work were fabricated in-house. Each sample starts off with a substrate, with the RCE-PD structure grown on top by molecular beam epitaxy (MBE).

4.1 Molecular Beam Epitaxy

Molecular beam epitaxy (MBE) is an epitaxial growth technique that creates thin layers with high control, high precision and a low concentration of impurities.¹⁵⁵ Epitaxy refers to the growth of a single crystalline structure on top of a substrate and differs from the unordered, random amorphous deposition techniques that do not provide the control and purity required for optoelectronic applications. MBE is used for research and commercial fabrication across the semiconductor industry, along with the more widely used metal organic chemical vapor deposition (MOCVD). These epitaxial growth techniques are used for the fabrication of a variety of electronic devices *e.g.* transistors, LEDs, lasers, photodetectors and more. Previously, simpler growth techniques, such as liquid phase epitaxy, were the most commonly used, but MBE and MOCVD have superseded them. These techniques offer more versatility and control.

MBE can be explained simply as the controlled evaporation of the materials directed to impinge onto the substrate, where the evaporated material reacts to form an ordered layer. The main components of an MBE system are a growth chamber, inside which the substrate sits, and a number of heated cells that each provide the flux

of one of the materials. The growth chamber is evacuated to ultra-low pressures, $\sim 10^{-9}$ mbar, to allow the molecular beams to flow unimpeded. The fluxes of the constituent materials travel from the cells onto the substrate, and require a clear line of sight. On the substrate the molecules react and crystallise to form a layer. Without the ultra-high vacuum (UHV) other molecules in the chamber would participate in the reaction on the substrate and form impurities in the epitaxial layer.

For this work a VEECO GENxplor MBE reactor is used for all fabricated structures. The reactor is set-up with a range of group-III and group-V source cells: gallium, indium, aluminium, arsenic and antimony. The group-III materials use Veeco SUMO cells, a patented design that promises high flux stability.¹⁵⁶ The group-V materials use valved cracker cells, allowing control of the flux through a combination of cell temperature and valve position. It is also equipped with dopant cells for n-type doping - GaTe (for Te) and Si - and p-type doping (Be).

The reactor comprises three chambers. The first chamber is for loading, which has a door to allow wafers to be loaded and unloaded from the outside. The pressure in this chamber is cycled with the loading process, but reaches base pressures of high 10^{-8} mbar using both a roughing pump and a turbo pump. This chamber is also used for the first stage of outgassing of the wafers and substrate holders before they are moved into the next chamber. The buffer chamber is separated from the loadlock by a gate valve, which is only opened when both chambers are at low pressures. This pressure in this chamber varies less than the loadlock, maintained by an ion pump at $\sim 1 \times 10^{-8}$ mbar. A section of this chamber is used to further outgas the wafer and holder at higher temperatures, to prepare the wafer for loading into the growth chamber. The growth chamber is separated from the buffer chamber by another gate valve, that stays closed other than during movement of wafers between the chambers. The gate valves maintain the UHV environment in the growth chamber, whilst allowing the necessary movement of the wafers.

Inside the growth chamber the wafers are held in place on metal carriers, which rest on top of three legs that protrude into the centre of the chamber. During growth, the legs rotate, which rotates the wafer and enhances the uniformity of the layers across

the entire wafer. A radiative heater is used to control the temperature of the wafer throughout the process. All of the material cells are angled towards the centre of the chamber, the location of the wafer, to provide the fluxes onto the wafer. During layer growth the group-III fluxes are controlled by the cell temperatures, and the group-V fluxes are controlled by a combination of cell temperatures and valve position. Each cell opening is also covered by a shutter that completely stops the flux when closed.

Growth of high-quality single crystal layers requires the lattice constant of the epilayer to closely match the lattice constant of the preceding layer, usually the substrate. Lattice-matched growth minimises the dislocations that can affect device performance and increase the dark currents. Small differences in lattice constants can be accommodated by the layer in the form of strain, without introducing dislocations; the maximum thickness of a strained layer is determined by the size of the mismatch.

The maximum layer thickness that can be grown as a strained layer, the critical thickness, can be estimated by the Matthews-Blakeslee model.¹⁵⁷ The critical thickness is¹⁵⁸

$$h_c = \frac{a_{sub} [\ln(\frac{\sqrt{2}h_c}{a_{sub}}) + 1] (1 - \frac{1}{4}\nu)}{2\pi\epsilon(1 + \nu)}, \quad (4.1)$$

where ν is the Poisson ratio of the epilayer, given by¹⁵⁹

$$\nu = \frac{c_{12}}{(c_{11} + c_{12})}. \quad (4.2)$$

c_{11} and c_{12} are the elastic constants of the layer. a_{sub} is the lattice constant of the substrate and ϵ is the strain factor, given by

$$\epsilon = \frac{a_{sub} - a_{epi}}{0.5(a_{sub} + a_{epi})}. \quad (4.3)$$

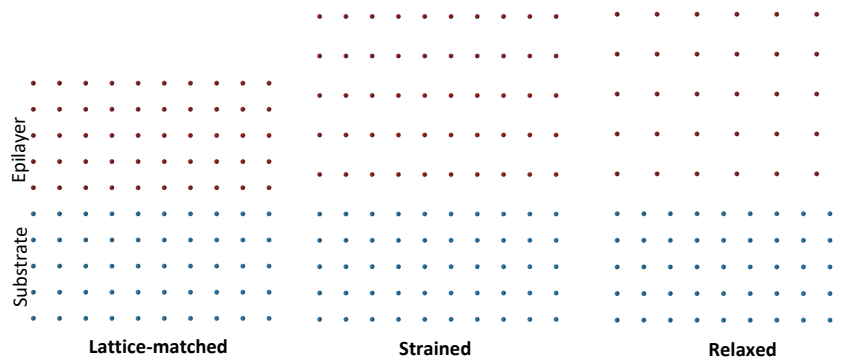


FIGURE 4.1: Atomic visualisation of epitaxial layers in comparison to the substrate. (not to scale). In lattice-matched layers the atomic spacing of the epitaxial layers matches the spacing of the substrate. If the layers are strained then the atomic spacing of the two layers matches parallel to the interface, but is mismatched parallel to the growth direction. If the layers are relaxed then the atomic spacing is mismatched in all dimensions between the substrate and the epilayer.

Where a_{epi} is the unstrained lattice constant of the epilayer. Lattice-mismatched layer thicknesses beyond the critical thickness result in relaxation of the epilayer; the atomic spacing between the atoms do not match and dislocations between the layers are introduced. 2D visualisations of lattice-matched, strained and relaxed layers are shown in figure 4.1. Lattice-matched layers are achieved by carefully controlling the fluxes from each of the cells during layer growth, to ensure the correct composition of the material. As an example of critical thickness from J. Pedrazzani, $AlAs_xSb_{1-x}$ grown on an InAs substrate and $x = 0.16$ has a critical thickness of $\gg 300$ nm. However, with a higher As fraction of $x = 0.20$ the critical thickness drops significantly to ~ 50 nm.²⁵ This demonstrates the importance of achieving the correct alloy composition in the epilayers.

A significant characteristic of MBE growth is the wide range of possible structures that can be grown, however, a majority of the steps taken during the growth process are the same between samples. Starting from a substrate, each growth follows the steps set out below:

- The substrate is loaded into a holder, held in place by the plates above and below.
- The wafer holder is loaded into the loadlock chamber, which is then evacuated.

- Surface contaminants are removed from the substrate and holder by heating the chamber to 200 °C. Suitable decontamination is determined to be when the loadlock chamber pressure approaches its base pressure.
- The holder is moved into the buffer chamber, and into the heated portion of this chamber.
- A second outgas of the substrate and holder is performed at a higher temperature, usually 350 °C for GaSb. Suitable decontamination is determined to be when the buffer chamber pressure approaches its base pressure.
- The substrate is moved into the growth chamber and the heater is lowered. Counterclockwise rotation of the substrate is started.
- The substrate is heated to a high temperature, above the growth temperatures, for oxide desorption from the surface. Constant group-V flux is provided to replace the atoms that sublime from the substrate surface. The substrate is held at the high temperature for approximately 10 minutes.
- The substrate temperature is decreased to the growth temperature of the substrate material, *e.g.* 500 °C for GaSb.
- A homoepitaxial buffer layer of ~ 500 nm is grown to improve the surface quality and smoothness - the prior oxide desorption can increase the surface roughness of the wafer, and increase the dislocation density.¹⁶⁰
- Each layer of the structure is grown in sequence.
- The wafer is cooled once the final layer in the structure has been grown.
- The wafer is unloaded from the growth chamber. First into the buffer chamber and then into the loadlock, through the gate valves. The loadlock door is used to collect the finished wafer.

During the oxide desorption, buffer layer growth and structure growth the surface of the wafer is monitored using reflection high energy electron diffraction (RHEED). The RHEED system delivers a high energy electron beam to the surface of the wafer

in the growth chamber. At a shallow incident angle the reflection of the beam does not penetrate far into the wafer and is sensitive to changes in the surface morphology. A diffraction pattern is formed from the reflected electrons incident on a fluorescent screen, the pattern is monitored by a camera and displayed on a computer monitor.¹⁶¹ The pattern can be used to determine the characteristics of the surface. During oxide desorption the beginning of the process is indicated by a 'spotty' pattern appearing. However, during layer formation the same 'spotty' pattern indicates a rough surface (3D growth), which can be due to cluster formation or relaxation; this is not desirable for single-crystal growth. A smooth layer with consistent crystal structure (2D growth) is indicated by lines or 'streaks' appearing on the diffraction pattern; this is expected during the growth of the layers.¹⁶²

As well as surface morphology the RHEED system is also used to measure the growth rates of each of the sources. The growth rate measurements are taken separately to any structure growths. The measurements are made beforehand to calibrate the cell temperatures to achieve the appropriate material compositions and layer thicknesses. The measurement utilises the intensity oscillations of the reflected spots as the layers are formed, each oscillation corresponds to the formation of one monolayer.

4.2 X-Ray Diffraction

As mentioned in section 4.1, to realise high-quality devices all layers are required to be either lattice-matched to the preceding layer or thin enough to be strained - *i.e.* thinner than the critical thickness. The critical thickness is inversely correlated to the misfit (the difference in lattice constant), so to reduce dislocations in the crystal the layer compositions are calibrated. The lattice constant of each layer is determined by high-resolution x-ray diffraction (HR-XRD) measurements.

HR-XRD measurements utilise the scattering of x-ray photons from the crystal lattice structure. In contrast to the RHEED measurements, the x-rays penetrate into the entire structure and substrate, so the diffraction pattern shows the lattice constants of the entire structure. The x-rays are reflected primarily due to interactions with

electrons associated with the atoms in the lattice. Due to the regular atomic spacing of the atoms the reflected x-rays constructively interfere only at specific angles (θ_B), called Bragg angles. The angles, θ_B , are determined by the atomic spacing following Bragg's law

$$2d \sin \theta_B = n\lambda, \quad (4.4)$$

where d is the spacing between the atomic planes, n is the order of the diffraction and λ is the wavelength of the x-rays. To determine the lattice constants of the epilayers a coupled $\omega - 2\theta$ scan is used. The angle between the source and the sample, ω , is varied simultaneously with the angle between the source and the detector, 2θ . The angles are varied together, so that $\omega = \theta$ throughout. The intensity of the reflected x-rays peak when $\theta = \theta_B$.

For all measurements a Bruker D8-discover diffractometer is used. For the best results multiple calibration measurements are performed before each $\omega - 2\theta$ scan. With the sample-under-test in place the horizontal position of the sample - viewed from the source, 'z' - is stepped in front of the beam to determine the correct focus on the sample, the position where the intensity of the beam at the detector is half of the maximum. The second measurements scans the ω angle independently around 0° to determine the angle of maximum intensity - this angle is set as the zero point. z and ω scans are repeated multiple times to iteratively improve the positions until little change is observed.

Prior to the $\omega - 2\theta$ scan the positions of ω and 2θ are set to the expected peak values, determined by the known lattice-constant of the substrate material. The angles that achieve the peak intensity of the scattered electron beam are determined through a series of uncoupled scans of ω , 2θ and the wafer holder angle, ϕ , around the angles of the expected maximum. The $\omega - 2\theta$ scan of angles around the maxima, is the final scan and is the one used to determine the lattice constants of the epilayers. The wavelength of the x-rays and the angle are known. The lattice constants, $a_0 = 2d$, are determined by angles of the peak intensities, θ_B for each epitaxial material and

the substrate.

The maximum intensity of each peak correlates to the thickness of the layer and depth of the layer below the surface. So, with multiple peaks it is possible to speculate which material correlates to each peak. The substrate is always the thickest layer, so it always produces a high-intensity diffraction peak, despite being at the bottom of the structure. The substrates used in this work are all binary materials, so the compositional variation is also lower than the more complex epitaxial alloys, which results in a narrower peak. The corresponding materials of the other peaks can be determined by comparing layer thicknesses to the peak intensities, if the differences in thickness are significant. Peaks of comparable intensity usually require calibration growths of individual layers to correctly determine the material and composition.

Materials that are lattice-matched to the substrate will produce a peak at the same wavelength as the substrate. Peaks that do not coincide indicate lattice-mismatch. The fractional difference in lattice constants, ϵ , is determined by

$$\epsilon = \frac{a_{sub} - a_{epi}}{0.5(a_{sub} + a_{epi})} = 2 \frac{\sin(\theta_{sub}) - \sin(\theta_{epi})}{\sin(\theta_{sub}) + \sin(\theta_{epi})}. \quad (4.5)$$

a_{epi} is the lattice constant of the epilayer, a_{sub} is the lattice constant of the substrate, θ_{sub} is the measured Bragg angle of the substrate and θ_{epi} is the measured Bragg angle of the epilayer.

The compositions of the layers that cause the peaks are determined using Bede RADS software. The structure is input into the software, material composition and thickness and the theoretical XRD pattern is plotted. Comparison of the theoretical pattern to the measured pattern allows the actual composition of the epilayers to be approximated. The compositions of the layers are incrementally varied until the theoretical and measured patterns match. A rule of thumb used as a starting point for compositions is that arsenic poor materials will result in a lower Bragg angle and antimony poor materials result in a higher Bragg angle (only applicable to III-As/Sb materials), an example XRD measurement of a material with less antimony than in-

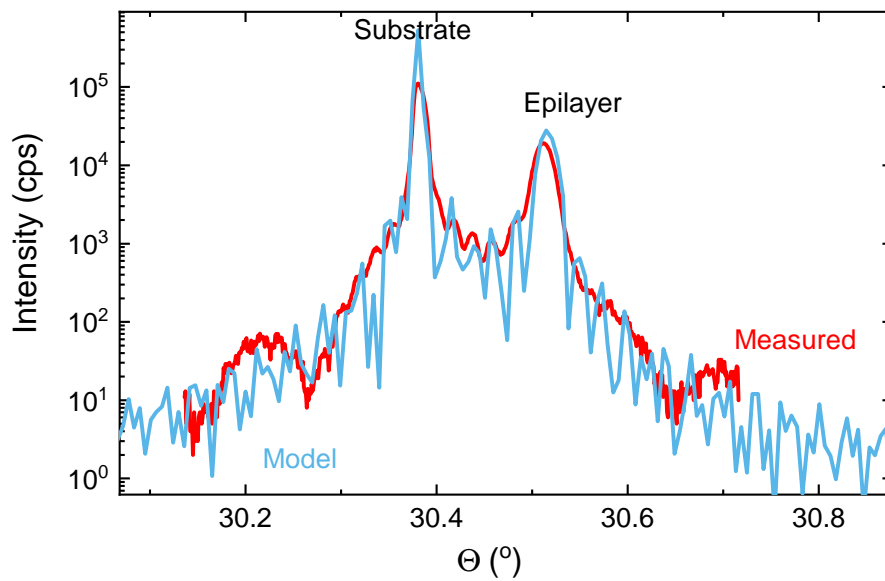


FIGURE 4.2: Example of a HR-XRD measurement of a single layer grown on a substrate (red) and calculated diffraction curve (blue). The epilayer is lattice-mismatched with respect to the substrate, seen here by the differing diffraction angles of the two peaks. The size of the mismatch is determined by the angle between the two peaks.

tended is shown in figure 4.2. The growth rates of the group-III materials are usually more stable, so an assumption is made that the group-III ratios are as expected and the group-V ratio is slightly off - only applicable to quaternary materials. For subsequent growths the cell temperatures and/or the valve positions are changed based on the actual compositions measured by the XRD.

4.3 Device Processing

The samples grown by MBE can be optically characterised immediately post-growth, after section 4.1; however, for electrical testing further fabrication steps are necessary. Processing is carried out in Lancaster University's Quantum Technology Centre cleanroom to create a set of individually testable devices on each sample. Each sample goes through a number of steps including etching and contact deposition - each step is described in order in section 4.3.7.

4.3.1 Photolithography

In general terms, each fabrication step either removes material - etching - or deposits material - thermal evaporation, chemical vapour deposition etc. Etching and deposition on only specific parts of the wafer are achieved through the use of photolithography techniques. Photolithography is a technique that masks sections of the sample to shield the masked areas from the subsequent process. Figure 4.3 shows each step of photolithography patterning using a positive photoresist - *e.g.* microposit S1813.¹⁶³

The patterning process starts with a clean and dry sample, 4.3a, onto which the photoresist is deposited by a pipette. An approximately uniform layer of the resist is created by spinning the sample at high speed, 4.3b. Speeds between 3000 rpm and 6000 rpm are used depending on the thickness of the resist required. As an example, a speed of 6000 rpm for 45 s creates a layer of S1813 of ~ 1300 nm. After coating the sample is heated on a hot plate to solidify the layer and remove solvents; a temperature of 115 °C for 2 minutes is used for S1813.

With a stabilised resist layer on the sample the next step is to expose the parts of the resist to be removed. Exposure to ultraviolet, UV, light causes a chemical reaction in the resist, which for positive resists increases the solubility of the resist in the developer (for negative resists exposure decreases solubility). A mask is used shield certain areas of the sample and only allow optical exposure to the areas of the resist that are to be removed before the subsequent process. The mask is a glass plate with a patterned chrome film on one side, used with a SUSS MicroTec MJB4 mask aligner, which provides the light for the exposure. The sample is placed onto a plate on the mask aligner, with the mask held above it by a vacuum, 4.3d. The distance between the two is adjusted by the semi-automated wedge error correction procedure that determines the ideal distance for the exposure. Alignment of the sample to the mask in the other two dimensions is then determined manually - this is necessary to match the position of subsequent fabrication steps to the first one. Two dimensions and the angle of the sample are adjusted individually until alignment is achieved.

After alignment the entire mask is then exposed to the UV light, of 365 nm, which is

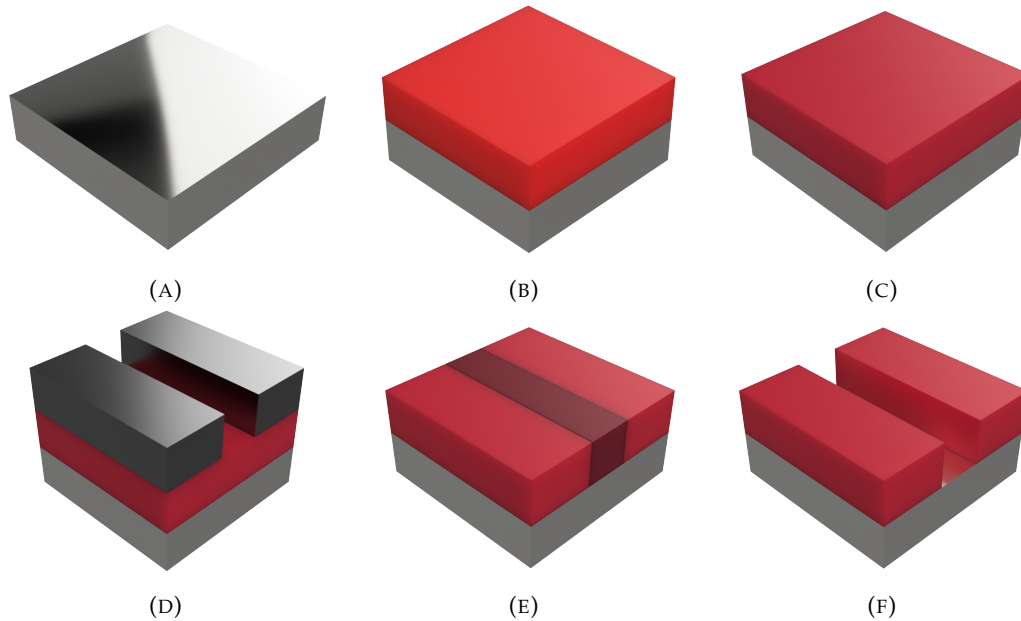


FIGURE 4.3: Single resist photolithography steps - for subsequent etching or deposition. Starting with a clean wafer, (A), a layer of resist is spun onto it, (B), before the wafer is heated to harden the resist, (C). A mask is placed on top of the resist, (D), to protect specific areas from exposure to light. The subsequent exposure to ultraviolet light causes a chemical reaction in the exposed parts of the resist, (E). When submerged in a developing solution, MF-CD-26, only the exposed parts of the resist react with the solution and are removed, (F).

transmitted only through the clear parts of the mask. The required time of the exposure depends on the power of the light and the ideal dose required by the resist; this can vary over time due to drift of the equipment or resist, but it is usually in the range of 1 - 3 s. The ideal exposure time is determined experimentally by testing multiple times and analysing the results under a microscope. Specific patterns are included on the mask to be used to check the exposure. Figure 4.4 shows the shape of the exposure pattern when it has been underexposed, correctly exposed and overexposed.

To remove the exposed areas of the resist (for positive resists) the sample is developed, in this case in MF-CD-26.¹⁶⁴ The sample is held in the developer and gently moved around to aid development in between small features. The exact time of development is determined experimentally, but is usually in the range of 30 s to 60 s. The developer is rinsed off with deionised water and the sample is then ready for the next process step: etching or deposition.

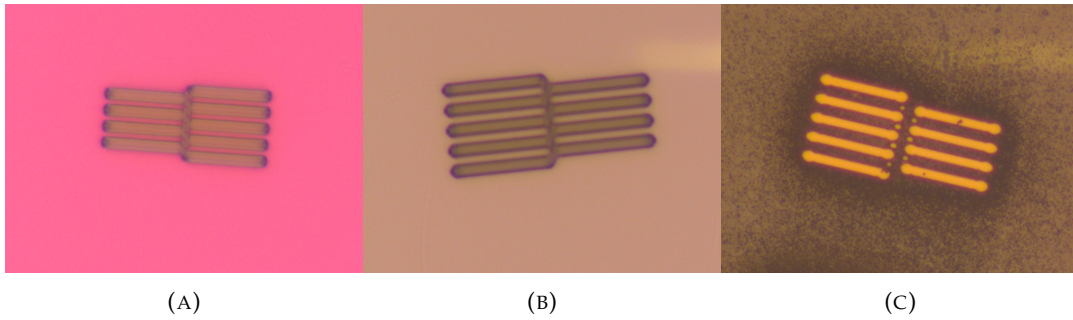


FIGURE 4.4: Exposure patterns of the resist after development. A) Underexposure B) Correct exposure C) Overexposure. In the underexposed resist the gap between the fingers is very narrow. In the correctly exposed resist the gap is approximately the same width as the fingers. In the overexposed resist the gap is wider than fingers. The colours are due to microscope lighting and do not signify exposure differences.

4.3.2 Chemical Etching

The method of etching used most during this work is chemical (wet) etching. Simply put, this is the removal of material by submersion in liquids (etchants). The etchant that is used is determined by the material that is to be etched and the materials that should not be etched (if any). An ideal etchant would rapidly etch the desired material whilst simultaneously not etching at all any other materials and leave a smooth surface.

To create devices from the RCE-PD structures two wet etches are required. One through the top DBR - to allow contacts to be placed - and one through the contact layer - to define the device mesas. To etch through the DBR an etchant that will etch both materials is ideal - an MF319 based etchant satisfies this requirement for all the DBR materials used in this work (GaSb, AlAsSb and GaAsSb) and etches all these alloys at approximately the same rate of ~ 200 nm/s. This solution also does not significantly etch majority indium alloys (*e.g.* InAs and InAsSb), which allows these materials to be used as etchstop layers just below the DBR.

The second etch through the contact layer is a very shallow etch (~ 30 nm) which is difficult to measure and, therefore it is important that the etch stops once through the contact layer. The contact layer materials used are all alloys containing indium and gallium (InAs, InAsSb and InGaAsSb) while the barrier layer beneath are all alloys of aluminium (AlAsSb and AlGaSb). For all combinations of contact layer

and barrier layer the etchant used is a solution of citric acid and hydrogen peroxide (2:1).

For all etch processes it is desirable to know the thickness that has been etched. A surface profiler (KLA-Tencor Alpha-Step IQ Surface Profiler) is used to measure the thickness before and after each etch. This serves as a check that the etchant is behaving as expected as well as allowing the etch rate to be determined. After etching the resist layer is removed from the sample by submersion in acetone.

4.3.3 Thermal Evaporation of Contacts

To create an electrical circuit through the devices, metal contacts are required to allow for probing and bonding. A layer of the metal is deposited on top of the sample which is then selectively removed to create the desired patterns. A pattern of resist is used to mask the areas that the metal will be removed from. The resist pattern is created similar to the method described in section 4.3.1, but with the addition of a second resist to aid the lift-off of the metal. Beneath the S1813, a layer of LOR3A resist is deposited and spun to a uniform layer. The LOR3A is soft-baked at 180 °C for 5 minutes. The process then continues in the same way as for S1813 as described in section 4.3.1, shown in figure 4.5.

Adhesion of the contacts can be affected by contamination on the surface of the sample, so excess exposed resist is removed post-development by plasma ashing to aid adhesion. Thermal evaporation is used to deposit the metal onto the sample. The sample is first placed in a chamber, with the air subsequently evacuated to create a low pressure environment. The metals to be deposited are held in baskets inside the chamber. To create a flux of the metal onto the sample the metal is heated by passing a current through the basket to heat it resistively. For this work a combination of titanium and gold are used; a thin (~ 20 nm) layer of titanium is deposited first, to aid adhesion of the subsequent thicker (~ 200 nm) layer of gold. During the evaporation the flux of the metal is monitored to gauge the thickness of the metal on the sample. A shutter is placed between the metal source and the sample to abruptly terminate the deposition once the desired thickness is reached.

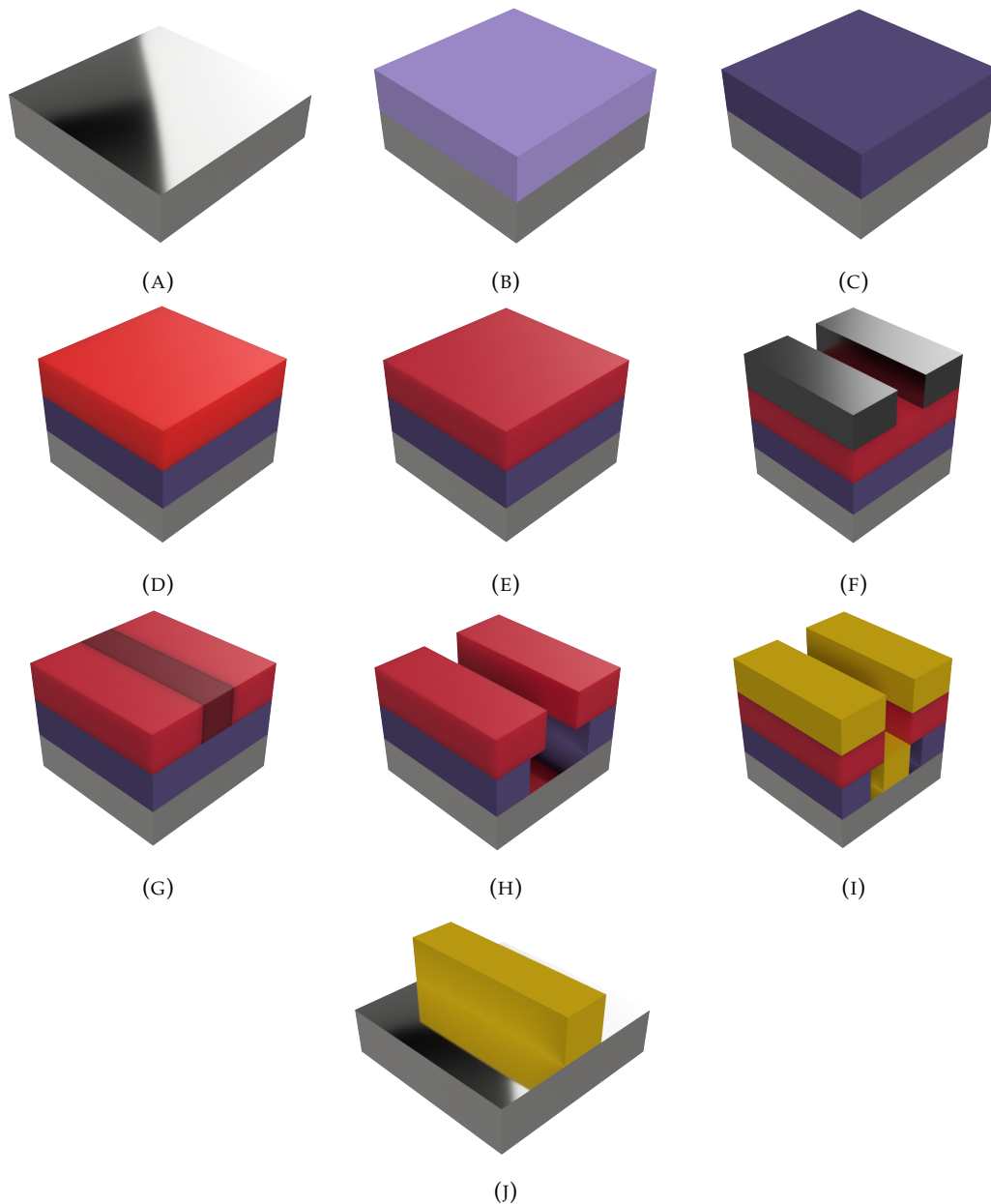


FIGURE 4.5: Two resist photolithography and thermal evaporation steps for metal contact deposition. Starting with a clean wafer, (A), a first layer of resist, a lift-off-resist, is spun onto it, (B), before the wafer is heated to harden the resist, (C). This resist is used to aid removal of the second resist later. The second resist is spun on, (D), and baked (E). A mask is placed on top of the resist, (F), to protect specific areas from exposure to light. The subsequent exposure to ultraviolet light causes a chemical reaction in the exposed parts of the resist, (G). When submerged in a developing solution, MF-CD-26, only the exposed parts of the resist react with the solution and are removed, (H). The metal is evaporated onto the exposed surfaces of the wafer, partially on the wafer surface and partially on the resist surface, (I). To leave only the metal on the wafer surface the resist, and metal above it, is stripped off. Removal of the second resist is aided by the more soluble lift-off-resist below, (J).

4.3.4 Plasma Enhanced Chemical Vapour Deposition

Plasma enhanced chemical vapour deposition (PECVD) is a deposition process used to deposit thin films onto wafers. For the RCE-PD samples this technique is used - with an Oxford instruments Plasma Technology PlasmaPro®HGP80 - to deposit a layer of silicon nitride (Si_3N_4) that acts as a dielectric between metal contacts and the semiconductor beneath. PECVD processes take place in an evacuated chamber, with the sample inside. A gas mixture is pumped into the chamber between two parallel electrodes. The top electrode is driven by radio frequency (RF) and the bottom electrode is grounded, to create a capacitive coupling between the two electrodes and excite the gases in between. For SiN deposition the reactant gases are silane and nitrogen (N_2). The gases are decomposed into the plasma and the resulting ions react with the surface of the sample, forming a layer of SiN. The sample sits on the bottom electrode, which is heated to a temperature of 100°C , set by standard cleanroom recipe. By utilising the strong electric field between the two electrodes to provide energy for the reaction a much lower temperature can be used than for thermally driven deposition techniques. This makes the deposition compatible with samples containing temperature sensitive materials, such as metal contacts.

The deposition rate of the SiN layer is approximately 50 nm/min , and film thicknesses of $\sim 200\text{ nm}$ are used. For the purpose of electrical insulation between metal and semiconductor the required thickness is determined by the breakdown voltage of the material and the bias voltage that will be applied during operation of the device. SiN has a reported breakdown voltage of more than $300\text{ V}/\mu\text{m}$ ¹⁶⁵ and the applied bias voltage is no more than a few volts; so a film thickness of $\sim 10\text{ nm}$ would most likely be thick enough to prevent a short circuit. The film thickness of $\sim 200\text{ nm}$ far exceeds the required thickness, however, the higher thickness can be used as there are no negative consequences to this precaution.

4.3.5 Reactive Ion Etching

The deposition of SiN creates a uniform layer of the material across the entire wafer. To remove the SiN from parts of the sample, it is first patterned with resist using the photolithography techniques described in section 4.3.1. The uncovered areas are

then etched by reactive ion etching (RIE), a 'dry' etching technique that selectively removes material by ion bombardment from an inductively coupled plasma.

The RIE equipment is also an Oxford instruments Plasma Technology PlasmaPro HGP80, but it is configured slightly differently for RIE instead of PECVD. The process chamber contains two vertically separated electrodes in both configurations. In the RIE configuration the lower electrode is driven by RF power and the top electrode is grounded; this configuration attracts ions to the lower electrode. The sample sits on the lower electrode during the process, in the path of the reactive ions. The plate and sample are unheated during this process, the energy for the reaction comes only from the strong electric field generated between the two electrodes.

For this work the RIE is used only for etching SiN layers. The reactant gases are trifluoromethane and oxygen (CHF_3 and O_2). The process method is similar to that of the PECVD method. The sample is first loaded onto the carrier wafer, inside the chamber, with the SiN layer facing upwards. The chamber is sealed and evacuated, down to a base pressure of $< 1 \times 10^{-5}$ mTorr. Once the pressure is low enough the reactant gases are pumped into the chamber, where they mix until a stable pressure is reached. A high RF voltage is applied between the electrodes to ionise the gas molecules, creating the plasma. The plasma is maintained for a time period, which is proportional to the required thickness to be etched. The process is selective between the SiN and III-V epilayers, so the SiN will be etched, but the semiconductor layers beneath will not. Therefore, usually the plasma time is slightly overestimated to make sure the layer is etched completely. Post plasma, the chamber is pumped to remove the reactant gases and ions. The chamber is then vented to allow the sample to be collected. The remaining photoresist is stripped in remover 1165 heated to 70°C .

4.3.6 SU-8 Passivation/Dielectric

A passivation layer on top of the epitaxial structure is deposited with the purpose of protection of the surface from subsequent chemical reactions - for example, it will remove the possibility of oxidation of the surface. One option as a passivation layer is SU-8 photoresist,¹⁶⁶ which is spun on, exposed and developed in a similar manner

to the photoresists used for masking during etching and depositions - section 4.3.1. A second use of SU-8 - and the main one for the RCE-PDs - is as a dielectric layer, to electrically isolate two layers. In the fabrication of the RCE-PDs a layer of SU-8 is used between the top semiconductor layer and a metal masking layer, to prevent current from flowing between the two. SU-8 is available in a range of formulations, allowing different thickness layers of between 500 nm and 200 μm to be created. The material has a high breakdown voltage of $\sim 112 \text{ V}/\mu\text{m}$,¹⁶⁷ so for the purpose of electrical isolation a thick layer is not necessary. Expected bias voltages of a few volts mean that the thinnest version of SU-8, 2000.5, is more than sufficient for this task and is the one used here.

The fabrication of the SU-8 starts with a dry sample cleaned in acetone and IPA. As with other photoresists it is important that there is no moisture left on the sample, so it is heated for a few minutes at 95 °C to evaporate any remaining on the surface. The SU-8 is deposited onto the sample by pipette, a few drops is enough to cover the surface, and subsequently spun to create an even layer on the sample. A slow rotation of 500 rpm is used to initially to spread out the SU-8 across the surface, followed by a higher speed of 3000 rpm for 30 s. The final rotation speed can be adjusted to control the thickness of the film; the thickness varies from 750 nm to 500 nm between 1000 rpm and 3000 rpm, according to the manufacturer.¹⁶⁶ The sample is then baked on a hot plate at 95 °C for 1 min, a so-called 'soft bake'. Exposure of the SU-8 layer is on the same mask aligner used for other resist patterning - section 4.3.1 - with the same steps followed for WEC and alignment. SU-8 is a negative photoresist, so the mask has windows over the areas to be kept and chrome covering the areas to be removed during development. A dose of 60 mJ cm^{-1} is required for optimal exposure, equating to ~ 2.0 s exposure on the MJB4 mask aligner, although the exact exposure time is calibrated through testing and analysis after the exposure.

A post exposure bake (PEB) of the sample takes place on a hotplate directly after exposure, at 95 °C for 1 min. The SU-8 is developed in 2-methoxy-1-methylethyl acetate (trade name SU-8 developer) for approximately 1 min; development times also require calibration through testing for optimal results. After adequate development only the cross-linked (exposed) SU-8 remains.

4.3.7 Design of Mask for RCE-PDs

Each step of the post-growth fabrication of the RCE-PD requires photolithography to create features in the structure; each step therefore, also requires a specific mask design. Mask designs determine the size and shapes of the devices, the location of the contacts and can impact the characteristics of the devices. For the RCE-PD structures the significant considerations include the path of light into the cavity and controlling the spectral response. The mask was designed in the program KLayout; where each mask step is a separate layer that can be visualised stacked together. The physical mask was created by Compugraphics.

The fabrication steps are shown in figure 4.6:

- A. The MBE grown structure, cleaned and dry.
- B. The top DBR is wet etched. The etch stops on either the contact layer or the etchstop layer (if required).
- C. The etchstop layer is etched (if present). The etch is timed to stop just into the contact layer - the difference in etch rates of the etchstop and contact layers usually makes this straightforward.
- D. A SiN layer is deposited by PECVD. RIE is then employed to etch all the areas not required for the final device. A rectangular pad of SiN is left to act as a dielectric layer between the bondpad and underlying semiconductor.
- E. The metal contacts are evaporated onto the contact layer in the structure. For the nBn structure in the cavity both the positive and ground contacts are evaporated simultaneously.
- F. The contact layer is etched to define the device mesas. This also cuts the direct path between the two contacts.
- G. An approximately 500 nm thick layer of SU-8 resist is spun onto the sample. The layer covers the area around the top DBR for a metal mask to sit on top of.

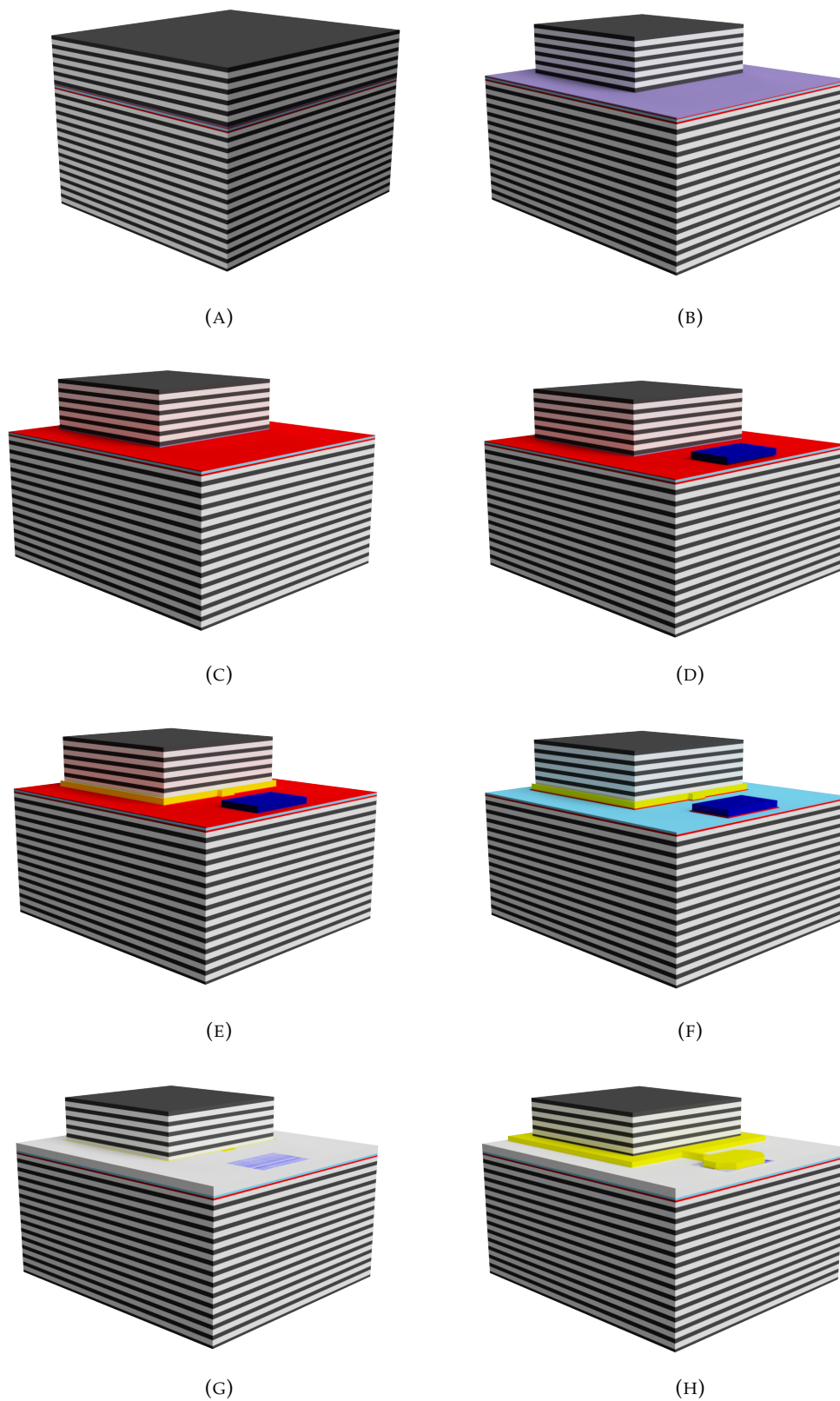


FIGURE 4.6: Post-growth device fabrication steps. (A) Epitaxial growth of layer III-V semiconductor structure. (B) Top DBR etch. (C) Contact layer etch. (D) SiN deposition. (E) Contact deposition. (F) Etch to define mesas. (G) SU-8 deposition. (H) Bond pad deposition.

H. The bondpad and metal mask are evaporated onto the SiN and SU-8 layers. The metal mask reflects light that would otherwise enter the cavity without going through the top DBR. The bondpad provides a large area separate from the device mesa that is easy to probe and wire bond to.

Initial versions of the RCE-PD devices used a much simpler fabrication process that did not include the surface passivation and bond pads. These samples demonstrated the intended resonant response, but also included a non-negligible broadband response. The cause of the broadband response was light entering the cavity without travelling through the top DBR. The fabrication process described in this section aims to eliminate the broadband response as much as possible, whilst not interfering with the resonant response - results shown in section 7.6. The SiN layer is necessary to allow for the bondpad deposition without short-circuiting of the metal contacts, but it may also lead to a slight increase in the dark current.¹⁶⁸ It is not expected to have a significant impact of the resonant response, but may slightly reduce the specific detectivity.

4.4 Characterisation

In this section, the techniques and equipment used for characterisation of the samples are detailed. Optical and electrical measurements offer significant insight into the behaviour of the photodetectors, and are used to compare structures and determine improvements. The transmittance and reflectance are purely optical measurements obtained by Fourier Transform Infrared (FTIR) spectroscopy; spectral response and quantum efficiency are optoelectronic measurements utilising the FTIR with the device-under-test (DUT) acting as the detector. dark currents are a purely electrical measurement obtained by contacting the detector inside a probestation.

4.4.1 Transmittance

The way that the light travels through the structure can be characterised by the spectrum of transmitted light. For resonant cavity-enhanced devices specifically the transmittance measurement shows the spectral positions of the mirror stopband and the resonant mode(s), both can be seen in figure 4.7. The transmittance measurements are performed on samples post-growth, but pre-processing; so the the measurement can be used to quickly determine the resonance wavelength of a sample, before committing to further time-consuming processing.

Transmittance measurements utilise an FTIR spectrometer, specifically a Bruker Vertex 70v. The sample is placed on a plate inside the inner compartment of the FTIR; the plate has a hole in it for light to pass through only a small part of the sample unobstructed. The operation of the FTIR can be understood with reference to figure 4.8. Infrared radiation comes from either a NIR source (a tungsten halogen lamp) or a MIR source (globar); one is chosen based on the spectral region of interest. Radiation from the source first gets reflected by a focusing mirror onto an aperture selector wheel, which can be changed to vary the power of light incident onto the sample. The next mirror collimates the light into a beam directed into the beamsplitter. The beamsplitter is a partial reflector; part of the incident light is transmitted onto one mirror and part is reflected onto a second mirror. This creates two beam paths, resulting in interference once they recombine into a single beam. The first mirror in the interferometer is continuously moving, while the second mirror is stationary. The

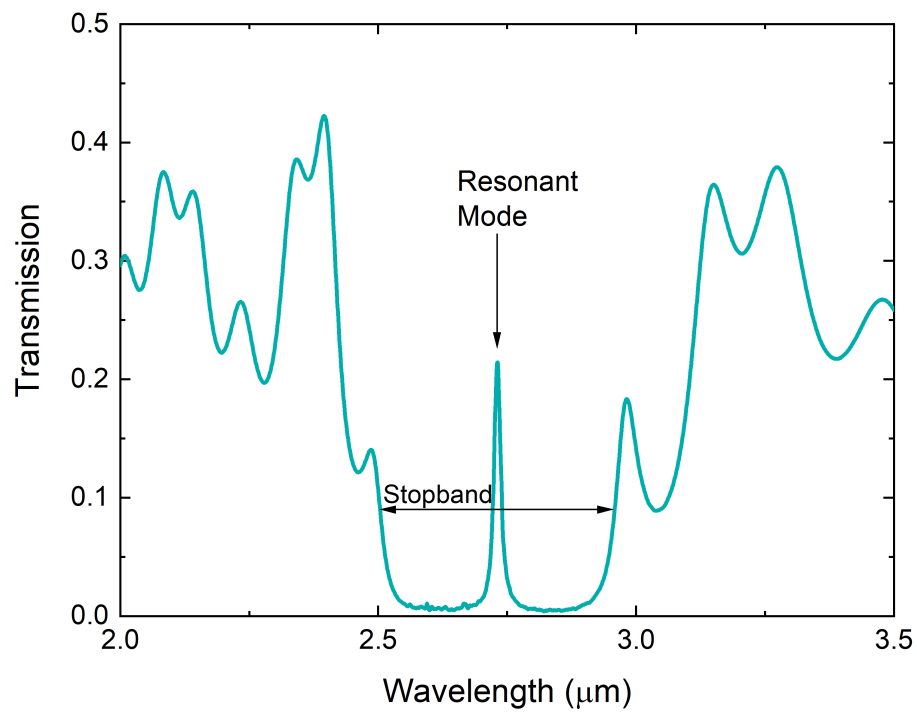


FIGURE 4.7: An example of a transmittance spectrum for an RCE-PD. The significant elements have been labelled. The stopband is the spectral region with very low transmission through the structure. The resonant mode is the wavelength that is highly absorbed in the cavity of an RCE-PD.

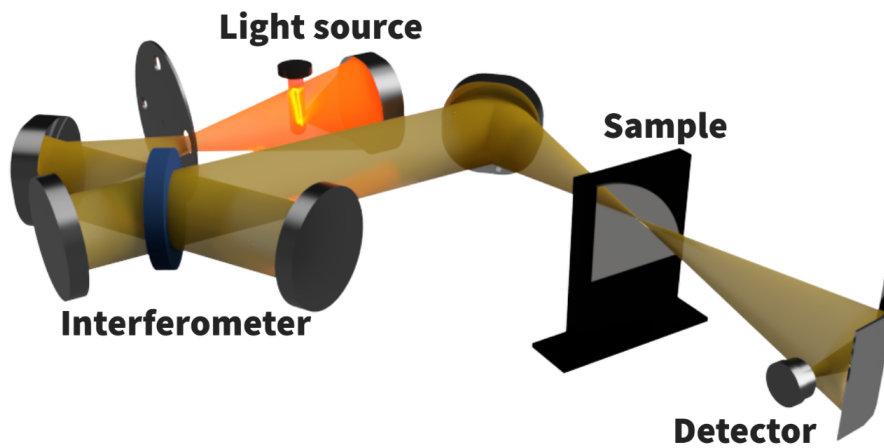


FIGURE 4.8: 3D render of the internal beam path of the FTIR. (not to scale) The light source emits the infrared light, that is then reflected off a focusing mirror, through an aperture of chosen diameter and then into the interferometer. The interferometer splits the light into two paths, of varying distance, which then are both directed off of another focusing mirror and through the sample. The light transmitted through the sample is then focused onto a detector.

result of the movement is a rapid variation in the path length difference of the two paths, varying the interference of the subsequent single beam. The single beam output is focused onto the sample by another mirror and the transmitted beam is then focused onto the internal spectrometer detector by a final mirror. The signal from the detector is time-varying, so, when sampled at multiple points in time - corresponding to different positions of the interferometer mirror - a varying interference pattern (interferogram) is created. The interferogram contains all the spectral information of the transmission, and the transmittance spectrum is recreated by Fourier transform of the interferogram.

The transmittance spectrum recreated by this method takes into account all the attenuation of the light along the path from the source to the detector. Since only the attenuation and reflection by the sample is of interest it is necessary to take a background transmittance measurement, with no sample in place. A piece of the substrate wafer can also be used in place of the sample to remove attenuation by the substrate from the final transmittance spectrum. The transmittance spectrum through the epitaxial structure only can then be recreated by dividing the sample spectrum by the background spectrum. These calculations are handled by the spec-

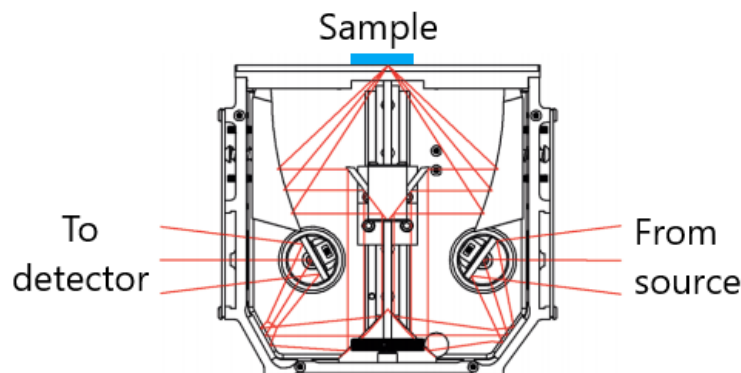


FIGURE 4.9: Beam path of the reflectance accessory for the FTIR. Image altered from datasheet.¹⁶⁹ The light from the internal interferometer of the FTIR is directed via a series of mirrors onto the surface of the sample at a set angle. The reflected light is then directed out of the accessory and onto the internal FTIR detector.

trometer's OPUS software, so the output text file is the transmittance through the epi-structure only.

4.4.2 Reflectance

Reflectance measurements utilise the same FTIR as the transmittance measurements, with the same internal light source and detector. The beam from the sample chamber is directed by a series of mirrors onto the surface of the sample. The beam reflected from the sample is directed back into the sample chamber and onto the FTIR detector in the same fashion as for the transmitted beam in section 4.4.1. The optics required for this are constructed into a movable box, that is placed in the sample chamber (a PikeTech Veemax III), the beam path of this accessory is shown in figure 4.9. The angle of the reflection is manually set at any angle between 30° and 80° , which is the main limitation of this setup. Normal incidence reflection is desirable to measure, because the angle of the incident light shifts the resonance wavelength of the sample, but the reflectance at a 30° angle can be used to estimate the reflectance at normal incidence.

To account for attenuation of the beam, other than due to the reflection off the sample, a background measurement is taken first. This is done with a highly reflective gold mirror in place of the sample. The calibrated spectrum, calculated by the Bruker

OPUS software, is the calculation of the measurement spectrum divided by the background spectrum.

This setup is also used to experimentally measure the angular dependence of the resonant cavity optical properties. The shift of the resonance wavelength and the photonic stopband are determined through reflectance measurements at multiple angles of incident light. The resonance and stopband can be read from the reflectance spectrum in the same way as the transmittance spectrum, labelled in figure 4.7.

4.4.3 Spectral Response

The spectral response of a device is a measurement of the electrical signal generated by light incident onto it. Since the current or voltage needs to be measured, this is a measurement made on a processed device with metal contacts used to connect the device into the measurement circuit. To be able to measure the response of the device as a function of the wavelength the light from an FTIR spectrometer is used. The light from the source inside the spectrometer follows the same path through the interferometer as for the transmittance measurement - figure 4.8 - but is then directed outside of the spectrometer, onto the device under test. The device is wire-bonded to a TO header and placed inside an Oxford Instruments optistat-D cryostat, evacuated to low pressure. The light from the FTIR is carefully aligned onto the device by an adjustable mirror. The cryostat is cooled by liquid nitrogen, for measurements at temperatures down to 77 K, and heated by a resistive heater.

To create the measurement circuit two legs of the header (connected to the positive and ground contacts of the device) are connected to wires that lead outside of the cryostat. The wires then connect to a pre-amplifier, which provides a bias voltage across the device (if necessary), amplifies the current signal and converts it to a voltage. The voltage is interpreted by the spectrometer and the software recreates the spectral response by Fourier transform; the measurement circuit is shown in figure 4.10. At this stage the spectral response signal does not have meaningful units, since the power of the incident light is unknown.

For a more meaningful result the amplitude of the spectral response is calculated

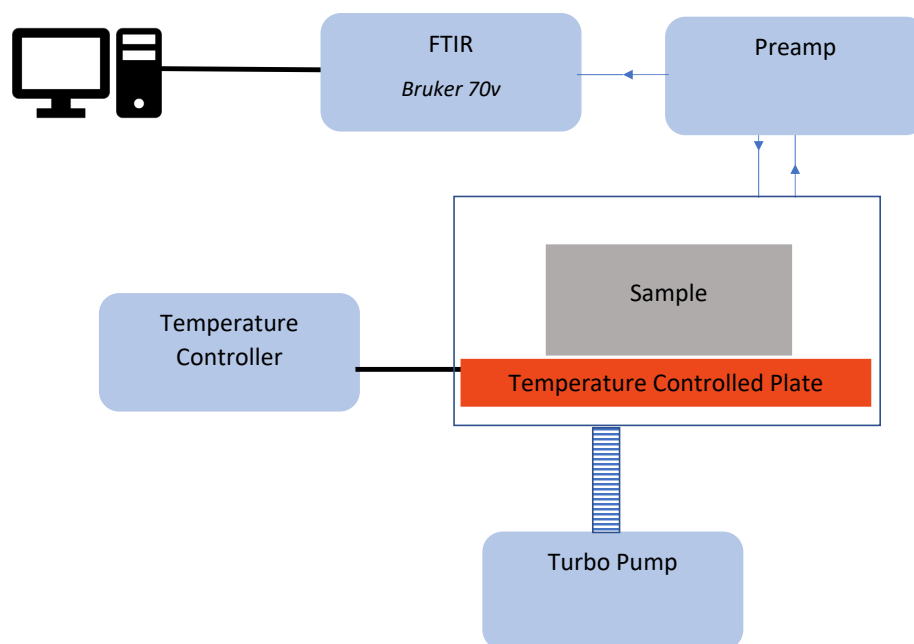


FIGURE 4.10: Measurement circuit for spectral response measurements using an FTIR. The sample is held inside a temperature-controlled cryostat, which is evacuated by a turbo pump. Light from the FTIR interferometer is directed onto the sample. The current generated in the device is measured through connection to a preamp, that provides a bias voltage and converts the current into a voltage signal. The analogue voltage signal is read by the FTIR electronics and converted to a digital reading.

with reference to a detector of known responsivity; a commercial MCT detector is used. A measurement of the reference detector in place of the device under test allows for the power per unit area of the incident light, P , to be calculated. The responsivity (R_i) is calculated from these measurements using

$$R_i = \frac{GV}{PA}, \quad (4.6)$$

V is the measured voltage signal from the device, G is the gain of the pre-amplifier and A is the photosensitive area of the device.

An example of the spectral responsivity of a device is shown in figure 4.11. The quantum efficiency, QE , is calculated from the responsivity using

$$QE = \frac{hcR_i}{\lambda} \approx \frac{1.24R_i}{\lambda}. \quad (4.7)$$

h is Planck's constant and c is the speed of light. The approximation uses the wavelength, λ , in microns.

4.4.4 Dark Currents

The term dark current refers to the current that flows between the two contacts with incident light blocked from entering the device structure. In other words, the current that is measured with no electromagnetic radiation incident on the device, not including background thermally generated radiation. The magnitude of the dark current can limit the sensitivity of a device. It is used in the calculation of the specific detectivity - a standard figure of merit that characterises the signal-to-noise performance of a detector, combining both the responsivity and dark current.

Measurement of the dark currents are a purely electrical measurement. The two contacts on a fully processed device are probed to form a circuit to measure the current. The simple circuit includes a sourcemeter at one end, to bias the device and measure the current, with the device under test connected by two wires. The device is probed within a Lakeshore TTPX cryogenic probestation, which is sealed

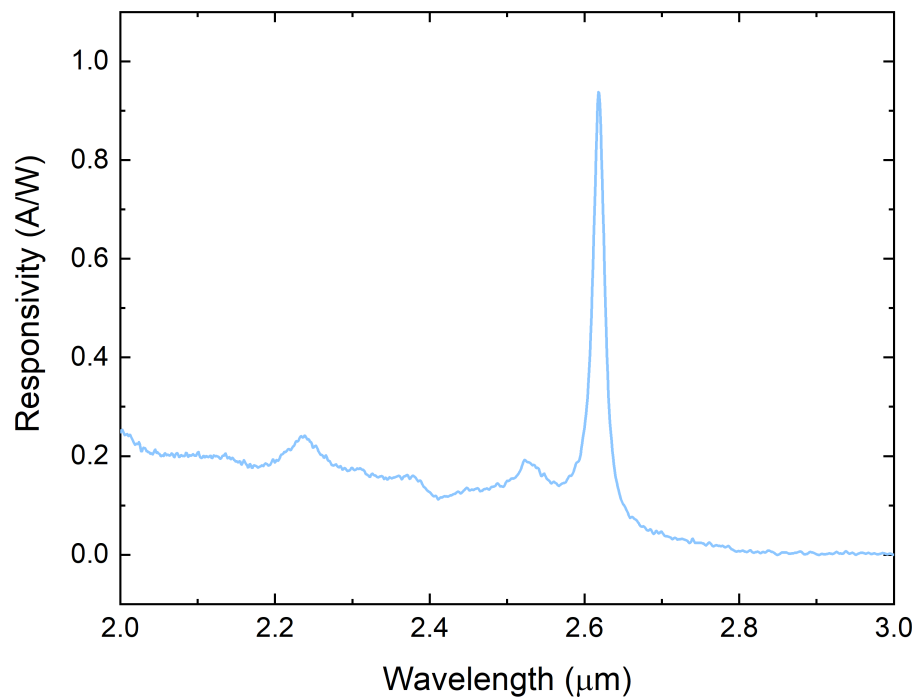


FIGURE 4.11: An example of a responsivity spectrum of an RCE-PD. The resonant response is the sharp peak at $\sim 2.6 \mu\text{m}$ and there is an underlying broadband response that cuts off at $\sim 2.8 \mu\text{m}$.

and evacuated to a base pressure of $\sim 10^{-5}$ mbar. The temperature of the chamber is controlled by a combination of liquid nitrogen cooling and resistive heating of the sample plate; temperatures in the range of 77 K to 400 K can be set. The bias voltage dependence of the dark currents are measured by a simple labview program - the bias voltage is swept from zero to the chosen maximum positive voltage, then from zero to the maximum negative voltage. A diagram of the setup is shown in figure 4.12.

It should be noted that the incident flux of electromagnetic radiation onto the sample is not zero. Steps are taken to minimise the background radiation seen by the detector, including using a chamber with opaque (to visible light) walls. The background thermal infrared radiation is reduced through implementation of a cryogenic cold shield surrounding the sample. The lower temperature of the surfaces within the field-of-view of the detector reduces the intensity of the background flux. The impact of thermal background radiation is usually highest at low temperatures (below ~ 150 K), due to no temperature dependence and other dark current mechanisms

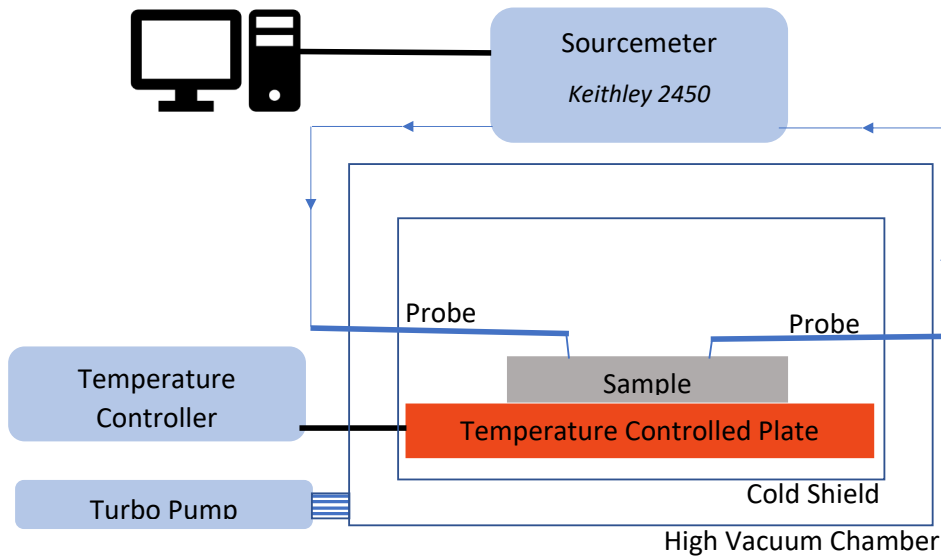


FIGURE 4.12: Equipment setup for measurement of dark currents. The sample sits inside a probestation with cooling provided by liquid nitrogen. The temperature is regulated on the plate the sample sits by resistive heating. The temperature of the inner chamber wall is also controlled by the same combination. The chamber is evacuated by turbo pump. Current measurements are taken by probing the device, connected to a sourcemeter that provides a bias voltage and reads the current.

increasing significantly at higher temperatures.

4.4.5 Optical Wafer Mapping

The chirped RCE-PDs are designed to have a shift in resonance wavelength across one-dimension of the wafer. To characterise the variation in resonance it is necessary to measure the transmittance as a function of position on the sample. The method is similar to the one described for a single position transmittance measurement in section 4.4.1, with changes to allow the position of the wafer to be controlled.

The light from the FTIR is directed outside of the main body, into a separate automated mapping stage - a Pike Technologies Map300. Through a series of mirror reflections the light is directed through the sample, at approximately normal incidence, and then further mirror reflections direct the transmitted light onto a Bruker RT-DLaTGS detector. The transmittance spectrum is recreated by the same Fourier transform method used for the single position transmittance measurement.

The sample sits in the middle of the mapping stage, held in place by three Delrin

clamps to prevent movement. The position of the stage is controlled by two motors, one for the radius and one for the angle. The motor controller electronics connect to a computer, which runs a dedicated program to send commands to the stage - to set the position of the stage. A 'map' of positions is created to determine the movement of the stage to the desired positions.

To collect a full set of transmittance spectra a simple python program is used to send commands to both the stage and the spectrometer in sequence. The stage starts off with the light directed approximately through the centre of the sample. A transmittance spectrum is collected by the spectrometer at this position, before the stage moves to the next position in the predetermined map. A second transmittance spectrum is collected at this point. This sequence is repeated until spectra have been collected for all points in the map.

A colourmap of the resonance wavelength as a function of position on the wafer is created by searching for the resonance mode in each spectrum, highlighted in figure 4.7. For larger numbers of positions this is done automatically by a python program that searches for the resonance peak; individual points are checked manually to ensure accuracy of the program. The resonance wavelengths of each position can be plotted in a colourmap, an example is shown in figure 4.13, where the x and y axes are the spatial position on the wafer and the colour represents the wavelength.

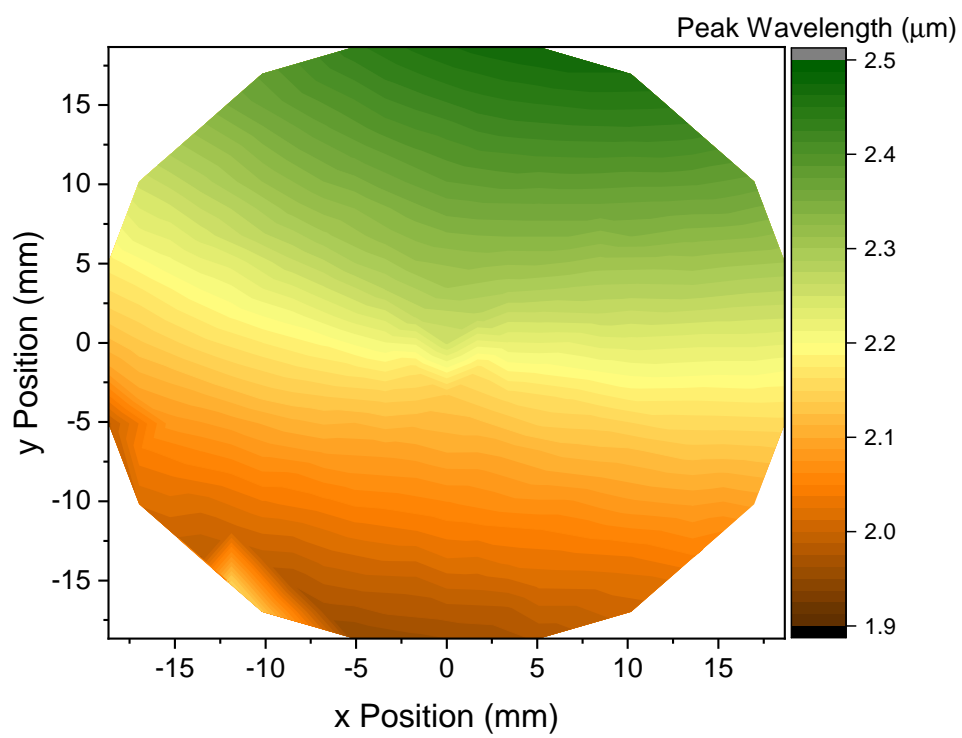


FIGURE 4.13: An example of a resonance wavelength colourmap for a chirped RCE-PD. The x and y axis are the position on the wafer and the colour indicates the resonance wavelength at that location.

Chapter 5

Results I: Short-Wave Infrared RCE-PDs

RCE-PDs are necessarily designed with a target spectral region considered from the start. The thicknesses of the DBR layers, cavity thickness and cavity materials are all strictly confined by the target region of the electromagnetic spectrum. This section details the design, fabrication and characterisation of RCE-PDs designed to sense at wavelengths in the short-wave infrared part of the spectrum. This spectral region is not well defined, but in this work the presented structures could be altered to sense at wavelengths between approximately 1.8 μm and 2.8 μm .

The structure can be split into two parts that are considered separately at first. The absorption structures in the cavity are discussed in section 5.1 and the distributed Bragg reflectors that form the two mirrors surrounding the cavity are discussed in section 5.2. The fabrication of the entire structure is presented in section 5.3. The optical and electrical properties of fabricated detectors are presented in sections 5.5 to 5.7.

5.1 Cavity

This section details the design and considerations for the cavity structure only. The first consideration for the design of a photon absorption structure is the choice of absorber material - the material must absorb photons at the intended target wave-

length. Multiple materials sensitive in the short-wave infrared have previously been demonstrated, including HgCdTe¹⁷⁰, InGaAs¹⁷¹, and InGaAsSb⁶⁷. For this work the choice of absorber was limited to III-V materials; the in-house MBE reactor is equipped with these materials only. InGaAsSb was chosen as the preferred absorber material in the cavity structure, due to the longer spectral range than InGaAs.

InGaAsSb can be grown at many different compositions lattice-matched to GaSb substrates. Depending on the composition a cutoff wavelength below 2 μm and up to almost 3 μm can be achieved. Following the equation proposed for the bandgap of InGaAsSb lattice-matched to GaSb by Adachi,¹⁷²

$$E_g = 0.28 - 0.16x - 0.60x^2, \quad (5.1)$$

the cutoff wavelength as a function of composition is calculated in figure 5.1. x is the gallium fraction in the alloy. The composition is kept lattice-matched to GaSb by altering the As fraction so that it follows a second equation proposed by Adachi¹⁷²,

$$y = \frac{A_0 + B_0x}{C_0 + D_0x}, \quad (5.2)$$

where x is the gallium fraction and y is the arsenic fraction. $A_0 = 0.3834$, $B_0 = -0.3834$, $C_0 = 0.4211$ and $D_0 = 0.0216$. This equation is most accurate at low indium fractions and has not been experimentally verified for the entire composition range.

Figure 5.1 does not tell the whole story for InGaAsSb absorption. This material contains a miscibility gap approximately between indium fractions of approximately 0.3 and 0.65¹⁷³; at these compositions the material can exhibit atomic scale composition variations¹⁷⁴. It is possible to grow epitaxial layers of materials with these compositions, but this can result in material degradation and poor surface morphology¹⁷⁵. For this work material compositions up to 28 % indium are used, intentionally avoiding the miscibility gap.

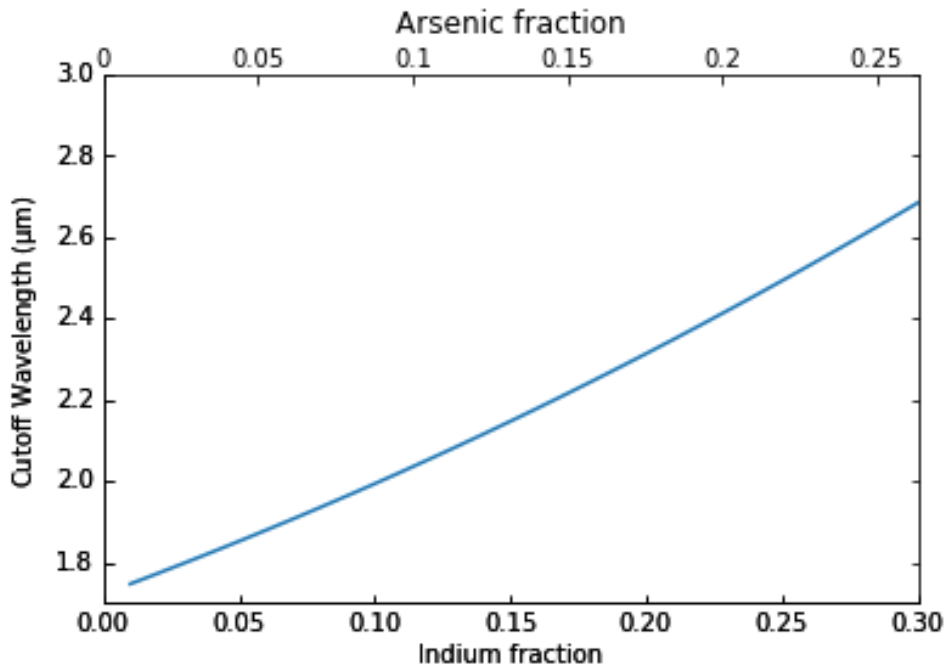


FIGURE 5.1: The theoretical cutoff wavelength as a function of the indium fraction for InGaAsSb lattice-matched to GaSb. The points are calculated based on equation 5.1, proposed by Adachi¹⁷².

The next decision in the cavity design is the type of detection structure to use. Common designs could all be implemented inside the cavity, a pn junction or pin photodiode are two options. For this work an nBn structure was chosen. This design reduces Shockley-Read-Hall and surface currents and has been shown to exhibit enhanced performance compared to pn junction photodiodes¹¹. This structure requires a material with a higher bandgap than the absorber to act as the barrier, to block the majority carrier current flow whilst simultaneously not impeding the flow of the minority carriers. This requirement simplifies down to a large conduction band offset and a minimal valence band offset. To complement the n layer of InGaAsSb the barrier layer of choice is AlGaSb, with the ideal group-III fraction determined by the composition of the InGaAsSb. The band offsets are modelled following the calculations of P. Krijn in figure 5.2,¹⁷⁶ and show that the material satisfies the requirements. It is not possible to alloy the materials in the barrier layer to perfectly match the lattice constant of GaSb (the substrate), but the mismatch is small. Previous demonstrations of these materials in an nBn structure have yielded high performance devices, despite the small lattice mismatch.^{67,68}

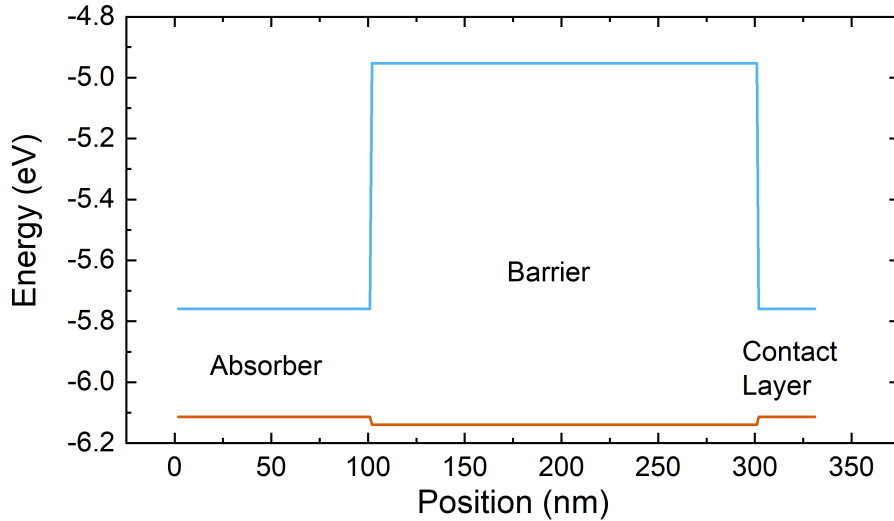


FIGURE 5.2: Calculated valence and conduction band energies of an $\text{In}_{0.25}\text{Ga}_{0.75}\text{As}_{0.22}\text{Sb}_{0.78}$ and $\text{Al}_{0.36}\text{Ga}_{0.64}\text{Sb}$ *nBn* structure,¹⁷⁶ to demonstrate the band offsets between the layers. The conduction band (blue) has a large energy offset between the absorber and the barrier, whilst the valence band (orange) has a very small energy offset between the two layers.

In a conventional, non-resonant structure the thicknesses of the layers are not constrained - the absorber can be as thick as it needs to be to achieve high absorption. Inside a resonant cavity the thicknesses are constrained by the wavelength matching to the DBRs - the cavity optical path length should ideally be a multiple of half the design wavelength.

The resonant enhancement also affects the thicknesses in an ideal structure - increasing the absorption on a single pass does not necessarily increase total absorption, so a very thick absorber layer in the cavity could decrease the absorption. If the absorber is too thick then only a small fraction of light might reach the bottom DBR, so the power of the light reflected off it will be very small in comparison to the incoming light. Therefore, the wave reflected off of the bottom DBR will not interfere significantly with the wave reflected off of the top DBR. This interference can usually result in destructive interference of the waves reflected out of the top of the structure and a fractionally small total reflection at the resonant wavelength. Without this interference the total reflection at the resonant wavelength will be higher, reducing the fraction of the incident light that can be absorbed in the cavity. So, the thickness of the absorber needs to be chosen, based on the material absorption coefficient, to

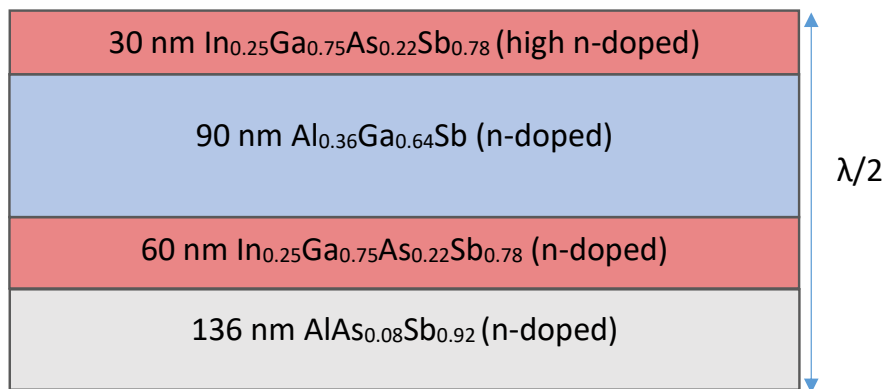


FIGURE 5.3: Example of the cavity structure for a detector with a target wavelength of $2.2\ \mu\text{m}$. From the bottom the purposes of the layers are: cavity spacer, absorber, barrier and contact layer. The layer thicknesses are calculated to put the centre of the absorber at the centre of the optical path length of the cavity.

avoid high total structure reflection at the resonance wavelength.

Related to this, the placement of the absorber needs to consider the electric field as a standing wave - for the highest absorption the absorber layer must be placed at an anti-node of the wave.

Combining all the requirements into a structure results in something that will vary for each specific design wavelength, but will be similar to the example in figure 5.3. This example cavity structure has a design wavelength, λ , of $2.2\ \mu\text{m}$ and a total optical path length of $\lambda/2$. The centre of the absorber is exactly at the centre of the optical path length of the cavity, which is the location of the anti-node for photons with a wavelength of λ . The lowest layer, of AlAsSb, is simply a filler layer - this is used to allow the absorber to be placed at the centre. AlAsSb is chosen because it has a wide bandgap, is transparent in the mid-infrared, and the alloy composition does not require extra calibration as it is also used in the DBRs.

5.2 GaSb/AlAsSb DBRs

The materials that can be used in the DBR layers are determined by the substrate. Each layer should ideally be lattice-matched to the substrate to avoid material dislocations and reduced device performance. It is also necessary that the top DBR

Material	Refractive Index	Bandgap (eV)
GaSb	3.86	0.73
InAsSb	3.54	0.29
AlAsSb	3.22	2.24
InGaAsSb	3.54 - 3.86	0.29 - 0.73
AlInAsSb	3.22 - 3.54	0.29 - 2.24

TABLE 5.1: The approximate refractive indices at 2.0 μm and bandgaps for III-V materials lattice-matched to GaSb.⁶¹ The range of values for the quaternary materials indicates the values for the ternary alloys at either end of their composition scale.

materials do not absorb photons at the target wavelength. In this case the GaSb substrate allows lattice-matched growth of the following III-V materials: GaSb, AlAsSb, InAsSb, AlInAsSb and InGaAsSb. It is helpful to compare the material properties to find the best pair of materials for the DBRs - table 5.1.

The reflectivity of a DBR is enhanced by both the number of pairs and the refractive index difference between the two materials, following equation 2.9. Therefore, to achieve a high reflectivity DBR the two materials with the biggest refractive index contrast offer the highest reflectivity. In this case GaSb and AlAsSb are the clear materials of choice. Both InGaAsSb and InAsSb absorb light in the targeted short-wave infrared region, so would not work in the DBR. AlInAsSb alloys can be transparent in the SWIR, but the refractive index sits between GaSb and AlAsSb. So, a DBR with AlInAsSb instead of AlAsSb would be less reflective.

With the choice of DBR materials decided, the number of repeats to use for both the top and bottom mirrors is a significant design choice that impacts the properties of the detector. The amplitude and width of the resonant response are both directly influenced by the reflectivities of the DBRs. The amplitude is generally enhanced by increased reflectivity, although this is dependent on the absorption structure inside the cavity - this is discussed further in section 5.3. The width of the resonance has a negative correlation to the reflectivities, so, if a narrow response is desired the reflectivity needs to be increased - by using more layers in the DBRs.

The impact of the number of pairs in the DBR on reflectivity can be seen in the modelled reflectance curves plotted in figure 5.4. Multiple curves are plotted for DBRs with between 5 and 25 pairs. There is a significant increase in reflectivity at

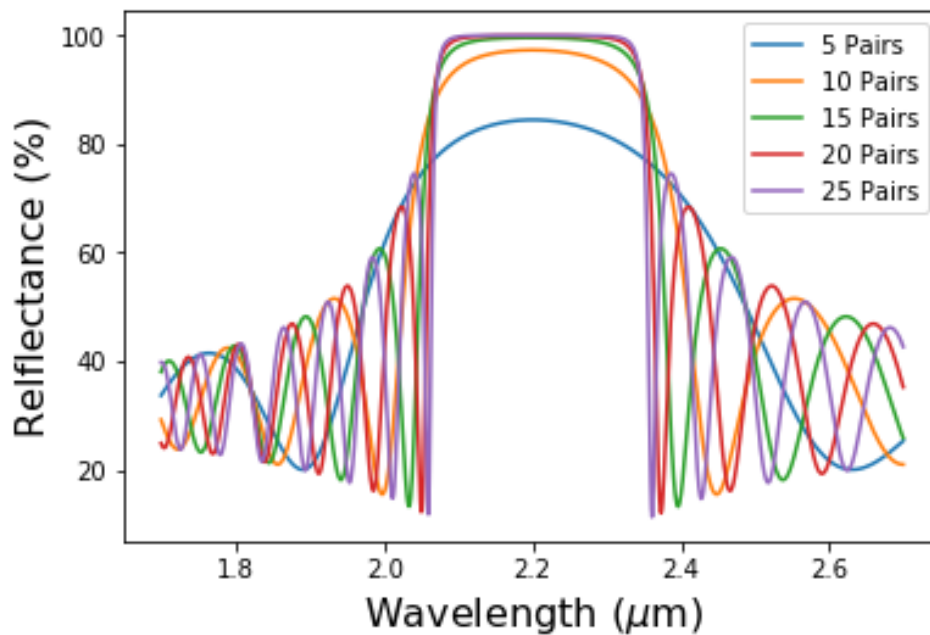


FIGURE 5.4: Modelled reflectance spectrum for an AlAsSb/GaSb DBR with varying numbers of layers. The transfer matrix model was used to create this figure, see section 2.4.1. The peak reflectance increases with number of pairs in the DBR, but tends to a maximum 100% limit.

the target wavelength as the number of pairs is increased. It is also clear from the plot that there is a case of diminishing returns as the number of pairs increases, adding more layers into the structure makes very little difference once a high reflectivity is achieved. This becomes relevant once the practical considerations of fabricating the structure are considered - discussed in more detail in section 5.3.

5.3 Complete SWIR RCE-PD

In this section, the cavity and mirror structures discussed in sections 5.1 and 5.2 are combined into a complete resonant cavity structure. The specific considerations for cavity and DBRs have already been discussed separately, but the full structure has further requirements that need to be considered. These are mostly practical requirements to allow fabrication methods to be used. The cavity structure is based on previous research into conventional nBn InGaAsSb detectors by A. Craig *et al.*⁶⁷

The fabricated structure is shown in figure 5.5, comprised of two DBRs surrounding the $\lambda/2$ thick cavity. The cavity follows the design laid out in section 5.1, only with

the addition of a 30 nm thick InAsSb layer at the top. This addition is driven by the need to place the contacts within the cavity. To allow for the contact deposition on the top n layer in the nBn structure the top DBR has to be etched. The etchant used to etch the top DBR selectively etches both GaSb and AlAsSb, whilst not etching the indium only alloys (InAs and InAsSb). The InGaAsSb that would otherwise be the top layer in the cavity is etched by the DBR etchant. Since the layers in the cavity are so thin it is difficult to be able to time the etch to stop in the correct place consistently. Therefore, an etchstop layer - which is not etched at all by the etchant - is a simple way to achieve the correct etch depth. InAsSb is the only lattice-matched material that can function as the etchstop layer. It should be noted that the InAsSb has a narrower bandgap than the InGaAsSb absorber, so it does absorb light at the resonant wavelength of the SWIR RCE-PD. However, it's location at the top of cavity reduces the loss caused by this absorption. The top of the cavity is the location of a node of the standing wave at the resonant wavelength, which reduces the absorption there.

The placement of the contacts, both on the same layer, is unique to barrier structures, such as the nBn structure used here. This contact system works because the positive contact is separated from the negative contact by etching the contact layer they sit on, so there is no short circuit. The barrier beneath the contact layer is not etched, but the electrons do not flow laterally through this layer due to large conduction band offset. So, the circuit between the two contacts is completed through the absorption layer.

With the structure design shown in figure 5.5, the current is measured with a small negative bias voltage applied. Under this condition, holes will drift towards the positive contact, whilst the photogenerated electrons stay in the absorber. To balance the charge, holes are injected from negative contact, where they can recombine with the electrons in the absorber. There is no pn junction or valence band barrier to block the flow of the holes, and the negative contact covers a much larger area than the mesa. So, the positioning of the negative contact on top of the contact layer is not expected to affect the measured current in comparison to a contact placed beneath the barrier.

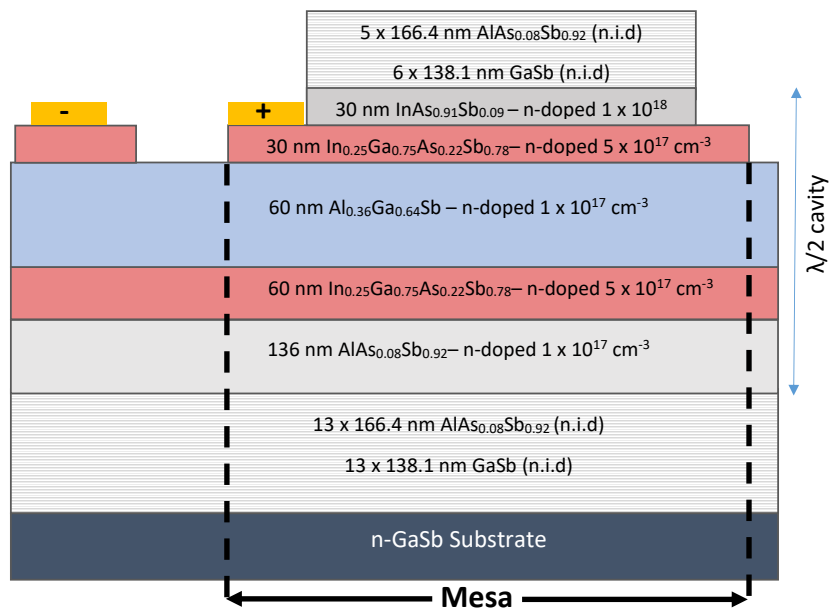


FIGURE 5.5: Structure of the fabricated RCE-PD targeted at sensing in the SWIR. The two contacts are placed on top of the InGaAsSb contact layer. The mesa is defined by etching through the contact layer. The area covered by the negative contact is much larger than the device mesa.

The design utilises a top DBR with 5.5 repeats - 5 AlAsSb layers and 6 GaSb - and a bottom DBR with 13 repeats. An ideal bottom mirror would reflect 100 % of the light at the resonance wavelength; the reflectivity will tend to this number as the number of repeats is increased. In a theoretical design it would make sense to have a very high number of repeats, but in a practical design the time required to grow the DBR has to be considered. Through modelling of the reflectivity the number of repeats is chosen to be 13, a balance between high reflectivity and low growth time.

The number of repeats in the top DBR is not as simple as aiming for the highest reasonable reflectivity. It is possible to create a high reflectivity top DBR that reduces the quantum efficiency of the device compared to a lower reflectivity DBR. Therefore, the reflectivity of the top DBR needs to be carefully controlled to achieve the optimum quantum efficiency. The number of repeats needed is dependent on the both the reflectivity of the bottom DBR and the attenuation in the cavity - a factor determined by the absorber thickness and the absorption coefficient. To best determine the ideal combination of DBR repeats and absorber thickness it is useful to model the quantum efficiency for each combination. The transfer matrix model -

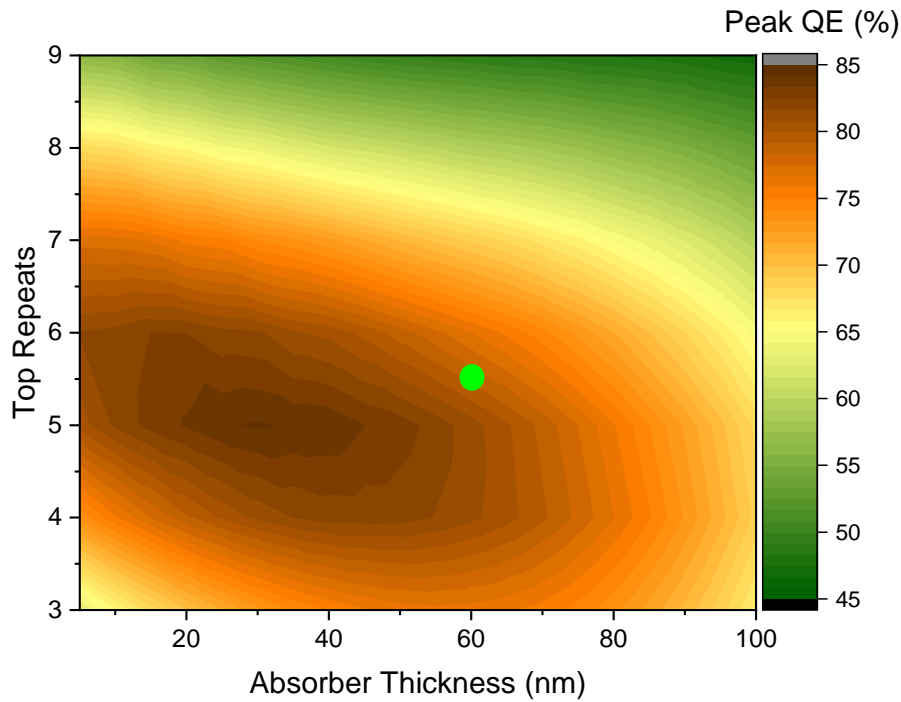


FIGURE 5.6: Modelled colourmap of the resonance quantum efficiency as a function of both absorber thickness and number of top DBR repeats. The bottom DBR is set to 13 repeats and the structure follows figure 5.5. The green dot indicates the position of the fabricated structure. With the set parameters, the highest QE is modelled to be at around 40 nm absorber thickness with 5 repeats in the top DBR.

chapter 2.4.1 - is used for the simulations. The quantum efficiency is approximated as the fraction of light that is neither reflected or transmitted. This is not a perfect assumption, but is suitable for comparison of different structures since the internal processes that reduce the QE are likely to be comparable in all the variations of the SWIR RCE-PD structure.

Figure 5.6 shows the combined effect of number of top DBR repeats and absorber thickness on the peak quantum efficiency. For these modelled values the number of bottom DBR repeats is set constant at 13 and an absorption coefficient of 7000 cm^{-1} is used throughout; also, the barrier and filler layers in the cavity are set to vary with absorber thickness to keep the entire cavity optical path length at a half of the design wavelength. With a constant absorption coefficient the variation in absorber thickness varies the attenuation of the light per single pass through the cavity. The plot shows that the highest QE is achieved with 5 repeats in the top DBR and an

absorber thickness of 25 nm to 45 nm. The final design - 5.5 - uses a slightly higher absorber thickness of 60 nm to give more leeway for position of the absorber in the cavity and for a reduction in absorption coefficient (which occurs as temperature decreases).

5.3.1 MBE Growth

The starting point for the RCE-PD sample is a tellurium doped GaSb (001) substrate. The first fabrication step is the epitaxial growth of the structure by molecular beam epitaxy - for full experimental details see section 4.1. The substrate is first out-gassed at 350 °C in the buffer chamber, then transferred into the growth chamber. It is heated up to 550 °C under Sb overpressure for oxide desorption for 10 minutes before cooling down to growth temperature of 500 °C. An approximately 500 nm thick GaSb buffer layer is grown immediately before the RCE-PD structure, to increase surface smoothness for following epilayers. All layers are grown at rates of ~ 1 ML/s and group-III to group-V ratios of 1.6 to 1.8 - the higher group-V fluxes compensate for the desorption from the substrate surface.

The bottom DBR is the first part of the structure to be grown. The Al and Ga cells are kept at the chosen growth temperatures throughout, with growth of the alternating layers controlled by the cell shutters. Between each layer growth the two group-III shutters are closed, whilst the As and Sb valve positions are set for the subsequent layer. As and or Sb overpressure is maintained during these periods. Growth of alternating layers is continued in the same way for all 13 repeats.

The cavity structure growth immediately follows the bottom DBR. The substrate growth temperature for the AlAsSb layer is the same 500 °C as the preceding layers. During the AlAsSb growth the In and Ga cell temperatures are stabilised for the InGaAsSb layer. For InGaAsSb growth the substrate is cooled to 450 °C under Sb overpressure. The As and Sb valve positions are setup immediately prior to the layer growth. The In, Ga and As shutter open simultaneously to begin the random-alloy layer growth, along with the GaTe cell for Te, n-type doping. Si could also be used as the n-type dopant, but Te was chosen due to increased incorporation in antimonides.¹⁷⁷

Following the absorber layer, the AlGaSb barrier layer is ideally grown at the same 500 °C as the DBR. However, raising the substrate temperature immediately after InGaAsSb could induce unequal group-V desorption from the surface, impacting the composition at the top of that layer. To avoid this ~ 20 nm of the AlGaSb layer is first grown without raising the temperature, to enclose the As from the surface. The substrate temperature is then increased to 500 °C under Sb overpressure, before continuation of AlGaSb growth.

Substrate temperature is again reduced to 450 °C for growth of the InGaAsSb contact layer. For the subsequent InAsSb etchstop layer the bulk As cell temperature is increased by 30 °C to increase the As flux and allow for the growth of the high As fraction. The As cell temperatures take approximately 1 hour to stabilise sufficiently, during which time all group-III shutters are closed and a low Sb flux replaces the Sb lost from the surface. Growth of the InAsSb layer occurs with a substrate temperature of 443 °C. The As cell temperature is immediately lowered to the previous temperature and stabilised for a further hour under As overpressure. Subsequent growth of the top DBR follows the same parameters as the bottom DBR until all repeats have been grown. The substrate is then cooled to 400 °C under Sb overpressure. The Sb shutter is closed below this temperature and the substrate is cooled down to ambient temperature.

To achieve the best structure it is necessary to optimise the parameters of the growth, *e.g.* substrate temperature for each material. For this structure all of these parameters were chosen based on prior knowledge from previous work. The DBR growth conditions were used for previously reported structures,⁹⁰ and the materials in the cavity had also been significantly optimised.^{67,178}

5.4 X-Ray Diffraction Analysis

The crystal quality of the epilayers is characterised by an $\omega - 2\theta$ scan on an x-ray diffractometer - full experimental details are given in section 4.2. The scan - shown in figure 5.7 - is used to analyse the lattice matching of the materials in the structure. The majority of the thickness of the structure is AlAsSb and GaSb, so the highest

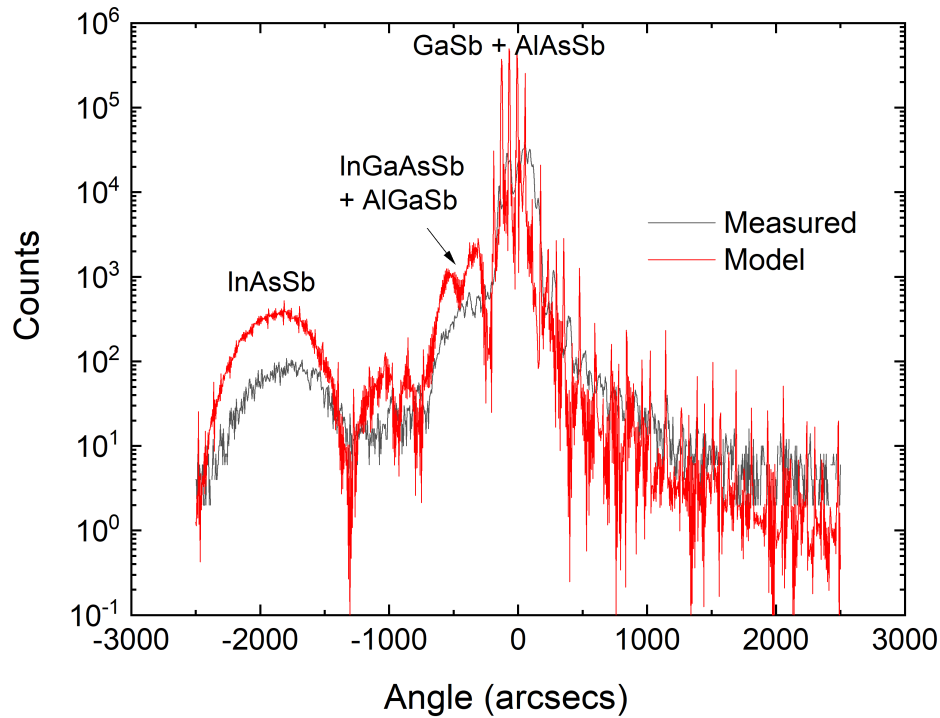


FIGURE 5.7: $\omega - 2\theta$ HR-XRD scan of the SWIR targeted epitaxial RCE-PD structure. The GaSb and AlAsSb epilayer peaks align closely with the substrate peak. The InGaAsSb and AlGaSb peaks are ~ -300 arcsecs lower (Sb rich) and the InAsSb is significantly mismatched at -1800 arcsecs.

peaks are expected to correspond to these materials - as indicated in the figure. The two peaks are within ~ 150 arcsecs, confirming good lattice matching of the AlAsSb. AlGaSb is intentionally lattice-mismatched to the substrate, and is expected to appear as a lower-amplitude peak a few hundred arcseconds away from the substrate. Both InGaAsSb and InAsSb compositions are targeted at closely lattice matching with the substrate, but for this sample they both appear at lower angles. The peak attributed to InGaAsSb is close to the AlGaSb peak at approximately -300 arcsecs relative to the GaSb peak. The small lattice-mismatch of these two layers is most likely to result in strained layers. Following the Matthew-Blakeslee model, equation 4.1, the critical thickness is much higher than the layer thicknesses of 60 nm. The InAsSb peak is more significantly mismatched at ~ -1800 arcsecs. However, this 30 nm layer is likely to still be below the critical thickness, again, following the Matthew-Blakeslee model.

Analysis of the measured curve is done using Bede RADS software - a tool that

models the diffraction patterns generated by semiconductor structures. Modelling of the designed structure shows a single main peak, with only one secondary peak caused by the mismatched AlGaSb. Adjusting the compositions of the layers in the modelled structure alters the diffraction pattern and reveals the compositions of the fabricated layers. For this structure the layers are relatively thin so it is assumed that they are not relaxed (not an ideal assumption, but a best guess with no way to measure relaxation). This method determines compositions of $\text{InAs}_{0.8}\text{Sb}_{0.2}$ and $\text{In}_{0.25}\text{Ga}_{0.75}\text{As}_{0.20}\text{Sb}_{0.8}$. With no way of separately measuring the group-III and group-V ratios in quaternary layers, it is assumed that the group-III fluxes are more consistent and the group-V ratio is the one that is incorrect.

5.5 Optical Properties

The transmittance spectrum of the structure is measured for the epitaxial structure without further processing post-growth. Utilising FTIR spectroscopy measurements as described in section 4.4.1, the transmittance through the epi-layers is calculated. Substrate attenuation is removed by reference measurement of a clean, unused GaSb substrate. The spectrum is measured from $\sim 1.3 \mu\text{m}$ to $> 20 \mu\text{m}$, but only the region of interest is shown in figure 5.8.

Figure 5.8 shows the measured spectrum in purple along with the modelled spectrum of the designed structure in red. The primary resonance wavelength is seen at $\sim 2.25 \mu\text{m}$, inside the stopband which spans from approximately $2.05 \mu\text{m}$ to $2.4 \mu\text{m}$. The resonance wavelength corresponds to the peak of spectral response; so it reveals that the response is slightly longer than the target wavelength ($\sim 2.25 \mu\text{m}$ compared to $2.20 \mu\text{m}$). One or more of the structure optical path lengths must be thicker than designed for the resonance to be higher. It is possible to use the rest of transmittance curve to narrow down the location of the thicker layer(s) to cavity or DBRs. The resonance peak is slightly to the right of centre of the stopband, this indicates that the cavity optical path length is longer than it should be to match the optical path lengths of the DBR layers. Therefore, it shows that the DBR layer thicknesses are approximately correct, but the cavity is slightly too thick - about 40 nm thicker from modelling.

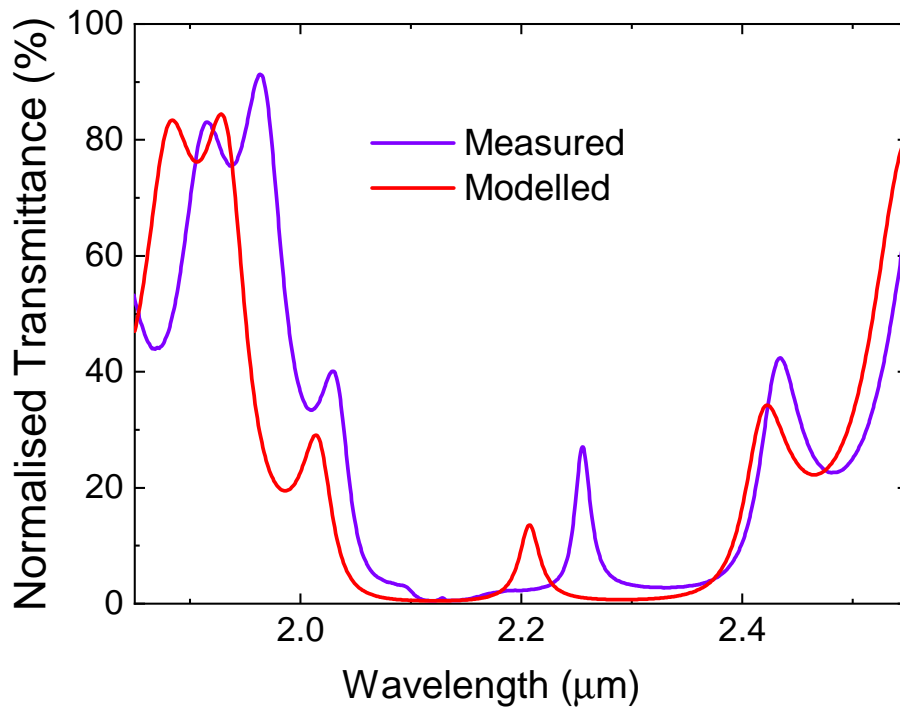


FIGURE 5.8: Measured transmittance spectrum of the fabricated SWIR RCE-PD (purple) and modelled (red). The resonance peak of the measured spectrum is at a longer wavelength than modelled, indicating higher layer thicknesses in the cavity.

One slight discrepancy between the modelled spectrum and the experimental data is the amplitude of the transmittance at the resonant mode. The height of this peak is significantly affected by multiple factors, including: mirror reflectivity and cavity attenuation. The model calculates the spectrum using known values for all the relevant coefficients, such as refractive indices and absorption coefficient. These values are not known with perfect precision, especially for InGaAsSb, and do also vary slightly with wavelength and temperature. Therefore, the calculated reflectivity and attenuation are not perfect, and small variations can incur large changes in the modelled spectrum. To highlight the affect these values figure 5.9 shows the transmittance at the resonance wavelength as a function of both absorption coefficient and GaSb refractive index, all other input parameters are not changed. Variation of the GaSb refractive index also changes the refractive index contrast between the two DBR materials, and therefore, impacts the reflectivity of the DBRs.

The measured transmittance at resonance is higher than the modelled value, with reference to figure 5.9 it can be inferred that the possible causes of this include lower

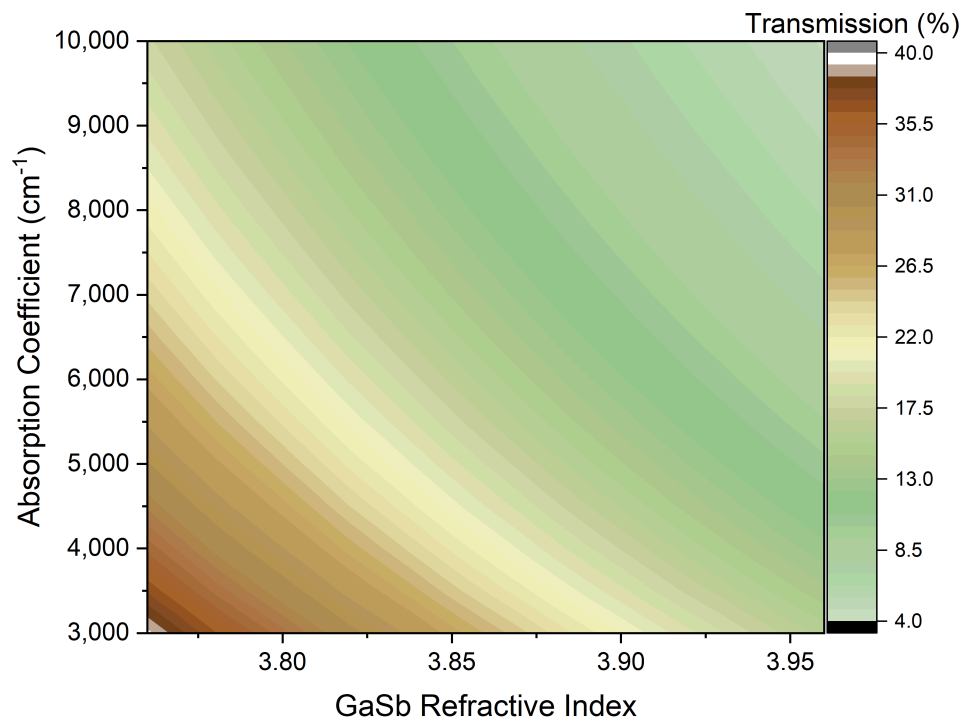


FIGURE 5.9: Colourmap of transmittance at the resonance wavelength, as a function of both absorption coefficient and GaSb refractive index. Both of these parameters are not easily controllable, but they are also not precisely known at the wavelengths of interest. This plot shows the significant effect of changes in these parameters on the resonance transmission, indicated by the colour.

cavity attenuation than expected or lower mirror reflectivity than expected.

5.6 Spectral Response

5.6.1 Responsivity/QE

The spectral response of a device is measured on a fully processed sample, with contacts deposited, see section 4.3, to be able to measure the current generated. A bias voltage of -100 mV is applied for all current measurements. Full measurement details for the spectral response are given in section 4.4.3. The spectral response of the RCE-PD is shown in figure 5.10. The narrow resonance can be seen centred at ~ 2.25 μm , but there is also a lower level broadband response below ~ 2.4 μm . The broadband response is caused by light bypassing the top DBR to reach the absorber, in the area of the mesa around the top contact that sits beneath the top DBR. At around 2.4 μm the cutoff wavelength of the absorber can be seen; the response is only noise above this wavelength. Comparison of figures 5.8 and 5.10 shows that the transmittance peak in the stopband aligns with the wavelength of the resonant response, as expected. The broadband response is not evident in the transmittance measurement, however, due to its origin from the processing methods.

5.6.2 Resonance Wavelength Temperature Dependence

The spectral response of the RCE-PDs shifts with temperature, as does the response of conventional broadband detectors. However, the temperature dependent shift in broadband detectors is mostly attributed to changes in the bandgap shifting the cutoff wavelength of the detector. RCE-PDs are not strongly influenced by the bandgap change, as long as the cutoff wavelength is not too close to the resonance. Instead, the shift of the resonance wavelength with temperature is due, most significantly, to the dependence of the refractive index on temperature. A change in the refractive indices changes the optical path lengths of the layers and this shifts the resonance wavelength that is solely dependent on the optical path lengths. The spectral response was measured at a range of temperatures, from 225 K to 350 K at 25 K intervals. Figure 5.11 shows the measured temperature dependence of the resonance wavelength along with the modelled shift expected due to refractive index varia-

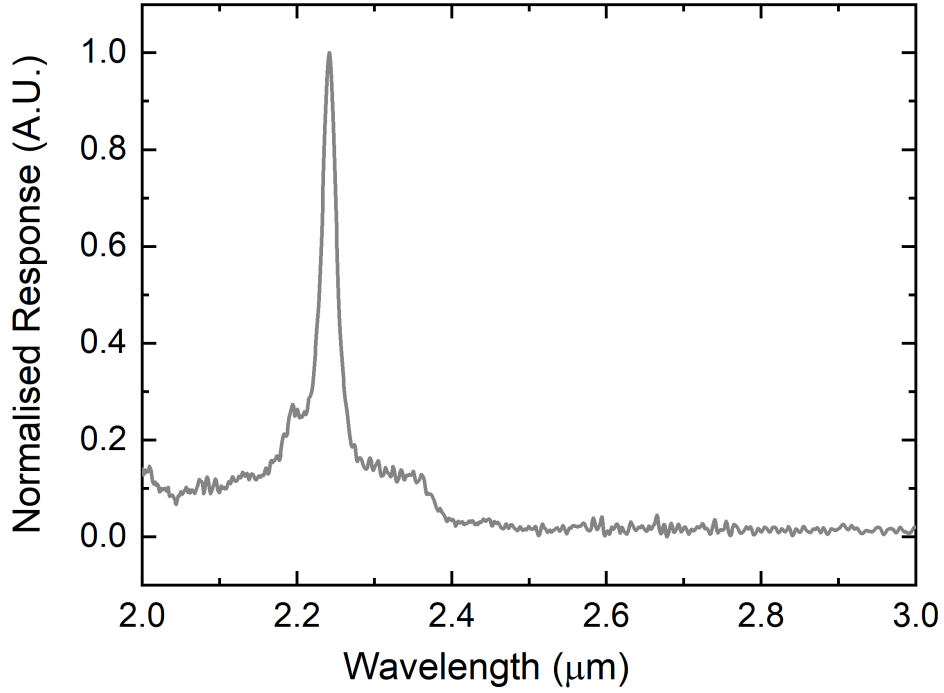


FIGURE 5.10: Normalised spectral response of the SWIR RCE-PD at room temperature. An applied bias voltage of -100 mV is used. The resonant response is at 2.25 μm and an underlying broadband response is seen at lower wavelengths, with a cutoff at 2.4 μm .

tions. The temperature shift of the resonance wavelength is significantly smaller than the shift of the cutoff wavelength, 0.23 nm/K compared to 1.4 nm/K. For the modelled values, the Moss relation determines the temperature dependent refractive index,¹⁷⁹ this relation uses the bandgap, E_g , change to approximate the refractive index, n change using

$$n^4 \propto \frac{1}{E_g}. \quad (5.3)$$

The 300 K values for refractive index and bandgap are set for all the materials in the structure, and the refractive index change is then calculated for shift in bandgap for each material. The bandgap is expected to follow the temperature dependence given by the Varshni equation:¹⁸⁰

$$E_0(T) = E_0(0) - \frac{\alpha T^2}{\beta + T}. \quad (5.4)$$

Material	$E_0(0)$ (eV)	α (10^{-4} eV/K)	β (K)
GaSb ¹⁸¹	0.809	5.3	234
GaAs ¹⁸²	1.519	5.58	220
AlAs ¹⁸³	2.229	6.0	408
AlSb ¹⁸⁴	1.686	4.2	140
InAs ¹⁸²	0.415	2.5	75
InSb ¹⁸⁵	0.24	6.0	500
AlAsSb*	1.642	4.3	161
InAsSb*	0.35	2.8	121
InGaAsSb ¹⁸¹	0.578	4.0	290

TABLE 5.2: Fitting parameters for the Varshni equation. * denotes parameters that have been calculated by interpolation, for $E_0(0)$ bowing parameters from Adachi¹⁷² are used.

Here, $E_0(0)$ is the bandgap at absolute zero. α and β are constants, with values summarised in table 5.2. The values for the binary materials are taken from the literature, whilst the ternary and quaternary values are calculated by interpolation where necessary (as a first approximation).

The refractive index for each material is calculated at each temperature using the fitting parameters, the 300 K refractive index and equations 5.3 and 5.4. The refractive indices are then used in the transmittance spectrum calculations for each temperature. The layer thicknesses used in the modelling are all scaled to produce a resonance wavelength that closely matches the fabricated structure - each temperature uses the same layer thicknesses.

The shift in resonance wavelength is also slightly dependent on the thermal expansion of the layers. However, separate modelling of the thermal expansion (not shown) reveals it causes a shift of the resonance ~ 25 times smaller than the shift due to the refractive indices.

5.6.3 Quantum Efficiency Temperature Dependence

As well as the spectral position of the resonance shifting with temperature the amplitude of the peak also varies significantly with temperature. The quantum efficiencies for a range of temperatures between 250 K and 350 K are shown in figure 5.12a. Below 225 K there is negligible resonant response, not shown. Above this temperature the QE increases rapidly with temperature, to a maximum at 275 K, and then de-

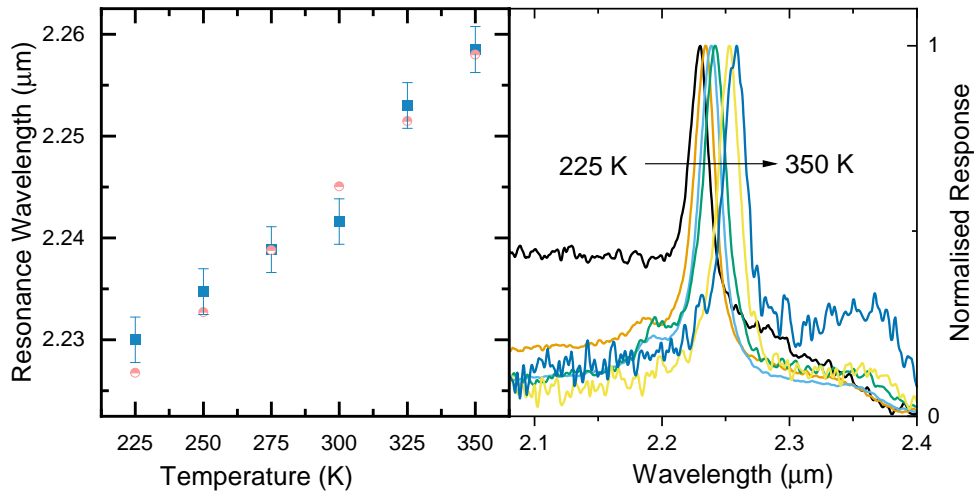


FIGURE 5.11: Left: Measured (squares) and modelled (circles) temperature dependence of the resonant peak wavelength of an RCE-PD with InGaAsSb absorber. The modelled used takes into account only changes in refractive indices of the layers. Right: Measured, normalised spectral response at temperatures between 225 K and 350 K, with 25 K steps. The data is plotted normalised for ease of peak comparison, so the amplitude at the resonance wavelengths is not meaningful.

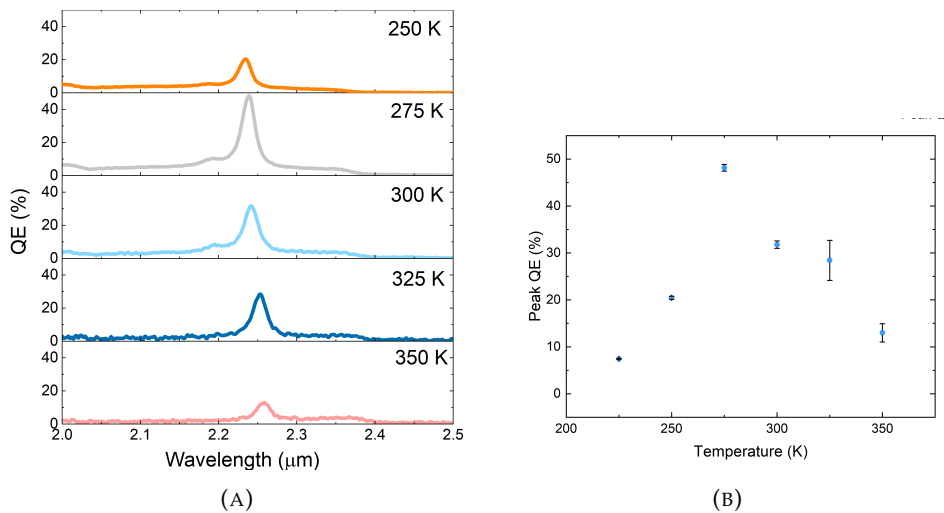


FIGURE 5.12: (A) Measured quantum efficiency spectra for the RCE-PD. Increasing temperature going down, from 225 K to 350 K, with 25 K steps. (B) Temperature dependence of the quantum efficiency at resonance, the values are taken from the peaks of (A) and the uncertainties are determined through comparison with measurements at five other bias voltages.

creases with temperature at higher temperatures. The temperature dependence of the QE at resonance is plotted in figure 5.12b. The underlying causes of the variations in QE are not as simple as the linear shift of the resonance wavelength. The QE is dependent on a number of factors that can vary with temperature to cause the rapid changes in QE with temperature that is seen in the plot. Factors include: DBR reflectivity, absorber optical path length and absorption coefficient.

To determine the impact of each factor it is best to consider each factor individually. The thermal expansion of the absorber is negligible over the operating temperature range, $< 1\%$, so has little impact on the cavity absorption. The change in refractive index of the absorber is more significant, up to a few percent decrease between 200 K and 400 K. Small changes in the optical path length of the absorber do not cause large differences in the quantum efficiency, so these variations in the absorber are unlikely to be the dominant cause of variations in the resonant response. The absorption coefficient can vary much more significantly, especially if the resonance wavelength is close to the cutoff wavelength. At the band edge the absorption coefficient reduces rapidly and can result in a similar rapid reduction in QE - figure 5.13 demonstrates the dependence of resonance QE on absorption coefficient.

Temperature effects on the DBRs can cause changes to the reflectivities, which can impact the quantum efficiency. As temperature increases the refractive indices of the two DBR materials decrease, but at different rates. The refractive index of GaSb decreases approximately six times faster than AlAsSb. This has the affect of reducing the refractive index contrast between the DBR layers, thereby reducing the overall reflectivity of the mirrors.

It is difficult to suggest a primary effect that causes the temperature variations on QE seen in figure 5.12. It is likely that a reduction in absorption coefficient at lower temperature is a significant factor in the decrease below 275 K. However, the cause of the decrease above 275 K is not clear. The lower reflectivity of the DBRs is expected to reduce the QE, but not as rapidly as seen in the experimental results.

It is a limitation of this work that all the potential causes of the QE variation have not been investigated. However, for completeness the electrical properties that could be

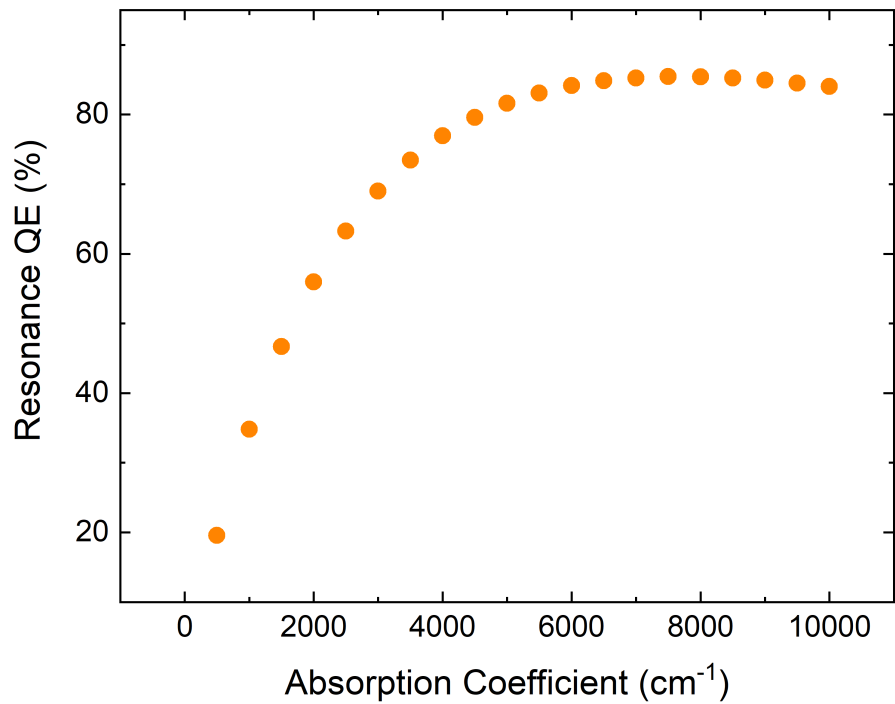


FIGURE 5.13: Modelled dependence of the QE at the resonance wavelength on the absorption coefficient of the absorber. As expected, the QE increase rapidly with absorption coefficient at lower absorption. However, there is also a slight decrease as the absorption coefficient gets much higher. This is due to the high single-pass absorption in the cavity reducing the reflectance from the bottom DBR and damping the standing wave affect.

the cause are mentioned. The reduction in diffusion length could reduce the number of photogenerated carriers reaching the contacts, thereby reducing the measured QE.⁶⁷ Previous studies suggest that *nBn* structures can demonstrate decreased lateral diffusion lengths at higher temperatures.¹⁸⁶ For the 600 μm side length mesas measured here, a sufficiently reduced lateral diffusion length would result in a fraction of the generated carriers not reaching the contact on the outer edge of the mesa.

In other studies of InGaAsSb based devices, higher non-radiative recombination has been observed with increasing temperatures.¹⁸⁷ This can be the cause of increased optical losses and a corresponding decrease in QE.

It is also possible that absorption in the DBRs increases with temperature, in particular absorption in the GaSb layers. The $\sim 1.7 \mu\text{m}$ cutoff wavelength of the GaSb layers increases more significantly with temperature than the resonance wavelength of the structure, so it is likely that a higher absorption will be seen in the GaSb DBR layers. However, from previous research into this material system, it is expected that this absorption will be negligible in comparison to the other factors.^{187–189}

5.6.4 Bandwidth Temperature Dependence

The width of the resonance is dependent on the reflectivity of the mirrors and the absorption in the cavity. These factors are dependent on temperature, so it follows that the full-width half-maximum of the resonance is also temperature dependent. Over a temperature range from 250 K to 350 K the FWHM ranges from 17.5 nm to 21.5 nm - figure 5.14. The experimental results do not show a consistent increase, but this is attributed to noisy measurements and lower amplitudes at temperatures above 300 K reducing the apparent FWHM. Up to 300 K a linear fit shows an increase in FWHM of 0.05 nm/K.

To understand the changes in FWHM with temperature the FWHM is modelled with dependence on two factors, the absorption coefficient and the the GaSb refractive index. Both of these values cannot easily be controlled, but do vary with temperature. The absorption coefficient varies more significantly than the optical path length of the absorber, so it is studied to determine the impact of cavity absorption on the

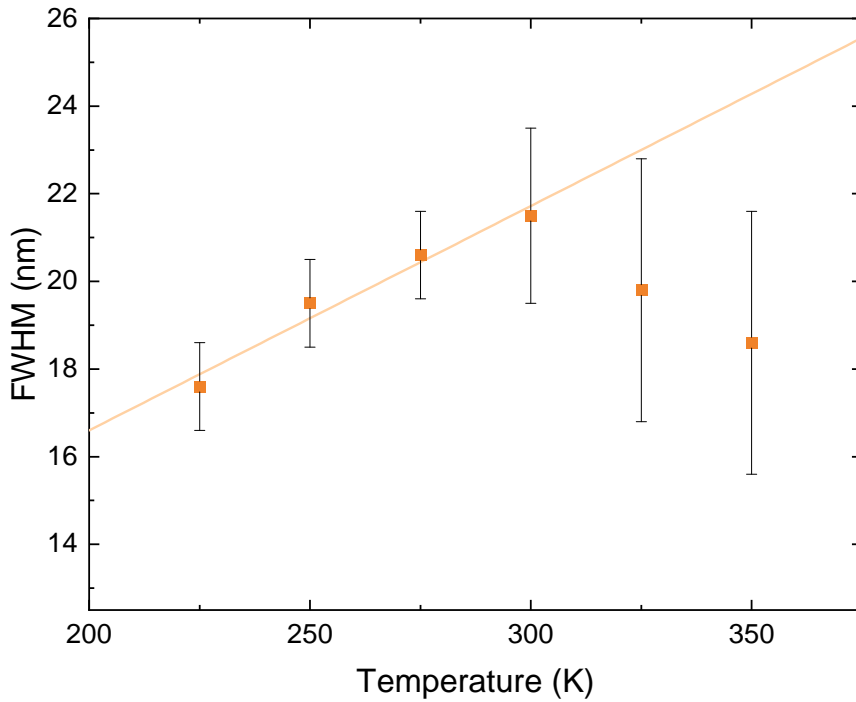


FIGURE 5.14: Measured FWHM of the resonance of the SWIR RCE-PD. At the lower temperatures there is linear increase in FWHM with temperature of 0.05 nm/K. There is a significant decrease above 300 K, possibly caused by enhanced noise in the measurements.

FWHM. An increased absorption coefficient increases the absorption of light on a single pass through the cavity and reduces the amplitude of light reflected by the bottom DBR. The FWHM increases with absorption coefficient due to a reduction in the enhancement effect. The fewer reflections through the cavity the lower the spectral selectivity is, increasing the FWHM. Figure 5.15 shows that the FWHM is linearly dependent on the absorption coefficient. The absorption coefficient is expected to increase with temperature, increasing the FWHM; however, the exact values depend on the composition of the InGaAsSb absorber material.

As an unpublished example from other members of the research group, the absorption coefficient was extracted from a single epitaxial layer of InGaAsSb grown on a GaAs wafer. An alloy of $\text{In}_{0.25}\text{Ga}_{0.75}\text{As}_{0.22}\text{Sb}_{0.78}$ was used - lattice-matched to GaSb following equation 5.2. The absorption coefficient was found to be $\sim 7000 \text{ cm}^{-1}$ at room temperature and at a wavelength of $2.2 \mu\text{m}$. At a lower temperature of 250 K this value decreases to 5000 cm^{-1} . The absorption coefficient varies significantly with wavelength close to the cutoff wavelength, which is dependent on the compo-

sition. So, accurate values for modelling of the QE would only be possible from a test sample grown with the same parameters at a similar time to the full RCE-PD structure.

The reflectivity of the DBRs is dependent on the refractive index difference between the two materials in the DBR. The refractive indices of both materials decrease with temperature, but GaSb decreases at a faster rate. To determine the impact of reflectivity on the FWHM the spectrum is modelled with dependence on GaSb refractive index, n_{GaSb} , which will vary the reflectivity when all other variables are kept constant. Figure 5.15 shows the modelled FWHM over a range of GaSb refractive indices from 3.76 to 3.96. This range is likely higher than the variations within the temperature range tested in figure 5.14 and shows an approximately linear increase of 3 nm. Between 250 K and 350 K the GaSb refractive index is expected to decrease from ~ 3.875 to ~ 3.845 ⁶⁴; the modelled results indicate this should increase the FWHM by ~ 0.5 nm. It is therefore likely that the increase in FWHM with temperature seen in figure 5.14 is most significantly driven by cavity absorption, but with a non-negligible contribution from the DBR reflectivities.

5.7 Electrical Properties

The electrical properties are measured on fully processed devices. The deposited contacts are probed inside a probestation to form a measurement circuit through the structure (see section 4.4.4 for more detail).

5.7.1 Dark Current

The dark current of a device is measured with the device in the dark, with negligible contribution to the current from photon absorption. The measured current is driven primarily by internal processes and not photon absorption. The device is placed within a cold shield to reduce thermally generated photons inside the test chamber. The current is measured as the bias voltage is swept to 0.5 V in the positive then negative direction. The temperature dependence of the current density is plotted in figure 5.16, in the temperature range 77 K to 350 K.

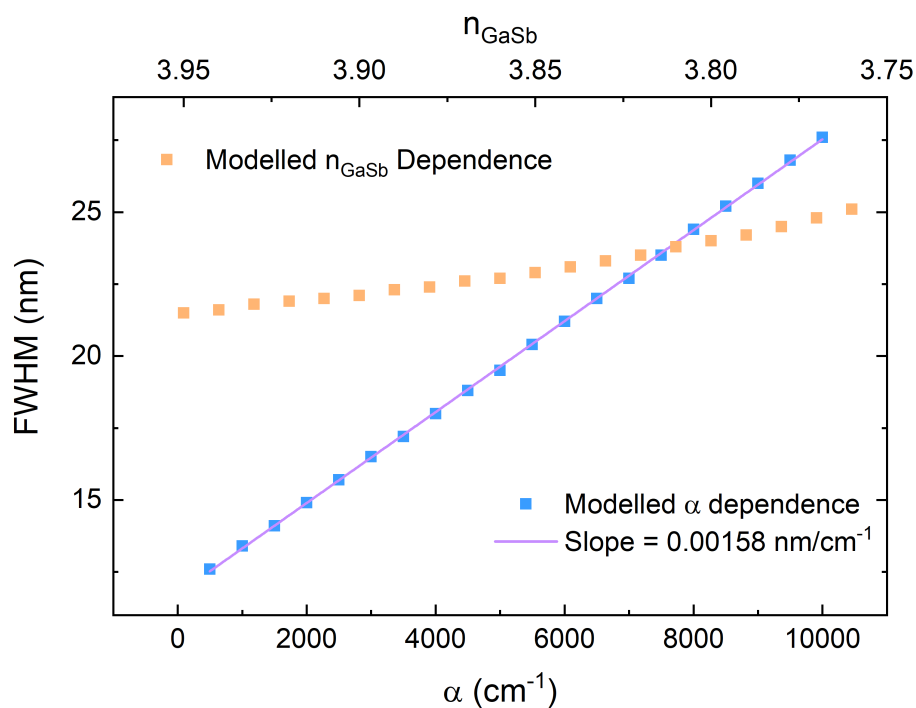


FIGURE 5.15: Modelled FWHM of the resonance for variations in absorption coefficient (bottom axis) and GaSb refractive index (top axis). Both of these parameters cannot be controlled and are subject to not well known temperature dependencies. The data can be used to infer the necessary variation in these parameters to cause the FWHM shift seen in the measured RCE-PD.

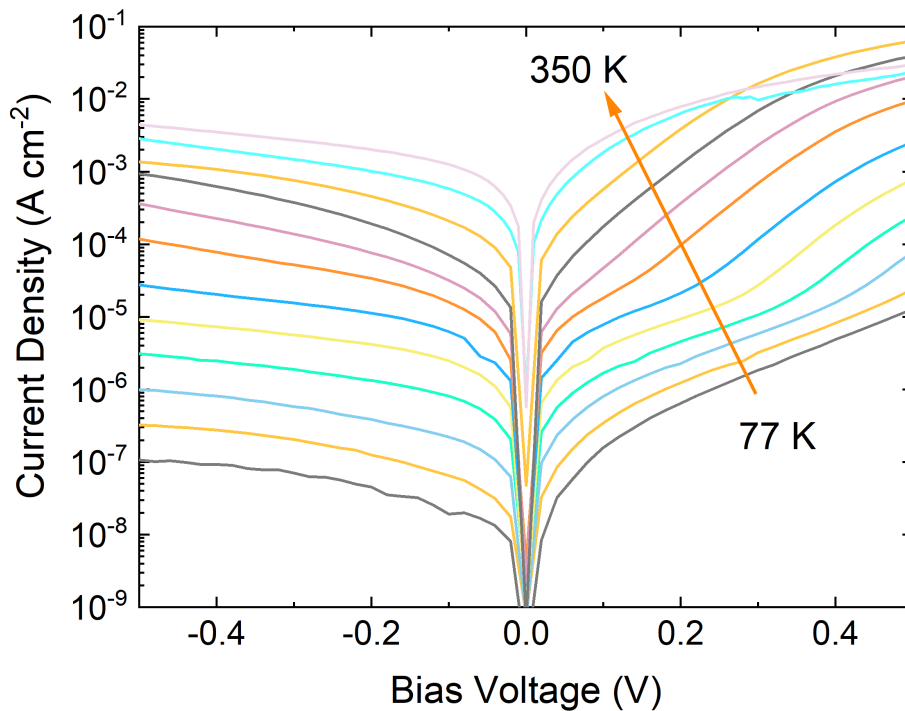


FIGURE 5.16: Temperature dependent dark current density for the SWIR RCE-PD from 77 K to 350 K, with 25 K steps. On the line of the orange arrow the current density increases monotonically with increasing temperature.

The current monotonically increases with temperature (the small change in the shape of the curve above 300 K is due to use of a different pixel) due to the same temperature dependencies as conventional nBn photodetectors. The nBn structure utilises a higher bandgap barrier layer that blocks the path of the electron current between the two contacts. This design should eliminate depletion region Shockley-Read-Hall generated currents as well as surface currents. The result is that the majority dark current should be due to Auger processes¹¹. The current density due to Auger processes is expected to follow the temperature dependence according to equation 2.4.

In figure 5.16 it can be seen that the dark current is higher with a forward applied bias voltage than a reverse bias voltage. This results from the nBn structure, where the dark current with a reverse bias voltage is mainly generated in the absorber region, but with a forward applied bias voltage it is mainly generated in the contact layer.¹⁹⁰ So, higher dark current under forward bias is due to increased efficiency of the generation mechanisms in the contact layer. The same alloy is used for both

layers, so Auger generation is not expected to be higher in the contact layer. Most likely, the Fermi level is closer to the centre of the bandgap in the contact layer, leading to an increase in defect related SRH generation.

Surface leakage currents are likely to dominate if they are present. However, they are discounted as a current generation mechanism here with a comparison of the current density of devices with different areas. Measurements were conducted on square devices with side lengths 150 μm , 250 μm , 400 μm and 600 μm . The measured current scaled linearly with device area, indicating majority current flow through the bulk semiconductor and not on the surface.

5.7.2 Activation Energies

To determine the dominant process causing the current it is helpful to plot the the current density at a single bias voltage against inverse temperature, creating an Arrhenius plot. The expected dependence is exponential in nature, so plotting the current density as a logarithm allows a linear fit to be used to determine the activation energy of the current mechanism. If there is a dominant dark current mechanism, the activation energy can indicate which process it is. Figure 5.17 is an Arrhenius plot of the dark current density with an applied bias voltage of -100 mV. The activation energy is given by

$$E_a = 1000k_B m \quad (5.5)$$

Where the Boltzmann constant (k_B) is in units of eV/K and the slope, m is given by $\frac{\Delta \ln(J)}{\Delta 1000/T}$.

The slope is not constant for the entire temperature range, indicating that the dominant current mechanism varies with temperature. The region of most interest around room temperature is fitted with an activation energy of 319 ± 5 meV, lower than the bandgap of the absorber at ~ 500 meV. The lower activation energy suggests that Shockley-Read-Hall generated currents are present and not eliminated as is expected with the nBn structure. At lower temperatures the activation decreases sig-

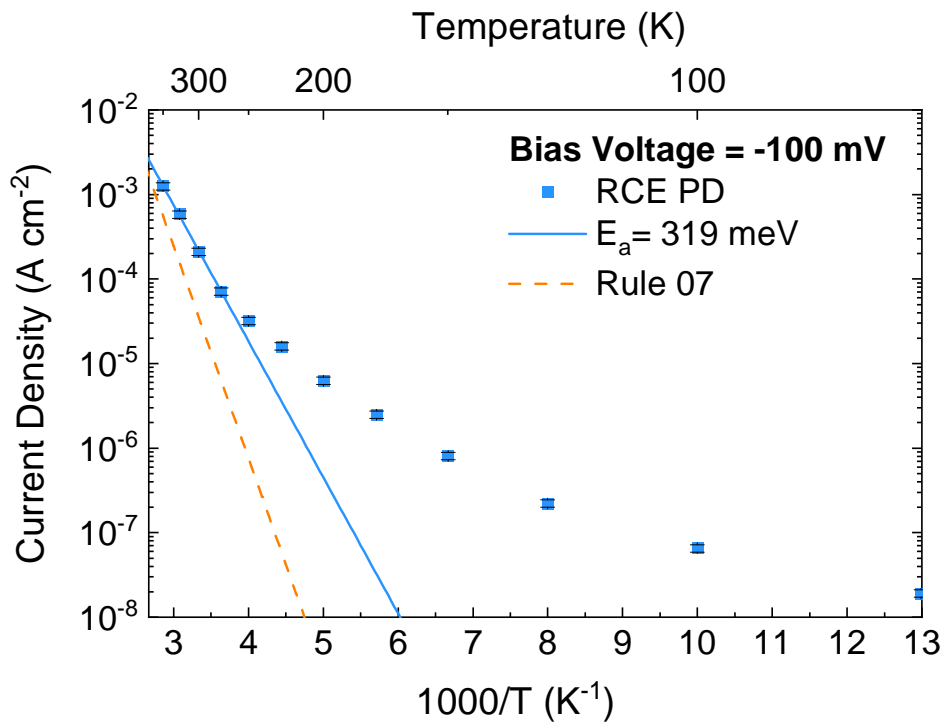


FIGURE 5.17: Arrhenius plot derived from the dark current density measurements in figure 5.16, at a bias voltage of -100 mV, and in temperature steps of 25 K. Blue squares are the measured data points, and the blue line represents an activation energy of 319 meV. The orange line is a comparison to the heuristic Rule 07, which represents the minimum Auger limited dark currents for MCT detectors.

nificantly to much less than $E_g/2$, indicating that the dominant current mechanism is not Auger or SRH and the leakage current is most likely dominated by thermal background radiative generation. This is expected for low temperature operation of detectors at short response wavelengths.²¹ Background limited performance has also previously been seen in similar RCE-PDs.¹⁹¹

A comparison line for Rule 07¹⁹² is included in figure 5.17. Rule 07 is a calculation that gives an approximate value for the highest performance possible by Auger limited MCT detectors - the current benchmark in infrared detectors. The dark current density of the SWIR RCE-PD is close to the Rule 07 line around room temperature, highlighting the low dark current characteristics of this design.

5.7.3 Dependence on Absorber Thickness

One of the principal theoretical benefits of the resonant cavity structure is the reduction in absorber volume, which is expected to translate into a proportional reduction in Auger 1 currents, the expected dominant current mechanism in n-type regions. The current density for Auger 1 generated currents is given by^{22,193}

$$J_{A1} = \frac{qL_{abs}N_{donor}}{2\tau_{A1}}. \quad (5.6)$$

The fabricated SWIR RCE-PD contains a 60 nm thick absorber, compared to conventional photodiodes that usually employ absorber thicknesses of at least 1 μm . The dependence of the absorber thickness on the dark currents is tested by comparison of the RCE-PD to a conventional nBn photodetector with a 2 μm absorber - reported by Craig et al.⁶⁷ Figure 5.18 shows the temperature dependence of the dark currents of both the RCE-PD and the reference nBn , both with applied bias voltages of -100 mV .

In figure 5.18 the RCE-PD is expected to show a dark current density 33 times lower than the conventional detector, calculated as the ratio of the absorber thicknesses. At lower temperatures the points for the two devices intersect as the current in the conventional device falls below that of the RCE-PD, so clearly does not agree with

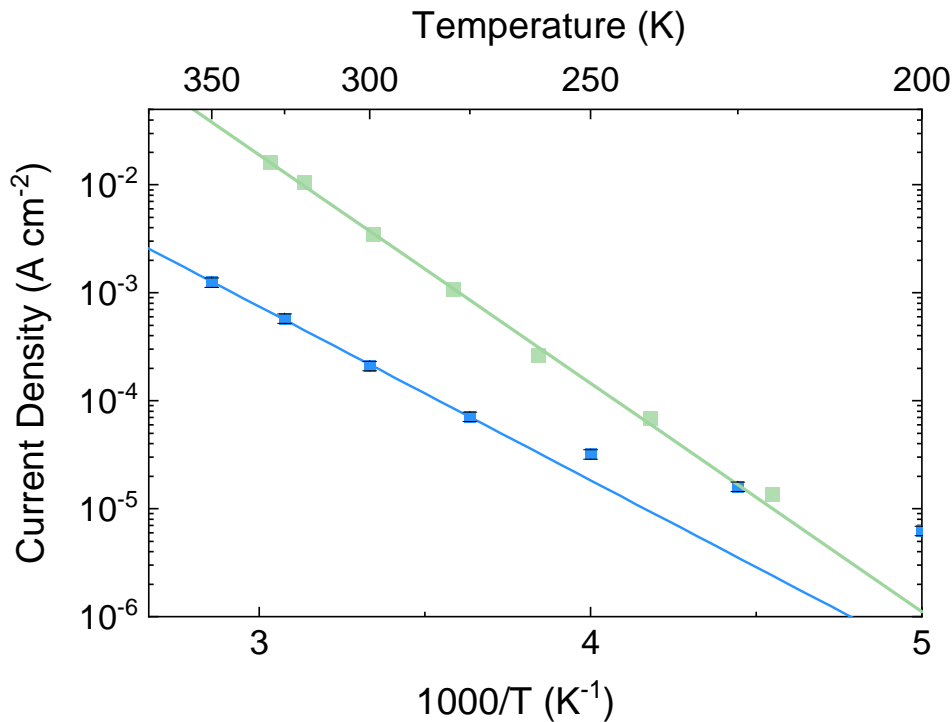


FIGURE 5.18: Arrhenius plot of the RCE-PD (blue squares) and the reference detector (green squares),⁶⁷ both with bias voltages of -100 mV. The blue line represents an activation energy of 319 meV and the green line represents an activation energy of 419 meV.

the reduction theory. At higher temperatures, however, the RCE-PD does demonstrate the lower dark current that is expected. The steeper slope of the conventional device indicates a higher activation energy, corresponding to differences in the current mechanisms causing the dark currents. This could be due to the use of the thin absorber in the RCE-PD increasing band bending at the interfaces and increasing the efficiency of the SRH process. Despite the RCE-PD not demonstrating the expected Auger limited dark current, there is still a significant decrease in the dark current - approximately 16 times lower at 300 K.

5.7.4 Specific Detectivity

The specific detectivity of a detector is a figure of merit that takes into account responsivity and noise to determine the suitability of a detector for sensing small signals. For the RCE-PD the peak specific detectivity is calculated at the resonance wavelength. The specific detectivity can be increased by either increasing the responsivity or decreasing the leakage currents, which act as noise during signal measurement. The temperature and bias voltage dependence of the peak specific detec-

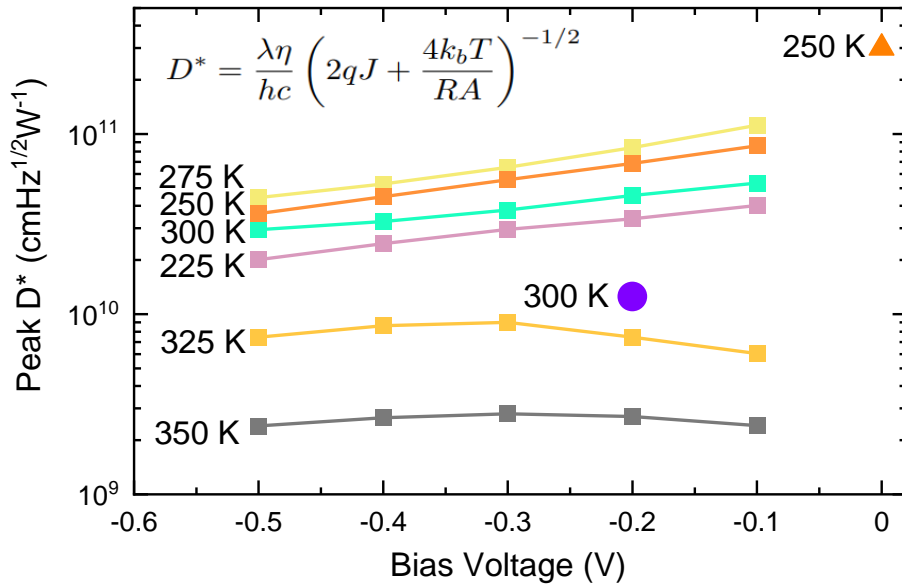


FIGURE 5.19: Specific detectivity at the resonance wavelength as a function of temperature and bias voltage for the RCE-PD (connected squares). Value for a conventional InGaAsSb nBn at 300 K (purple circle).⁶⁷ Comparison value to a commercially available extended-InGaAs photodiode with a peak at 2.2 μm and at a temperature of 250 K (orange triangle).¹⁹⁴

tivity is shown in figure 5.19. Both Johnson and shot noise are taken into account. The highest specific detectivity of $1 \times 10^{11} \text{ cm}\sqrt{\text{Hz}}/\text{W}$ is achieved at a temperature of 275 K, by reason of the high responsivity at this temperature. Lower temperatures see reduced detectivity despite the lower leakage currents due to the significantly lower responsivities. The detectivity decreases rapidly at higher temperatures due to the undesirable combination falling responsivity and increasing leakage currents. A maximum room temperature (300 K) specific detectivity of $5 \times 10^{10} \text{ cm}\sqrt{\text{Hz}}/\text{W}$ is measure, five times higher than the value achieved by a comparable conventional nBn .⁶⁷ Higher specific detectivities have been achieved by extended-InGaAs photodiodes,¹⁹⁴ above $10^{11} \text{ cm}\sqrt{\text{Hz}}/\text{W}$, but with further refinement it is expected that a SWIR RCE-PDs can exceed the background limited performance of conventional detectors. This has been shown to be possible in other spectral regions.¹⁹¹

5.8 Spectral Tuning

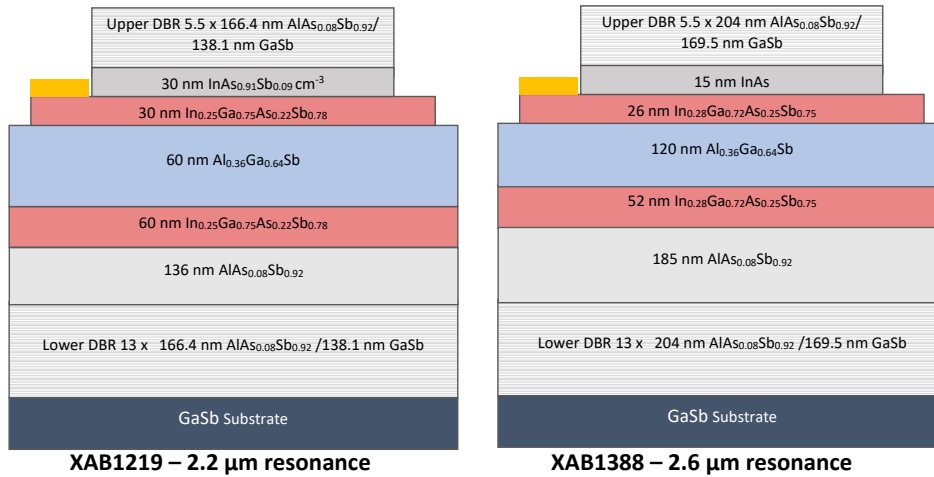
One of the promises made by the RCE-PD concept is the ability to tune the spectral response of a structure simply by altering the layer thicknesses. In this way, the same

design can be utilised to sense at a range of wavelengths, only limited by the spectral range covered by the absorber. The composition of the InGaAsSb alloy used as the absorber in the SWIR RCE-PD structure can be varied to have a cutoff wavelength as high as $\sim 2.8 \mu\text{m}$.¹⁹⁵ An increase in the indium fraction is required to lengthen the cutoff wavelength, as well as a corresponding increase in the arsenic fraction to maintain lattice-matching to the GaSb substrate.

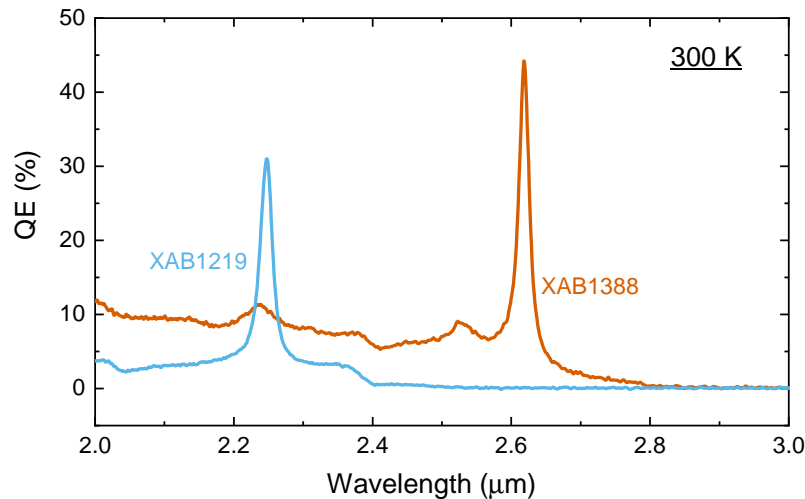
A second sample utilising the InGaAsSb/AlGaSb nBn cavity structure has been fabricated, with a higher resonance wavelength of $\sim 2.63 \mu\text{m}$. The structures of the two samples are shown in figure 5.20a for comparison. The thicknesses of the DBR layers are scaled based on resonance wavelength, which results in an increase of $\sim 20\%$ for the longer resonance wavelength structure. The optical path length of the cavity is also necessarily increased by the same fraction. The etchstop and contact layers are reduced in thickness, to reduce absorption in the structure outside of the InGaAsSb absorber. So, the necessary extra thickness is created by increasing the AlGaSb barrier and AlAsSb buffer layers. The thickness of the absorber is similar in both structures. The only other requirement for the design to work at the longer wavelength is an increase in absorber cutoff wavelength, achieved by increasing the indium fraction in the absorber to 28%.

It is important to ensure that the cutoff wavelength of the absorber is longer than the resonance wavelength of the cavity, otherwise there will be no absorption in the cavity. A first attempt at a longer resonance wavelength resulted in a device with no spectral response as a result of a low cutoff wavelength. Transmittance measurements through the sample show the resonant mode at the intended wavelength of $2.7 \mu\text{m}$, figure 5.21, but there is no spectral response at the resonance wavelength. The lack of absorption in the cavity can also be seen as a higher transmittance at resonance, which is seen most clearly when compared to a similar structure with cavity absorption - figure 5.21.

Comparison of the QE spectra of the two different thickness fabricated SWIR RCE-PD structures is shown in figure 5.20b. Despite the use of very similar absorber thicknesses the difference in spectral responses is clear. Both show the unwanted



(A)



(B)

FIGURE 5.20: A) Structures of XAB1219 (2.2 μm resonance) and XAB1388 (2.6 μm resonance). The longer resonance wavelength of XAB1388 is achieved with thicker DBRs and a thicker cavity (optical path length scaled linearly with resonance wavelength). B) Room temperature QE spectra of both structures. The thicker layers of XAB1388 result in a longer resonance wavelength. The differences in peak QE and shape of the spectrum are not due to the thicker layers specifically, and are caused by variations in absorber alloy composition, different etchstop material, crystal growth quality and other variations. The structures are only intended as a comparison of resonance wavelength.

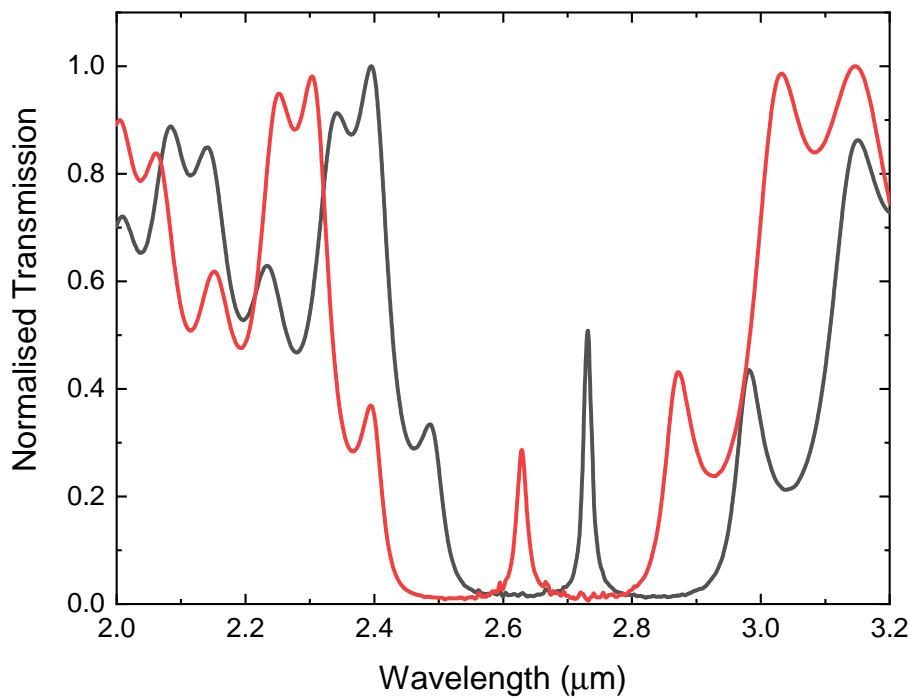


FIGURE 5.21: Normalised transmittance measurements of two samples, one with cavity absorption (red) and one without (black). The structure with cavity absorption has a lower resonant mode in the stopband, due to higher absorption at the resonant mode wavelength.

broadband response caused by light bypassing the top DBR into the absorber; it is expected that this would be much reduced by employing the surface passivation and cavity shielding of the new mask. The resonant responses of the two samples do not overlap at all, demonstrating the versatility of RCE devices. A narrow band of incident light could cause a significant response in one device without any response in the other - this is premise for their use in spectral sensing, where one acts as the measurement channel and the second acts as a reference channel.

5.9 Conclusions and Future Work

This chapter presented and discussed the design, fabrication and testing of RCE-PDs with resonance wavelengths in the short-wave infrared (more specifically, between 1.8 μm and 2.8 μm). Section 5.1 analysed the potential materials and structures that are used for the cavity, with the most significant choice of InGaAsSb as the absorber material. Limited to III-V semiconductor materials, this material was chosen because it has a cutoff wavelength that can be tuned to cover the entire SWIR region,

and can be grown lattice-matched to the chosen GaSb substrate. The DBRs discussed in section 5.2 are limited most significantly by the desire to maintain lattice-matching throughout the entire structure. This narrows the choice of materials, and AlAsSb/GaSb represents the highest refractive index contrast possible with this limitation. Section 5.3 combined the cavity and DBRs into a full RCE-PD structure and discusses the details of the epitaxial growth of the structure.

Crystal quality of the fabricated structure was confirmed by the x-ray diffraction measurements presented in section 5.4. Only the thin InAsSb etchstop layer had higher lattice-mismatch than is desirable, but the layer was most likely still strained due to the low thickness. The optical transmission properties, shown in section 5.5, were used to determine the resonance wavelength and position of the resonant mode in the cavity. The spectral positioning shows the mode was slightly off-centre (longer wavelength) which can be interpreted as a slight mismatch between the cavity thickness and DBR layer thicknesses. For optimal performance a future refinement of the fabricated sample would reduce the cavity thickness slightly, to obtain closer thickness matching.

The sample was etched as appropriate and contacts were evaporated to create devices that can be electrically probed. The electrical response of the structure to incident light was then able to be measured. The wavelength and temperature dependencies of the response were demonstrated and analysed in section 5.6. The detector showed high responsivity at room temperature and measurable response up to 350 K; this signifies that it can be used uncooled, even at high ambient temperatures. The width and height of the resonant peak were shown to vary with temperature, properties that would need to be accounted for during applied use of the detectors. Next, the noise properties were investigated in section 5.7. Low leakage currents were demonstrated, close to the Rule 07 target. These low currents contribute to the high signal-to-noise ratio achieved, calculated as a maximum specific detectivity value of $1 \times 10^{11} \text{ cm}\sqrt{\text{Hz}}/\text{W}$. Commercial extended InGaAs photodiodes can achieve specific detectivities of $> 10^{12} \text{ cm}\sqrt{\text{Hz}}/\text{W}$ at $2.2 \mu\text{m}$,⁶⁵ and it is expected that a refined RCE-PD structure could exceed this performance.

Finally, section 5.8 demonstrated one of the key promises of resonant cavities - the ability to tune the resonance by altering the layer thicknesses. Comparison of two fabricated devices with very similar structures produces spectral responses approximately 400 nm apart.

5.9.1 Future Work

Utilising surface passivation and cavity masking, described in section 4.3.7, for the fabrication of future samples would enable more clearly defined resonant responses. The broadband response would be minimised. The benefit of reducing the broadband response is increased sensitivity for spectral sensing measurements - there would be less photocurrent due to off-resonance photons and the measurement would be more specific to the narrow resonance band.

Further refinement of the doping in the cavity layers is also likely to improve device performance *i.e.* lower leakage currents and higher internal quantum efficiency. The RCE-PD structure utilises much thinner layers in the cavity than the conventional nBn structures previously reported.^{67,68,195} The thin layers can result in significant band bending that is not seen in the thicker structures,^{191,196} and as a result the doping throughout the cavity needs to be optimised specifically for the thinner layers.

The low activation energy (lower than the absorber bandgap) indicates the presence of significant SRH generated dark currents, that can be eliminated by the nBn structure. Improved lattice-matching of the epitaxial ternary and quaternary alloys would reduce dislocations and reduce the efficiency of the SRH mechanism. The low activation energy also indicates that the Fermi level is not close to the conduction band edge that is expected in an ideal nBn .¹¹ This might be as a result of the band-bending. A future investigation into the ideal doping concentrations in the absorber and barrier would be expected to reduce this issue. In the absorber an ideal doping level would move the Fermi level closer to the conduction band, to reduce the efficiency of the SRH generation. However, a balance needs to be found because an increase in doping increases the dark current due to Auger generation.²²

Detectors with resonance wavelengths between 2.2 μm and 2.6 μm are demonstrated. Extension of this wavelength range is possible with this materials system, from 1.7 μm to 2.8 μm . This would be worth exploring, to cover as many spectral absorption lines as possible *e.g.* water at 1.9 μm .¹⁹⁷

Chapter 6

Results II: Mid-Wave Infrared RCE-PDs

This section details the design, fabrication and characterisation of RCE-PD structures designed to sense at wavelengths in the mid-wave infrared (MWIR), specifically wavelengths between $\sim 3.0\ \mu\text{m}$ and $\sim 3.5\ \mu\text{m}$. This spectral region is of specific interest for optical spectroscopy due to absorption peaks caused by vibrations of C-H bonds occupying this region. C-H bonds are found in many significant substances, including hydrocarbons. The narrow spectral response of RCE-PDs offers the potential for optical identification of substances in this region without interference from neighbouring absorption peaks. In other words, a specific hydrocarbon, *e.g.* methane, could be identified without the measurement results complicated by the presence of other hydrocarbons.

Similar to the RCE-PDs that sense in the SWIR presented in chapter 5 the structure design necessarily starts with the substrate. Structures that are lattice-matched to the substrate are chosen and the DBR materials are narrowed down to lattice-matched alloys that do not absorb at the target wavelength. For this region of the spectrum there are two III-V material systems that have been investigated. On a GaSb substrate $\text{InAs}_{0.91}\text{Sb}_{0.09}$ absorbs up to a cutoff wavelength of $\sim 4.4\ \mu\text{m}$,⁹⁰ and on an InAs substrate an InAs absorber can be utilised for sensing up to $\sim 3.5\ \mu\text{m}$.²⁵ Within the research group RCE-PDs utilising InAsSb absorbers have been demonstrated previously, albeit at a slightly longer resonance wavelength of $3.72\ \mu\text{m}$.¹⁹¹ The InAs based

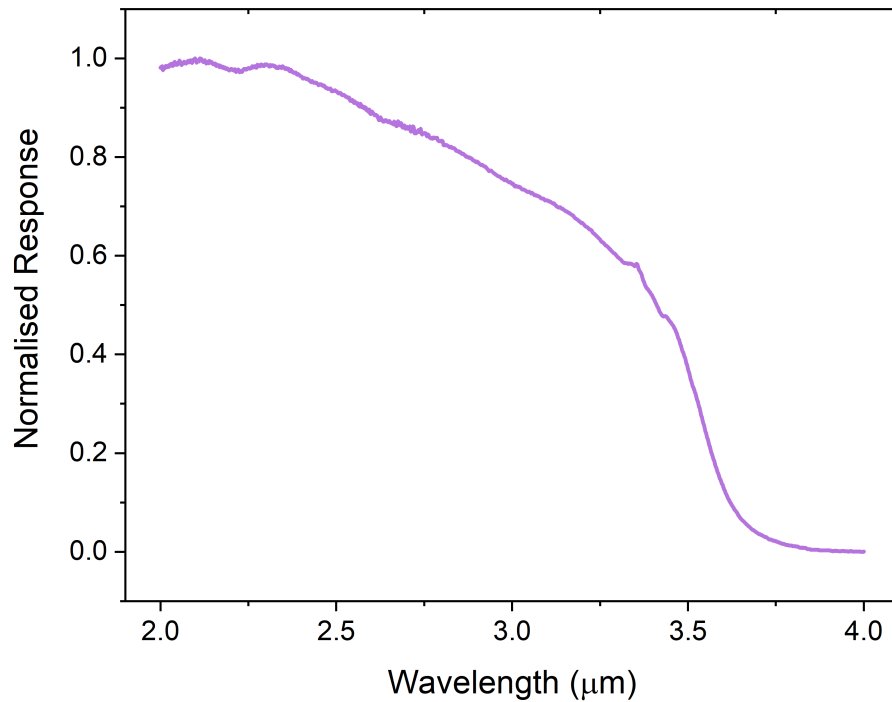


FIGURE 6.1: 300 K normalised response of a bulk InAs nBn . This wafer was grown on the same MBE, with comparable growth parameters to the RCE-PD structures in this chapter. Therefore, it represents a very high similarity to material used for the RCE-PD structures.

RCE-PDs represent new work undertaken and, therefore, are the focus of this chapter.

6.1 InAs/AlAsSb nBn

For spectral response in the MWIR InAs is a suitable material that is well-known^{2,88} and is simple. For III-V epitaxial growth a bulk, binary material is the simplest possible material. Unlike the InGaAsSb absorber used in the SWIR nBn , growth of InAs does not require careful control of the beam fluxes to achieve the correct composition. The room temperature bandgap of InAs is 359 meV, correlating to a cutoff wavelength of 3.5 μm - demonstrated by the 300 K response of a conventional InAs detector in figure 6.1.

To create an nBn structure on the chosen InAs substrate a barrier needs to be chosen that has a larger bandgap than the InAs absorber, ideally with a high conduction band offset and low valence band offset. Lattice-matched to the substrate is a condi-

Material	Bandgap (eV)
InAs	0.359
AlAsSb	2.23
GaAsSb	0.685
InGaAsSb	0.359 - 0.662

TABLE 6.1: Bandgaps for selected III-V alloys, lattice-matched to InAs. Values calculated from parameters suggested by S. Adachi.¹⁷²

tion also imposed here as the aim is to create a high-quality, high Q-factor resonant structure that benefits from the low defect density possible with lattice-matched epitaxial layers. Table 6.1 shows a selection of the possible alloys lattice-matched to InAs, and their bandgaps. AlAs_{0.16}Sb_{0.84} has the widest by bandgap by a significant margin and is the choice for the barrier in the InAs-based nBn .

Modelling of the band structures for a InAs/AlAsSb/InAs nBn also reveals that the desired combination of high conduction band offset and low valence band offset is expected - figure 6.2. The structure has a conduction band offset of ~ 1.8 eV, enough to block the majority electron current and thermal excitation of the electrons. There is also a small valence band offset of 0.064 eV, but this should not significantly impede the flow of the minority hole current. A zero valence band offset can be achieved with an alloy of AlAs _{x} Sb _{$1-x$} , but requires a higher arsenic fraction of ~ 0.2 , which is not lattice-matched to the InAs substrate.²⁵

The thicknesses of the layers in the structure also need to be considered. In a conventional detector the absorber is required to be thick enough for a high absorption of photons with the target wavelength. Inside a resonant cavity the total attenuation is dependent on the reflectivity of the DBRs and positioning of the absorber in the cavity - this is discussed in more detail in section 6.3. The thickness of the barrier does not have the same dependencies and so can be directly translated from the conventional structure to the resonant structure. The main consideration for the barrier thickness is the probability of electrons tunnelling through it. Calculations by J. Pedrazzani indicate that a few tens of nanometres is enough to reduce the tunnelling current through defect-free material to negligible levels.²⁵ Experimental results taken by A. Craig indicate that electron tunnelling reduces significantly between 20 nm and 80 nm,¹⁵⁸ possibly due to the presence of midgap states increasing

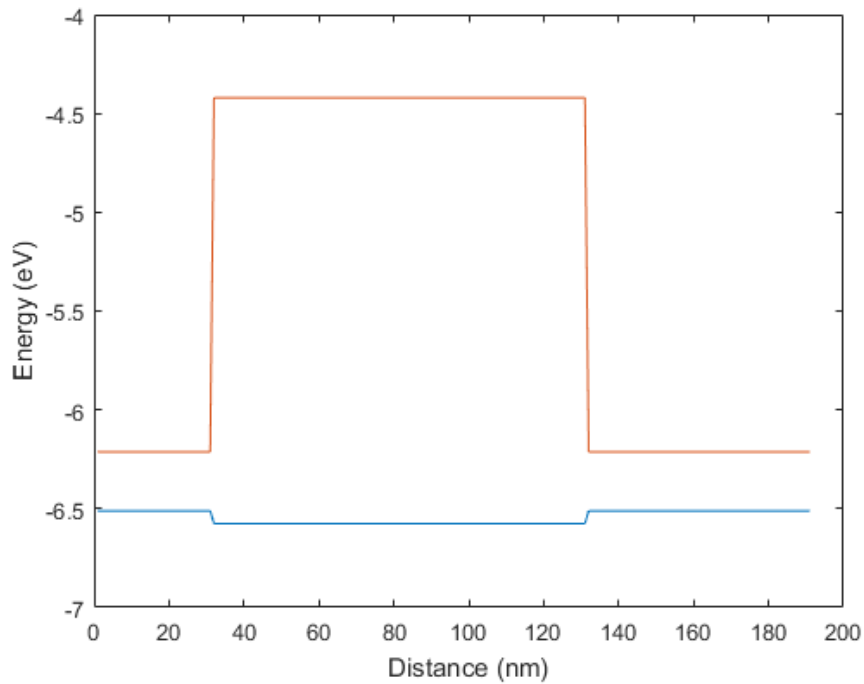


FIGURE 6.2: Calculated valence and conduction band energies of a InAs/AlAsSb/InAs *nBn*.¹⁷⁶ The figure demonstrates the band offsets between the layers. The conduction band (blue) has a large energy offset between the absorber and the barrier, whilst the valence band (orange) has a very small energy offset between the two layers.

the probability of tunnelling in real material. The maximum ideal thickness of the barrier is dependent on the critical thickness to keep the layer strained, and not introduce dislocations into the lattice. For compositions close to lattice-matched the critical thickness is hundreds of nanometres.²⁵ Therefore, there is a clear window of thickness that reduces tunnelling and allows for strained epitaxial growth - 100 nm to 200 nm is used in structures in this work.

The thickness of the contact layer is a compromise between robustness of the layer for contacting and reduction of photon absorption; any light absorbed in this layer does not contribute to the measured photocurrent. For a conventional detector a contact layer thickness of the order of 30 nm is thick enough to be robust, without significant photon absorption.¹¹

Material	Refractive Index
InAs	3.59 ⁶¹
AlAsSb	3.16
GaAsSb	3.72
InGaAsSb	3.59 - 3.72

TABLE 6.2: Approximate refractive indices at 3.3 μm for materials lattice-matched to InAs. Refractive index ranges for quaternaries are determined from the refractive indices of the binary/ternary alloy at either end of the composition scale.

6.2 GaAsSb/AlAsSb DBRs

Since DBRs are constructed from two alternating materials, a simple choice for one of the materials is usually the substrate material *e.g.* GaSb/AlAsSb DBRs on GaSb substrates and GaAs/AlGaAs DBRs on GaAs. This is not possible with the InAs substrate used here, with a target wavelength in the MWIR anyway, due to the high absorption by InAs in this spectral region. This has the consequence that two more complex alloys are required for lattice-matched epilayers. For the best chance of a high-quality, low defect crystal growth the use of ternary alloys is preferred to quaternary or even more complex alloys. This constraint suggests that $\text{AlAs}_{0.16}\text{Sb}_{0.84}$ and $\text{GaAs}_{0.08}\text{Sb}_{0.92}$ are the materials to use in the DBRs. It is also desirable for the refractive index difference between the two materials used in the DBRs to be high (to achieve high reflectivities with fewer pairs). Table 6.2 gives the approximate refractive indices at 3.3 μm of a selection of materials lattice-matched to InAs. AlAsSb and GaAsSb are also the best choice to obtain the highest refractive index contrast.

Compared to the GaSb/AlAsSb DBRs, the GaAsSb/AlAsSb materials have a slightly lower refractive index contrast, approximately 0.67 compared to 0.56. Therefore, the reflectivity of a GaAsSb/AlAsSb DBR is lower with the same number of repeats. To quantify the differences the reflectivity has been modelled for DBRs made from these two material systems. Figure 6.3 shows the reflectivity of DBRs with 7 layer repeats, with thicknesses chosen to centre the stopband at 3.3 μm . For the GaAsSb/AlAsSb DBR the reflectivity of 9 layer repeats is also shown (dashed line).

The consequence of the lower refractive index contrast of GaAsSb/AlAsSb can be seen in figure 6.3; with the same number of repeats (7) the DBR has a significantly

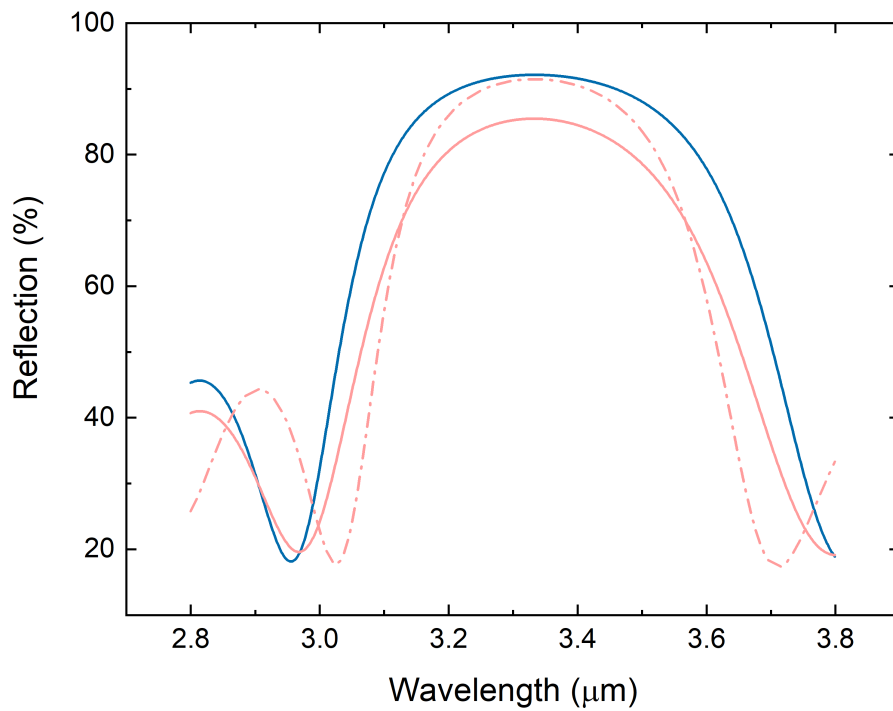


FIGURE 6.3: Modelled comparison of the reflectivity of DBRs constructed from GaSb/AlAsSb (blue) and GaAsSb/AlAsSb (pink). Solid lines represent 7 pair DBRs and the dashed line represents a 9 pair DBR. The lower refractive index delta of the GaAsSb/AlAsSb DBR results in lower peak reflectivity and a narrower stopband. The reflectivity can be increased with more repeats in the DBR. The transmission matrix model was used for all calculations.

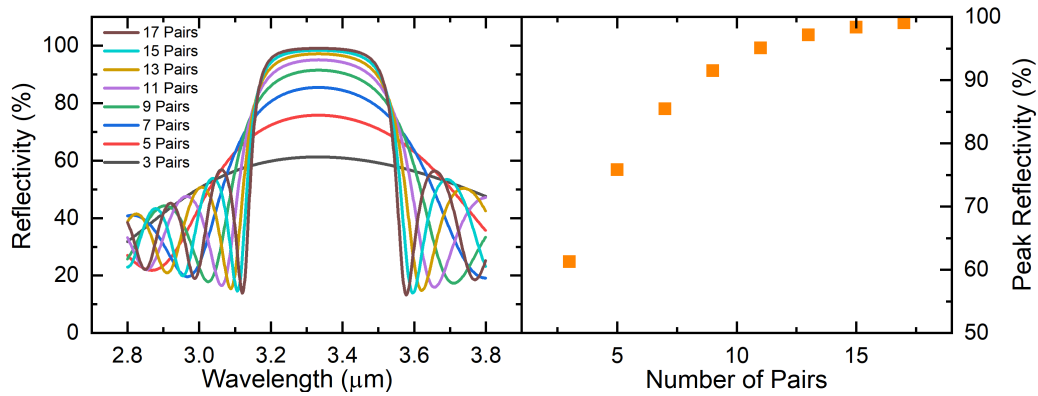


FIGURE 6.4: Left: modelled reflectivity curves for GaAsSb/AlAsSb DBRs with numbers of pairs between 3 and 17. The peak reflectivity increases monotonically with increasing pairs, and the stopband edge gets sharper. Right: peak reflectivity taken from the plot on the left.

lower maximum reflectivity. 85.5 % for the GaAsSb/AlAsSb DBR compared to 92.1 % for the GaSb/AlAsSb DBR. The lower reflectivity can be counteracted by increasing the number of pairs from 7 to 9. However, it should be noted that increasing the number of pairs has the additional consequence of reducing the width of the stopband.

Figure 6.4 shows the modelled reflectivity of GaAsSb/AlAsSb DBRs with the number of pairs ranging from 3 to 17. The peak reflectivity monotonically increases with the number of pairs, and tends to a maximum reflectivity of 100 %. At higher reflectivities the benefit of increasing the number of layers is much reduced.

6.3 Complete RCE-PD on InAs Substrate

The full structure of the RCE-PD on an InAs substrate combines the nBn and DBRs discussed in sections 6.1 and 6.2, respectively. There are two significant choices for the structure not already discussed, the thickness of the absorber and the number of repeats in the DBRs. These two factors are intertwined, so ideally should be chosen together. Figure 6.5 shows the dependence of the QE on both the absorber thickness and the number of repeats in the top DBR. For simplicity the number of repeats in the bottom DBR has been set at 12 - this is a compromise between achieving the highest reflectivity and minimising growth time. The total cavity optical path length is kept at approximately half the target wavelength by varying the thicknesses of the other

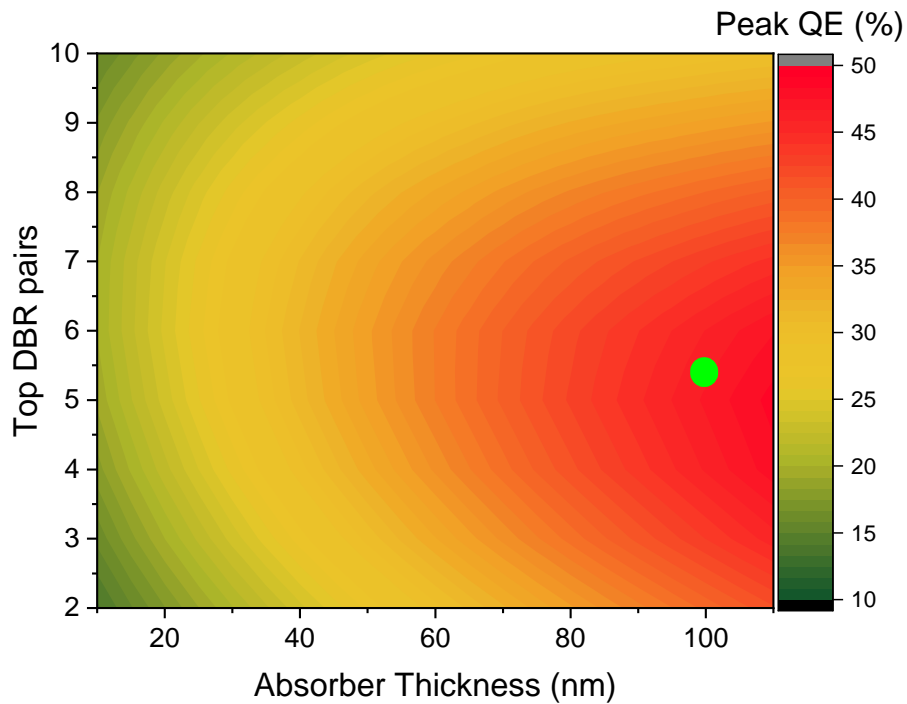


FIGURE 6.5: Model of peak QE as a function of both number of layer pairs in the top DBR and absorber thickness. The number of repeats in the bottom DBR was set at 12. The green dot indicates the position of the fabricated structure. The colour represents the peak QE in the modelled spectrum, with the transfer matrix model used.

layers as the absorber thickness changes. The absorber is also centred in the cavity for all calculations.

The absorption coefficient used in the model is a nominal value of 4000 cm^{-1} . Since this value is not experimentally verified there is a significant source of uncertainty here and this highlights the limitation of using the model to design structures. The accuracy of a design can only be as good as the accuracy of the input parameters. Differences between the theoretical parameters and real values are likely to be the cause of any significant differences between the model and experimental results. The absorption coefficient of InAs could be determined through transmittance measurements on an epilayer, although it would preferably be grown on a transparent (at the target wavelength) substrate *e.g.* GaAs instead of InAs. However, this is outside the scope of this work.

The calculations in figure 6.5 indicate that the optimal absorber thickness and top DBR pairs combination is 100 nm and 5 pairs. The optimal absorber thickness of

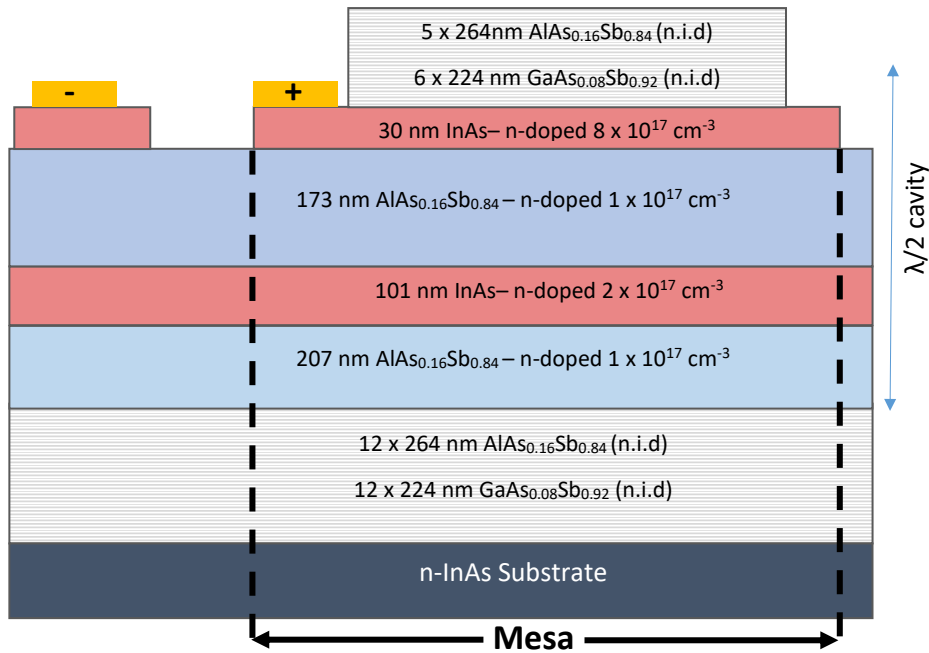


FIGURE 6.6: Structure of the fabricated RCE-PD designed to target the MWIR spectral region. The structure uses an InAs and AlAsSb nBn in the cavity, surrounded by two DBRs with GaAsSb/AlAsSb layers and an InAs substrate. The device mesas are defined by etching the contact layer at the top of the cavity.

100 nm is much higher than the 40 nm calculated for the SWIR RCE-PD in section 5.3. This is explained by a combination of factors. The lower absorption coefficient results in an increased absorber thickness required for the same single-pass attenuation. Also, the choice of lower reflectivity of the bottom DBR reduces the amplitude of the backwards travelling wave and reduces the resonant enhancement as a consequence. Higher single-pass attenuation is favoured as the resonant enhancement decreases, in other words, they are negatively correlated.

The calculations and considerations discussed in the first sections of this chapter are used to design a structure for fabrication and experimental testing. The fabricated structure is shown in figure 6.6. The lower part of the cavity includes a filler layer of AlAsSb, included to tune the optical path length of the cavity to half of the target wavelength. This layer is necessary for the absorber to be placed in the centre of the cavity, at the anti-node of the electric field.

The use of InAs as the contact layer has the benefit of not requiring a separate etch-stop layer. The ammonia based etchant used to etch the top DBR is selective between aluminium and gallium based alloys, which are etched, and indium based alloys, which are not measurably etched. This reduces the complexity of the growth and processing of the structure.

The structure is grown on an n-type (sulphur) doped InAs substrate by molecular beam epitaxy; full experimental procedure detailed in section 4.1. In the growth chamber the wafer first undergoes oxide desorption at 525 °C. The substrate temperature is reduced to 465 °C for growth of the epi-layers. An InAs buffer layer is grown first, followed immediately by the epi-structure shown in figure 6.6.

Post-growth the lattice-matching of the epitaxial layers is determined by high resolution x-ray diffraction measurements, detailed in section 4.2. Figure 6.7 shows the measured diffraction curve, overlaid with a modelled curve that is calculated using Bede RADS software. The compositions of the ternary alloys are adjusted within the modelled structure until a diffraction curve that matches the measured data is achieved. The substrate material is assumed to be tallest, narrow peak at about 30.4° and the two ternary alloys are the cause of the lower peaks either side. One of the alloys is slightly Sb-rich, indicated by the shoulder to the left of the substrate peak, but this is only a small lattice-mismatch as it is within ~ 100 arcsecs of the substrate. The second alloy has a higher mismatch of ≤ 200 arcsecs and is As-rich. It is difficult to determine which alloy corresponds to which peak from this plot alone, but from previous setup growths the presumption is that the AlAsSb is As-rich and the GaAsSb is Sb-rich. The model curve indicates that the likely compositions of the alloys are $\text{GaAs}_{0.075}\text{Sb}_{0.925}$ and $\text{AlAs}_{0.17}\text{Sb}_{0.83}$. These compositions are expected to have a critical thickness higher than the layer thicknesses in the structure and, therefore, the epi-layers are most likely strained.

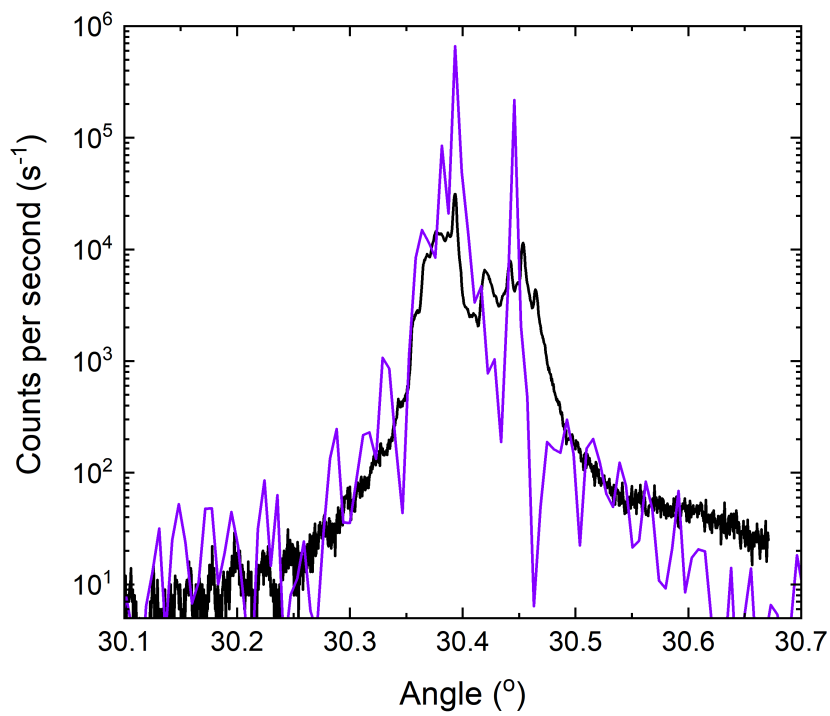


FIGURE 6.7: HR-XRD measurement of the fabricated MWIR RCE-PD (black). Modelled diffraction curve (purple). The highest peak is assumed to be the substrate material, InAs. The second peak on the right is caused by slightly As-rich AlAsSb at ~ 200 arcsecs from the substrate peak. The GaAsSb layers are the cause of the shoulder to the left of the substrate peak.

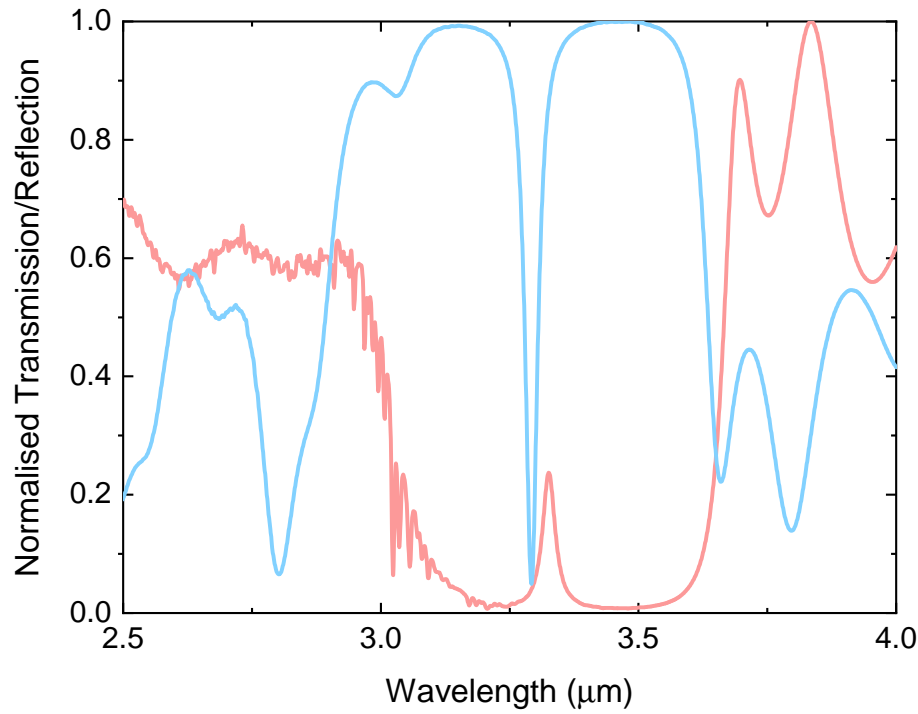


FIGURE 6.8: Normalised transmittance at normal incidence (red) and reflectance at 30° (blue) measurements on the epitaxial MWIR RCE-PD. The difference between the peaks at the resonant mode can be used to estimate the fraction of light that is absorbed in the structure.

6.4 Optical Properties

6.4.1 Transmittance and Reflectance

The transmittance spectrum is measured through the unprocessed epitaxial structure, including the substrate - described in section 4.4.1. The substrate attenuation is removed by using a background transmittance measurement with a piece of substrate in place. Figure 6.8 shows the room temperature transmittance spectrum. The noise on the curve is very high below $\sim 3.2 \mu\text{m}$, this is due to the high substrate attenuation below this wavelength reducing the flux incident on the spectrometer detector. Substrate attenuation is not an issue at higher wavelengths. The resonant mode is seen at a wavelength of $3.33 \mu\text{m}$, coinciding closely to the target wavelength of $3.3 \mu\text{m}$.

Also shown in figure 6.8 is the normalised reflectance spectrum at an angle of 30° on the top of the unprocessed sample. The measurement is carried out as described in section 4.4.2, with a background spectrum taken first with a highly reflect-

tive gold mirror in place of the sample. The reflectance curve is not affected by the substrate attenuation that hinders the transmittance measurement, because the light does not need to travel through it to reach the detector. The resonance wavelength determined by the reflectance spectrum is lower than the one seen in transmittance, values of 3.29 μm and 3.33 μm , respectively. This is caused by differences in the angles of the incident light, normal incidence for the transmittance and 30° for the reflectance. The dependence of the resonance wavelength with angle is due to differences in the distances the light has to travel through each layer; this is discussed in more detail in section 6.4.3.

As well as the wavelength of the resonance, it is also possible to use the combination of reflectance and transmittance measurements to approximate the maximum quantum efficiency possible from the sample. The power of the incident light has to all be accounted for, so the light that is absorbed by the structure can be calculated using

$$A = 1 - T - R, \quad (6.1)$$

where A is the fraction of absorbed light, T is the transmittance and R is the reflectance.

To more accurately calculate A the shift due to the angle of the reflectance measurement needs to be corrected for - in other words, the reflectance spectrum is shifted so that the resonance wavelengths of both spectra coincide. Due to differences in the two measurements the spectra have slight variations that make accurately estimating the QE spectrum using this method difficult, however, the single result for the maximum QE at resonance is more accurate. From the two curves plotted in figure 6.8 the estimated external QE is 70 %, this is the percentage of incident light that is neither reflected or transmitted. The normalised curves are used for this calculation, to reduce the influence on external factors, such as differences in the background measurements and the true background spectra (these factors cause impossible $> 100\%$ transmittance at certain wavelengths in the un-normalised spectra). It

is not ideal, but is likely to produce a more accurate result.

6.4.2 Responsivity/QE

The quantum efficiency can be more accurately determined through measurement of the spectral response, as described in section 4.4.3. To measure the response of the structure to incident light, the current through the absorption structure in the cavity is measured. An electrical circuit is created by etching the top DBR, evaporating metal contacts and etching to define the mesa, described in more detail in section 4.3.

The spectral response is measured using the light from the mid-infrared source of the spectrometer, directed onto a device that is wire-bonded onto a standard TO header package. The current measurement is converted into a voltage by a pre-amplifier, to allow the spectrometer software to be able to interpret it into an interferogram, which is converted into a responsivity spectrum by utilising a reference measurement from a commercial detector of known responsivity. Figure 6.9 shows the temperature dependent quantum efficiency of the fabricated MWIR RCE-PD. The QE at resonance varies significantly with temperature, monotonically increasing up to 350 K before decreasing slightly at higher temperatures. The highest measured QE of 65 % is lower than the value estimated by the transmittance and reflectance measurements, but that calculation does not account for any losses inside the device (internal quantum efficiency). It is worth noting that the spectral response of this InAs-based RCE-PD structure is not reduced at high temperatures in the same way as the SWIR RCE-PD presented in chapter 5. This is most likely due to the higher crystal quality of this sample, which has fewer defects and is less likely to have spectral response limited by the diffusion length as a result.

Below 200 K there is no resonant response as a result of the cutoff wavelength of the InAs absorber shifting to below the resonance wavelength. Observation of the low level broadband response also present in the spectral response measurements allows for the temperature dependence of the cutoff wavelength to be approximated. A shift from $\sim 3.70 \mu\text{m}$ to $\sim 3.35 \mu\text{m}$ between 375 K and 200 K demonstrates a decrease of 2 nm K^{-1} , shown in figure 6.10. The cutoff wavelength is of particular importance

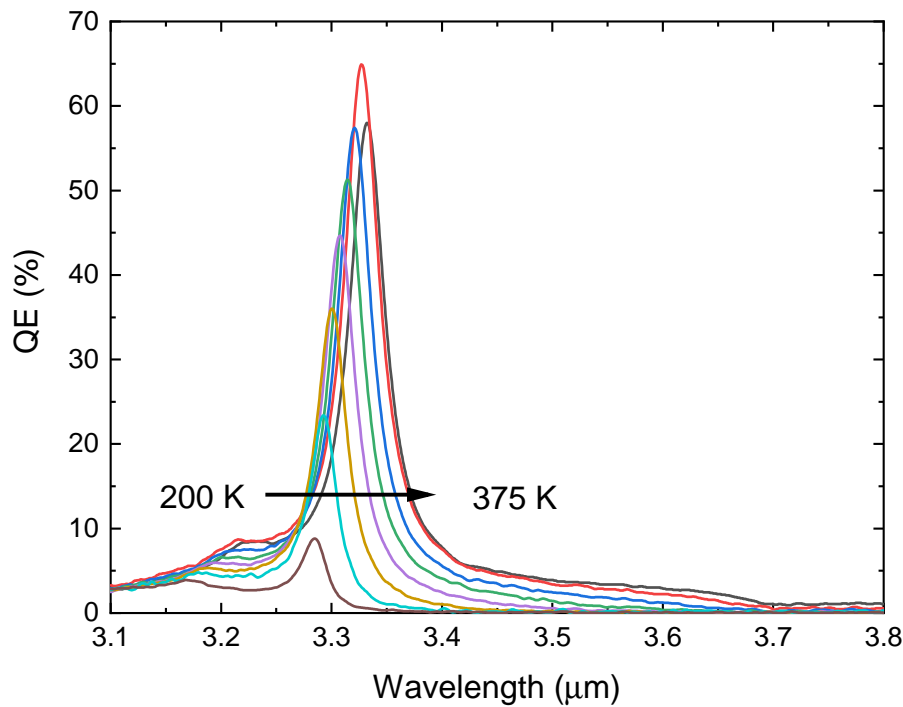


FIGURE 6.9: Temperature dependent quantum efficiency spectra for the RCE-PD. 25 K steps between 200 K and 375 K. A bias voltage of -0.3 V is applied across the device for all measurements. The resonance peak shifts slightly longer with increasing temperature.

for this structure because the target wavelength is close to the room-temperature cutoff wavelength. Therefore, the situation arises where the absorption of photons at the resonance wavelength decreases to zero at low temperatures. The flexibility of the RCE-PD design means that the thicknesses of the layers can be adjusted to change the resonance wavelength of future fabricated devices. An RCE-PD targeted at a slightly lower wavelength would not suffer from this problem.

The high temperature dependence of the QE is also possibly caused by the spectral positioning of the resonance wavelength close to the cutoff wavelength. The absorption coefficient of the InAs absorber decreases rapidly close to the band-edge, which decreases the overall absorption of the structure. A high quantum efficiency could be achieved with a low absorption coefficient, but it would require the DBRs to have higher reflectivities than is achieved with the 12 and 5 layers in used in the fabricated structure, 6.6. A thicker absorption layer could also be used to increase the total absorption. Both of these changes would only be suitable if the absorption coefficient is known to be low, if high reflectivity DBRs are used in conjunction with

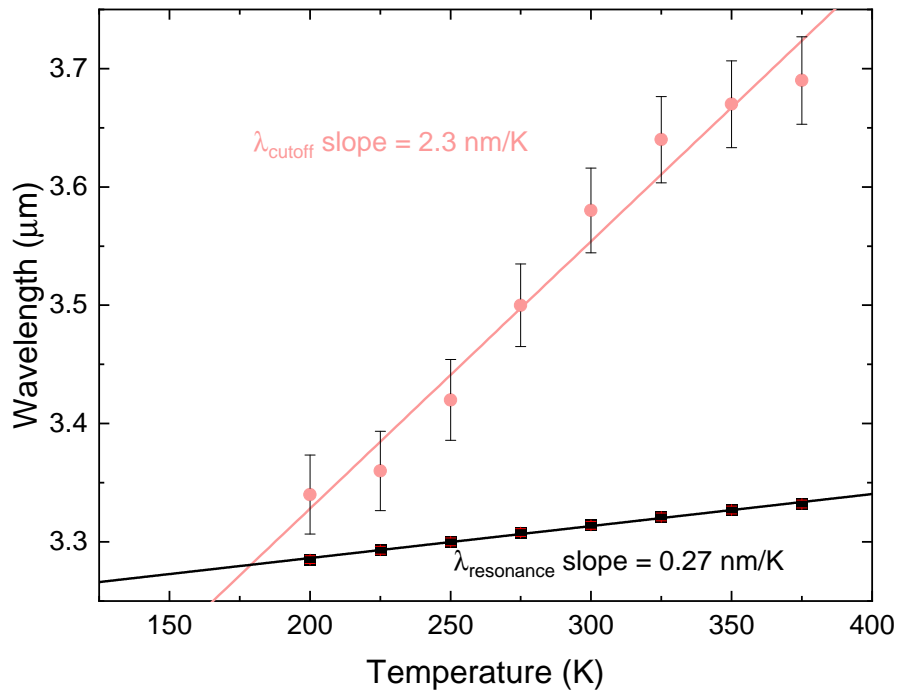


FIGURE 6.10: Temperature dependence of both the resonance wavelength (black) and cutoff wavelength of the InAs absorber (pink), for the MWIR RCE-PD. The resonance wavelength has a much lower temperature dependence than the cutoff wavelength, 0.27 nm/K and 2.3 nm/K, respectively.

a highly absorbing cavity then the resonant enhancement would be damped. For this reason, knowledge of the absorption coefficient of the absorber material at the target wavelength is important for precise structure design.

6.4.3 Resonant Peak

The amplitude (QE) and position (wavelength) of the resonance have been analysed, but the spectral bandwidth of the response is also a significant parameter for the intended spectroscopic sensing application of RCE-PDs. The width of the spectrum covered by the detector determines the specificity possible with the detector, *e.g.* can closely spaced absorption lines be distinguished? This is particularly pertinent to the RCE-PD targeted at $\sim 3.3 \mu\text{m}$ due to high concentration of common substances with absorption peaks nearby. One substance of particular interest with an absorption line in this spectral region is methane. The specific absorption line is due to vibrations of the C-H bond in the molecule; which is a bond shared with most organic compounds and as a result many other substances also have absorption lines

close to this wavelength. The precise wavelength of the absorption line is influenced by the rest of the molecular structure, so the lines do not coincide at the same wavelength. However, they are closely spaced, so a narrow spectral response is required to optically measure the absorption at a specific wavelength without interference from neighbouring absorption lines. As an example, there is some overlap between the absorption peaks of methane and ethane, but the ~ 30 nm spectral width of the RCE-PDs presented here could cover the absorption peak of one substance and a low absorption region for the second substance.¹ Careful control of the resonance wavelength would, however, be required.

The full-width half-maximum (FWHM) of the RCE-PD shifts with temperature, as shown in figure 6.11. The increase is not insignificant, between 200 K and 350 K the FWHM increases from 26 nm to 39 nm. Modelling of the RCE-PD structures suggests that the FWHM is linearly proportional to the resonance wavelength, which might be expected to cause the increase in FWHM. However, this is not the most significant factor, since the FWHM increases by $\sim 50\%$ compared to an increase in the resonance wavelength of $\sim 1.5\%$ over the measured temperature range. The two other factors that are most significant to the width of the resonance are the reflectivity of the DBRs and the cavity attenuation. Both of these factors do vary with temperature, and will be considered separately.

Firstly, the reflectivity of the DBRs varies most significantly due to the temperature dependence of the refractive indices of the constituent materials. Exact temperature dependencies of the refractive indices have not previously been extensively studied, but from the literature it is expected that the refractive index of GaAsSb will decrease with temperature at a faster rate than the refractive index of AlAsSb. So, the refractive index difference between the two materials will reduce at higher temperatures. The effect of these changes in refractive indices is that the DBRs are expected to be less reflective at higher temperatures, with a corresponding increase in FWHM. The spectral response of the structure is modelled with the expected temperature dependencies of the materials taken into account; temperature coefficients are approximated using values from the literature.^{62,64} The temperature coefficients of the refractive indices are approximated as single values, to give linear variations in the

refractive indices; the coefficient for GaAsSb used in the model is ~ 7 times higher than the coefficient for AlAsSb that is used.

Modelling of the shift of the resonance peak due to the temperature dependence of the refractive indices only shows an approximately linear increase in the FWHM with temperature of 0.019 nm K^{-1} , figure 6.11a. It is important to note here that the absolute value of FWHM coefficient is highly dependent on the structure, and the initial FWHM that is determined by the structure *e.g.* a structure with higher reflectively DBRs will have a lower temperature coefficient of FWHM, but a higher fractional variation in the FWHM. The measured temperature dependence of the FWHM does not demonstrate a single linear dependence, but rather two approximately linear variations at high and low temperature regions. A lower temperature dependence is seen at temperatures above 275 K and varies at approximately 0.036 nm K^{-1} , higher than the increase calculated due to variations in the refractive indices. Since the dependencies do not match, this indicates that either the refractive indices shift much more with temperature than expected, or they are not the primary factor causing the temperature shift of the FWHM.

The second factor that impacts the FWHM of the resonance peak is the attenuation in the cavity. Cavity attenuation is determined by two parameters, the thickness of the absorber and the absorption coefficient of the InAs epi-layers. The thickness does not vary significantly with temperature, by a fraction of less than $1 \times 10^{-5} \text{ K}^{-1}$.¹⁹⁸ The absorption coefficient varies much more significantly with temperature and is used here as a substitute for cavity attenuation (they are almost proportional). The exact absorption coefficient, and the temperature variation of it, is not known - precise measurements are outside the scope of this work. However, to determine the impact the absorption coefficient has on the FWHM the spectral response of the structure has been modelled with a range of absorption coefficients between 3000 cm^{-1} and 7000 cm^{-1} - this is the expected range around room temperature.

It can be seen in figure 6.11b that the FWHM shift above 275 K can be explained by a temperature dependence of the absorption coefficient of $18 \text{ cm}^{-1} \text{ K}^{-1}$. This is the variation necessary if the entire FWHM shift is due to the absorption coefficient,

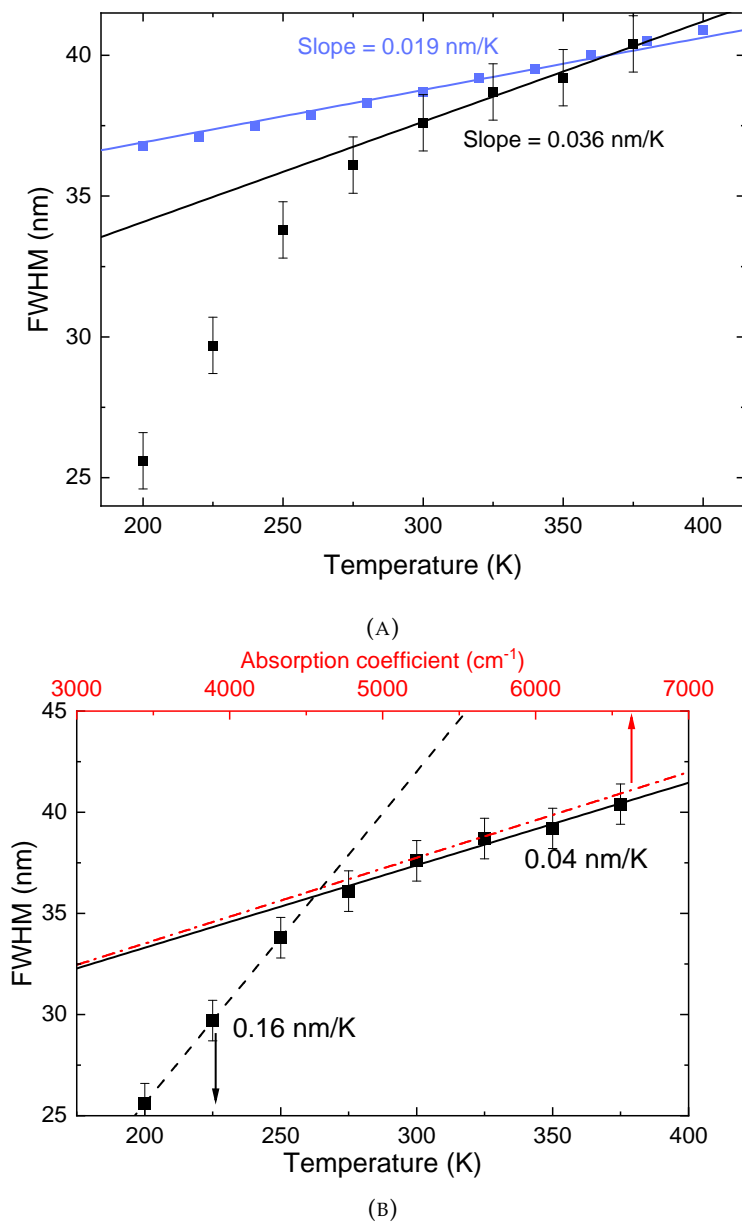


FIGURE 6.11: A) Measured FWHM (black) and modelled FWHM based on temperature dependent refractive indices (purple). The measured FWHM has a high temperature dependence below 300 K and a moderate dependence above. The dependence of FWHM on refractive indices is less than the measured dependence at all temperatures. B) Measured FWHM (black) and modelled FWHM dependency on absorption coefficient (red). The dependence of the absorption coefficient at the resonance wavelength with temperature is not well known, but the range of 3000 cm^{-1} to 7000 cm^{-1} is realistic. The dashed red line follows the high temperature dependence of the measured FWHM and represents a $\frac{d\alpha}{dT}$ of 18 $\text{cm}^{-1} \text{K}^{-1}$.

however, there is likely to be a significant minority contribution from the refractive indices of the DBRs. Below 275 K there is a much more significant shift in the FWHM. This is attributed to a high rate of change of the absorption coefficient as the cutoff wavelength of the absorber gets close to the resonance wavelength.

Considering the modelling of the FWHM dependence on both refractive indices and absorption coefficient it becomes clear there is scope for future structures to be designed to have specific bandwidths. If the various coefficients are known precisely, *i.e.* refractive indices and absorption coefficients, then a desired bandwidth could be designed through modelling of the structure. The number of DBR pairs were not considered in this section, because they can't be changed once a structure is fabricated, but they can also be used to control the bandwidth - along with the other factors. One crucial piece of understanding seen as a result of the modelling in this section is the significant decrease in FWHM for low attenuation cavities. Narrow bandwidths are desirable for many of the spectroscopic applications of this structure, so reducing the cavity attenuation to reduce the bandwidth is a consideration for future structures.

6.5 Electrical Properties

The electrical properties of the RCE-PD encompass the dark current, that is independent of the incident light, and the combined photocurrent and dark current properties that determines the signal-to-noise ratio and combined figures of merit.

6.5.1 Dark Currents

The dark currents are measured inside an opaque chamber, protected from thermally generated radiation by a surrounding cold shield. Therefore, the majority of the current measurement is from internally generated processes, with negligible contribution from photon generated currents. The temperature and bias voltage dependent current measurements, shown in figure 6.12, cover the expected range of use for the detector. At higher negative bias voltages the dark currents are higher, with no corresponding increase in photocurrent; a bias voltage of -0.3 V is an ideal compro-

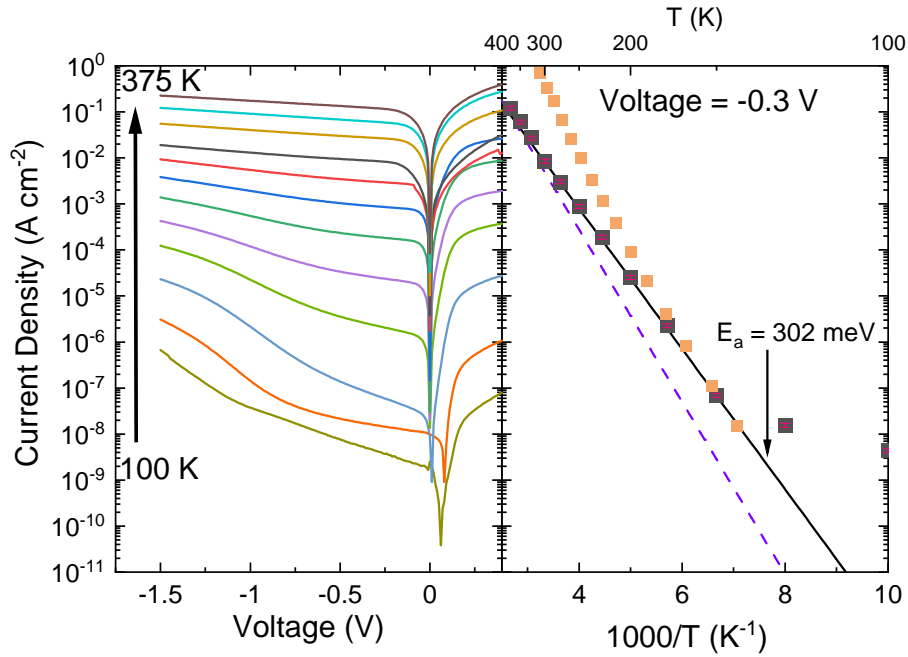


FIGURE 6.12: Left: Temperature dependent dark currents for the MWIR RCE-PD, between 100 K and 375 K, with 25 K steps. Right: Arrhenius plot derived from the dark current density with a bias voltage of -0.3 V (black). The black lines represents an activation energy of 302 meV. There are comparisons to Rule 07 (purple) and a conventional InAs nBn (orange).²⁵

mise between high responsivity and low dark current. The detector would not be expected to be used outside the temperature range measured. For low-temperature use, a thermoelectric cooler is the most likely choice, with a low temperature limit of ~ 180 K. At the other end of the temperature range a high ambient room temperature would be the most likely situation, which is well within the upper temperature of 375 K measured.

The Arrhenius plot in figure 6.12 shows the dark current measured with an applied bias voltage of -0.3 V. There are two distinct regions of the Arrhenius plot, with a crossover temperature of ~ 150 K. The higher temperature region has an activation energy of 302 meV, close to the room temperature bandgap of InAs of ~ 350 meV. This indicates a diffusion limited dark current, which has an activation energy equal to the bandgap of the absorber, and is expected for the nBn architecture used in the cavity structure. Below ~ 150 K the activation energy is much lower. However, the current at these temperatures is close to the noise floor of the sourcemeter, so the real activation energy cannot be determined.

Also included on the Arrhenius plot is a line denoting 'Rule 07'¹⁹² for a cutoff wavelength of 3.5 μm - the room temperature cutoff wavelength of the InAs absorber. 'Rule 07' estimates the dark current performance of the best Auger-1 limited MCT detectors and is the highest target for other material systems. It can be seen on figure 6.12 that the dark currents of the MWIR RCE-PD are similar to 'Rule 07' at high temperatures. The thinner absorber employed in the resonant cavity is expected to proportionally reduce the dark currents; previously reported InAs *nBn* detectors have dark currents orders of magnitude higher than 'Rule 07'.²⁵ The use of a thin absorber achieves a reduction in dark currents and with further refinement could exceed the target of 'Rule 07'.

6.5.2 Specific Detectivity

The peak specific detectivity of MWIR RCE-PD is plotted in figure 6.13 with both temperature and bias voltage dependence. The peak value, at the resonance wavelength, is the most useful figure to compare; for wavelengths outside the resonance the specific detectivity is very low - similar to the quantum efficiency spectrum. The general trend is a decrease in peak specific detectivity as temperature increases. This is the predominant trend expected in conventional detectors as well, due significantly to the increase in dark current with temperature. The responsivity of the MWIR RCE-PD also increase with temperature, up to 350 K, which increases the specific detectivity - but not enough to counteract the decrease in detectivity due to the dark currents. The shift of the two important factors, responsivity and dark currents, in opposite directions as temperature is increased does have the affect of reducing the variation of the specific detectivity. The highest value measured at 200 K of $8 \times 10^{10} \text{ cm}\sqrt{\text{Hz}}/\text{W}$ is less than an order of magnitude higher than the value measured at 350 K of $1 \times 10^{10} \text{ cm}\sqrt{\text{Hz}}/\text{W}$. This demonstrates that the fabricated device has high performance at both high and low temperatures, so could be incorporated into systems designed to work over a large range of temperatures. In comparison, commercial MCT detectors for sensing in this spectral region can achieve similar specific detectivities at room temperature of $3 \times 10^{10} \text{ cm}\sqrt{\text{Hz}}/\text{W}$,⁷³ and $1 \times 10^{10} \text{ cm}\sqrt{\text{Hz}}/\text{W}$.⁷⁵

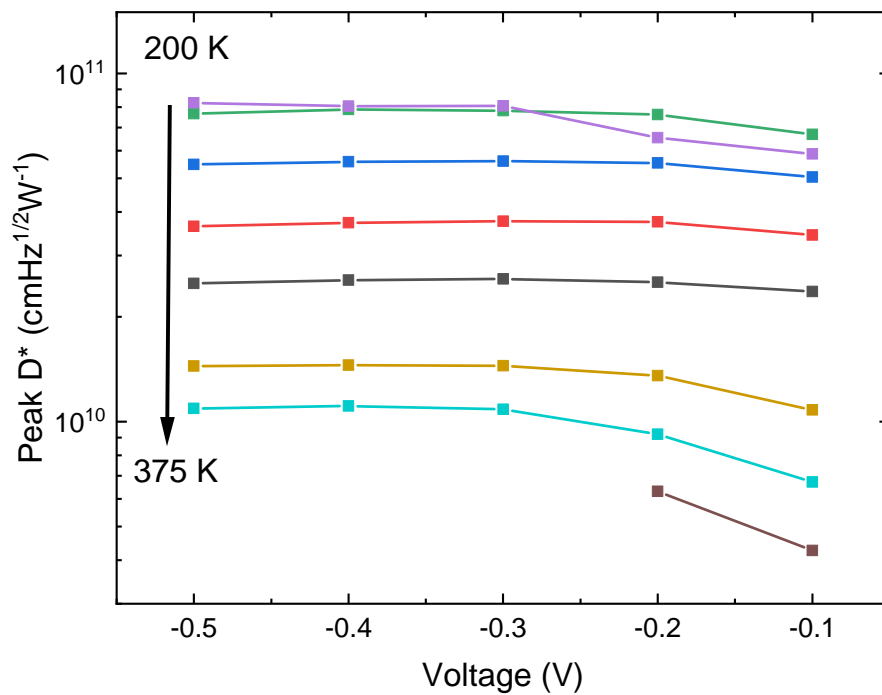


FIGURE 6.13: Peak specific detectivity measurements for the MWIR RCE-PD, using responsivity and dark current measurements. The specific detectivity decreases with temperature with an applied bias voltage of -0.3 V , but the different temperature dependencies of responsivity and dark current density result in a low temperature dependence of the specific detectivity.

6.6 Conclusions and Future Work

This chapter presents the design, fabrication and testing of RCE-PDs designed to sense at wavelengths in the mid-wave infrared, specifically the spectral band between $3.0\ \mu\text{m}$ and $3.5\ \mu\text{m}$ - to cover the absorption lines caused by C-H bond stretching vibrations. The fabricated sample is designed for a target resonant response at $3.3\ \mu\text{m}$, with an intended application of sensing the corresponding absorption line of methane.

The first section, 6.1, discusses the reasoning for the choice in cavity design. An InAs absorber is chosen for its appropriate bandgap (cutoff wavelength at $3.5\ \mu\text{m}$) and simple epitaxial growth. An AlAsSb barrier provides the ideal combination of high conduction band offset and low valence band offset. Section 6.2 analyses the material choices for DBRs lattice-matched to the InAs substrate. The use of two ternary alloys (AlAsSb/GaAsSb) increases the complexity of the DBR growth, but is the best compromise with the imposed lattice-matched constraint. The refractive index contrast of the two alloys is $\sim 20\%$ lower than the AlAsSb/GaSb DBRs used on GaSb substrates, requiring a higher number of layer repeats to achieve the same reflectivity. The full MWIR RCE-PD structure discussed in section 6.3 combines the InAs/AlAsSb *nBn* and AlAsSb/GaAsSb DBRs. The absorber thickness of $101\ \text{nm}$ is optimised based on the optical modelling of the structure and the number of repeats chosen for the DBRs.

Section 6.4 presents and analyses all the optical measurements performed on the sample; transmittance, reflectance and responsivity. The combination of reflectance and transmittance is used to estimate the light absorbed within the structure, with a value of 71% calculated (at $300\ \text{K}$). The external quantum efficiency at resonance is measured to be 52% , also at $300\ \text{K}$, indicating that a high proportion of the absorbed light is converted into the photocurrent. Below $200\ \text{K}$ no resonant response is seen, as a result of a shift of the cutoff wavelength of InAs to below the resonance wavelength. Future structures utilising an InAs absorber should take the temperature dependence of the cutoff wavelength into account to avoid the creation of a structure with no resonant response; this limits the cooled operation of this structure at

~ 3.3 μm .

The electrical properties of the MWIR RCE-PD are presented in section 6.5. The leakage currents get close to 'Rule 07' at room temperature and demonstrate up to two orders of magnitude improvement in comparison to previously reported InAs *nBn* photodiodes. The combination of low leakage currents and high responsivity result in a high signal-to-noise ratio, even at high temperatures. A maximum specific detectivity of $8 \times 10^{10} \text{ cm}\sqrt{\text{Hz}}/\text{W}$ is demonstrated at 200 K, and high temperature performance is demonstrated by a specific detectivity of $1 \times 10^{10} \text{ cm}\sqrt{\text{Hz}}/\text{W}$ at 350 K.

6.6.1 Future Work

The room temperature signal-to-noise of the fabricated sample is very good, but at lower temperatures the responsivity decreases and the leakage currents don't decrease as rapidly as 'Rule 07'. The activation energy is not as high as the bandgap, indicating the leakage currents are not solely limited by the Auger mechanism. Further refinements of the crystal growth, doping concentrations and fabrication processes should allow for the realisation of an Auger limited leakage current. This would reduce the leakage currents at lower temperatures and increase the maximum sensitivity possible.

The *nBn* structure in the cavity includes an InAs contact layer, that also functions as an etchstop during processing. Since this is the same material as the absorber it absorbs some of the light at the resonance wavelength and, therefore, reduces the power of the light absorbed in the absorber. Photons absorbed in the contact layer do not contribute to the photocurrent. It would be desirable to design a cavity that is transparent at the resonance wavelength other than through the absorber. InAs is used as the contact layer because the etchant used to go through the DBR is selective against it, and metallic contacts can stick well to the surface. Future contact layer materials need to ideally satisfy these two requirements, with a further requirement of a wider bandgap than the absorber.

One possible alloy for the contact layer is the quaternary AlInAsSb. Further testing

is required, but initial measurements have shown that this material isn't etched by MF319 if the composition includes 50 % indium and the bandgap is wider than that of InAs. However, this alloy is not as simple to grow as a high-quality crystal and would require an additional time-intensive calibration cycle to achieve appropriate lattice-matching to the substrate.

Chapter 7

Results III: Chirped RCE-PDs

This section presents a concept that was conceived as part of this work. The previous results sections, 5 and 6, focus on RCE-PDs targeted at specific single-wavelengths. During the development of these detectors the author's supervisor, Dr Andrew R. J. Marshall, formed the initial concept of chirped wavelength RCE-PDs. Led by the aspiration of multiple distinct single-wavelength RCE-PDs fabricated on a single wafer, the concept proposes a thickness gradient of the layers in the structure, to shift the resonance wavelength across the wafer. The concept and design is not seen previously in the literature and as such is considered to be the first implementation of this type. A patent has been applied for by Lancaster University on behalf of the author and supervisor under UK patent application number 2110690.1¹⁹⁹.

7.1 Theory and Purpose

The thicknesses of the layers in conventional detectors do not usually alter the spectral positioning of the response to incident light. The thickness of the absorber might change the amplitude of the response, the responsivity, but the shape of the spectrum is not dependent on the layer thicknesses. However, the behaviour of the spectral response of RCE-PDs is highly dependent on the layer thicknesses. The thicknesses of the DBR layers determine the spectral position and width of the stopband, the spectral band that is highly reflected by the DBRs. Similarly, the total thickness of the cavity influences the spectral position of the resonance wavelength. The combination of these layer thicknesses directly determine the wavelengths that produce

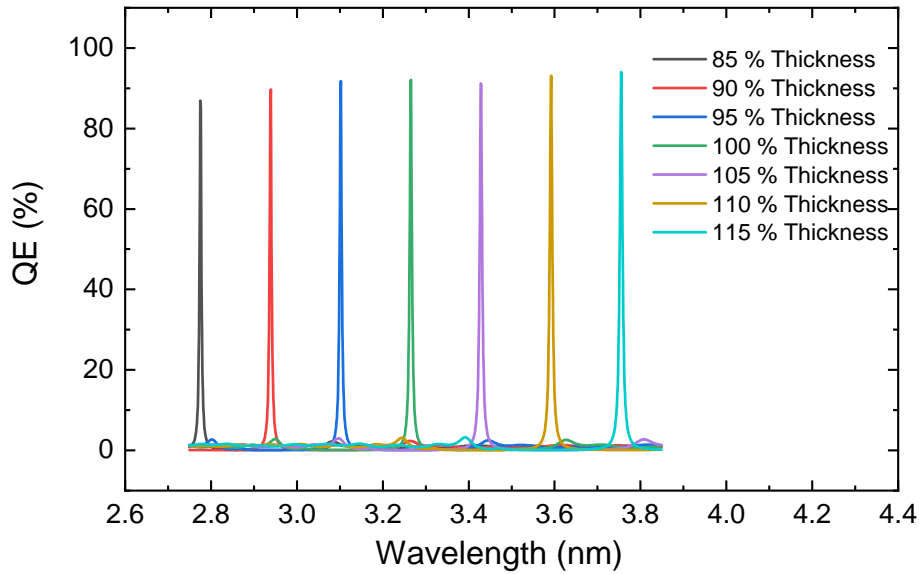


FIGURE 7.1: Modelled spectral responses of an example RCE-PD structure to demonstrate the dependence on layer thicknesses. All layer thicknesses are scaled equally in comparison to a nominal 100 % structure (green line). Layer thicknesses between 85 % (black line) and 115 % of the nominal structure are modelled (teal line).

a strong response and, importantly, the wavelengths that produce little or no response. To visualise the significance of the layer thicknesses, figure 7.1 shows the calculated spectral response of an RCE-PD with thicknesses of all the layers varied between 85 % and 115 % of a nominal design thickness. It can be seen that the resonance wavelength scales linearly with the layer thicknesses. The linear scaling is true when all layers are graded. Later in the chapter, in section 7.2.4, grading of the DBRs and cavity are treated separately and compared.

The significance of the thickness dependence is important for the design of single-wavelength RCE-PDs, to achieve a specific resonance wavelength the layer thicknesses of all the layers need to be carefully controlled during the growth of the structure. In many instances it is necessary to calibrate the exact growth times of the layers by conducting multiple growths of the same structure, to obtain the correct thicknesses of the layers. The concept of chirped RCE-PDs utilises the thickness dependence of the resonance wavelength to induce a shift of the resonance wavelength across the wafer; this is achieved by introducing a thickness gradient of one or more of the layers across the wafer.

The primary purpose of the resonance wavelength shift is the possibility of extracting more spectral information about incident light than is possible with a single-wavelength RCE-PD chip. The single-wavelength chips fabricated for the measurements in chapters 5 and 6 each have multiple separate devices on them. It would be possible to measure the photocurrent from multiple devices simultaneously, but this would not provide any more information about the incident light, since all the devices respond to the same wavelengths. Each device on a detector chip created from a chirped RCE-PD wafer has a slightly shifted spectral response compared to neighbouring devices, so the photocurrent measurement of each device will not be the same - depending on the incident spectrum. If the spectral response of each device along a linear array is known, then the measured photocurrents can be used to calculate the spectrum of the incident light.

Figure 7.2 demonstrates the principle of spectrum recreation using an array of RCE-PDs. The top plot shows the spectral response of 11 devices with a shift in resonance wavelength between each device - these spectral responses are created by increasing the thicknesses of half of the cavity layers in the structure. The bottom plot shows the QE of each device at $3.4\ \mu\text{m}$, along with a Gaussian fit of the points. The peak wavelength of each device is noted on the top x-axis. The blue line indicates the peak of the Gaussian fit and shows it corresponds to a resonance wavelength of $3.401\ \mu\text{m}$. This is a simple, idealised model, that demonstrates the ability of a linear array of RCE-PD devices to determine the wavelength of incident light of a single-wavelength. Of course, real incident spectra are likely to be much more complex - but this modelling demonstrates the concept using simple techniques and simple analysis. Real spectral responses of a fabricated array are also likely to be less uniform, in terms of QE and FWHM, but this can be accounted for in the data analysis - if these parameters for all pixels are measured beforehand.

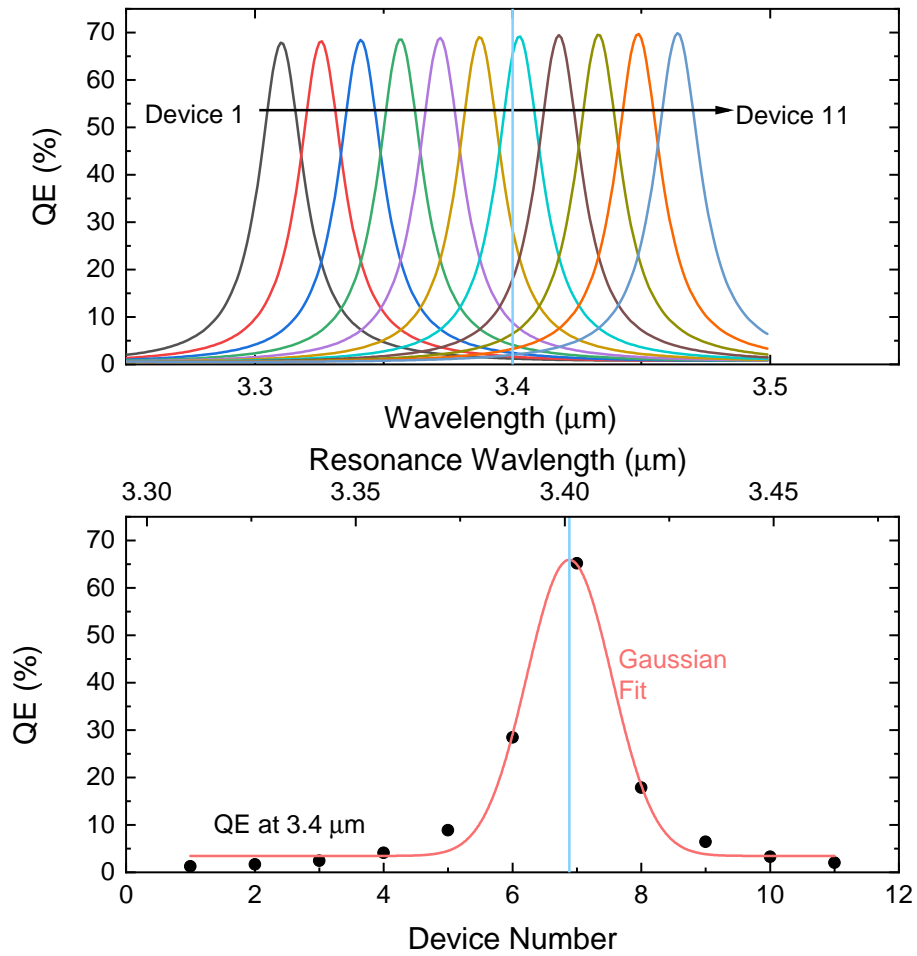


FIGURE 7.2: Top: theoretical spectral responses of 11 pixels. For simplicity the peak QE and FWHM are identical for all, but the resonance wavelength is shifted for each device. Bottom: calculated response of the same pixels due to monochromatic light with a wavelength of 3.4 μm . The response between each pixel varies, due to the shift in resonance wavelength.

7.2 Design Parameters, Considerations and Modelling

7.2.1 Epitaxial Chirp Method

The fabrication technique to create the thickness gradient is specific to the MBE method used to grow the epitaxial layers of the structure. Throughout the growth process the wafer is usually rotated to enhance the uniformity of the layer compositions and layer thicknesses across the wafer. To induce a thickness gradient the rotation is simply stopped. Without rotation the flux from the cells is not evenly distributed across the wafer and the rate of adsorption varies across the wafer, in one-dimension. Figure 7.3 demonstrates the path of the flux from a cell to the wafer. The path length from the cell to the wafer is not consistent for every point on the wafer ($l_1 < l_2$), this results in a flux intensity that is also not consistent across the wafer. The points on the wafer that are closer to the cell receive a higher flux of material and, therefore, the growth rate is higher. Since the wafer to cell distance varies approximately linearly across the wafer, the result is a growth rate that also varies approximately linearly across the wafer. Thus, the thickness variation is produced.

The diagram of the beam path in figure 7.3 shows the flux only for a single material cell in the MBE chamber. In a real system there are multiple cells, for each material. To grow a binary layer a beam of each of the two materials is required for the deposition of the layer. Growth of III-V binary materials, such as GaAs, GaSb and InAs require a flux of group-III molecules and also a flux of group-V molecules. The growth rate of the binary layer is controlled by the group-III flux. All the group-III atoms that impinge on the surface are incorporated into the layer - forming the binary material as long as there are enough free group-V molecules on the surface of the wafer. Conversely, the group-V atoms are only incorporated into the layer as part of the reaction of the group-III atom.²⁰⁰ The effect of this is that the group-V flux does not effect the growth rate of the binary layer, but the flux must be high enough to maintain group-V species on the surface of the wafer. An overpressure of group-V flux is usually used to achieve this. What this means for the growth of thickness graded binary layers is that the variation in thickness is determined by

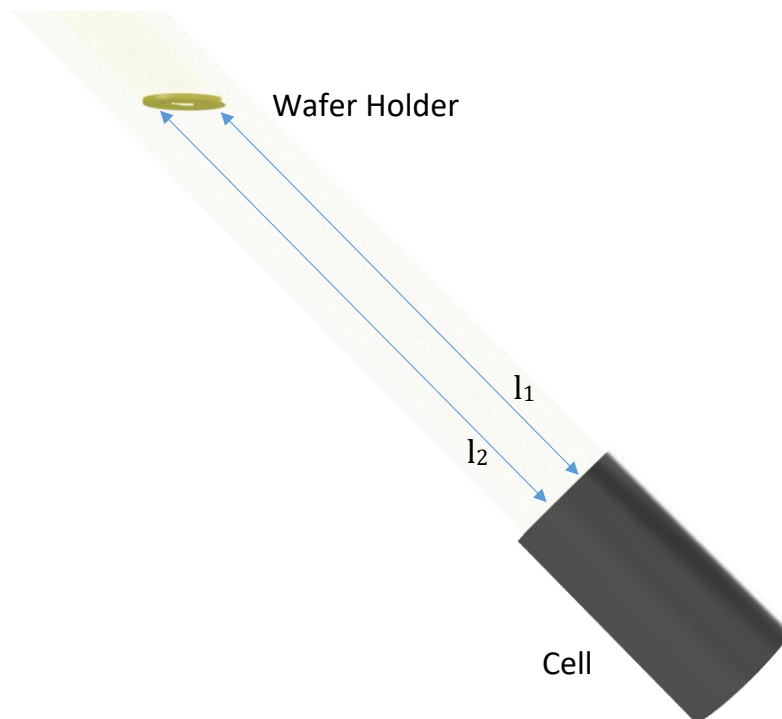


FIGURE 7.3: Visualisation of the inside of the MBE. Demonstrating the beam from a single cell onto the wafer. Without rotation, one side of the wafer is closer to the source cell (l_1) and one side is further from it (l_2). The flux onto the wafer is dependent on distance from the source cell, so if there is a distance variation, one side of the wafer receives a higher flux.

the differences in the group-III flux across the wafer. The only requirement of the group-V flux is that the pressure is high enough so that there is still an overpressure across the entire wafer.

The compositions of binary layers do not depend on the incident beam fluxes, however, the compositions of more complicated ternary and quaternary alloys are dependent on the ratio of the fluxes. For this reason, during growth of these materials without rotation the thickness will be graded, but also the composition will be graded. The size of the composition variation depends on the location of the cells and the dispersion of the beams. Composition variations that occur without wafer rotation presents a significant challenge to the inclusion of more complex alloys into the chirped RCE-PD design. For ternary alloys it is impossible to keep the entire layer lattice-matched without wafer rotation. Quaternary alloys could potentially be lattice-matched with a composition gradient, but for that to be achieved the positions of the cells would be important and the theoretical requirements are unlikely to be practically possible. The bandgap of the alloy would certainly change with the composition across the layer, which may also impact the characteristics and performance of the structure. For all alloys the compositional variations could be minimised by locating the necessary cells adjacent to each other on the growth chamber. This would be expensive, time-consuming and each alloy would require different cell locations. The remainder of this chapter is focused on the grading of binary layers only.

The variation in growth rate achieved by ceasing rotation of the wafer can be estimated. It is necessary to make certain assumptions that are likely to only be partially accurate and, also, the variation in growth rate will depend on the specifications of each individual MBE reactor. The first simplification is that the fractional variation in growth rate is equivalent to the fractional variation in group-III flux. This should be approximately true for a binary layer with an overpressure of group-V in the growth chamber. The variations in flux across a wafer is set out in the book '*Molecular Beam Epitaxy*'.²⁰¹ The variation in the intensity of the flux is dependent on cell to wafer distances. The calculations in²⁰¹ shows that for the specific distances chosen the flux intensity varies across a 50 mm wafer between ~ 28 and ~ 61 (arbitrary units). This

variation is larger than expected for the MBE used for this work. The Veeco GENxplor uses effusion cells that are angled towards the wafer, expected to reduce the flux variation. The flux variation depends on the dispersion of the molecular beam, which also depends on a number of factors that are not simple to calculate. The distribution of the melt in the cell and the formation of the beam are not constant over long periods of time. So, overall, calculations are not likely to match the experimental results - but the flux variation calculated in '*Molecular Beam Epitaxy*' is worth discussing. If their growth rate variations are achieved then the resonance wavelength could double across a 50 mm wafer, for a sample with graded thicknesses of all epi-layers. This highlights how significant this method could be for thickness grading.

The first step in designing an RCE-PD with graded layers is considering which layers to grade. The aim of grading the thickness is to shift the resonance wavelength, which is dependent on the thicknesses of the DBR layers as well as the total cavity thickness. The limitation of grading only binary layers represents the most significant consideration. At least one of the DBR materials is a ternary alloy, for the structures presented in this work, which cannot be thickness graded easily. Also, the majority of the cavity thickness in the structures presented in chapters 5 and 6 are ternary and quaternary alloys. Thickness grading of layers in the cavity and the DBRs will be considered separately first, based on the fabricated design used in 5 - reprinted in figure 7.4.

7.2.2 Cavity Only Thickness Gradient

The cavity in the non-graded design does not contain any binary alloy materials. The solution is simply to include an extra layer of GaSb in the cavity, beneath the lower AlAsSb - as shown in figure 7.4. In an ideal structure the total optical path length of the cavity is a multiple of half the target wavelength, λ , so a thicker cavity can be used to accommodate the extra GaSb layer, as long as this condition is followed. The impact of variations of the cavity GaSb layer thickness on the optical properties of the structure have been modelled. The most significant factor of interest is the coefficient of the shift of the resonance wavelength per percentage thickness change.

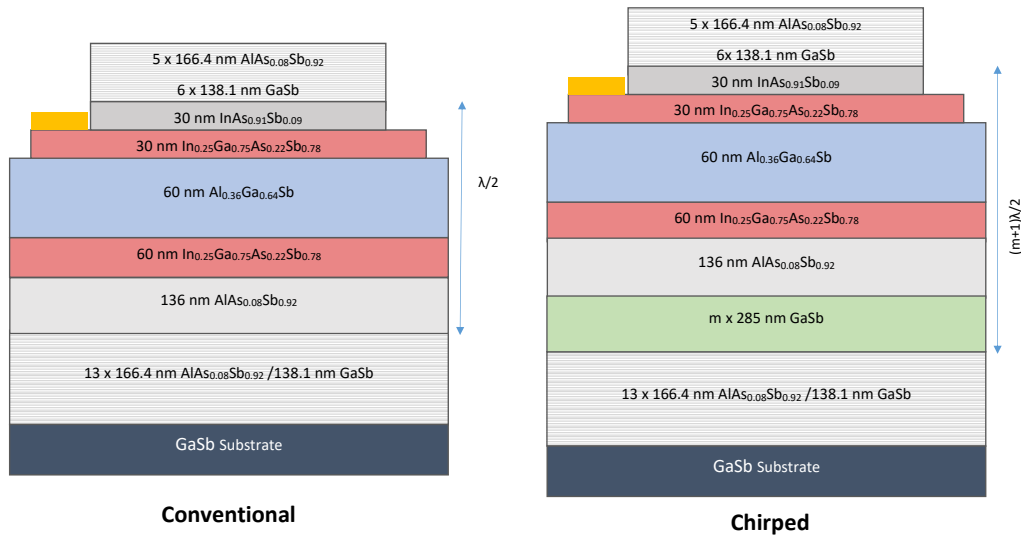


FIGURE 7.4: Left: conventional SWIR RCE-PD, the structure presented in chapter 5. Right: thickness graded cavity SWIR RCE-PD. The graded structure is almost identical to the conventional RCE-PD, but contains an additional layer in the cavity that is thickness graded. This also results in a thicker cavity, $m\lambda/2$, where $m \geq 2$.

Figure 7.5 shows the dependence of the resonance wavelength on the optical path length of the cavity. The data is presented as a dependence on two factors. First, the designed optical path length of the GaSb layer in the cavity, as an integer number of $m\lambda/2$, where each line is different value of m . Secondly, the fractional thickness of the GaSb layer *i.e.* the designed thickness multiplied by a percentage. The plot shows that, as expected, a thicker graded layer in the cavity results in a higher coefficient of chirp of the resonance wavelength. In other words the higher the proportion of the cavity that is graded, the bigger the shift of the resonance wavelength. Increasing the thickness of the cavity, *e.g.* to λ or $3\lambda/2$, does introduce extra anti-nodes that do not coincide with the absorber. However, this should not significantly affect the performance of the device. Assuming that the added thickness does not absorb significantly at the resonant wavelength and the absorber is not moved from the centre of the top $\lambda/2$.

Figure 7.5 also shows that there is a maximum shift in the resonance wavelength that is possible. The reason for this comes back to optical path length of an ideal cavity, which is a multiple of $m\lambda/2$. When the thickness of the GaSb varies too much then the total optical path length of the cavity is closer to the next multiple of $m\lambda/2$, and

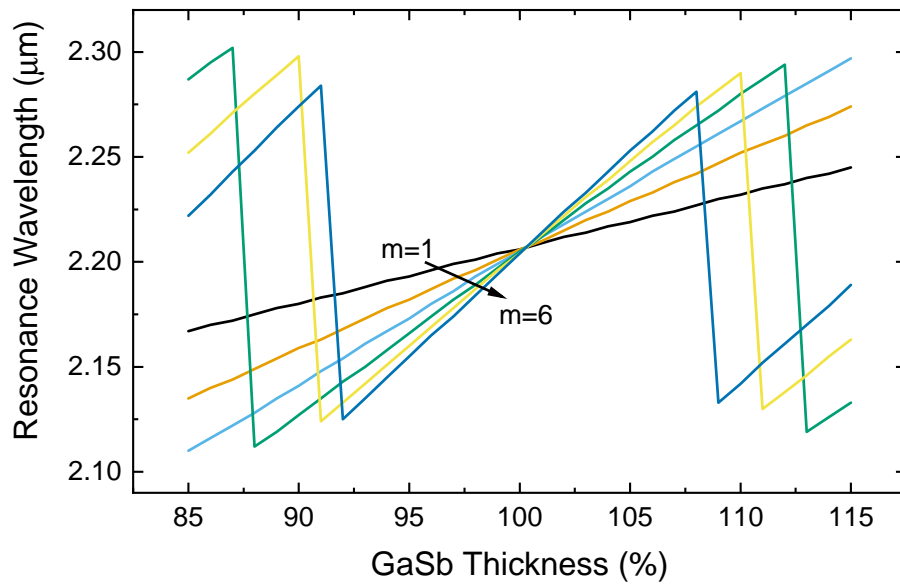


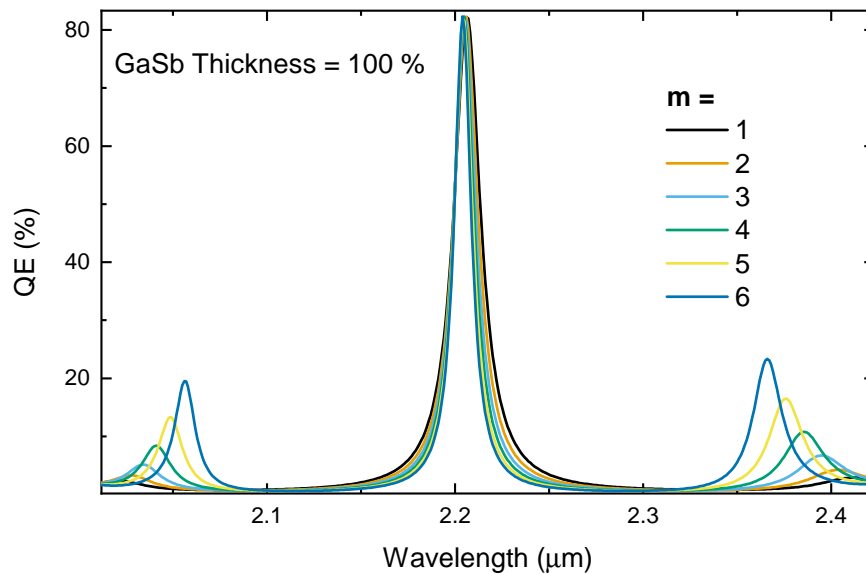
FIGURE 7.5: Modelled dependence of the resonance wavelength on both design cavity optical path length, between $m = 1$ and $m = 6$ in $m\lambda/2$, and the thickness variation of the cavity GaSb layer between 85% and 115% of the design thickness. For $m = 1, 2, 3$ the variation in the GaSb thickness results in a corresponding linear change in the resonance wavelength. For $m = 4, 5, 6$ small variations in the GaSb thickness results in a linear change in resonance wavelength. However, larger variations in the GaSb thickness also contain a step change in the primary resonance wavelength at the point when the neighbouring resonance peak is closer to the ideal for the cavity thickness, *i.e.* the cavity thickness is closer to $(m \pm 1)\lambda/2$ than $m\lambda/2$.

the highest peak is then determined by the difference between that multiple and the actual optical path length. It is also shown that as higher values of m are used for the cavity optical path length the maximum possible shift of the resonance decreases. This is because the free spectral range ($\Delta\lambda_{FSR}$) - the optical spacing of the resonance peaks - is inversely proportional to the optical path length of the cavity (l_{cav}). The free spectral range varies by

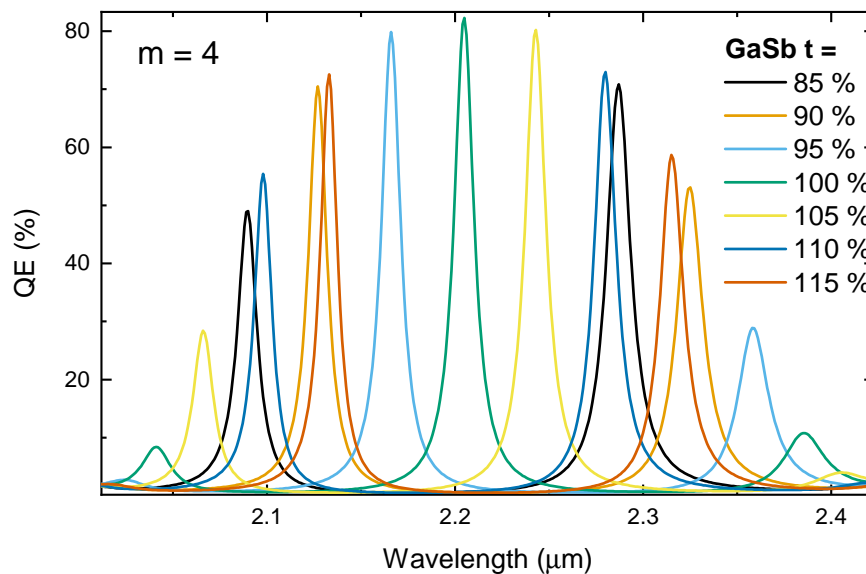
$$\Delta\lambda_{FSR} \propto \frac{\lambda^2}{l_{cav}}, \quad (7.1)$$

where λ is the wavelength of incident light. A lower free spectral range (FSR) also results in more than one resonance peak within the spectral stopband of the DBRs. The $\lambda/2$ cavity optical path length used in the non-graded structures gives the highest possible free spectral range and the peaks neighbouring the central resonance are further away than the edge of the stopband. Therefore, these wavelengths of light are not transmitted into the cavity. The higher optical path length cavities modelled in figure 7.5 cause a reduction in the free spectral range that results in neighbouring peaks that are within the stopband of the DBRs. Therefore, the spectral response of these structures contain multiple peaks, as shown in figure 7.6. All the modelled spectra are for the graded structure, shown in figure 7.4, only with variations in the thickness of the cavity GaSb layer. The thickness variations are considered in two ways. The first, shown in figure 7.6a, demonstrates the impact of increasing the cavity thickness - but keeping the total cavity optical path length (l_{cav}) matched to the optical path lengths of the DBR layers (l_{DBR}). That is $l_{cav} = 2l_{DBR}(m + 1)$, where m is a positive integer. This shows that as m increases, the FSR decreases and the amplitudes of the minor resonance peaks increases. So, even when all the layer thicknesses perfectly match to the same target wavelength the thicker cavity causes the minor peaks to become more significant. The presence of these peaks is not ideal for highly spectrally specific measurements.

The variation in GaSb thickness is also considered in the way that the thickness gradient across a wafer would cause. In this case the optical path lengths of the cavity and DBRs do not match consistently, $l_{cav} \neq 2l_{DBR}(m + 1)$ for all GaSb thicknesses,



(A)



(B)

FIGURE 7.6: A) Modelled QE spectra for SWIR RCE-PD structures with cavity optical path lengths between λ ($m = 1$) and $7/2\lambda$ ($m = 6$). The secondary peaks become slightly more prominent with increasing cavity thickness. B) Modelled QE spectra for SWIR RCE-PD structures with a design cavity optical path length of $5/2\lambda$ and variations of the thickness of cavity GaSb layer between 85% and 115% of the design thickness. The secondary peaks become much more prominent with variations in cavity thickness away from the ideal design thickness.

other than 100%. This modelling shows the effect of grading only the cavity layers on the spectral response. Figure 7.6b shows the spectral response for multiple thicknesses of the cavity GaSb layer, with a central cavity optical path length thickness of $5/2\lambda$ ($m = 4$). The GaSb cavity layer thickness is varied as a fraction of the thickness necessary to create this cavity optical path length. When the cavity optical path length matches the path lengths of the DBR layers there is a high amplitude major resonance peak and two much smaller minor resonance peaks. The minor peaks are much more significant as the thickness of the GaSb layer shifts away from ideal - the minor peaks are more than half the amplitude of the major peaks at certain thicknesses. The resonances are still narrow spectral bands, but the presence of two in the spectral response reduces the spectral specificity of the detector. For these reasons the total cavity optical path length should be kept as short as possible, whilst fulfilling the wavelength matching condition. It should also be noted that it would still be possible to create a spectrometer out of an array of RCE-PDs with two significant resonances. With more complex post processing it is possible to distinguish the wavelength of incident light from an array with overlapping multiple resonances.²⁰² However, a single resonance is still preferable for simpler and more robust post processing.

7.2.3 DBR only Chirp

This section describes and analyses the impact on the spectral response of grading the DBR layer thicknesses. The same initial structure is used as section 7.2.2, but the chirped structure is different. The total optical path length of the cavity is half the target wavelength, $\lambda/2$, and does not contain a chirped GaSb layer. Instead, the GaSb layers in both DBRs are chirped - figure 7.7.

In an ideal RCE-PD the optical path lengths of the DBR are a quarter of the target wavelength, $l_{DBR} = \lambda/4$. By varying the thickness of one of the DBR layers only, this condition will not be met exactly across the whole wafer. However, the total thickness of each layer pair (AlAsSb + GaSb layers) is the same for every repeat in both DBRs at each position on the wafer, *i.e.* the thickness variation is approximately the same for each repeat. The DBRs can tolerate some optical path length

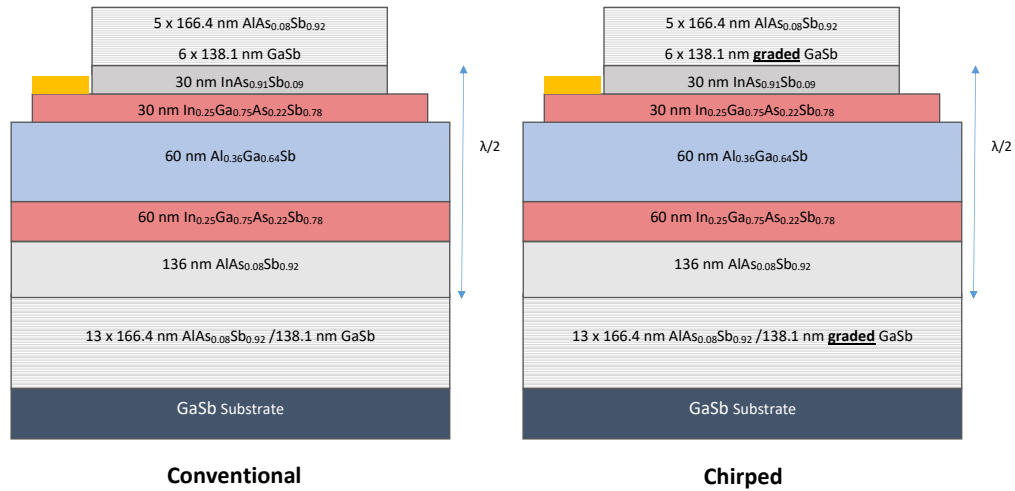
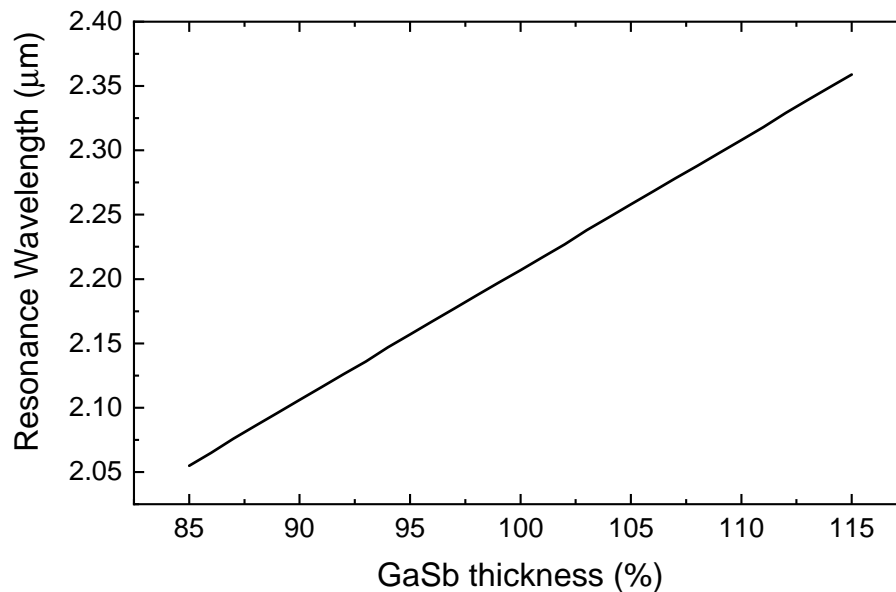


FIGURE 7.7: Left: conventional SWIR RCE-PD, the structure presented in chapter 5. Right: thickness graded DBR SWIR RCE-PD. The graded structure is almost identical to the conventional RCE-PD, but the GaSb layers in the DBR are graded in thickness. The cavity thickness is $\lambda/2$ for this structure.

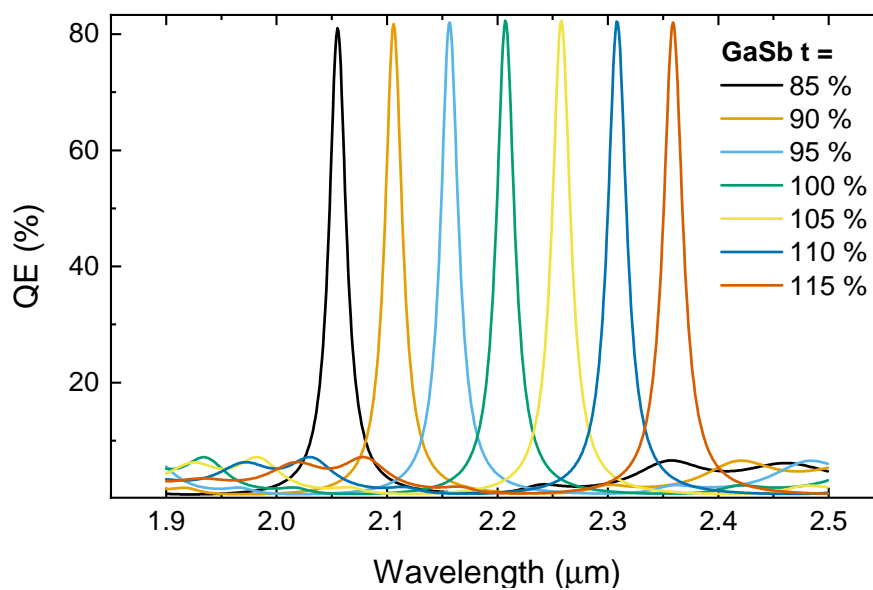
mismatch between the two layers, with only negligible reduction in reflectivity - and therefore device performance. Variations of up to 40 % have been modelled without significant reflectance reduction. Therefore, grading only one layer does not hinder development of high-performance devices. However, it is important to note that low thickness variation, $< 5\%$, between the repeats in the DBRs is necessary.

Figure 7.8a shows the resonance wavelength as a function of DBR GaSb layer thickness, labelled as a percentage of the design thickness. Similar to the cavity only chirp, the resonance wavelength is linearly dependent on the thickness of the GaSb layers. However, within $\pm 15\%$ of the ideal thickness there is no limit to the shift of the resonance wavelength. The limit to the shift is much higher, because the thickness of the cavity does not change - and so, the free spectral range does not change. Therefore, there is only one significant resonant peak for GaSb thicknesses of less than $\pm 15\%$ of the design thickness.

Figure 7.8b shows the spectral response of the thickness graded DBR structure for various thicknesses of the GaSb layers in the DBRs. The minor resonant peaks are not significant and much lower than the minor peaks caused by only grading the thickness of the cavity. So, grading the thickness of the DBR layers only does not



(A)



(B)

FIGURE 7.8: A) Modelled dependence of the resonance wavelength on thickness of the GaSb layers in the DBRs. The variation in GaSb thickness results in a linear variation in resonance wavelength across the entire range. B) Modelled QE spectra for structures with DBR GaSb layer thicknesses between 85% and 115% of the design thickness. The shape and amplitude of the QE spectrum does not change significantly and the amplitude of the secondary peaks does not increase significantly either. The shift in resonance wavelength is the only notable effect.

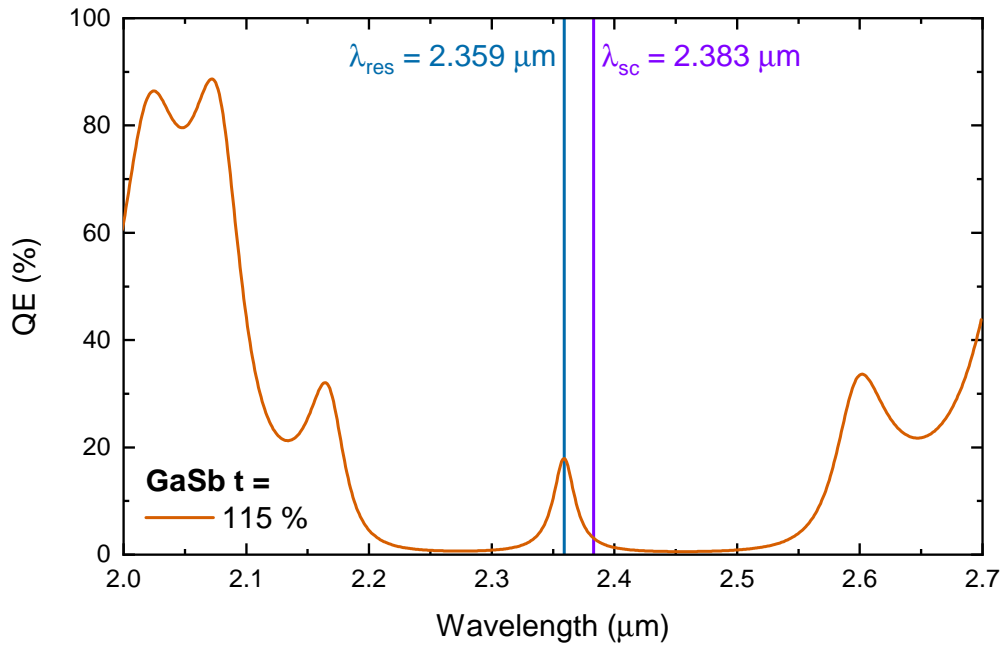


FIGURE 7.9: Modelled transmittance spectrum of a SWIR RCE-PD with thicker optical path lengths of GaSb layers in the DBR. The optical path lengths of the GaSb layers are $1.15\lambda/4$, away from the ideal $\lambda/4$. Even 15% higher than ideal thickness only results in a shift of the resonant mode (teal line) of 24 nm away from the centre of the stopband (purple line).

cause the same problem as grading the cavity thickness only. However, since the cavity optical path length is constant, the centre wavelength of the DBR stopbands (λ_{sc}) do not line up with the cavity optical path length across the entire wafer. That is $2l_{cav} \neq \lambda_{sc}$. This is best understood through analysis of the transmittance spectrum - figure 7.9. This shows that the resonance mode, λ_{res} , does not line up with the centre of the stopband when the optical path lengths of the cavity and DBRs do not match. In other words, the spectral shift of the resonance does not match the spectral shift of the stopband, as the DBR layer thicknesses are varied.

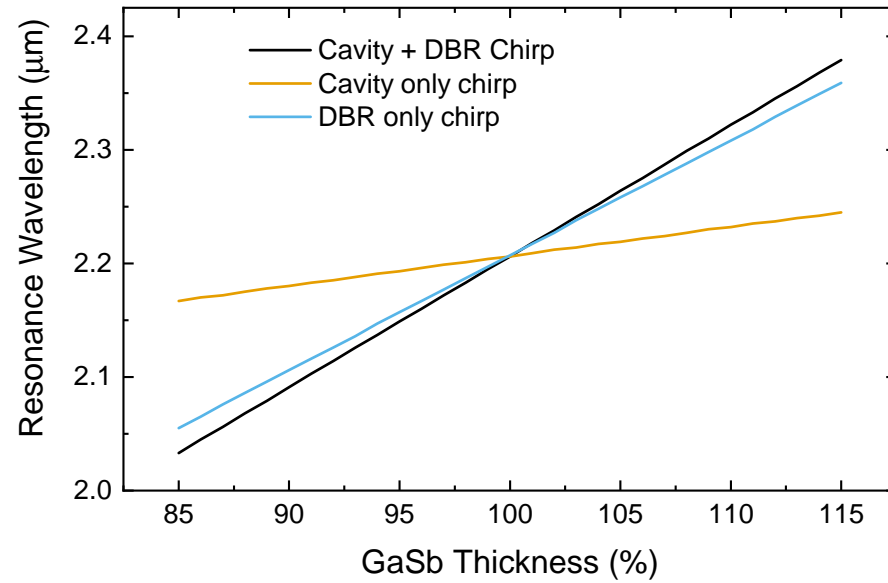
7.2.4 Cavity and DBR Chirp

One solution to keep the resonance mode centred in the stopband is to grade the thickness of both the DBRs and the cavity simultaneously. Changing the thickness of a layer in the cavity so that the optical path length of the cavity is an exact multiple of the optical path length of each DBR layer pair *i.e.* $l_{cav} = n(l_{DBR-1} + l_{DBR-2})$, where l_{DBR-1} is the thickness of the DBR GaSb layers and l_{DBR-2} is the thickness of the DBR

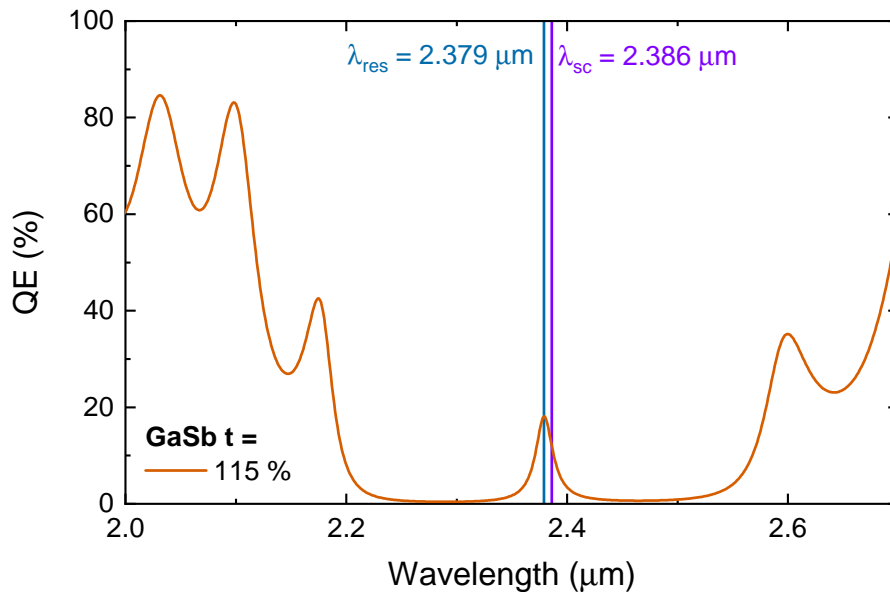
AlAsSb layers. This is achieved by grading the thickness of layers in the cavity that equate to half the optical path length of the cavity, while simultaneously grading the thickness of the GaSb layers in the DBRs. To avoid the significant minor resonance peaks caused by thicker cavities, demonstrated in figure 7.6a, it is preferable to keep the cavity optical path length as either $1/2\lambda$ or 1λ . Grading both cavity and DBRs simultaneously also increases the coefficient of shift of the resonance wavelength per change in growth rate.

Figure 7.10a compares the resonance wavelength shift as a function of percentage GaSb thickness. Only grading layers in the cavity shifts the resonance wavelength between 2167 nm and 2245 nm over the range of GaSb thicknesses of 85 % and 115 %, $\Delta\lambda_{res} = 78$ nm. Over the same thickness range, only grading the layers in the DBR shifts the resonance wavelength between 2055 nm and 2359 nm, $\Delta\lambda_{res} = 304$ nm. Simultaneously grading the cavity and DBR shifts the resonance wavelength between 2033 nm and 2379 nm, $\Delta\lambda_{res} = 346$ nm. So, it can be seen that the thickness variation of the DBR layers is the majority contributor to the shift of the resonance wavelength. However, while the cavity thickness variation might only contribute slightly to the shift of the resonance it is necessary for the resonance to be approximately centred in the stopband at all GaSb thicknesses.

Overall, this section has discussed the impact of grading the thickness of certain layers on three parameters - the resonance wavelength, the amplitude of minor resonance peaks and the spectral position of the resonance in the stopband. The shift of the resonance wavelength determines the width of the spectral band that can be covered by devices on a single wafer, in other words, how much of the spectrum a single linear array can sense. It is also necessary to understand the amplitude of the minor peaks, as they will impact how the devices respond to incident light, which is especially important for the spectrally specific measurements that the arrays are intended for. If there are multiple significant peaks it is not possible to equate each pixel to a specific wavelength - as shown in figure 7.2. Finally, control of the shift of the resonance within the stopband is desirable. At higher thickness variations the optical path lengths of the cavity and DBRs will not match, indicated by the resonance wavelength positioning closer to the edge of the stopband. This causes a reduction



(A)



(B)

FIGURE 7.10: A) Modelled dependence of the resonance wavelength on thickness of the GaSb layers. A nominal 1λ thick cavity is used for both cavity only and cavity + DBR chirped calculations. A $1/2\lambda$ thick cavity is used for DBR only chirped calculations. Grading the DBRs causes a much larger variation in the resonance wavelength in comparison to grading the cavity. B) Modelled transmittance spectrum for the SWIR RCE-PD structure with the half of the cavity thickness graded and the DBRs scaled by 115% of the design thickness. The combination of DBR and cavity grading results in a only a very small shift of the resonant mode (teal line) away from the centre of the stop-band (purple line) of 7 nm.

in the resonant enhancement effect and, therefore, a reduction in the light coupled into the cavity. Small variations do not appear to cause significant reductions in the quantum efficiency, but larger variations are expected to reduce the measured QE. Large variations can be avoided by matching the optical path lengths of the cavity and DBRs, demonstrated by the central positioning of the resonant mode in figure 7.10b. The combined thickness grading of both the cavity and DBRs ensures that the QE will be high across the entire wafer. The analysis of the modelling discussed in this section can be used to form a set of good design practices for chirped RCE-PDs (assuming high wavelength shift, single peaks are desired):

- Only binary layers should be graded.
- Total cavity optical path length should be no more than the design wavelength, $l_{cav} \leq \lambda$.
- The fraction of the cavity optical path length that is graded should match the fraction of the DBR optical path length that is graded.

7.3 Experimental Results for InGaAsSb RCE-PDs

This section presents the experimental results for fabricated chirped RCE-PDs. Multiple test wafers were fabricated as part of this work. Initial testing involved grading the thickness of the cavity only, which results in either small shifts in the resonance or multiple significant resonant peaks. The shift in the resonance wavelength is determined through transmittance measurements at a series of positions on the wafer, as described in section 4.4.5. The resonance wavelength is extracted from the spectrum at each position and a 2D colourmap is created from the results.

Since these samples utilise a novel growth technique and structure designs with significant variations compared to the single-wavelength RCE-PDs it is expected that initial attempts will require further refinement. Each sample is presented in order of growth, as the subsequent designs are refined based on previous results.

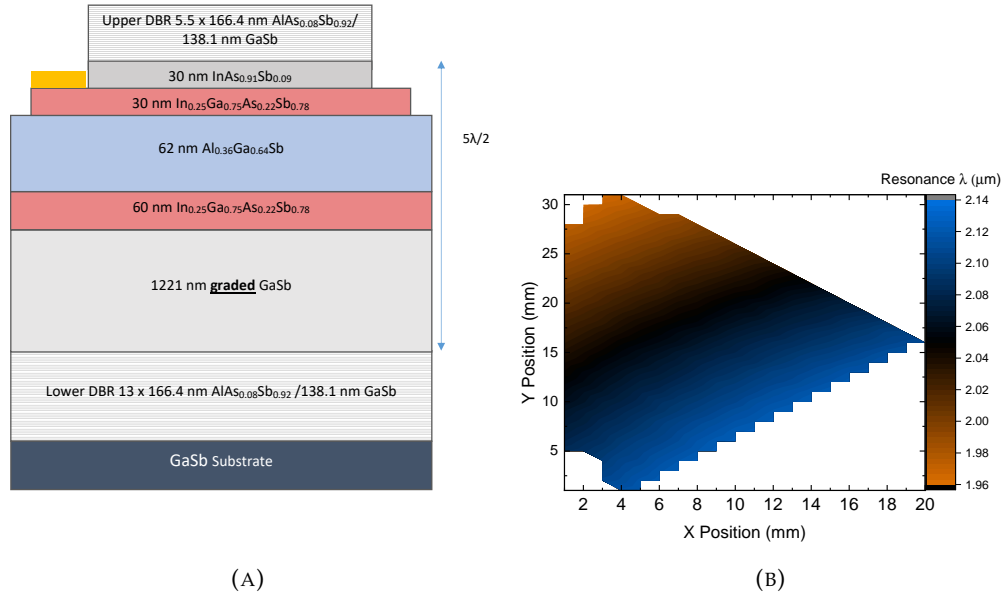


FIGURE 7.11: A) Structure of the first chirped RCE-PD attempt (XAC1076). The structure is comparable to the one presented in chapter 5, with an increased cavity thickness of $5\lambda/2$. B) Colourmap of the resonance wavelength across XAC1076. There is a clear one-dimensional variation in the resonance wavelength across the wafer.

7.3.1 Chirped Cavity Only Samples

$5/2\lambda$ Cavity - Attempt 1

The very first sample copies the structure presented in chapter 5, with the key difference of swapping the AlAsSb cavity buffer layer for a thicker GaSb layer that is graded during growth - figure 7.11a. The rotation is stopped during the growth of this layer only. A quarter of a 2-inch GaSb substrate is used and the growth of the sample follows the steps set out in section 5.3.1, with the exception of the rotation pause during the cavity buffer layer growth. Everything else is identical to the single-wavelength SWIR RCE-PD.

The parameter of most interest is the resonance wavelength and the spatial dependence of it across the wafer. The colourmap in figure 7.11b shows the 2D variations of the resonance wavelength. The resonance only significantly varies in one-dimension, as expected. The coefficient of resonance wavelength chirp per unit length is ~ 6.8 nm/mm across the wafer.

5/2 λ Cavity - Attempt 2

Results for a second structure with a 5/2 λ cavity optical path length are shown in figure 7.12. The sample, labelled XAB1229, is grown on a 2-inch GaAs substrate - the larger wafer is used to increase the total chirp in comparison to the first attempt. The epitaxial growth utilises an interfacial misfit array²⁰³ (IMF) immediately below the structure layers, which are lattice-matched to GaSb. GaAs has a shorter cutoff wavelength than GaSb, so this substrate is used to reduce attenuation through the substrate in the spectral band of interest. This reduces the noise in transmittance measurements. The structure is based on the same one used for attempt 1; the most significant changes are the substrate material and use of the IMF array. The thickness graded layer in the cavity has the same optical path length of 2 λ and is the only layer that is graded in this sample.

The sample is fabricated by MBE using the techniques described previously, in sections 4.1 and 5.3.1. A GaAs buffer is grown as the first epilayer, followed by the IMF and a GaSb buffer layer. The rest of the structure is grown in the same way as the conventional SWIR RCE-PD, with the exception of the graded GaSb layer. For this layer the rotation is stopped, with the angle chosen so that the thickness would be graded along the chosen axis.

The structure is designed with a thick cavity and is grown on a whole 2-inch wafer in an attempt to maximise the shift of the resonance wavelength. However, as a result of the thick cavity used in this structure there are two significant resonance peaks seen in the spectral responses across the majority of the wafer; spectral response measurements for a few pixels are shown in figure 7.12. Significant minor peaks are seen in all of the spectra, for pixels up to 8 mm apart on the wafer, with one measurement even showing two peaks of similar amplitudes. These experimental results confirm that a thick cavity causes high amplitude minor peaks, as calculated for some of the structures modelled in section 7.2.2. The shift of the resonance wavelength over the entire wafer is mapped from transmittance measurements, figure 7.12, and shows a total shift in the resonance wavelength, $\Delta\lambda_{res}$, of ~ 200 nm. The maximum shift in resonance is approximately the same as the free spectral range

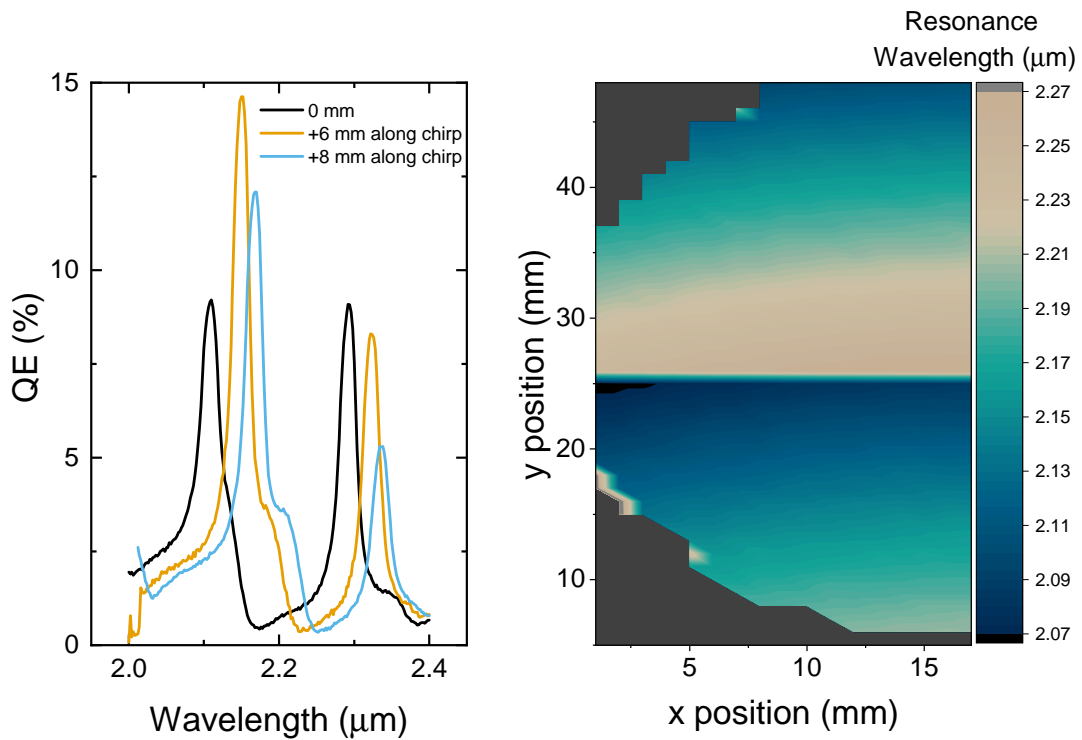


FIGURE 7.12: Left: Measured QE spectra for three pixels on XAB1229. The pixels are separated by 6 mm and 8 mm approximately along the dimension of the resonance chirp. The resonance wavelength shifts with position on the wafer, but the prominence of the secondary resonance does as well. Right: colourmap of resonance wavelength across the wafer. There are two regions of approximately one-dimensional variations in the resonance wavelength, separated by a step change in the middle. The step change is where the cavity thickness becomes closer to the next $m\lambda/2$ ideal thickness.

between the peaks, indicating that this is the limit of shift possible with this structure. A higher cavity thickness variation across the wafer would not increase the difference between the maximum and minimum resonance wavelengths.

This sample, XAB1229, does not show the desired results, but the measurements are included here because they clearly demonstrate the effect of increasing the cavity thickness on the free spectral range of the resonances. From these results it is also possible to approximate the percentage thickness change of the GaSb layer across the wafer. From the transmittance map, figure 7.12, the coefficient of resonance wavelength chirp per unit length is ~ 7.3 nm/mm. Comparison of this coefficient to the modelled shift of the resonance per percentage thickness change, figure 7.5, can be used to determine a coefficient of thickness change per unit length on the wafer - $\sim 0.95\%$ /mm. This is an approximation because the colourmap also shows that the resonance does not shift across the wafer in a perfect one-dimensional shift. The thickness variation is caused by variations in the flux of gallium across the wafer due to the divergence of the beam from the gallium cell. Therefore, as well as the intentional one-dimensional thickness gradient (vertical on the colourmap), differences in beam path lengths horizontally on the wafer also cause a slight thickness variation in the horizontal dimension. It is necessary for the horizontal variation in resonance wavelength to be considered, but it is negligible compared to the vertical wavelength chirp.

5/2 λ Cavity - Attempt 3

Analysis of sample XAB1229 shows that the thickness mismatch between the DBRs and cavity layers is most significant in the centre of the wafer, indicated by the sudden change from high to low fundamental resonance wavelength in figure 7.12. This is not actually a sudden change, but simply the position on the wafer where the relative amplitudes of the two resonances swap. It is preferable for the lowest thickness mismatch to be at the centre of the wafer, as it is the widest part of the wafer and the most usable. The third attempt - sample XAB1379 - uses the same structure as XAB1229, but targets a low thickness mismatch at the centre of the wafer. The thick cavity is kept in an attempt to maximise the range of the spectral shift.

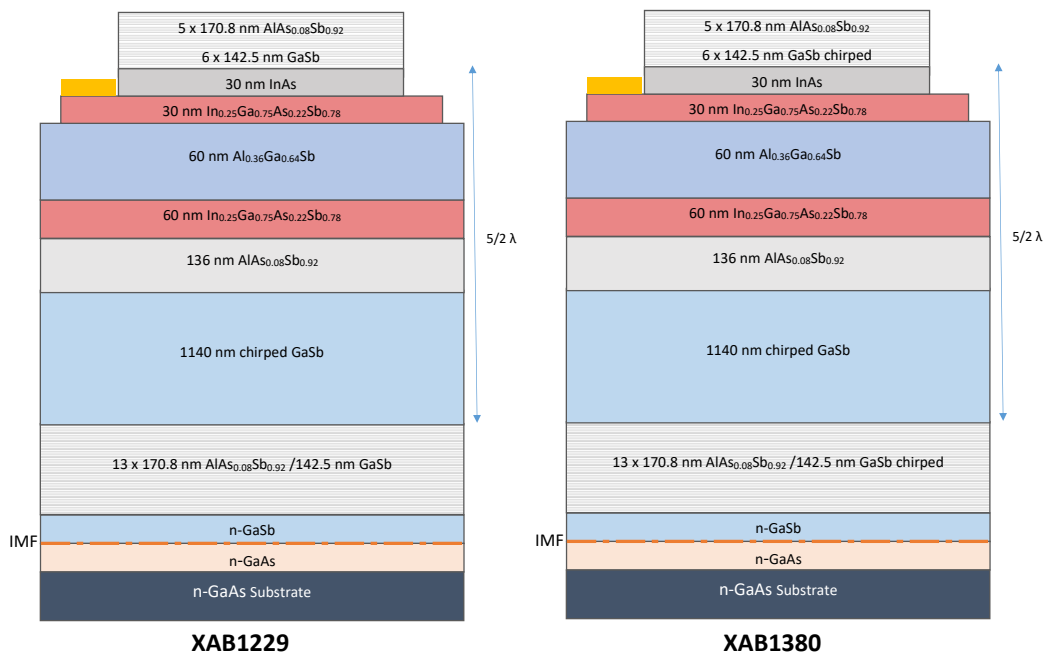


FIGURE 7.13: Structures of three fabricated samples, XAB1229/XAB1379 and XAB1380. Both structures are based on the one presented in chapter 5, with changes including a GaAs substrate (for higher transparency), an interfacial misfit array (IMF - to reduce dislocations caused by lattice mismatch) and thickness graded layers. Only the cavity GaSb is graded in XAB1229/XAB1379. Both the cavity GaSb and the GaSb in the DBRs is graded in XAB1380.

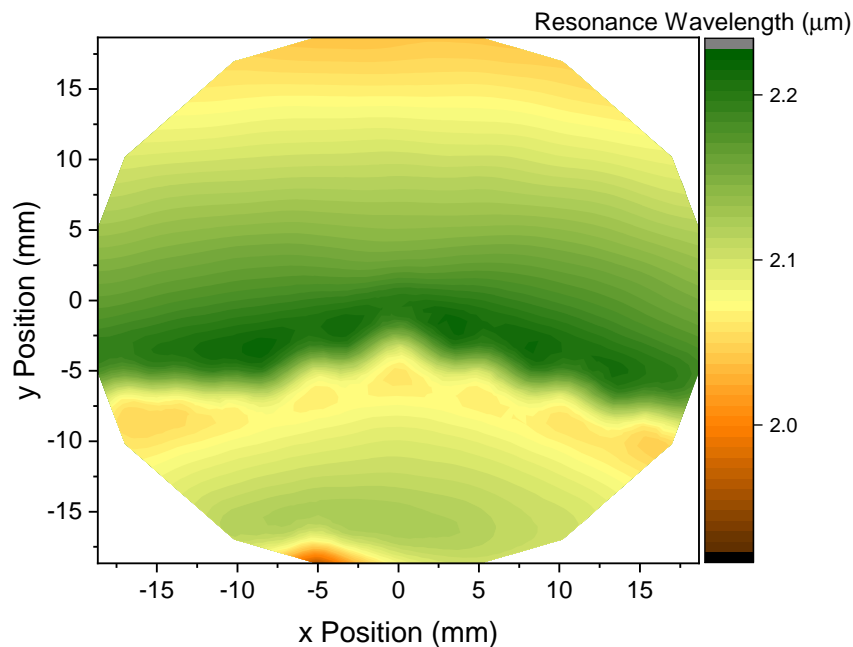


FIGURE 7.14: Colourmap of the resonance wavelength determined from transmittance spectra on sample XAB1379. There are two zones of one-dimensional variation in the resonance wavelength and a step change in between caused by the large thickness variation in the cavity only. The step change is the point where the relative amplitudes of the major and minor resonances swap over.

Figure 7.14 shows the 2D spatial dependence of the primary resonance wavelength on sample XAB1379. The result is very similar to the previous sample (XAB1229), but with the range of resonance wavelengths shifted slightly lower. The maximum range of resonance wavelengths is approximately the same. The thickness mismatch is still high close the centre.

The results from this sample and the previous two attempts with thick cavities show that grading only the thickness of the cavity is not ideal. There are two significant peaks seen at each position across all samples. At the positions of lowest thickness mismatch the secondary peak is a much lower amplitude than the primary peak, as can be seen in the spectral response measurements in figure 7.12. However, the majority of the wafer sees two significant resonance peaks for samples with thickness grading of only the cavity.

7.3.2 Chirped Cavity and DBRs Sample

The intended end use of the graded RCE-PD array is as a form of spectrometer, where the photocurrent from each pixel in the array approximately corresponds to a specific wavelength. The presence of two peaks is undesirable for this, because there is no way to split the photocurrents from each peak for a single pixel. Therefore, the development focuses on creating an array with only one significant peak along the entire length of the array. The first attempt to achieve this was with the sample XAB1380, the structure is shown in figure 7.13. The only difference compared to XAB1229 is that the GaSb layers in the DBRs are graded as well. This sample has a thick, $5/2\lambda$, cavity. The thicker cavity enhances the coefficient of resonance wavelength chirp per unit length, which is desirable. However, it is also the cause of the significant secondary peak. It is expected that the simultaneous chirp of the DBR layers will reduce the thickness mismatch between the DBRs and the cavity. The modelling in figure 7.6b shows that the minor peak is much lower when the layers are closely matched. So, the relative amplitude of the minor peak should be much reduced with the structure employed for XAB1380.

It is also possible to reduce the influence of the secondary peaks by introducing a broadband filter that covers only the primary resonant peaks of the entire array.

This option is relatively simple, the technology is not novel. However, it adds an extra component to any system that would utilise the linear array. The small size of the linear array is the most significant advantage of this concept over traditional spectrometer techniques. Since it is relatively straightforward to reduce the significance of the secondary peaks, by reducing the cavity thickness, this is the preferred option.

The spectral response of multiple pixels in a linear array created on a piece of the wafer (XAB130) is shown in figure 7.15a. The y-axis is the normalised response - the spectrum is divided by the amplitude - to highlight the relative amplitudes of the primary resonance and minor resonance of each pixel. The primary resonances all have an amplitude of 1 and the minor resonances have amplitudes ranging between 0.3 and 0.55- still higher than ideal, although the relative amplitudes could be reduced with further optimisation of the thicknesses of the fabricated layers. For completeness, the non-normalised spectral responses of the primary resonances are shown in the inset. There are significant variations in amplitude, but this is mostly attributed to the non-optimised cleanroom fabrication processes resulting in variations across the wafer.

The distance on the wafer between pixel 1 and pixel 26 is ~ 9 mm, so comparisons can be made to the spectral responses presented for XAB1229 over a similar distance of 8 mm distance in figure 7.12. The relative amplitudes of the minor resonance for XAB1229 range between 0.5 and 1, so, the graded DBRs used in XAB1380 reduce the amplitude of the minor resonance slightly. However, the amplitude of the minor resonance does vary across the wafer, which indicates that the DBRs and cavity thicknesses do not match across the entire wafer. Pixel 1 has a more significant minor resonance and is close to the edge of the wafer. Pixel 26 is closer to the centre of the wafer and has a lower minor resonance. Therefore, it can be inferred that the layer thicknesses are more closely matched at the centre of the wafer and the thickness grading causes an increase in mismatch further from the centre. The main conclusion that can be drawn from these measurements is that the the $5/2\lambda$ thick cavity causes a significant second resonance peak for each pixel and the thickness grading of only the GaSb layers in the DBRs is not enough to keep the thicknesses

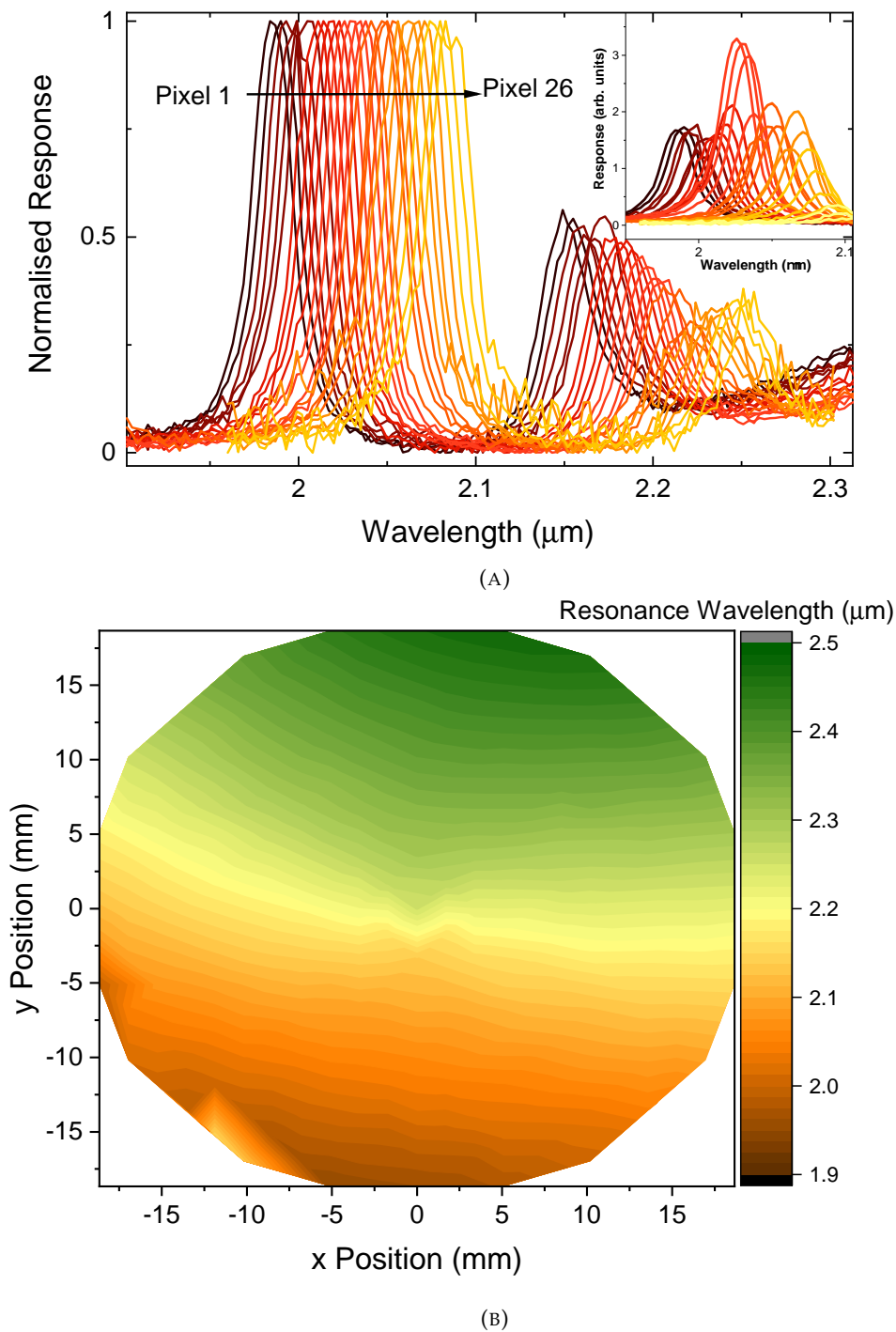


FIGURE 7.15: A) Measured normalised response of pixels along a linear array on sample XAB1380. There are significant secondary resonances, caused by the use of a thick cavity, but shift in primary resonance wavelength is linear. Inset: non-normalised spectral response of the primary resonances. B) Colourmap of the resonance wavelength determined from transmittance spectra on sample XAB1380. Despite the presence of secondary resonances, the primary resonance wavelength shift is linear and in approximately one dimension. There is no step change due to the use of thickness graded DBRs as well as the thickness graded cavity.

of the layers matched across the entire wafer. So, further refinements to reduce the minor peak will necessitate a reduction in cavity thickness.

A colourmap of the resonance wavelength across the sample is shown in figure 7.15b. An approximately linear one-dimensional wavelength chirp is seen between wavelengths of 1.9 μm and 2.5 μm , corresponding to a shift in resonance wavelength per unit length of 14 nm/mm. So, although the sample does not demonstrate the desired single peak response, the coefficient of resonance wavelength chirp per unit length is almost double the 7.3 nm/mm demonstrated by grading only the cavity thickness. A high coefficient of resonance shift is desirable for intended use of the linear array as a micro-scale spectrometer, as it allows a larger spectral band to be covered by the array. Therefore, this structure demonstrates that grading the DBR is a useful enhancement that should be utilised in future structures. Comparison of the measured coefficient of resonance shift to the calculated values gives a coefficient of thickness change per unit length on the wafer as $\sim 1\%$ /mm; this confirms the coefficient determined from the first sample - XAB1229.

7.4 Spectrum Recreation Tests

The previous sections, 7.2.2 and 7.3.2, present and analyse the fabricated structures. This section utilises the linear arrays created from the fabricated samples to identify the wavelengths of incident light. The basic principle of spectrum recreation is briefly discussed in section 7.1. The known spectral response of each pixel along an array is used to determine the spectrum of the incident light. Since the resonance shifts slightly between each neighbouring pixel the photocurrent generated due to a specific wavelength varies between pixels. Put simply, if the wavelength of incident light is close to the resonance wavelength then a high photocurrent is generated. If the incident wavelength is not close to the resonance then little or no photocurrent is generated. A single-wavelength RCE-PD is used in this way to measure at a specific wavelength, but because it can only measure one point on the spectrum it is impossible to determine the precise wavelength of the incident light. The chirped RCE-PD array measures at multiple spectral points, to be able to determine the wavelength of the incident light more precisely.

A demonstration is the best way to understand the concept. A linear array of 19 pixels created from XAB1380 is used. The pixel pitch is $330\ \mu\text{m}$, which equates to a shift of the resonance wavelength of $4.6\ \text{nm}/\text{pixel}$ based on the $14\ \text{nm}/\text{mm}$ measured across the wafer. The fabricated linear array is not perfectly aligned to the dimension of the thickness grading, so the wavelength shift between each pixel is slightly reduced - to $4.0\ \text{nm}/\text{pixel}$. The FWHM of each pixel is $\sim 29\ \text{nm}$, so there is significant overlap in the spectral responses of neighbouring pixels. Therefore, incident light at a single wavelength will generate photocurrents in more than one pixel, but the amplitudes of the currents will not be equal.

A Bentham PVE300 QE measurement system is used for these measurements. A monochromator generates the incident light at the set wavelengths, with bandwidths of $5 - 10\ \text{nm}$. The light is directed through a series of mirrors and collimators onto the sample. This system can only measure the signal from one pixel at a time, so a series of measurements are required. The photocurrent is measured for the first pixel, then the next pixel is moved into place before a second photocurrent measurement is taken. This is repeated for all 19 pixels in the linear array. The light from the monochromator is passed through a chopper, to allow lock-in of the photocurrent and rejection of the leakage currents from each measurement.

The measured photocurrents are scaled by the known peak responsivity of each pixel, although this assumes the shape of the resonance is consistent between pixels. At this stage the aim of the measurements is only to identify the wavelength of the incident light the amplitude is not required, so the scaled photocurrents are normalised for simplicity. In real situations the power of incident light is not uniform, so the responsivity of each device would need to be taken into account. This could be easily included in the post-processing with techniques such as spectrum recreation by minimising the residual norm.¹⁵³ Figure 7.16 shows the normalised photocurrent for each pixel under the illumination of light from the monochromator, set at a specific wavelength. Four wavelengths are tested separately. A Gaussian curve is fitted to the data points to determine the peak of the photocurrents. The corresponding resonance wavelengths of the pixels are shown on the top x-axis, which allows the corresponding wavelength to be determined for the peak of each Gaussian.

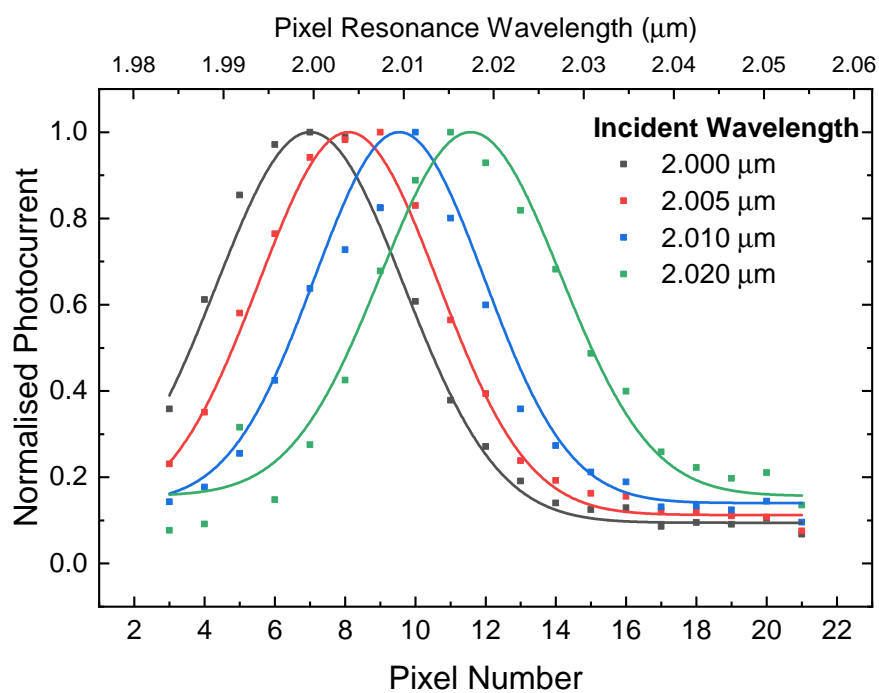


FIGURE 7.16: Measured photocurrents of pixels along a linear array (sample XAB1380) under illumination from four single-wavelengths of light. The current is normalised by the peak response for each pixel and the four curves are also normalised with respect to the peak of the curve. The coloured lines are fitted Gaussians, as a guide to the eye.

It can be seen in figure 7.16 that wavelengths as close as 5 nm apart can be distinguished. The peak wavelengths of the Gaussians line up with the set wavelengths with an uncertainty of ± 2 nm, which includes the uncertainty in the monochromator light of ± 0.5 nm. These initial measurements demonstrate the concept of the chirped RCE-PD spectrometer. They are simple in comparison to the aim of complete spectrum recreation, but prove that the concept does work. The use of monochromatic light does remove the issue of the secondary peaks in the spectral responses, but it is possible for spectrum recreation techniques to be used with any arbitrary spectral responses.^{153,202} So, the secondary peak is not expected to be a limiting factor, even if not filtered out.

It is also important to understand that these measurements are minimally processed. Each pixel measurement is considered individually on the plot, but to increase the sensitivity and precision of the spectrometer it might be necessary to combine the measurements. One method to recreate a spectrum from multiple measurements is presented by Z. Yang *et al.*¹⁵³ using adaptive regularisation to find the spectrum that produces the measured set of photocurrents.

7.5 Analysis

The previous sections, 7.3 and 7.4, present the experimental results for multiple chirped RCE-PD structures and demonstrate the variations in measurements caused by different wavelengths of incident light. This section analyses the overall results in more detail and discusses some of the important properties that should be considered for the applied use of the RCE-PD arrays.

7.5.1 Thickness Gradient Coefficient

The colourmaps of the resonance wavelength across the wafers, shown in section 7.3, are used in conjunction with the spectrum modelling to determine the coefficient of thickness variation across the wafer. The results from the two structures show that the thickness of the graded GaSb layers vary by $\sim 1\%/mm$. A similar value is

determined from both structures, despite the grading of different layers. Therefore, this appears to be a quite consistent rate.

A large number of variables impact the spatial coefficient of the thickness gradient, so it is a coefficient that has to be determined for each unique MBE system and each material in each system. So far, only GaSb layers have been graded, but even though the geometries inside the growth chamber are similar for each material cell it is expected that the coefficients for other materials would not be exactly the same. The coefficients would need to be measured and taken into account if more than one material is graded in the same structure.

The variation in thicknesses that are measured in the fabricated structures are created with no changes to the MBE reactor that could enhance the coefficient of thickness variation. Other MBE systems, with different cell geometries, are likely to be able to achieve a higher thickness variation. For the broadest use of the RCE-PD arrays it is desirable to cover a large bandwidth of the spectrum; which can be increased by a higher thickness variation. In other words, the presented results do not represent the highest achievable spectral bandwidth and it would certainly be possible for commercial semiconductor manufacturers to improve on the research samples. An MBE system configured specifically to enhance the thickness gradient would be the best, albeit costly, way to increase spectral bandwidth covered by the wavelength chirped RCE-PD wafers.

7.5.2 Angular Dependence

The angle of incidence of the light affects the resonance wavelength of RCE-PDs. The resonance of each of the pixels along an array will shift in the same direction, but it means that the photocurrents produced by incident light will change if the angle is changed. The simplest solution is to ensure that the light falling onto the pixels is at normal incidence. However, if necessary the angle of the incident light (if known) could be used to calibrate the measurement. Figure 7.17 shows the angular dependence of sample XAB1380, of $1.2 \text{ nm}/^\circ$, determined from the resonance mode in reflectance measurements at multiple angles. The shift of the resonance of each

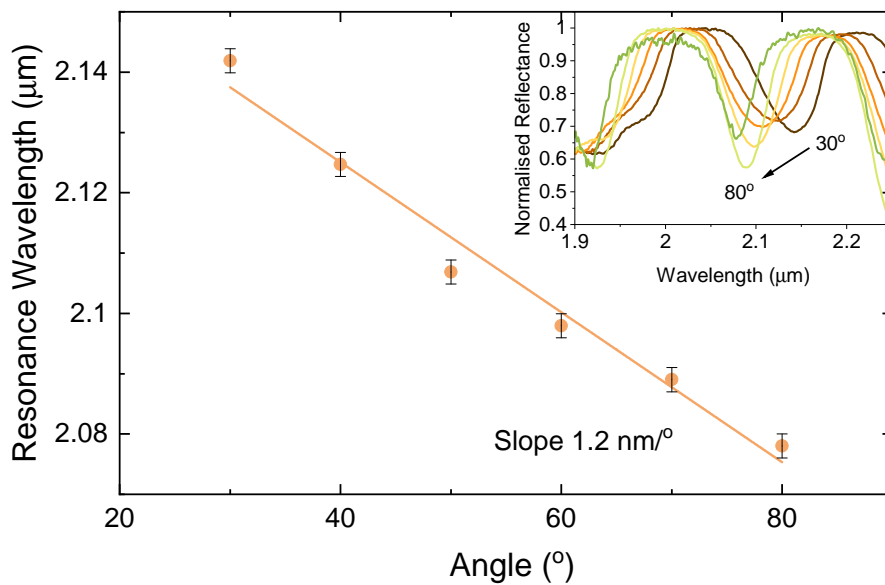


FIGURE 7.17: The angular dependence of the resonance wavelength, determined from reflectance measurements on the unprocessed XAB1380 sample. Inset: The normalised reflectance curves from which the resonance wavelengths were extracted, from the resonant modes.

pixel should be very similar, so one offset could be applied to the measurements from all pixels to account for light that is not at normal incidence.

7.5.3 Temperature Dependence

Variations in the temperature also shifts the resonance wavelength. It is an approximately linear shift, measured for a pixel on XAB1380, of 0.17 nm/K - figure 7.18. The shift is caused by changes in the refractive indices of the layers, so it will be almost identical for each pixel along the array. So, a single offset could be applied to the resonances of every pixel, determined by the differences in temperature. The necessary offset will be the same for every sample with the same structure, and will not change significantly between pixels and samples with the same structure.

7.5.4 FWHM

The FWHM of the spectral responses of the pixels has a significant effect on the precision of the spectrum that can be measured by the RCE-PD array. A high FWHM results in low spectral specificity of each pixel and low precision of the measured wavelength. This is demonstrated in figure 7.19, which shows the expected re-

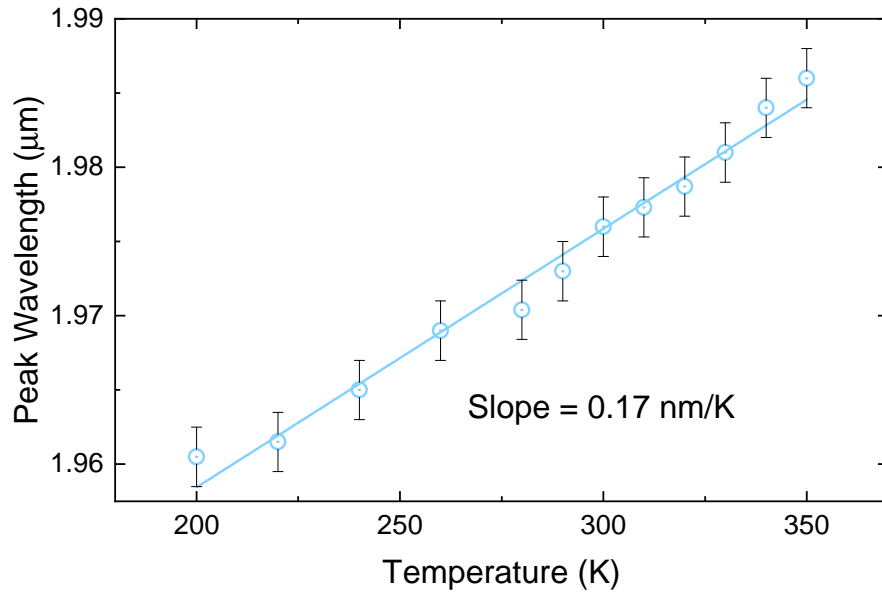


FIGURE 7.18: The temperature dependence of the primary resonance wavelength for a single pixel on XAB1380. There is a clear linear dependence across the entire temperature range.

sponses of a modelled array of pixels to incident light of a single wavelength of 2104 nm. The responses of four arrays with different FWHM, ranging from 10 nm to 40 nm are modelled. The resonance shift between neighbouring pixels is kept constant for all calculations, at 4 nm/pixel. The peak response is at the same pixel, 21, for all arrays, however the number of pixels with significant responses to the single wavelength increases significantly with FWHM. With 10 nm FWHM only 3 pixels have a non-negligible response, but at 40 nm there are 11 pixels with a non-negligible response. If the incident light is known to be a single wavelength, *e.g.* a laser, then this is not an issue (the peak of the fitted Gaussian determines the incident wavelength). If the incident light is an unknown spectrum, then the higher FWHM will hinder the distinction between multiple spectral lines in the incident light.

The benefit of a narrower FWHM, and the lower spectral response overlap that results, can be clearly seen when the incident light contains two wavelengths. Figure 7.20 shows the calculated responses of the same array as in figure 7.19, but with two incident wavelengths that are 20 nm apart. There is a much greater distinction between the two incident wavelengths for the low FWHM array. With 10 nm FWHM there are two pixels with negligible responses between the two peak responses. However, with a 40 nm FWHM the responses of 8 pixels are all close to the

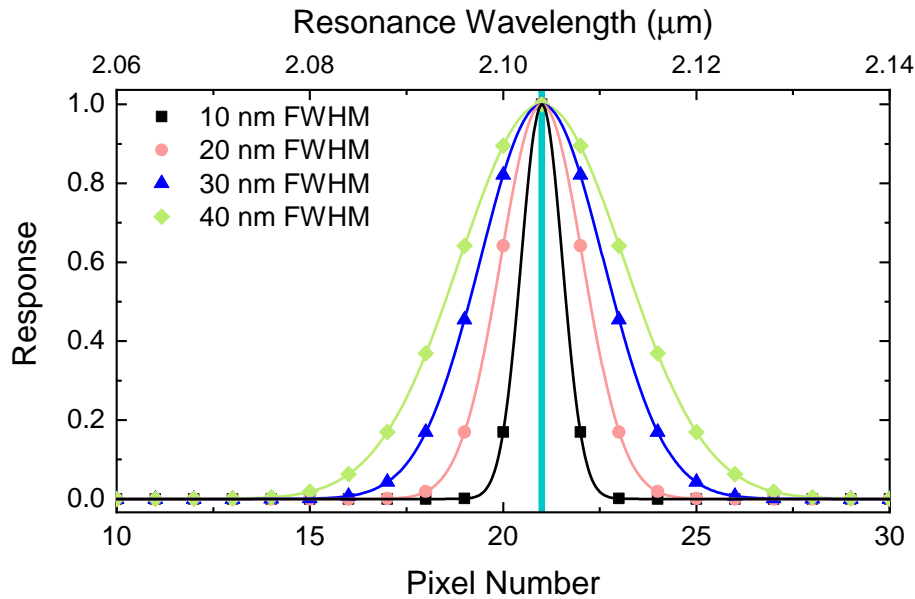


FIGURE 7.19: Modelled normalised responses due to single wavelength of incident light (2104 nm - vertical line) of a linear array with a resonance shift of 4 nm/pixel. Each plotted line represents the response of a comparable linear array, only with different FWHM for the resonant responses - from 40 nm to 10 nm. Lower FWHM results in fewer pixels responding to the monochromatic light.

maximum response, reducing the distinction between the separate incident wavelengths.

It would be possible to use the known spectral response curves and analytical techniques to recreate the incident spectrum from the the combined photocurrent responses of the 40 nm array. So, a low FWHM is not a prerequisite for the creation of a high resolution spectrometer from the RCE-PD arrays. However, it is desirable to recreate the incident spectrum as precisely as possible, before utilising more complex data analysis techniques. A low FWHM offers the possibility of spectrum recreation with little or no data analysis - the photocurrents of each pixel could simply be plotted on the y-axis with the known resonance wavelengths on the x-axis. In other words, an array with a low FWHM has an intrinsically high spectral resolution, whereas an array with a high FWHM does not.

7.5.5 Linear Array Design

Some of the properties of the fabricated linear arrays presented in this chapter are determined by the photolithography mask used for the processing. Pixel area, pixel

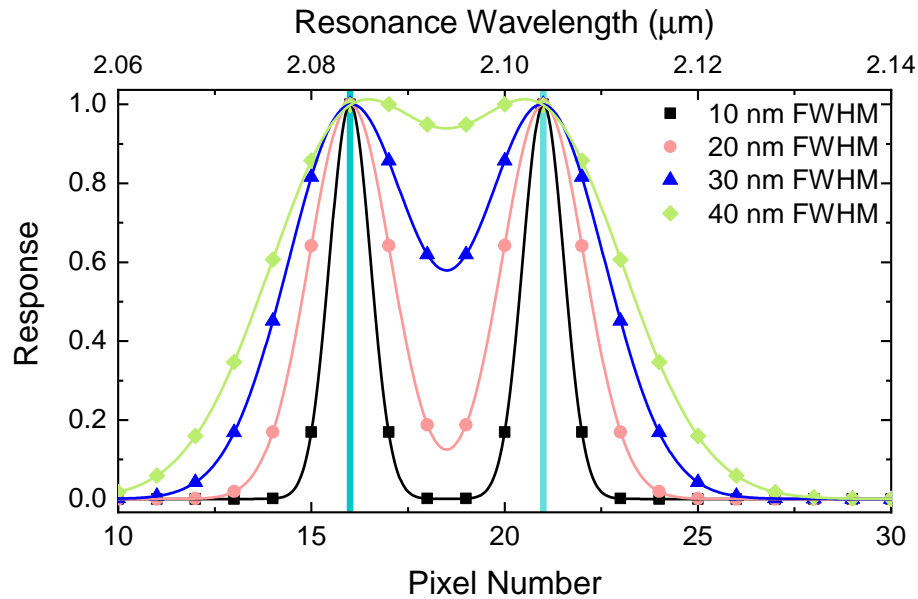


FIGURE 7.20: Modelled normalised responses due to incident light with two wavelengths, 20 nm apart - vertical lines, of a linear array with a resonance shift of 4 nm/pixel. Each plotted line represents the response of a comparable linear array, only with different FWHM for the resonant responses - from 40 nm to 10 nm. Lower FWHM results in less overlap of the responses to the two separate monochromatic light wavelengths.

spacing and pixel pitch are all determined by the mask; they can't be changed without use of a new mask. The pixels have a light-sensitive area of $466\ \mu\text{m}$ by $166\ \mu\text{m}$ and a pitch of $333\ \mu\text{m}$. The gap between each pixel is $133\ \mu\text{m}$. These parameters were all chosen before the first arrays were fabricated and tested, and so were an estimate for the ideal values.

Future linear arrays would likely benefit from a revised pixel design, particularly the width of the pixel in the chirped dimension and the pixel pitch. Changing these factors will vary the overlap between the spectral responses of neighbouring pixels - some overlap is necessary for there to be no gaps in the spectrum that is measured, but too much overlap reduces the spectral precision possible. Sample XAB1380 has significant overlap of the spectral responses, as can be seen in figure 7.15a. The FWHM of the spectral responses are $\sim 29\ \text{nm}$ and the shift of the resonance is 4 nm per pixel; this leads to a large overlap since $\text{FWHM} \gg \text{shift}$. A lower overlap would mean that fewer pixels have a strong response to a specific wavelength of light, increasing the precision of spectral response measurements. The lower FWHM of 10 nm would be ideal for this pixel pitch, there would only be a slight overlap of

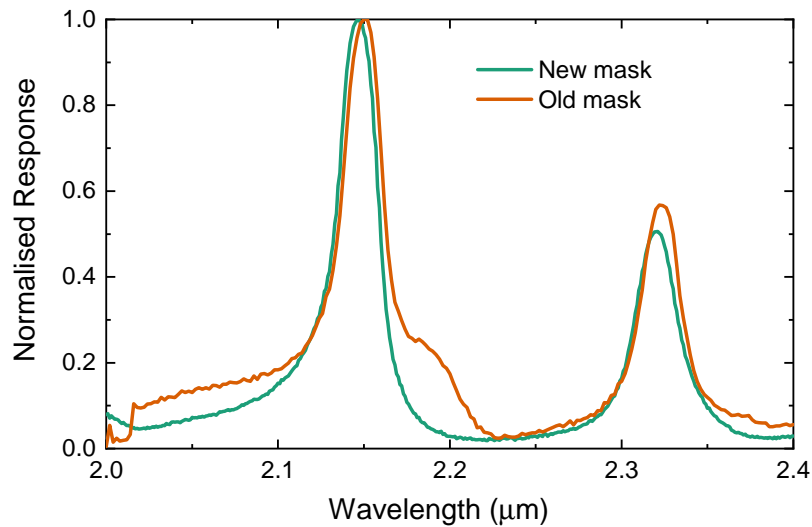


FIGURE 7.21: Comparison of the spectral response for pixels with surface passivation and metallic shielding (green) and without (orange). The surface passivation and metallic shielding reduces the prominence of the broadband response, without affecting the resonant response.

the spectral responses (shifted by 4 nm/pixel). Future arrays should be designed with the spectral response properties of the pixels in mind, the pixel pitch should be tuned based on the FWHM to avoid large spectral overlaps between neighbouring pixels.

Cavity Shielding

The RCE-PD mask discussed in section 4.3.7 is designed specifically for the unique requirements of the resonant cavity structures. It is a refinement of an original mask, intended to reduce the undesirable broadband response. This is achieved by shielding the etched sections of the mesa with a metallic mask, so light can only enter the cavity through the top DBR. For spectral sensing measurements, such as the ones discussed in section 7.4, reducing the broadband response is beneficial for the sensitivity. Any response outside of the resonance reduces the resolution possible from the linear array. Therefore, it is advisable for RCE-PD fabrication processes to be designed with metallic shielding or other features to stop light outside of the DBR area entering the cavity. A comparison of the spectral response for a sample (XAB1229) with and without metallic shielding is shown in figure 7.21. The broadband response is significantly reduced with the metallic shielding in place.

7.6 Conclusions

This chapter presents the concept of wavelength chirped RCE-PDs, a novel method for hyperspectral infrared imaging from a single epitaxial structure. The thicknesses of certain layers in the structure are graded, by pausing rotation during growth, to chirp the resonance wavelength across the wafer. The technique has been tested for multiple combinations of graded layers. Structures in which only a layer (2λ) in the cavity is graded demonstrate the intended spectral shift of the resonance, but only chirps the resonance across the wafer by ~ 7 nm/mm. These structures also have the negative consequence of introducing a second resonance peak into the cavity. This is caused by the thick cavity reducing the free-spectral-range between neighbouring resonant peaks. The coefficient of resonance wavelength chirp per unit length is enhanced by additionally grading the thickness of half the DBR layers. A similar structure, with a 2λ thick graded layer in the cavity, and all GaSb layers in the DBRs graded demonstrates a coefficient of resonance shift that is doubled - to ~ 14 nm/mm. However, the spectral responses of pixels on this wafer also show two significant resonance peaks.

Modelling has shown that the amplitude of secondary resonance peaks is much reduced for structures with a thinner cavity, either 1λ or $1/2\lambda$ optical path lengths are appropriate. The coefficient of wavelength chirp per unit length for similar structures, with DBR layers graded, but only a $1/2\lambda$ thick graded layer in the cavity is expected to be slightly reduced, to ~ 11 nm/mm. Crucially, the layer thicknesses of the DBR and cavity are approximately matched across the whole wafer by utilising a thinner cavity - so, the total shift of the resonance wavelength is not limited by the mismatch.

The values for the coefficient of resonance shift per unit length are specific to these structures and the MBE equipment used for the growth. The coefficient also increases linearly with target wavelength. Due to variations in geometry within the chamber it is expected that the coefficient will not be the same if the thickness of other material layers are graded, even within the same MBE chamber. The measured results provide a proof-of-concept that can be utilised for other structures and

equipment, but testing would be required to determine the expected results.

Arrays fabricated from the chirped samples have proven that the concept does work for hyperspectral sensing on a single wafer. Photocurrent measurements of each pixel in the arrays show the variations in response to a single wavelength of incident light. The light causes negligible response in the pixels where the resonance is not aligned to the incident wavelength, and high response in pixels with resonances that are closely tuned to incident wavelength. Therefore, with prior measurement of the spectral responses of each pixel, the wavelength of the incident light can be determined with a precision of ± 2 nm.

7.6.1 Future Work

Modelling of variations on the fabricated structures has shown that there are improvements to be made. Use of a thinner cavity, as already discussed, can reduce the amplitude of secondary resonances. This leaves a single high-amplitude resonance for higher spectral specificity and negligible interference from secondary resonances.

Tuning of the FWHM of the resonance peak can also improve the precision of the linear array spectral measurements. Lower FWHM reduces the overlap of the responses of neighbouring pixels, leading to improved discrimination of the incident wavelength(s). The FWHM can be reduced by a combination of more repeats in the DBRs - to increase reflectivity - and reducing the absorber thickness - to reduce absorption for a single-pass through the cavity. These changes increase the finesse of the cavity, reducing the width of the resonance.

Further investigation into the positioning of the absorber within the cavity and choice of contact layer material would be useful for further refinement of the structures. The contact layer materials used in all the presented structures is the same as the absorber, but if the finesse of the cavity is increased then the percentage of light absorbed in the contact layer will increase. Use of materials that are transparent at the target resonance wavelength should be investigated to remove the contact layer as a source of attenuation. The absorber positioning could also be investigated to

increase the finesse of the cavity. The presented samples all place the absorber approximately at one of the anti-nodes of the standing wave in the cavity, to increase absorption. However, lower single-pass absorption, achieved by positioning the absorber away from the anti-node, could increase the finesse.

The presented testing of the RCE-PD linear arrays for spectral sensing is relatively simple. A narrow band, approximately single wavelength of incident light is used. Future measurements could increase the complexity of the incident light, multiple specific wavelengths at first, then increasingly complex arbitrary spectra. The suggested improvements to the structure design should make this possible. On top of the refinement of the structure, more complex data analysis techniques could be implemented. This is outside the scope of the current work, but can enhance the accuracy and precision of the recreated spectra.

Chapter 8

Review of Research and Future Work

8.1 Review of Research

The overall aim of this project was to develop resonant cavity-enhanced photodiodes for spectral sensing in the mid-infrared. The structures were developed based on III-V materials and the technical understanding of these materials based on previous research conducted within Dr Marshall's research group. Samples were successfully fabricated with narrow spectral responses, targeted to sense in multiple significant spectral regions in the short-wave infrared (chapter 5) and the mid-wave infrared (chapter 6). While the presented structures do not represent the highest possible performance, they demonstrate the benefits of resonant cavity enhancement for photodiodes. Namely, low spectral bandwidth, reduced leakage currents and easily tuned spectral response.

The RCE-PD structure presented in chapter 5 could be tuned to sense at wavelengths in the region $1.8\ \mu\text{m}$ to $2.8\ \mu\text{m}$, covering the spectral absorption lines of some significant substances, including, glucose, acetone and carbon dioxide. The low width of the measured spectral response would potentially allow each of these substances to be measured independently. The resonance wavelength is known to be dependent on optical path length of the layers in the structure, and this was shown to also determine the shift in resonance due to temperature changes. The resonance wave-

length increases with temperature, most significantly as a result of variations in the refractive indices altering the optical path lengths. The exact coefficient of the shift is dependent on the materials used in the structure and the thicknesses of the layers. Spectral sensing with these structures would need to account for these variations of the response due to temperature, as well as the angle of the incident light, which also shifts the resonance wavelength.

Spectral sensing within another significant spectral region, 3.0 μm to 3.5 μm , was the motivation for the development of an RCE-PD structure with an InAs absorber. This region covers the absorption lines due to stretching of C-H bonds, which are found in most organic molecules. The resonance wavelength of the fabricated RCE-PD was closely aligned to the targeted absorption peak of the methane, demonstrating the control of spectral response that is possible with RCE-PDs. Detailed analysis of the width of the resonance peak suggests it is highly dependent on the single-pass absorption in the cavity. The absorption coefficient of InAs at the resonance wavelength reduces at lower temperatures due to a widening of the bandgap, and the cavity absorption is reduced as a result. This results in a significant decrease of the width of the resonance peak at lower temperatures. This highlights the requirement for precise measurements of the material parameters to be able accurately design RCE-PDs. The most significant parameters are the refractive indices and the absorption coefficients.

The final results chapter, 7, details the concept of wavelength chirped RCE-PDs - that was not part of the original aim of the project. This research was driven by the motivation of multi-spectral sensing from detectors on a single wafer. The structures are very similar to ones presented for single-wavelength measurements, but include a thickness gradient that chirps the resonance wavelength across the wafer. The thickness gradient is achieved by pausing the rotation of the wafer during the epitaxial growth of the appropriate layers. The concept has been demonstrated to cover a spectral region of up to 500 nm on a single wafer. The fabricated linear arrays were used to determine the wavelength of monochromatic infrared light with an accuracy of ± 2 nm from initial measurements. Overall, the samples created for this purpose have proven the concept. The measurements have been used to develop an under-

standing of which layers to grade in the structure. Initial samples demonstrated an important lesson, do not use a thick cavity unless multiple resonance peaks are desired. Refined structures utilise graded DBR layers and a thin cavity (1λ), with approximately half the optical path length of both thickness graded. This achieves the best compromise between high rate of chirp across the wafer and single resonance response.

8.2 Future Work

The modelling of the resonant cavity structures has proven to be extremely useful for developing high-quality devices. However, for greater control over the properties of the final design it would be beneficial to know accurate values for refractive indices and absorption coefficients of all alloys used. A study into the wavelength and temperatures dependence of these values would allow for precise modelling and design of future structures.

The chirped RCE-PD concept has a significant amount of potential to be taken further. Refinement of the structures could improve their sensitivity for hyperspectral sensing. The research into the structures could focus on reducing the width of the resonance peaks and also increasing the coefficient of resonance wavelength chirp per unit length across the wafer. Lower resonance width will reduce the overlap of the spectral responses between neighbouring pixels and increase the spectral specificity possible. Taken to the extreme, a very narrow width could be used to create an array where each pixel detects at an almost single wavelength, with negligible response at all other wavelengths. Potentially, a high sensitivity spectrometer could be created. Increasing the coefficient of resonance wavelength chirp per unit length is likely to be more difficult; the main area of research that could enable this is the thickness grading of ternary alloys. There is potential for lattice-mismatch, but if ternary alloys could be graded without significant degradation of the crystal quality then almost all layers in the RCE-PD structures could be graded. This is not likely to be simple though.

Bibliography

- [1] Inc. Coblentz Society. *Evaluated Infrared Reference Spectra*. eng. Gaithersburg MD, 20899: National Institute of Standards and Technology, 2012. ISBN: 012387839X. URL: <https://doi.org/10.18434/T4D303> (visited on 06/01/2021).
- [2] Teledyne Judson. *Indium Arsenide Detectors*. Accessed: 01.07.2021. Teledyne Judson. URL: <http://www.teledynejudson.com/products/indium-arsenide-detectors>.
- [3] Teledyne Judson. *Photoconductive Mercury Cadmium Telluride Detectors*. Accessed: 01.07.2021. Teledyne Judson. URL: <http://www.teledynejudson.com/products/photoconductive-mercury-cadmium-telluride-detectors>.
- [4] H. Bourdouce and J.A. Jervase. "Design of ultra-fast dual-wavelength resonant-cavity-enhanced Schottky photodetectors". In: *IEEE Journal of Quantum Electronics* 37.1 (2001), pp. 63–68. DOI: [10.1109/3.892725](https://doi.org/10.1109/3.892725).
- [5] Peter J. Winzer, David T. Neilson, and Andrew R. Chraplyvy. "Fiber-optic transmission and networking: the previous 20 and the next 20 years (Invited)". In: *Opt. Express* 26.18 (2018), pp. 24190–24239. DOI: [10.1364/OE.26.024190](https://doi.org/10.1364/OE.26.024190). URL: <http://www.opticsexpress.org/abstract.cfm?URI=oe-26-18-24190>.
- [6] Jane Hodgkinson and Ralph P Tatam. "Optical gas sensing: a review". In: *Measurement Science and Technology* 24.1 (2012), p. 012004. DOI: [10.1088/0957-0233/24/1/012004](https://doi.org/10.1088/0957-0233/24/1/012004). URL: <https://doi.org/10.1088/0957-0233/24/1/012004>.
- [7] Trevor A. O'Loughlin *et al.* "Mid-IR resonant cavity detectors". In: *Journal of Vacuum Science & Technology B* 35.2 (2017), 02B111. DOI: [10.1116/1.4977780](https://doi.org/10.1116/1.4977780). URL: <https://doi.org/10.1116/1.4977780>.

- [8] A. Rogalski. *Infrared Photon Detectors*. Bellingham, Washington: SPIE-The International Society for Optical Engineering, 1995.
- [9] “p-n Junctions”. In: *Physics of Semiconductor Devices*. John Wiley Sons, Ltd, 2006, pp. 77–133. ISBN: 9780470068328. DOI: <https://doi.org/10.1002/9780470068328.ch2>. eprint: <https://onlinelibrary.wiley.com/doi/pdf/10.1002/9780470068328.ch2>. URL: <https://onlinelibrary.wiley.com/doi/abs/10.1002/9780470068328.ch2>.
- [10] Shun Lien Chuang. *Physics of photonic devices*. John Wiley & Sons, 2012.
- [11] S. Maimon and G. W. Wicks. “nBn detector, an infrared detector with reduced dark current and higher operating temperature”. In: *Applied Physics Letters* 89.15 (2006), p. 151109. DOI: [10.1063/1.2360235](https://doi.org/10.1063/1.2360235). URL: <https://doi.org/10.1063/1.2360235>.
- [12] B. T. Marozas *et al.* “Surface dark current mechanisms in III-V infrared photodetectors”. In: *Opt. Mater. Express* 8.6 (2018), pp. 1419–1424. DOI: [10.1364/OME.8.001419](https://doi.org/10.1364/OME.8.001419). URL: <http://opg.optica.org/ome/abstract.cfm?URI=ome-8-6-1419>.
- [13] Donald A. Neamen. *Semiconductor physics and devices : basic principles*. eng. New York, New York: McGraw-Hill, 2012. ISBN: 0-07-741884-0.
- [14] W.W. Anderson. “Tunnel contribution to Hg_{1-x}Cd_xTe and Pb_{1-x}Sn_xTe pn junction diode characteristics”. In: *Infrared Physics* 20.6 (1980), pp. 353–361. ISSN: 0020-0891. DOI: [https://doi.org/10.1016/0020-0891\(80\)90052-4](https://doi.org/10.1016/0020-0891(80)90052-4). URL: <https://www.sciencedirect.com/science/article/pii/0020089180900524>.
- [15] A. Unikovsky and Y. Nemirowsky. “Trap-assisted tunneling in mercury cadmium telluride photodiodes”. In: *Applied Physics Letters* 61.3 (1992), pp. 330–332. DOI: [10.1063/1.107927](https://doi.org/10.1063/1.107927).
- [16] G.R. Savich *et al.* “Benefits and limitations of unipolar barriers in infrared photodetectors”. In: *Infrared Physics Technology* 59 (2013). Proceedings of the International Conference on Quantum Structure Infrared Photodetector (QSIP) 2012, pp. 152–155. ISSN: 1350-4495. DOI: <https://doi.org/10.1016/j>.

- infrared.2012.12.031. URL: <https://www.sciencedirect.com/science/article/pii/S1350449512001466>.
- [17] Chih-tang Sah, Robert N. Noyce, and William Shockley. "Carrier Generation and Recombination in P-N Junctions and P-N Junction Characteristics". In: *Proceedings of the IRE* 45.9 (1957), pp. 1228–1243. DOI: [10.1109/JRPROC.1957.278528](https://doi.org/10.1109/JRPROC.1957.278528).
- [18] G. R. Nash and T. Ashley. "Reduction in Shockley–Read–Hall generation-recombination in AlInSb light-emitting-diodes using spatial patterning of the depletion region". In: *Applied Physics Letters* 94.21 (2009), p. 213510. DOI: [10.1063/1.3147207](https://doi.org/10.1063/1.3147207). eprint: <https://doi.org/10.1063/1.3147207>. URL: <https://doi.org/10.1063/1.3147207>.
- [19] David R. Rhiger *et al.* "Analysis of III–V Superlattice nBn Device Characteristics". In: *Journal of Electronic Materials* 45.9 (2016), pp. 4646–4653. ISSN: 1543-186X. DOI: [10.1007/s11664-016-4545-y](https://doi.org/10.1007/s11664-016-4545-y). URL: <https://doi.org/10.1007/s11664-016-4545-y>.
- [20] B Tuck. "Mechanisms of atomic diffusion in the III-V semiconductors". In: *Journal of Physics D: Applied Physics* 18.4 (1985), pp. 557–584. DOI: [10.1088/0022-3727/18/4/002](https://doi.org/10.1088/0022-3727/18/4/002). URL: <https://doi.org/10.1088/0022-3727/18/4/002>.
- [21] Antoni Rogalski. *Narrow-gap semiconductor photodiodes*. eng. SPIE Press monograph ; PM77. Bellingham, Wash.: SPIE Optical Engineering Press, 2000. ISBN: 0819436194.
- [22] Gregory Robert Savich. "Analysis and suppression of dark currents in mid-wave infrared photodetectors". PhD thesis. The Institute of Optics Arts, Sciences, Engineering Edmund A. Hajim School of Engineering, and Applied Sciences, 2015.
- [23] A. Rogalski, M. Kopytko, and P. Martyniuk. *Antimonide-based Infrared Detectors: A New Perspective*. Press Monographs. SPIE Press, 2018. ISBN: 9781510611399. URL: <https://books.google.co.uk/books?id=OZF7tAEACAAJ>.

- [24] Philip Klipstein. ““X_{Bn}” barrier photodetectors for high sensitivity and high operating temperature infrared sensors”. In: *Infrared Technology and Applications XXXIV*. Ed. by Bjørn F. Andresen, Gabor F. Fulop, and Paul R. Norton. Vol. 6940. International Society for Optics and Photonics. SPIE, 2008, pp. 935–946. DOI: [10.1117/12.778848](https://doi.org/10.1117/12.778848). URL: <https://doi.org/10.1117/12.778848>.
- [25] Janet Renee Pedrazzani. “Characteristics of InAs-based nBn photodetectors grown by molecular beam epitaxy”. PhD thesis. The Institute of Optics Arts, Sciences, Engineering Edmund A. Hajim School of Engineering, and Applied Sciences, 2010.
- [26] Chih-Tang Sah. “Effect of surface recombination and channel on P-N junction and transistor characteristics”. In: *IRE Transactions on Electron Devices* 9.1 (1962), pp. 94–108. DOI: [10.1109/T-ED.1962.14895](https://doi.org/10.1109/T-ED.1962.14895).
- [27] SHI Qian *et al.* “Progress on nBn infrared detectors”. In: *J. Infrared Millim. Waves* 41.1 (2022), p. 139. DOI: [10.11972/j.issn.1001-9014.2022.01.010](https://doi.org/10.11972/j.issn.1001-9014.2022.01.010).
- [28] C J R Sheppard. “Approximate calculation of the reflection coefficient from a stratified medium”. In: *Pure and Applied Optics: Journal of the European Optical Society Part A* 4.5 (1995), pp. 665–669. DOI: [10.1088/0963-9659/4/5/018](https://doi.org/10.1088/0963-9659/4/5/018). URL: <https://doi.org/10.1088/0963-9659/4/5/018>.
- [29] Carl W Wilmsen, Henryk Temkin, and Larry A Coldren. *Vertical-cavity surface-emitting lasers: design, fabrication, characterization, and applications*. Vol. 24. Cambridge University Press, 2001.
- [30] Fumio Koyama. “Recent Advances of VCSEL Photonics”. In: *J. Lightwave Technol.* 24.12 (2006), pp. 4502–4513. URL: <http://opg.optica.org/jlt/abstract.cfm?URI=jlt-24-12-4502>.
- [31] T. Knodl *et al.* “RCE photodetectors based on VCSEL structures”. In: *IEEE Photonics Technology Letters* 11.10 (1999), pp. 1289–1291. DOI: [10.1109/68.789720](https://doi.org/10.1109/68.789720).
- [32] Holger Moench *et al.* “ViP-VCSEL with integrated photodiode and new applications”. In: *Vertical-Cavity Surface-Emitting Lasers XXVI*. Ed. by Chun Lei, Kent D. Choquette, and Luke A. Graham. Vol. 12020. International Society

- for Optics and Photonics. SPIE, 2022, pp. 23–32. DOI: [10.1117/12.2607345](https://doi.org/10.1117/12.2607345). URL: <https://doi.org/10.1117/12.2607345>.
- [33] Holger Moench *et al.* “VCSEL-based sensors for distance and velocity”. In: *Vertical-Cavity Surface-Emitting Lasers XX*. Ed. by Kent D. Choquette and James K. Guenter. Vol. 9766. International Society for Optics and Photonics. SPIE, 2016, pp. 40–50. DOI: [10.1117/12.2209320](https://doi.org/10.1117/12.2209320). URL: <https://doi.org/10.1117/12.2209320>.
- [34] M A Green. “Solar cells: operating principles, technology, and system applications”. In: (Jan. 1982). URL: <https://www.osti.gov/biblio/6051511>.
- [35] Charalambos C. Katsidis and Dimitrios I. Siapkas. “General transfer-matrix method for optical multilayer systems with coherent, partially coherent, and incoherent interference”. In: *Appl. Opt.* 41.19 (2002), pp. 3978–3987. DOI: [10.1364/AO.41.003978](https://doi.org/10.1364/AO.41.003978). URL: <http://www.osapublishing.org/ao/abstract.cfm?URI=ao-41-19-3978>.
- [36] Ryan B Balili. “Transfer matrix method in nanophotonics”. In: *International Journal of Modern Physics: Conference Series*. Vol. 17. World Scientific. 2012, pp. 159–168.
- [37] Max Born *et al.* *Principles of Optics: Electromagnetic Theory of Propagation, Interference and Diffraction of Light*. 7th ed. Cambridge University Press, 1999. DOI: [10.1017/CB09781139644181](https://doi.org/10.1017/CB09781139644181).
- [38] P. Yeh. *Optical Waves in Layered Media*. Wiley Series in Pure and Applied Optics. Wiley, 2005. ISBN: 9780471731924. URL: <https://books.google.co.uk/books?id=-yZBAQAAIAAJ>.
- [39] Tom Wilson. “The Design, Optimisation, and Characterisation of GaSb/GaAs Quantum Ring-Based Vertical-Cavity Devices Emitting at Telecoms Wavelengths.” English. PhD thesis. Lancaster University, Feb. 2022. DOI: [10.17635/lancaster/thesis/1550](https://doi.org/10.17635/lancaster/thesis/1550).
- [40] Mihail M. Dumitrescu *et al.* “Resonant cavity light-emitting diodes: modeling, design, and optimization”. In: *SIOEL '99: Sixth Symposium on Optoelectronics*. Ed. by Teodor Necsoiu, Maria Robu, and Dan C. Dumitras. Vol. 4068.

- International Society for Optics and Photonics. SPIE, 2000, pp. 597–607. DOI: [10.1117/12.378731](https://doi.org/10.1117/12.378731). URL: <https://doi.org/10.1117/12.378731>.
- [41] Max Born and Emil Wolf. *Principles of optics*. Cambridge University Press, 1970, p. 40.
- [42] Patrick Schygulla *et al.* “Determination of the complex refractive index of compound semiconductor alloys for optical device modelling”. In: *Journal of Physics D: Applied Physics* 53.49 (2020), p. 495104. DOI: [10.1088/1361-6463/abb270](https://doi.org/10.1088/1361-6463/abb270). URL: <https://doi.org/10.1088/1361-6463/abb270>.
- [43] S.O. Kasap. *Principles of Electronic Materials and Devices*. McGraw-Hill International Edition. McGraw-Hill, 2006. Chap. 9. ISBN: 9780073104645. URL: <https://books.google.co.uk/books?id=EeCeAQAAIAAJ>.
- [44] David J Griffiths. *Introduction to Electrodynamics*. eng. 4th ed. Harlow: Pearson Education UK, 2013, pp. 387–392. ISBN: 9781292034652.
- [45] M. Selim Ünlü and Samuel Strite. “Resonant cavity enhanced photonic devices”. In: *Journal of Applied Physics* 78.2 (1995), pp. 607–639. DOI: [10.1063/1.360322](https://doi.org/10.1063/1.360322). URL: <https://doi.org/10.1063/1.360322>.
- [46] N. A. Stathopoulos *et al.* “A transmission line model for the optical simulation of multilayer structures and its application for oblique illumination of an organic solar cell with anisotropic extinction coefficient”. In: *Journal of Applied Physics* 110.11 (2011), p. 114506. DOI: [10.1063/1.3662952](https://doi.org/10.1063/1.3662952). URL: <https://doi.org/10.1063/1.3662952>.
- [47] Amin Khavasi *et al.* “Transmission line model for extraction of transmission characteristics in photonic crystal waveguides with stubs: optical filter design”. In: *Opt. Lett.* 37.8 (2012), pp. 1322–1324. DOI: [10.1364/OL.37.001322](https://doi.org/10.1364/OL.37.001322). URL: <http://opg.optica.org/ol/abstract.cfm?URI=ol-37-8-1322>.
- [48] R. Pieper, M. Shirvaikar, and J. Salvatierra. “A transmission line model for analysis of thin film optical filters”. In: *2006 Proceeding of the Thirty-Eighth Southeastern Symposium on System Theory*. 2006, pp. 186–191. DOI: [10.1109/SSST.2006.1619086](https://doi.org/10.1109/SSST.2006.1619086).

- [49] H. Meng *et al.* "A transmission line model for high-frequency power line communication channel". In: *Proceedings. International Conference on Power System Technology*. Vol. 2. 2002, 1290–1295 vol.2. DOI: [10.1109/ICPST.2002.1047610](https://doi.org/10.1109/ICPST.2002.1047610).
- [50] Simona M. Cristescu, Dan C. Dumitras, and Doru C. A. Dutu. "Characterization of a resonant photoacoustic cell using the acoustic transmission line model". In: *SIOEL '99: Sixth Symposium on Optoelectronics*. Ed. by Teodor Necsoiu, Maria Robu, and Dan C. Dumitras. Vol. 4068. International Society for Optics and Photonics. SPIE, 2000, pp. 261–270. URL: <https://doi.org/10.1117/12.378679>.
- [51] Bhag Singh Guru and Hüseyin R Hiziroglu. *Electromagnetic Field Theory Fundamentals*. eng. Cambridge: Cambridge University Press, 2004. ISBN: 0521830168.
- [52] M. Slurzberg and W. Osterheld. *Essentials of Electricity for Radio and Television*. McGraw-Hill, 1950. URL: <https://books.google.co.uk/books?id=GQ001C0tGv8C>.
- [53] L.E. Kinsler *et al.* *Fundamentals of Acoustics*. Wiley, 1982. ISBN: 9780471029335. URL: <https://books.google.co.uk/books?id=ibTvAAAAMAAJ>.
- [54] Daniel D. Traficante. "Maximum power transfer and percent efficiency: Which is more important?" In: *Concepts in Magnetic Resonance* 9.1 (1997), pp. 13–16. DOI: [https://doi.org/10.1002/\(SICI\)1099-0534\(1997\)9:1<13::AID-CMR2>3.0.CO;2-Q](https://doi.org/10.1002/(SICI)1099-0534(1997)9:1<13::AID-CMR2>3.0.CO;2-Q).
- [55] Hermann A Haus. *Waves and fields in optoelectronics*. eng. Prentice-Hall series in solid state physical electronics. Englewood Cliffs, NJ: Prentice-Hall, 1984. ISBN: 0139460535.
- [56] Steven W. Ellingson. *Electromagnetics, Vol. 1*. eng. Blacksburg, VA: VT Publishing, 2018. ISBN: 0521830168. DOI: <https://doi.org/10.21061/electromagnetics-vol-1>.
- [57] NIST. eng. Gaithersburg MD, 20899: National Institute of Standards and Technology, 2018. URL: <http://physics.nist.gov/cgi-bin/cuu/Value?z0> (visited on 07/11/2022).

- [58] David K. Cheng. *Field and wave electromagnetics*. eng. The Addison-Wesley series in electrical engineering. Reading, Mass.: Addison-Wesley Pub. Co., 1989. ISBN: 0201528207.
- [59] George L Matthaei. *Microwave filters, impedance-matching networks, and coupling structures*. eng. New York: McGraw-Hill, 1964.
- [60] T J Wilson *et al.* "A detailed comparison of measured and simulated optical properties of a short-period GaAs/Al_xsub/subGasub1-x/subAs distributed Bragg reflector". In: *Semiconductor Science and Technology* 35.5 (2020), p. 055003. DOI: [10.1088/1361-6641/ab76af](https://doi.org/10.1088/1361-6641/ab76af). URL: <https://doi.org/10.1088/1361-6641/ab76af>.
- [61] Sadao Adachi. "Optical dispersion relations for GaP, GaAs, GaSb, InP, InAs, InSb, Al_xGa_{1-x}As, and In_{1-x}Ga_xAs_yP_{1-y}". In: *Journal of Applied Physics* 66.12 (1989), pp. 6030–6040. DOI: [10.1063/1.343580](https://doi.org/10.1063/1.343580). URL: <https://doi.org/10.1063/1.343580>.
- [62] Glen D. Gillen *et al.* "Temperature-dependent refractive index measurements of wafer-shaped InAs and InSb". In: *Appl. Opt.* 47.2 (2008), pp. 164–168. DOI: [10.1364/AO.47.000164](http://ao.osa.org/abstract.cfm?URI=ao-47-2-164). URL: <http://ao.osa.org/abstract.cfm?URI=ao-47-2-164>.
- [63] J. Talghader and J. S. Smith. "Thermal dependence of the refractive index of GaAs and AlAs measured using semiconductor multilayer optical cavities". In: *Applied Physics Letters* 66.3 (1995), pp. 335–337. DOI: [10.1063/1.114204](https://doi.org/10.1063/1.114204). URL: <https://doi.org/10.1063/1.114204>.
- [64] Łukasz Pisorski and Robert P. Sarzala. "Material parameters of antimonides and amorphous materials for modelling the mid-infrared lasers". In: *Opt. Appl.* 46.2 (2016), pp. 227–240. DOI: [10.5277/oa160207](https://doi.org/10.5277/oa160207).
- [65] Hamamatsu. *Selection guide / Infrared detectors*. Accessed: 29.07.2022. Hamamatsu. URL: https://www.hamamatsu.com/content/dam/hamamatsu-photonics/sites/documents/99_SALES_LIBRARY/ssd/infrared_kird0001e.pdf.

- [66] Arnaud Dumas *et al.* "Evaluation of a HgCdTe e-APD based detector for 2 μm CO₂ DIAL application". In: *Appl. Opt.* 56.27 (2017), pp. 7577–7585. DOI: [10.1364/AO.56.007577](https://doi.org/10.1364/AO.56.007577). URL: <http://opg.optica.org/ao/abstract.cfm?URI=ao-56-27-7577>.
- [67] A. P. Craig *et al.* "Short-wave infrared barrier detectors using InGaAsSb absorption material lattice matched to GaSb". In: *Applied Physics Letters* 106.20 (2015), p. 201103. DOI: [10.1063/1.4921468](https://doi.org/10.1063/1.4921468). URL: <https://doi.org/10.1063/1.4921468>.
- [68] Nong Li *et al.* "High performance nBn detectors based on InGaAsSb bulk materials for short wavelength infrared detection". In: *AIP Advances* 9.10 (2019), p. 105106. DOI: [10.1063/1.5124093](https://doi.org/10.1063/1.5124093). URL: <https://doi.org/10.1063/1.5124093>.
- [69] D. Cohen-Elias *et al.* "Minority carrier diffusion length for electrons in an extended SWIR InAs/AlSb type-II superlattice photodiode". In: *Applied Physics Letters* 111.20 (2017), p. 201106. DOI: [10.1063/1.5005097](https://doi.org/10.1063/1.5005097).
- [70] Pedro Pereira *et al.* "Quantum Well Infrared Photodetector for the SWIR Range". In: *Developments and Advances in Defense and Security*. Singapore: Springer Singapore, 2020, pp. 363–370. ISBN: 978-981-13-9155-2.
- [71] P. Capper *et al.* *Mercury Cadmium Telluride: Growth, Properties and Applications*. Wiley Series in Materials for Electronic & Optoelectronic Applications. Wiley, 2011. ISBN: 9781119957577. URL: <https://books.google.co.uk/books?id=oPsZ2D5casUC>.
- [72] Pierre-Yves Emelie. "Mercury cadmium telluride auger-suppressed infrared detectors under non-equilibrium operation". PhD thesis. University of Michigan, Jan. 2009.
- [73] Vigo Photonics. *PVI-4-1x1-TO39-NW-36 detector datasheet*. Accessed: 29.07.2022. Vigo Photonics. URL: <https://vigo.com.pl/wp-content/uploads/2022/04/PVI-4-1x1-TO39-NW-36-datasheet.pdf>.

- [74] Vigo Photonics. *PVI-2TE-4-1x1-TO8-wAl₂O₃-36 detector datasheet*. Accessed: 29.07.2022. Vigo Photonics. URL: [https://vigo.com.pl/wp-content/uploads/2021/04/PVI-2TE-4-1x1-TO8-wAl₂O₃-36-datasheet.pdf](https://vigo.com.pl/wp-content/uploads/2021/04/PVI-2TE-4-1x1-TO8-wAl2O3-36-datasheet.pdf).
- [75] Thorlabs. *VL5T0-SpecSheet*. Accessed: 29.07.2022. Thorlabs. URL: <https://www.thorlabs.com/drawings/6fc624f99db1bb7e-E1DD4AC6-DOE4-6899-371328FB695F8DA9/VL5T0-SpecSheet.pdf>.
- [76] Emrah Şaşmaz. “Molecular beam epitaxial growth and characterization of extended short wavelength infrared mercury cadmium telluride detectors”. MA thesis. Middle East Technical University, 2017.
- [77] Teledyne Judson Technologies. *Specifications for 2.5µm SWIR PV MCT Detectors 10-24-2017*. Accessed: 09.08.2022. Teledyne Judson Technologies. URL: <https://www.teledynejudson.com/news/Documents/Specifications%20for%20SWIR%20.5%20MCT%20detectors%20FINAL.pdf>.
- [78] Xing you Chen, Yi Gu, and Yong gang Zhang. “Epitaxy and Device Properties of InGaAs Photodetectors with Relatively High Lattice Mismatch”. In: *Epitaxy*. Ed. by Miao Zhong. Rijeka: IntechOpen, 2017. Chap. 9. DOI: 10.5772/intechopen.70259. URL: <https://doi.org/10.5772/intechopen.70259>.
- [79] Teledyne Judson Technologies. *Specifications for Performance Enhanced 2.6µm Extended InGaAs Detectors 10-23-2017*. Accessed: 09.08.2022. Teledyne Judson Technologies. URL: <https://www.teledynejudson.com/news/Documents/Specifications%20for%20Enhanced%20Performance%20.6%20extended%20InGaAs%20FINAL.pdf>.
- [80] Hamamatsu. *InGaAs PIN photodiodes*. Accessed: 10.08.2022. Hamamatsu. URL: https://www.hamamatsu.com/content/dam/hamamatsu-photonics/sites/documents/99_SALES_LIBRARY/ssd/g12183_series_kird1119e.pdf.
- [81] EOC. *InGaAs Photodiodes – Extended TE Cooled*. Accessed: 10.08.2022. EOC. URL: <https://www.eoc-inc.com/ir-detectors/ingaas-photodiodes-extended-te-cooled/>.
- [82] C. Besikci. “Extended short wavelength infrared FPA technology: status and trends”. In: *Quantum Sensing and Nano Electronics and Photonics XV*. Ed. by

- Manijeh Razeghi *et al.* Vol. 10540. International Society for Optics and Photonics. SPIE, 2018, 105400P. DOI: [10.1117/12.2289822](https://doi.org/10.1117/12.2289822). URL: <https://doi.org/10.1117/12.2289822>.
- [83] Lars Zimmermann *et al.* "Extended wavelength InGaAs on GaAs using InAlAs buffer for back-side-illuminated short-wave infrared detectors". In: *Applied Physics Letters* 82.17 (2003), pp. 2838–2840. DOI: [10.1063/1.1569042](https://doi.org/10.1063/1.1569042).
- [84] G. W. Wicks *et al.* "Extended-shortwave infrared unipolar barrier detectors". In: *Quantum Sensing and Nanophotonic Devices XII*. Ed. by Manijeh Razeghi, Eric Tournié, and Gail J. Brown. Vol. 9370. International Society for Optics and Photonics. SPIE, 2015, p. 937023. DOI: [10.1117/12.2083861](https://doi.org/10.1117/12.2083861). URL: <https://doi.org/10.1117/12.2083861>.
- [85] Nong Li *et al.* "The investigations to eliminate the bias dependency of quantum efficiency of InGaAsSb nBn photodetectors for extended short wavelength infrared detection". In: *Infrared Physics Technology* 111 (2020), p. 103461. ISSN: 1350-4495. DOI: <https://doi.org/10.1016/j.infrared.2020.103461>. URL: <https://www.sciencedirect.com/science/article/pii/S1350449520305090>.
- [86] I. Shafir *et al.* "High responsivity InGaAsSb p–n photodetector for extended SWIR detection". In: *Applied Physics Letters* 118.6 (2021), p. 063503. DOI: [10.1063/5.0037192](https://doi.org/10.1063/5.0037192).
- [87] Antoni Rogalski *et al.* "Trends in Performance Limits of the HOT Infrared Photodetectors". In: *Applied Sciences* 11.2 (2021). ISSN: 2076-3417. DOI: [10.3390/app11020501](https://doi.org/10.3390/app11020501). URL: <https://www.mdpi.com/2076-3417/11/2/501>.
- [88] Hamamatsu. *InAs photovoltaic Detectors*. Accessed: 19.08.2021. Hamamatsu. URL: https://www.hamamatsu.com/resources/pdf/ssd/p10090-01_etc_kird1099e.pdf.
- [89] Hamamatsu. *InAsSb photovoltaic Detectors*. Accessed: 10.08.2022. Hamamatsu. URL: https://www.hamamatsu.com/content/dam/hamamatsu-photonics/sites/documents/99_SALES_LIBRARY/ssd/p16612-011ca_kird1145e.pdf.

- [90] Adam Craig *et al.* "InAsSb-based detectors on GaSb for near-room -temperature operation in the mid-wave infrared". English. In: *Applied Physics Letters* (June 2021). ISSN: 0003-6951.
- [91] David Z. Ting *et al.* "Advances in III-V semiconductor infrared absorbers and detectors". In: *Infrared Physics Technology* 97 (2019), pp. 210–216. ISSN: 1350-4495. DOI: <https://doi.org/10.1016/j.infrared.2018.12.034>. URL: <https://www.sciencedirect.com/science/article/pii/S1350449518305218>.
- [92] Baile Chen *et al.* "SWIR/MWIR InP-Based p-i-n Photodiodes With InGaAs/GaAsSb Type-II Quantum Wells". In: *IEEE Journal of Quantum Electronics* 47.9 (2011), pp. 1244–1250. DOI: [10.1109/JQE.2011.2160450](https://doi.org/10.1109/JQE.2011.2160450).
- [93] Y. Uliel *et al.* "InGaAs/GaAsSb Type-II superlattice based photodiodes for short wave infrared detection". In: *Infrared Physics Technology* 84 (2017). Quantum Structure Infrared Photodetector 2016 (QSIP2016), pp. 63–71. ISSN: 1350-4495. DOI: <https://doi.org/10.1016/j.infrared.2017.02.003>. URL: <https://www.sciencedirect.com/science/article/pii/S1350449516306028>.
- [94] A. M. Hoang *et al.* "Demonstration of shortwavelength infrared photodiodes based on type-II InAs/GaSb/AlSb superlattices". In: *Applied Physics Letters* 100.21 (2012), p. 211101. DOI: [10.1063/1.4720094](https://doi.org/10.1063/1.4720094).
- [95] Anh Minh Hoang *et al.* "High performance bias-selectable three-color Short-wave/Mid-wave/Long-wave Infrared Photodetectors based on Type-II InAs/GaSb/AlSb superlattices". In: *Scientific Reports* 6.1 (2016), p. 24144. ISSN: 2045-2322. DOI: [10.1038/srep24144](https://doi.org/10.1038/srep24144). URL: <https://doi.org/10.1038/srep24144>.
- [96] G.B. Airy. "VI. On the phænomena of Newton's rings when formed between two transparent substances of different refractive powers". In: *The London, Edinburgh, and Dublin Philosophical Magazine and Journal of Science* 2.7 (1833), pp. 20–30. DOI: [10.1080/14786443308647959](https://doi.org/10.1080/14786443308647959). URL: <https://doi.org/10.1080/14786443308647959>.
- [97] A. A. Michelson and E. W. Morley. "On the relative motion of the Earth and the luminiferous ether". In: *American Journal of Science* s3-34.203 (1887), pp. 333–345. ISSN: 0002-9599. DOI: [10.2475/ajs.s3-34.203.333](https://doi.org/10.2475/ajs.s3-34.203.333). URL: <https://www.ajsonline.org/content/s3-34/203/333>.

- [98] H. A. Rowland. "On concave gratings for optical purposes". In: *American Journal of Science* s3-26.152 (1883), pp. 87–98. ISSN: 0002-9599. DOI: [10.2475/ajs.s3-26.152.87](https://doi.org/10.2475/ajs.s3-26.152.87). URL: <https://www.ajsonline.org/content/s3-26/152/87>.
- [99] C. Fabry and A. Pérot. "Théorie et applications d'une nouvelle méthode de spectroscopie interférentielle". In: *Ann. de Chim. et de Phys.* 16.7 (1899).
- [100] Megh Nad Saha. "On the Limit of Interference in the Fabry-Perot Interferometer". In: *Phys. Rev.* 10 (6 1917), pp. 782–786. DOI: [10.1103/PhysRev.10.782](https://doi.org/10.1103/PhysRev.10.782). URL: <https://link.aps.org/doi/10.1103/PhysRev.10.782>.
- [101] William V. Houston. "A Compound Interferometer for Fine Structure Work". In: *Phys. Rev.* 29 (3 1927), pp. 478–484. DOI: [10.1103/PhysRev.29.478](https://doi.org/10.1103/PhysRev.29.478). URL: <https://link.aps.org/doi/10.1103/PhysRev.29.478>.
- [102] J.J. Goedbloed. "Responsivity of avalanche photodiodes in the presence of multiple reflections". English. In: *Electronics Letters* 12 (14 1976), 363–364(1). ISSN: 0013-5194. URL: https://digital-library.theiet.org/content/journals/10.1049/el_19760278.
- [103] Haruhisa Soda *et al.* "GaInAsP/InP Surface Emitting Injection Lasers". In: *Japanese Journal of Applied Physics* 18.12 (1979), pp. 2329–2330. DOI: [10.1143/jjap.18.2329](https://doi.org/10.1143/jjap.18.2329). URL: <https://doi.org/10.1143/jjap.18.2329>.
- [104] A. Chailertvanitkul. "GaInAsP/InP surface emitting laser (= 1.4 m, 77 K) with heteromultilayer Bragg reflector". English. In: *Electronics Letters* 21 (7 1985), 303–304(1). ISSN: 0013-5194. URL: https://digital-library.theiet.org/content/journals/10.1049/el_19850216.
- [105] R.S. Geels and L.A. Coldren. "Narrow-linewidth, low threshold vertical-cavity surface-emitting lasers". In: *12th IEEE International Conference on Semiconductor Laser*. 1990, pp. 16–17. DOI: [10.1109/ISLC.1990.764408](https://doi.org/10.1109/ISLC.1990.764408).
- [106] M. S. Ünlü *et al.* "Resonant cavity enhanced AlGaAs/GaAs heterojunction phototransistors with an intermediate InGaAs layer in the collector". In: *Applied Physics Letters* 57.8 (1990), pp. 750–752. DOI: [10.1063/1.103410](https://doi.org/10.1063/1.103410). URL: <https://doi.org/10.1063/1.103410>.

- [107] M. S. Ünlü *et al.* "A theoretical study of resonant cavity-enhanced photodetectors with Ge and Si active regions". In: *Journal of Applied Physics* 71.8 (1992), pp. 4049–4058. DOI: [10.1063/1.350829](https://doi.org/10.1063/1.350829). URL: <https://doi.org/10.1063/1.350829>.
- [108] B. Corbett *et al.* "Resonant cavity light emitting diode and detector using epitaxial liftoff". In: *IEEE Photonics Technology Letters* 5.9 (1993), pp. 1041–1043. DOI: [10.1109/68.257185](https://doi.org/10.1109/68.257185).
- [109] Albert Chin and T. Y. Chang. "Multilayer reflectors by molecular-beam epitaxy for resonance enhanced absorption in thin high-speed detectors". In: *Journal of Vacuum Science & Technology B: Microelectronics Processing and Phenomena* 8.2 (1990), pp. 339–342. DOI: [10.1116/1.585066](https://doi.org/10.1116/1.585066). URL: <https://avs.scitation.org/doi/abs/10.1116/1.585066>.
- [110] A.G. Dentai. "High quantum efficiency, long wavelength InP/InGaAs microcavity photodiode". English. In: *Electronics Letters* 27 (23 1991), 2125–2127(2). ISSN: 0013-5194. URL: https://digital-library.theiet.org/content/journals/10.1049/el_19911316.
- [111] B.M. Onat *et al.* "100-GHz resonant cavity enhanced Schottky photodiodes". In: *IEEE Photonics Technology Letters* 10.5 (1998), pp. 707–709. DOI: [10.1109/68.669338](https://doi.org/10.1109/68.669338).
- [112] M. Gokkavas *et al.* "Design and optimization of high-speed resonant cavity enhanced Schottky photodiodes". In: *IEEE Journal of Quantum Electronics* 35.2 (1999), pp. 208–215. DOI: [10.1109/3.740742](https://doi.org/10.1109/3.740742).
- [113] Ekmel Özbay *et al.* "High-speed >90% quantum-efficiency p-i-n photodiodes with a resonance wavelength adjustable in the 795–835 nm range". In: *Applied Physics Letters* 74.8 (1999), pp. 1072–1074. DOI: [10.1063/1.123485](https://doi.org/10.1063/1.123485). URL: <https://doi.org/10.1063/1.123485>.
- [114] Alex M Green *et al.* "∼ 3 μm InAs resonant-cavity-enhanced photodetector". In: *Semiconductor Science and Technology* 18.11 (2003), pp. 964–967. DOI: [10.1088/0268-1242/18/11/310](https://doi.org/10.1088/0268-1242/18/11/310). URL: <https://doi.org/10.1088/0268-1242/18/11/310>.

- [115] Jianfei Wang *et al.* "Resonant-cavity-enhanced mid-infrared photodetector on a silicon platform". In: *Opt. Express* 18.12 (2010), pp. 12890–12896. DOI: [10.1364/OE.18.012890](https://doi.org/10.1364/OE.18.012890). URL: <http://www.opticsexpress.org/abstract.cfm?URI=oe-18-12-12890>.
- [116] Tetsuya Asano *et al.* "Design Consideration and Demonstration of Resonant-Cavity-Enhanced Quantum Dot Infrared Photodetectors in Mid-Infrared Wavelength Regime (3–5 μm)". In: *IEEE Journal of Quantum Electronics* 46.10 (2010), pp. 1484–1491. DOI: [10.1109/JQE.2010.2052351](https://doi.org/10.1109/JQE.2010.2052351).
- [117] R. Kuchibhotla *et al.* "Low-voltage high-gain resonant-cavity avalanche photodiode". In: *IEEE Photonics Technology Letters* 3.4 (1991), pp. 354–356. DOI: [10.1109/68.82110](https://doi.org/10.1109/68.82110).
- [118] A. Shen *et al.* "Resonant-cavity-enhanced p-type GaAs/AlGaAs quantum-well infrared photodetectors". In: *Applied Physics Letters* 77.15 (2000), pp. 2400–2402. DOI: [10.1063/1.1317548](https://doi.org/10.1063/1.1317548). URL: <https://doi.org/10.1063/1.1317548>.
- [119] Li Jun *et al.* "Design of a resonant-cavity-enhanced GaInAsSb/GaSb photodetector". In: *Semiconductor Science and Technology* 19 (2004), pp. 690–694.
- [120] J. G. A. Wehner *et al.* "Mercury cadmium telluride resonant-cavity-enhanced photoconductive infrared detectors". In: *Applied Physics Letters* 87.21 (2005), p. 211104. DOI: [10.1063/1.2133914](https://doi.org/10.1063/1.2133914). URL: <https://doi.org/10.1063/1.2133914>.
- [121] Martin Arnold, Dmitry Zimin, and Hans Zogg. "Resonant-cavity-enhanced photodetectors for the mid-infrared". In: *Applied Physics Letters* 87.14 (2005), p. 141103. DOI: [10.1063/1.2061855](https://doi.org/10.1063/1.2061855). URL: <https://doi.org/10.1063/1.2061855>.
- [122] Joseph A. Faucher, George M. McManus, and Hans J. Trurnit. "Simplified Treatment of Ellipsometry". In: *J. Opt. Soc. Am.* 48.1 (1958), pp. 51–54. DOI: [10.1364/JOSA.48.000051](https://doi.org/10.1364/JOSA.48.000051). URL: <http://opg.optica.org/abstract.cfm?URI=josa-48-1-51>.
- [123] Frank L McCrackin *et al.* "Measurement of the thickness and refractive index of very thin films and the optical properties of surfaces by ellipsometry". In:

- Journal of Research of the National Bureau of Standards. Section A, Physics and Chemistry* 67.4 (1963), p. 363.
- [124] S. Roux *et al.* "Mid-infrared characterization of refractive indices and propagation losses in GaSb/Al_xGa_{1-x}AsSb waveguides". In: *Applied Physics Letters* 107.17 (2015), p. 171901. DOI: [10.1063/1.4934702](https://doi.org/10.1063/1.4934702). eprint: <https://doi.org/10.1063/1.4934702>. URL: <https://doi.org/10.1063/1.4934702>.
- [125] H.M. Shabana. "Determination of film thickness and refractive index by interferometry". In: *Polymer Testing* 23.6 (2004), pp. 695–702. ISSN: 0142-9418. DOI: <https://doi.org/10.1016/j.polymeresting.2004.01.006>. URL: <https://www.sciencedirect.com/science/article/pii/S014294180400011X>.
- [126] O. G. Lorimor and W. G. Spitzer. "Infrared Refractive Index and Absorption of InAs and CdTe". In: *Journal of Applied Physics* 36.6 (1965), pp. 1841–1844. DOI: [10.1063/1.1714362](https://doi.org/10.1063/1.1714362). eprint: <https://doi.org/10.1063/1.1714362>. URL: <https://doi.org/10.1063/1.1714362>.
- [127] C. Alibert *et al.* "Refractive indices of AlSb and GaSb-lattice-matched Al_xGa_{1-x}As_ySb_{1-y} in the transparent wavelength region". In: *Journal of Applied Physics* 69.5 (1991), pp. 3208–3211. DOI: [10.1063/1.348538](https://doi.org/10.1063/1.348538).
- [128] R. E. Fern and A. Onton. "Refractive Index of AlAs". In: *Journal of Applied Physics* 42.9 (1971), pp. 3499–3500. DOI: [10.1063/1.1660760](https://doi.org/10.1063/1.1660760).
- [129] M. Garriga *et al.* "Optical properties of AlAs". In: *Solid State Communications* 61.3 (1987), pp. 157–160. ISSN: 0038-1098. DOI: [https://doi.org/10.1016/0038-1098\(87\)90021-4](https://doi.org/10.1016/0038-1098(87)90021-4). URL: <https://www.sciencedirect.com/science/article/pii/0038109887900214>.
- [130] P. P. Paskov. "Refractive indices of InSb, InAs, GaSb, InAs_xSb_{1-x}, and In_{1-x}Ga_xSb: Effects of free carriers". In: *Journal of Applied Physics* 81.4 (1997), pp. 1890–1898. DOI: [10.1063/1.365360](https://doi.org/10.1063/1.365360).
- [131] M Cross and MJ Adams. "Effects of doping and free carriers on the refractive index of direct-gap semiconductors". In: *Opto-electronics* 6.3 (1974), pp. 199–216.

- [132] S. Adachi. *Properties of Group-IV, III-V and II-VI Semiconductors*. Wiley Series in Materials for Electronic & Optoelectronic Applications. Wiley, 2005. ISBN: 9780470090336. URL: <https://books.google.co.uk/books?id=0zttCBkw5-sC>.
- [133] Thomas G. Mayerhöfer, Susanne Pahlow, and Jürgen Popp. “The Bouguer-Beer-Lambert Law: Shining Light on the Obscure”. In: *ChemPhysChem* 21.18 (2020), pp. 2029–2046. DOI: <https://doi.org/10.1002/cphc.202000464>. eprint: <https://chemistry-europe.onlinelibrary.wiley.com/doi/pdf/10.1002/cphc.202000464>. URL: <https://chemistry-europe.onlinelibrary.wiley.com/doi/abs/10.1002/cphc.202000464>.
- [134] M Levinshtein, S Rumyantsev, and M Shur. *Handbook Series on Semiconductor Parameters*. WORLD SCIENTIFIC, 1996. DOI: [10.1142/2046-vol1](https://doi.org/10.1142/2046-vol1). eprint: <https://www.worldscientific.com/doi/pdf/10.1142/2046-vol1>. URL: <https://www.worldscientific.com/doi/abs/10.1142/2046-vol1>.
- [135] Jack R Dixon and James M Ellis. “Optical properties of n-type indium arsenide in the fundamental absorption edge region”. In: *Physical Review* 123.5 (1961), p. 1560.
- [136] A. I. D’Souza *et al.* “Electrooptical Characterization of MWIR InAsSb Detectors”. In: *Journal of Electronic Materials* 41.10 (2012), pp. 2671–2678. ISSN: 1543-186X. DOI: [10.1007/s11664-012-2182-7](https://doi.org/10.1007/s11664-012-2182-7). URL: <https://doi.org/10.1007/s11664-012-2182-7>.
- [137] M. A. Marciniak *et al.* “Optical characterization of molecular beam epitaxially grown InAsSb nearly lattice matched to GaSb”. In: *Journal of Applied Physics* 84.1 (1998), pp. 480–488. DOI: [10.1063/1.368051](https://doi.org/10.1063/1.368051).
- [138] J. Borrego, M. Zierak, and G. Charache. “Parameter extraction for TPV cell development”. In: *AIP Conference Proceedings* 321.1 (1995), pp. 371–378. DOI: [10.1063/1.47046](https://doi.org/10.1063/1.47046).
- [139] G. W. Charache *et al.* “InGaAsSb thermophotovoltaic diode: Physics evaluation”. In: *Journal of Applied Physics* 85.4 (1999), pp. 2247–2252. DOI: [10.1063/1.369533](https://doi.org/10.1063/1.369533).

- [140] E. D. Palik. *Handbook of optical constants of solids*. eng. San Diego: Academic Press, 1998. ISBN: 9781601192707.
- [141] Michael W. Dashiell *et al.* "Quaternary InGaAsSb Thermophotovoltaic Diodes". In: *IEEE Transactions on Electron Devices* 53.12 (2006), pp. 2879–2891. DOI: [10.1109/TED.2006.885087](https://doi.org/10.1109/TED.2006.885087).
- [142] M. Nurul Abedin *et al.* "Characterization and analysis of InGaAsSb detectors". In: *Infrared Technology and Applications XXIX*. Ed. by Bjorn F. Andresen and Gabor F. Fulop. Vol. 5074. International Society for Optics and Photonics. SPIE, 2003, pp. 332–342. DOI: [10.1117/12.486345](https://doi.org/10.1117/12.486345). URL: <https://doi.org/10.1117/12.486345>.
- [143] V. Weldon *et al.* "H₂S and CO₂ gas sensing using DFB laser diodes emitting at 1.57 μm". In: *Sensors and Actuators B: Chemical* 29.1 (1995). Proceedings of the 2nd European Conference on Optical Chemical Sensors and Biosensors, pp. 101–107. ISSN: 0925-4005. DOI: [https://doi.org/10.1016/0925-4005\(95\)01669-4](https://doi.org/10.1016/0925-4005(95)01669-4).
- [144] Alexandru Mereuta *et al.* "In(Al)GaAs–AlGaAs Wafer Fused VCSELs Emitting at 2 μm Wavelength". In: *IEEE Photonics Technology Letters* 20.1 (2008), pp. 24–26. DOI: [10.1109/LPT.2007.910757](https://doi.org/10.1109/LPT.2007.910757).
- [145] D. Weidmann *et al.* "Mid-infrared trace-gas sensing with a quasi-continuous-wave Peltier-cooled distributed feedback quantum cascade laser". In: *Applied Physics B* 79.7 (2004), pp. 907–913. ISSN: 1432-0649. DOI: [10.1007/s00340-004-1634-z](https://doi.org/10.1007/s00340-004-1634-z). URL: <https://doi.org/10.1007/s00340-004-1634-z>.
- [146] GASCARD NG. Edinburgh Sensors. 2021. URL: <https://edinburghsensors.com/products/oem-co2-sensor/>.
- [147] Andreas Genner *et al.* "A Quantum Cascade Laser-Based Multi-Gas Sensor for Ambient Air Monitoring". In: *Sensors* 20.7 (2020). ISSN: 1424-8220. DOI: [10.3390/s20071850](https://doi.org/10.3390/s20071850). URL: <https://www.mdpi.com/1424-8220/20/7/1850>.
- [148] Hamamatsu. *Devices for Gas Measurement*. Accessed: 10.08.2022. Hamamatsu. URL: https://www.hamamatsu.com/content/dam/hamamatsu-photonics/sites/documents/99_SALES_LIBRARY/ssd/CAFP1002E.pdf.

- [149] Daniel Popa and Florin Udrea. "Towards Integrated Mid-Infrared Gas Sensors". In: *Sensors* 19.9 (2019). ISSN: 1424-8220. DOI: [10.3390/s19092076](https://doi.org/10.3390/s19092076). URL: <https://www.mdpi.com/1424-8220/19/9/2076>.
- [150] Hiromi Fujita *et al.* "AlInSb Mid-Infrared LEDs of High Luminous Efficiency for Gas Sensors". In: *physica status solidi (a)* 215.8 (2018), p. 1700449. DOI: <https://doi.org/10.1002/pssa.201700449>. URL: <https://onlinelibrary.wiley.com/doi/abs/10.1002/pssa.201700449>.
- [151] N. Pelin Ayerden and Reinoud F. Wolffenbuttel. "The Miniaturization of an Optical Absorption Spectrometer for Smart Sensing of Natural Gas". In: *IEEE Transactions on Industrial Electronics* 64.12 (2017), pp. 9666–9674. DOI: [10.1109/TIE.2017.2719600](https://doi.org/10.1109/TIE.2017.2719600).
- [152] MohammadSadeqh Faraji-Dana *et al.* "Compact folded metasurface spectrometer". In: *Nature Communications* 9.1 (2018), p. 4196. ISSN: 2041-1723. DOI: [10.1038/s41467-018-06495-5](https://doi.org/10.1038/s41467-018-06495-5). URL: <https://doi.org/10.1038/s41467-018-06495-5>.
- [153] Zongyin Yang *et al.* "Single-nanowire spectrometers". In: *Science* 365.6457 (2019), pp. 1017–1020. ISSN: 0036-8075. DOI: [10.1126/science.aax8814](https://doi.org/10.1126/science.aax8814). URL: <https://science.sciencemag.org/content/365/6457/1017>.
- [154] Brandon Redding *et al.* "Compact spectrometer based on a disordered photonic chip". In: *Nature Photonics* 7.9 (2013), pp. 746–751. ISSN: 1749-4893. DOI: [10.1038/nphoton.2013.190](https://doi.org/10.1038/nphoton.2013.190). URL: <https://doi.org/10.1038/nphoton.2013.190>.
- [155] R.F.C. Farrow. *Molecular Beam Epitaxy - Applications to Key Materials*. William Andrew Publishing/Noyes, 1995. ISBN: 978-0-8155-1371-1. URL: <https://app.knovel.com/hotlink/khtml/id:kt005HSZQ1/molecular-beam-epitaxy/technology-introduction>.
- [156] Veeco. *SUMO Source*. Accessed: 18.08.2021. Veeco. URL: <https://www.veeco.com/products/sumo-source/>.
- [157] J.W. Matthews and A.E. Blakeslee. "Defects in epitaxial multilayers: I. Misfit dislocations". In: *Journal of Crystal Growth* 27 (1974), pp. 118–125. ISSN: 0022-

0248. DOI: [https://doi.org/10.1016/S0022-0248\(74\)80055-2](https://doi.org/10.1016/S0022-0248(74)80055-2). URL: <https://www.sciencedirect.com/science/article/pii/S0022024874800552>.
- [158] Veronica Letka. "Medium- and long-wavelength InAs/InAsSb strained-layer superlattices for applications in infrared nBn detectors". English. PhD thesis. Lancaster University, 2019. DOI: [10.17635/lancaster/thesis/598](https://doi.org/10.17635/lancaster/thesis/598).
- [159] S.L. Chuang. *Physics of Optoelectronic Devices*. Wiley Series in Pure and Applied Optics. Wiley, 1995. ISBN: 9780471109396. URL: <https://books.google.co.uk/books?id=ect6QgAACAAJ>.
- [160] Imtiaz Madni *et al.* "MBE-growth of CdTe on GaSb substrates: A case study on the influence of substrate quality". In: *Materials Chemistry and Physics* 214 (Apr. 2018). DOI: [10.1016/j.matchemphys.2018.04.096](https://doi.org/10.1016/j.matchemphys.2018.04.096).
- [161] G. Koster, M. Huijben, and G. Rijnders. *Epitaxial Growth of Complex Metal Oxides*. Elsevier, 2015. ISBN: 978-1-78242-245-7. URL: <https://app.knovel.com/hotlink/khtml/id:kt00UD3Y83/epitaxial-growth-complex/basic-principles-rheed>.
- [162] Philip I. Cohen. Ayahiko Ichimiya. *Reflection High-Energy Electron Diffraction*. Cambridge University Press, 2004. ISBN: 9780521453738. URL: <https://www.cambridge.org/gb/academic/subjects/engineering/materials-science/reflection-high-energy-electron-diffraction?format=HB&isbn=9780521453738>.
- [163] *Microposit s1800 series photo resists*. Shipley. 2021. URL: https://amolf.nl/wp-content/uploads/2016/09/datasheets_S1800.pdf.
- [164] *Microposit MF CD-26 Developer*. Shipley. 2021. URL: https://kayakuam.com/wp-content/uploads/2019/10/MF_CD_26_Data_Sheet.pdf.
- [165] H. U. Rahman *et al.* "Fabrication and characterization of PECVD silicon nitride for RF MEMS applications". In: *Microsystem Technologies* 19.1 (2013), pp. 131–136. ISSN: 1432-1858. DOI: [10.1007/s00542-012-1522-0](https://doi.org/10.1007/s00542-012-1522-0). URL: <https://doi.org/10.1007/s00542-012-1522-0>.

- [166] SU-8 2000 Permanent Negative Epoxy Photoresist. SU-8 2000. ver. 1. Kayaku. 2020. URL: <https://kayakuam.com/wp-content/uploads/2020/08/KAM-SU-8-2000-2000.5-2015-Datasheet-8.13.20-final.pdf>.
- [167] SU-8 for Dielectrics in Organic TFT Back-Planes. URL: <https://kayakuam.com/products/display-dielectric-layers/>.
- [168] Pin Jem Ker *et al.* "Surface passivation of InAs avalanche photodiodes for low-noise infrared imaging". In: *2016 IEEE 6th International Conference on Photonics (ICP)*. 2016, pp. 1–3. DOI: [10.1109/ICP.2016.7510018](https://doi.org/10.1109/ICP.2016.7510018).
- [169] VeeMAX III – The Ultimate Variable Angle Specular Reflectance Accessory. VeeMax III. Pike Technologies. 2018. URL: https://www.piketech.com/files/pdfs/PIKE_VeeMAX_III_Specular_Reflectance_Data_Sheet.pdf.
- [170] Antoni Rogalski. "Infrared detectors: status and trends". In: *Progress in Quantum Electronics* 27.2 (2003), pp. 59–210. ISSN: 0079-6727. DOI: [https://doi.org/10.1016/S0079-6727\(02\)00024-1](https://doi.org/10.1016/S0079-6727(02)00024-1). URL: <https://www.sciencedirect.com/science/article/pii/S0079672702000241>.
- [171] Howard W. Yoon, Matt C. Dopkiss, and George P. Eppeldauer. "Performance comparisons of InGaAs, extended InGaAs, and short-wave HgCdTe detectors between 1 μm and 2.5 μm ". In: *Infrared Spaceborne Remote Sensing XIV*. Ed. by Marija Strojnik. Vol. 6297. International Society for Optics and Photonics. SPIE, 2006, pp. 16–25. DOI: [10.1117/12.684614](https://doi.org/10.1117/12.684614). URL: <https://doi.org/10.1117/12.684614>.
- [172] Sadao Adachi. *III-V Ternary and Quaternary Compounds*. Springer, Cham: Springer Handbooks, 2017, pp. 725–741. DOI: [10.1007/978-3-319-48933-9_30](https://doi.org/10.1007/978-3-319-48933-9_30).
- [173] M. Astles *et al.* "Studies of the Ga_{1-x}In_xAs_{1-y}Sb_y quaternary alloy system I. liquid-phase epitaxial growth and assessment". In: *Journal of Electronic Materials* 15.1 (1986), pp. 41–49. ISSN: 1543-186X. DOI: [10.1007/BF02649949](https://doi.org/10.1007/BF02649949). URL: <https://doi.org/10.1007/BF02649949>.
- [174] Thomas F. Kuech, Susan E. Babcock, and Luke Mawst. "Growth far from equilibrium: Examples from III-V semiconductors". In: *Applied Physics Re-*

- views* 3.4 (2016), p. 040801. DOI: [10.1063/1.4944801](https://doi.org/10.1063/1.4944801). URL: <https://doi.org/10.1063/1.4944801>.
- [175] E. Tournié *et al.* "High temperature liquid phase epitaxy of (100) oriented GaInAsSb near the miscibility gap boundary". In: *Journal of Crystal Growth* 104.3 (1990), pp. 683–694. ISSN: 0022-0248. DOI: [https://doi.org/10.1016/0022-0248\(90\)90012-A](https://doi.org/10.1016/0022-0248(90)90012-A). URL: <https://www.sciencedirect.com/science/article/pii/002202489090012A>.
- [176] M P C M Krijn. "Heterojunction band offsets and effective masses in III-V quaternary alloys". In: *Semiconductor Science and Technology* 6.1 (1991), pp. 27–31. DOI: [10.1088/0268-1242/6/1/005](https://doi.org/10.1088/0268-1242/6/1/005). URL: <https://doi.org/10.1088/0268-1242/6/1/005>.
- [177] S. Subbanna, G. Tuttle, and H. Kroemer. "N- type doping of gallium antimonide and aluminum antimonide grown by molecular beam epitaxy using lead telluride as a tellurium dopant source". In: *Journal of Electronic Materials* 17.4 (1988), pp. 297–303. ISSN: 1543-186X. DOI: [10.1007/BF02652109](https://doi.org/10.1007/BF02652109). URL: <https://doi.org/10.1007/BF02652109>.
- [178] A.P. Craig *et al.* "Reprint of "Mid-infrared InAsSb-based nBn photodetectors with AlGaAsSb barrier layers – grown on GaAs, using an interfacial misfit array, and on native GaSb"". In: *Infrared Physics Technology* 70 (2015). Proceedings of International Conference on Quantum Structures Infrared Photodetectors, 2014, pp. 107–110. ISSN: 1350-4495. DOI: <https://doi.org/10.1016/j.infrared.2015.05.006>. URL: <https://www.sciencedirect.com/science/article/pii/S1350449515001000>.
- [179] S.K. Tripathy. "Refractive indices of semiconductors from energy gaps". In: *Optical Materials* 46 (2015), pp. 240–246. ISSN: 0925-3467. DOI: <https://doi.org/10.1016/j.optmat.2015.04.026>. URL: <https://www.sciencedirect.com/science/article/pii/S0925346715002542>.
- [180] Y. P. Varshni. "Temperature dependence of the energy gap in semiconductors". In: *Physica* 34.1 (Jan. 1967), pp. 149–154. DOI: [10.1016/0031-8914\(67\)90062-6](https://doi.org/10.1016/0031-8914(67)90062-6).

- [181] Martín Muñoz *et al.* "Temperature dependence of the energy and broadening parameter of the fundamental band gap of GaSb and $\text{Ga}_{1-x}\text{In}_x\text{As}_y\text{Sb}_{1-y}$ /GaSb ($0.07 < x < 0.22$, $0.05 < y < 0.19$) quaternary alloys using infrared photoreflectance". In: *Phys. Rev. B* 62 (24 2000), pp. 16600–16604. DOI: [10.1103/PhysRevB.62.16600](https://doi.org/10.1103/PhysRevB.62.16600). URL: <https://link.aps.org/doi/10.1103/PhysRevB.62.16600>.
- [182] Pallab Bhattacharya. *3.2 The Effect of Temperature and Pressure on InGaAs Band Structure*. 1993. URL: <https://app.knovel.com/hotlink/khtml/id:kt003LY032/properties-lattice-matched/effect-temperature-pressure>.
- [183] J. Singh. "Physics of Semiconductors and Their Heterostructures". In: 1992.
- [184] I. Vurgaftman, J. R. Meyer, and L. R. Ram-Mohan. "Band parameters for III–V compound semiconductors and their alloys". In: *Journal of Applied Physics* 89.11 (2001), pp. 5815–5875. DOI: [10.1063/1.1368156](https://doi.org/10.1063/1.1368156). URL: <https://doi.org/10.1063/1.1368156>.
- [185] C. L. Littler and D. G. Seiler. "Temperature dependence of the energy gap of InSb using nonlinear optical techniques". In: *Applied Physics Letters* 46.10 (1985), pp. 986–988. DOI: [10.1063/1.95789](https://doi.org/10.1063/1.95789). URL: <https://doi.org/10.1063/1.95789>.
- [186] Elena Plis *et al.* "Lateral diffusion of minority carriers in InAsSb-based nBn detectors". In: *Applied Physics Letters* 97.12 (2010), p. 123503. DOI: [10.1063/1.3492853](https://doi.org/10.1063/1.3492853). eprint: <https://doi.org/10.1063/1.3492853>. URL: <https://doi.org/10.1063/1.3492853>.
- [187] A. B. Ikyo *et al.* "Temperature stable mid-infrared GaInAsSb/GaSb Vertical Cavity Surface Emitting Lasers (VCSELs)". In: *Scientific Reports* 6.1 (2016), p. 19595. ISSN: 2045-2322. DOI: [10.1038/srep19595](https://doi.org/10.1038/srep19595). URL: <https://doi.org/10.1038/srep19595>.
- [188] A Perona *et al.* "AlAsSb/GaSb doped distributed Bragg reflectors for electrically pumped VCSELs emitting around 2.3 μm , journal = Semiconductor Science and Technology," in: 22.10 (2007), pp. 1140–1144. DOI: [10.1088/0268-1242/22/10/010](https://doi.org/10.1088/0268-1242/22/10/010). URL: <https://doi.org/10.1088/0268-1242/22/10/010>.

- [189] Alexander Andrejew, Stephan Sprengel, and Markus-Christian Amann. "GaSb-based vertical-cavity surface-emitting lasers with an emission wavelength at $3\ \mu\text{m}$ ". In: *Opt. Lett.* 41.12 (2016), pp. 2799–2802. DOI: [10.1364/OL.41.002799](https://doi.org/10.1364/OL.41.002799). URL: <http://opg.optica.org/ol/abstract.cfm?URI=ol-41-12-2799>.
- [190] Dekang Chen *et al.* "Demonstration of infrared nBn photodetectors based on the AlInAsSb digital alloy materials system". In: *Applied Physics Letters* 119.3 (2021), p. 031101. DOI: [10.1063/5.0058462](https://doi.org/10.1063/5.0058462). eprint: <https://doi.org/10.1063/5.0058462>. URL: <https://doi.org/10.1063/5.0058462>.
- [191] A. P. Craig *et al.* "Resonant cavity enhanced photodiodes on GaSb for the mid-wave infrared". In: *Appl. Phys. Lett.* 114.15 (2019), p. 151107. DOI: [10.1063/1.5082895](https://doi.org/10.1063/1.5082895).
- [192] W.E. Tennant *et al.* "MBE HgCdTe Technology: A Very General Solution to IR Detection, Described by "Rule 07", a Very Convenient Heuristic". In: *J. Electron. Mater.* 37.9 (2008), 1406–1410. DOI: [10.1007/s11664-008-0426-3](https://doi.org/10.1007/s11664-008-0426-3).
- [193] J.S. Blakemore. *Semiconductor Statistics*. Dover Books on Physics Series. Dover, 2002. ISBN: 9780486495026. URL: <https://books.google.co.uk/books?id=cc4HE2YM1FIC>.
- [194] *Indium Gallium Arsenide Detectors*. URL: http://www.teledynejudson.com/prods/Documents/InGaAs_shortform_Sept2003.pdf (visited on 07/20/2022).
- [195] H. Hao *et al.* "Extended-wavelength InGaAsSb infrared unipolar barrier detectors". In: *AIP Adv.* 8.9 (2018), p. 095106. DOI: [10.1063/1.5026839](https://doi.org/10.1063/1.5026839).
- [196] V. Letka *et al.* "A superlattice-based resonant cavity-enhanced photodetector operating in the long-wavelength infrared". In: *Applied Physics Letters* 117.7 (2020), p. 073503. DOI: [10.1063/5.0013553](https://doi.org/10.1063/5.0013553). eprint: <https://doi.org/10.1063/5.0013553>. URL: <https://doi.org/10.1063/5.0013553>.
- [197] George M. Hale and Marvin R. Querry. "Optical Constants of Water in the 200 nm to 200 μm Wavelength Region". In: *Appl. Opt.* 12.3 (1973), pp. 555–563. DOI: [10.1364/AO.12.000555](https://doi.org/10.1364/AO.12.000555). URL: <http://ao.osa.org/abstract.cfm?URI=ao-12-3-555>.
- [198] N. N. Sirota and L. I. Berger. In: *Inzh. Fiz. Zhurnal* 2.104 (1959).

-
- [199] University of Lancaster. *Resonant cavity enhanced photodetectors*. UK Patent Application No. 2110690.1. 2021.
- [200] Mohamed Henini. *Molecular Beam Epitaxy: From Research to Mass Production*. eng. Saint Louis: Elsevier Science Technology, 2012. ISBN: 012387839X.
- [201] Robin F. C. Farrow. *Molecular Beam Epitaxy*. Elsevier Science Technology, 2014, p. 95. ISBN: 9780815518389.
- [202] Kaylee D. Hakkell *et al.* "Integrated near-infrared spectral sensing". In: *Nature Communications* 13.1 (2022), p. 103. ISSN: 2041-1723. DOI: [10.1038/s41467-021-27662-1](https://doi.org/10.1038/s41467-021-27662-1). URL: <https://doi.org/10.1038/s41467-021-27662-1>.
- [203] Shenghong Huang, Ganesh Balakrishnan, and Diana L. Huffaker. "Interfacial misfit array formation for GaSb growth on GaAs". In: *Journal of Applied Physics* 105.10 (2009), p. 103104. DOI: [10.1063/1.3129562](https://doi.org/10.1063/1.3129562).